Luminescent downshifting Silicon and Perovskite quantum dots for efficiency enhancement of crystalline Silicon solar cells.

University of East Anglia

Qais Masaadeh

A thesis submitted to UEA for the degree of

Doctor of Philosophy (PhD)

School of Engineering

University of East Anglia (UEA)

May 2024

Declaration of originality

I certify that the work contained in this thesis, submitted to the University of East Anglia (UEA) for the degree of *Doctor of Philosophy (PhD)*, is my original work, except where due reference is made to other authors. No part of this thesis has been previously submitted by me for a degree at this or any other university.

All necessary permissions for the use of third-party copyrighted works incorporated into this thesis are detailed in the appendix, including references to the specific works and the nature of the permissions obtained.

Qais Abed Alsalam Ali Masaadeh

May 2024

Signature:

Abstract

Quantum Dots (QDs) with Luminescent Downshifting (LDS) properties have been investigated for the efficiency enhancement of solar cells. In this thesis, in-house synthesised Phenylacetylene-capped Silicon quantum dots (PA SiQDs) and commercially acquired $CsPbI_3$ perovskite quantum dots (PQDs) have been applied as LDS coatings on 39 mm × 39 mm polycrystalline Silicon solar cells (pc-Si), by direct Drop Casting (DC) and a novel coating method named Liquid Ethylene-Vinyl Acetate (LEVA).

The PA SiQDs coated solar cells presented an average increase in the short circuit current (I_{SC}) of 0.75% and 1.06% for DC depositions of 0.15 and 0.01 mg, respectively. The increase was further enhanced by full thermal encapsulation of the samples leading to overall improved performance of about 3.4% in terms of I_{SC} when compared to the performance of full thermally-encapsulated reference samples.

The $CsPbI_3$ PQDs coated solar cells (via LEVA) presented an average increase of 0.93% in the I_{SC} for depositions of 0.01 mg, with a maximum of 1.55%.

Reflectance measurements revealed that PA SiQDs coatings achieved reductions of 75.7% in specular reflectance and 43.1% in diffuse reflectance between 350-450 nm. Whereas $CsPbI_3$ PQDs presented reductions of 58.2% in diffuse reflectance and 9.2% in specular reflectance between 350-400 nm, and 64.5% in diffuse reflectance between 400-930 nm. Changes in reflectance were confirmed as a product of LDS that further aided in the electrical enhancements (I_{SC}).

Using SCAPS-1D, a model validated experimental results by simulating the LDS effect through modifying the solar radiation spectrum (AM1.5G). PA SiQDs and $CsPbI_3$ PQDs both showed I_{SC} increases of 1.15% and 1.76%, respectively, both corresponding to 0.01 mg LDS experimental coating.

The observed systematic increase in the I_{SC} is a promising indicator for the use of PA SiQDs and $CsPbI_3$ PQDs as LDS material to improve the power conversion efficiency of pc-Si solar cells.

Acknowledgement

All praise to God.

My passion for science stemmed from my awe of this world and the universe itself. It all began with physics. Through physics, I learned to think, process, and appreciate mankind's existence. As I grew older, my appreciation for applied sciences deepened in ways that theoretical sciences never quite reached. Yet, I always perceived a gap between these two realms, which I yearned to narrow, until it dawned on me: energy! The world needs energy. And what better way to investigate this than by giving life to theories through applications? That was when I decided to become an Energy Engineer, embarking on my journey into the world of energy and research.

This work is the culmination of all the good I have received, directly and indirectly, from everyone I have met in my life. Whether it was for a second, a minute, an hour, a day, or a year, everyone has contributed to this. This acknowledgment is but a fraction of my appreciation for you all.

My greatest gratitude goes to my primary supervisor, Dr. Eleni Kaplani. Her support and guidance are things I will always be indebted for. Her admirable passion for photovoltaics has always fascinated me and spurred me on to achieve more. It is without a doubt that her consistent support, vast expertise, and patience are why I am here today. It has been a privilege to be both her PhD and MSc student.

I would also like to thank Dr. Yimin Chao for welcoming me as a PhD student and sharing his remarkable knowledge in the field of nanotechnology. My thanks extend to his team members, Dr. Chenghao Yue, and especially Dr. Jayshree Ahire, for their kindness, patience, and support.

Of course, I could never forget my friends who always find a way to brighten my day. To Haroon, Peter, Osama, Mohammad Ali, Mohammad Sohrab, Yusuf, and Ameer, thank you for making Norwich feel like home. And to Amar, Mustafa (Tofy), Mustafa (Steve), Zaid, Abdullah, Tariq, Raghad, Moe Tal, Sultan, and many more, thank you for keeping home feeling so close. Special thanks to Mohamad Al-Jayyousi, a brother I never had.

I am forever thankful to my family. To my father, Dr. Abed Alsalam Masaadeh, the most reasonable and resilient person in my life, whose advice I always cherish. To my mother, Intesar Batayneh MSc BSc, the smartest person I have ever met. Not a single civil engineering equation escapes her, a major inspiration for my engineering aspirations. To my sister, Dr. Ruba Masaadeh, in my opinion, the best Doctor of Dental Surgery out there. Her passion and artistic skillset in

dentistry are marvellous. She always brings a smile to my face, whether in her clinic or as my sister.

Last but not least, to my wife, Eloise, whom I appreciate infinitely. She's the secret behind my strength, always knowing how to make life fun and even funnier. I am certain her passion for education will make her an exceptional teacher, perhaps one of the greatest ever. Or perhaps a stand-up comedian – she really is funny, sometimes.

Thank you,

Qais

List of Publications

Journal publications:

Q. Masaadeh, E. Kaplani, and Y. Chao, 'Luminescent Downshifting Silicon Quantum Dots for Performance Enhancement of Polycrystalline Silicon Solar Cells', Electronics (Basel), vol. 11, no. 15, p. 2433, Aug. 2022, doi: 10.3390/electronics11152433.

Note: a second paper with the tentative title of 'Room Temperature Luminescent Downshifting $CsPbI_3$ Perovskite Quantum Dots for Performance Enhancement of Polycrystalline Silicon Solar Cells -Experimental and Simulation Results' is in preparation.

List of Contents

List of Contents

List of Contents

List of Tables

List of Tables

List of Figures

List of Figures

List of Figures

List of Abbreviations

AE: Absolute Error

APTES: (3-Aminopropyl)triethoxysilane

ARC: Anti-Reflection Coating

CAGR :Compound Annual Growth Rate

c-Si: Crystalline Silicon

$CsPbI_3$ PQDs: Caesium-Lead-Iodide PQDs

$CsPbX_3$ PQDs: Caesium-Lead-Halide PQDs, where X=Cl, or Br, or I

CVD: Chemical Vapour Deposition

DC: Drop Casting/Casted

DCM: Dichloromethane

DCon: Down-Conversion

DFT: Density Functional Theory

DS: Directional Solidification

EQE: External Quantum Efficiency

EVA: Ethylene-Vinyl Acetate

FF: Fill Factor

FT-IR: Fourier Transform Infrared Spectroscopy

IEC: International Electrotechnical Commission

I_{MP}: Current at P_M

IRENA: International Renewable Energy Agency

I_{SC}: Short Circuit Current

J_{SC}: Short Circuit Current Density

LARP: Ligand-assisted reprecipitation

LAT: Laser Ablation

List of Abbreviations

LCOE: Levelized Cost Of Electricity

LDS: Luminescent Downshifting

LEVA: Liquid EVA

LPD: Liquid-Phase Deposition

LQE: Luminescent Quantum Efficiency

MAE: Mean AE

mono-Si: Monocrystalline Silicon

NIR: Near Infrared

PA SiQDs: Phenylacetylene-capped SiQDs

PCE: Power Conversion Efficiency

pc-Si: Polycrystalline (or Multicrystalline) Silicon

PECVD: Plasma-Enhanced Chemical Vapour Deposition

PL: Photoluminescence

PLQY: Photoluminescence Quantum Yield

P_M or MPP: Maximum Power Point

PMMA: Polymethylmethacrylate

PQDs: Perovskite Quantum Dots

PSC: Perovskite solar cells

PV cell: Photovoltaic cell

PVD: Physical Vapour Deposition

QC: Quantum Cutting

QD: Quantum Dot

QE: Quantum Efficiency

QY: Quantum Yield

RE: Relative Error

List of Abbreviations

R_S: Series Resistance

R_{Sh}: Shunt Resistance

SC: Spin Coating/Coated

Scanning Electron Microscopy: SEM

SiQDs: Silicon Quantum Dots

SOG: Spin-on-Glass

SS: Sodium Silicate

STC: Standard Test Conditions:

STD: Standard Deviation

THF: Tetrahydrofuran

Transmission Electron Microscopy: TEM

UC: Upconversion

UV-Vis: Ultraviolet/Visible

Vis-NIR: Visible/Near Infrared

V_{MP}: Voltage at P_M

V_{OC}: Open Circuit Voltage

XRD: X-Ray Diffraction

1. Introduction

1.1. Background and motivation

The world's demand for energy is continually on the rise, driven by several significant factors such as the exponential growth in population and advancements in faster automated manufacturing. Simultaneously, there is a growing global awareness of the need for alternative, cleaner, and more sustainable energy sources, leading to a shift towards greener resources, including renewable and nuclear energy. Solar energy technologies, in particular, have gained increasing reliability and popularity, positioning Photovoltaics (PVs) as the fastest-growing renewable energy source.

As depicted in Figure 1.1 below, the average annual growth rate of solar photovoltaics surged to 36% between 1990 and 2019, and 37.5% between 2000 and 2020 [1]. This growth rate far exceeds the 22.6% and 19.1% increase observed in wind energy, for the same intervals respectively, which is the second-largest contributor to renewable energy expansion.
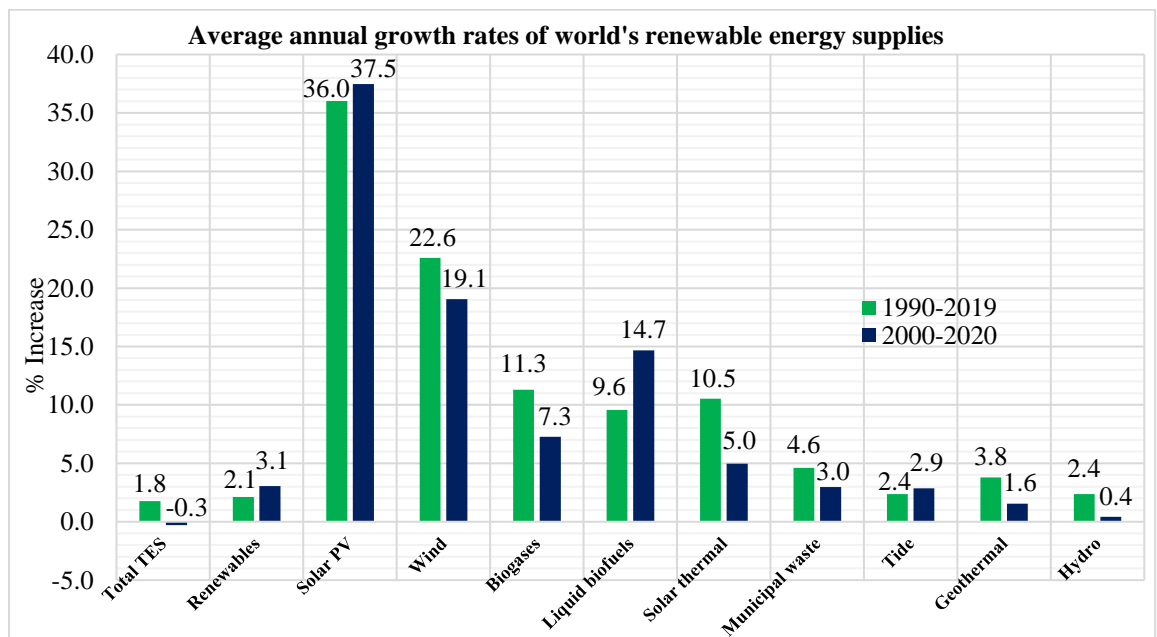
Figure 1.1 Average annual growth rates of world's renewable energy supplies: 2 intervals [1].

Following that up, the Compound Annual Growth Rate (CAGR) for PVs between 2010 and 2021 was 30% [2], this corresponds to an increase in cumulative installed solar PV capacity from 40.3 GWp in 2010 and up to 945 GWp at the end of 2021 [2], [3], with 37% of this peak capacity installed in China, followed by 22% in Europe.
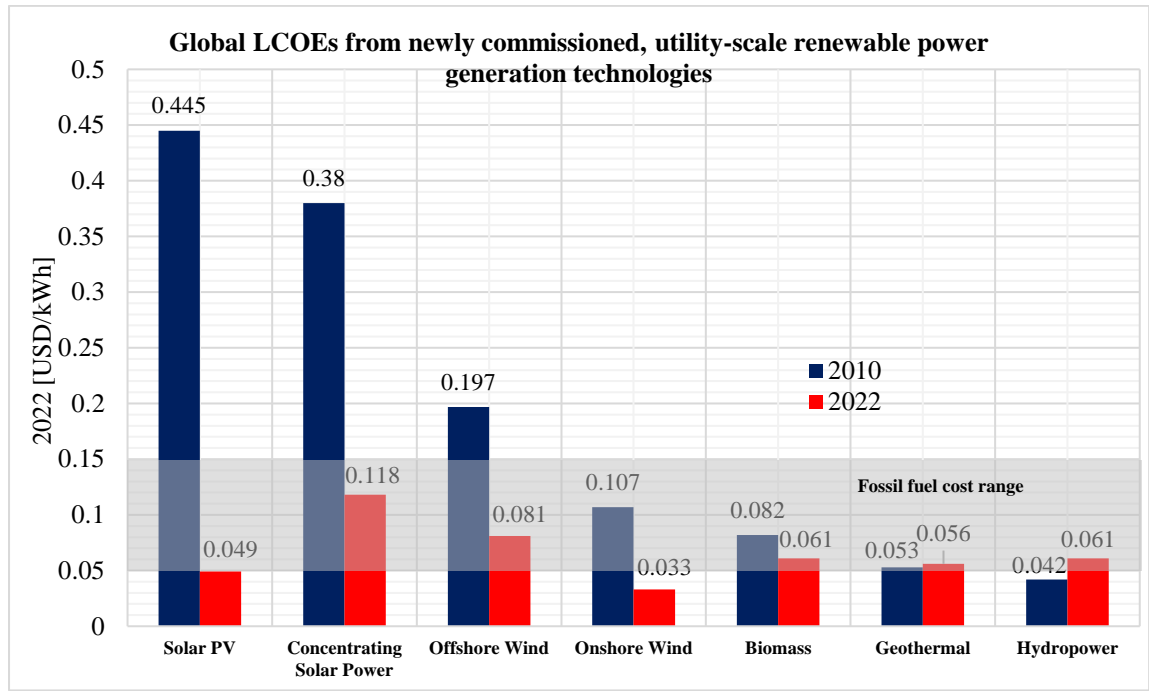
Figure 1.2 Global LCOEs from newly commissioned, utility-scale renewable power generation technologies, 2010-2022 [4].

According to the International Renewable Energy Agency (IRENA), the solar PV has experienced the steepest cost reduction since 2010 compared to any other renewable power generation technologies. This is quantified by a decrease in the Levelized Cost Of Electricity (LCOE) from 0.445 USD/kWh in 2010 to just 0.049 USD/kWh in 2022, an 89% reduction; the steepest decrease compared to any other utility-scale renewable power technology. This can be similarly seen on concentrating solar power electrical technologies too. Although solar PV's global LCOE was the highest in 2010 at 0.445 USD/kWh, it dropped steeply down to 0.049 USD/kWh in 2022 which is now cheaper than Offshore wind evaluated at 0.081 USD/kWh.

The substantial reduction in LCOE over the years is driven by declines in module prices, declines production costs, and reductions in capital and operative costs, where prices fell by 90% from 2009 to 2022 [4]. According to Fraunhofer ISE (2023) [2], as the PV module production doubles, the price went down by 25%, true for the last 41 years.

Silicon-based PV technologies accounted for 95% of the total commercial solar panels production in 2021, with 84% share going to monocrystalline Silicon (mono-Si) solar modules. This massively increased from 24% in 2015 where polycrystalline Silicon (pc-Si) solar modules dominated with more than 70% market share at the time [2].

Although pc-Si solar modules started dominating the market in the early 2000s, its production quantities have significantly declined starting from 2017. The increased interest in mono-Si solar cells was driven by several factors, one of which efficiency and the decreasing cost of manufacturing. Mono-Si solar cells' structure and performance tend to be more consistent at generating higher efficiencies when compared to pc-Si solar cells due to its continuous and uniform single-crystalline structure. Therefore, manufacturers are expected to deviate towards mono-Si solar cells especially when its productions techniques are evolving to be easier and more cost-effective. This was a major reason in its comeback and production market domination.

Efficiencies of single-junction commercial Silicon solar cells improves as technology improves and production costs decrease. As of 2023, the Power Conversion Efficiencies (PCE) recorded for the best well-known Silicon solar cells PV technologies are 26.8% for mono-Si [5], [6] and 24.4% for pc-Si wafer-based technologies [6], [7] as seen in Figure 1.3. Even though mono-Si solar cell efficiencies have been historically in the lead, pc-Si solar cells are showing promising improvements. As mentioned previously, mono-Si solar PV cells possess higher efficiencies due to the physical nature of the cells. They are usually manufactured using Czochralski (C.Z.) growth process where Silicon ingots are grown into high-purity uniform crystals; the solar cells are made up of one piece of Silicon crystals hence the "mono" terminology.

Mono-Si & pc-Si solar cell efficiencies (2018-2023); single-junction.

	Jan-18	Jul-18	Jan-19	Jul-19	Jan-20	Jul-20	Jan-21	Jan-22	Jul-22	Jan-23
mono-Si	26.7	26.7	26.7	26.7	26.7	26.7	26.7	26.7	26.8	26.8
pc-Si	22.3	22.3	22.3	23.2	23.8	24.4	24.4	24.4	24.4	24.4

Solar cell efficiency tables (Versions 52-62)
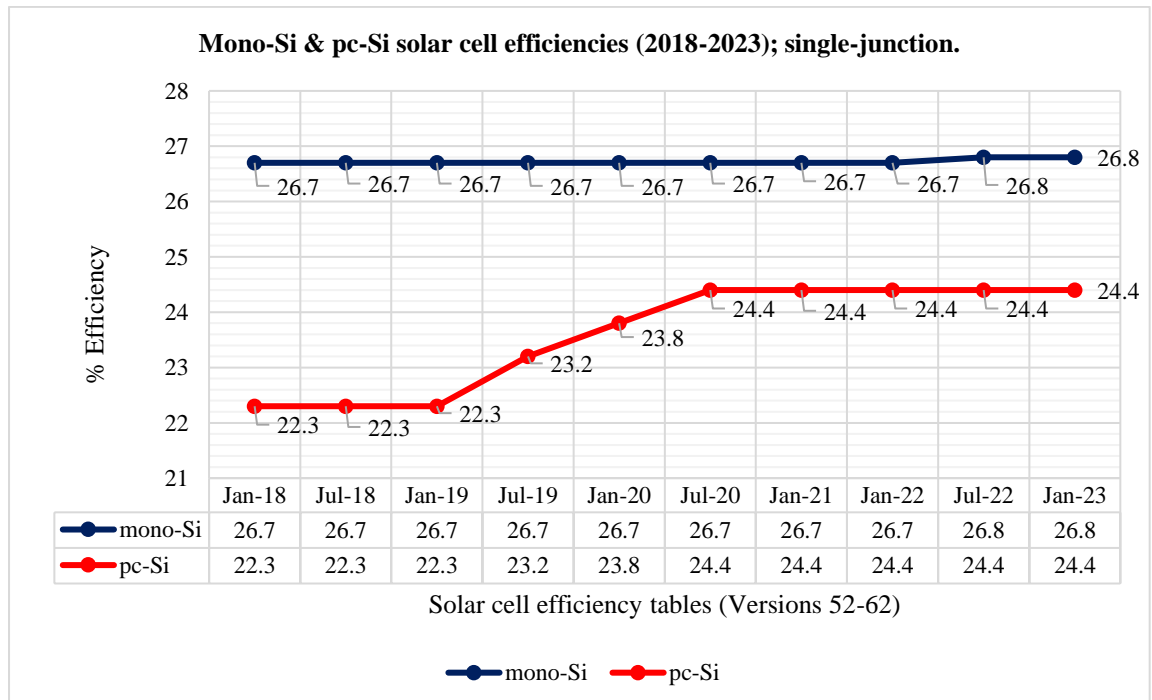
Figure 1.3 Mono-Si & pc-Si solar cell efficiencies (2018-2023); single-junction. Measured under the global AM1.5 spectrum (1000 W/m2 at 25°C (IEC 60904-3: 2008 or ASTM G-173-03 global) [2, 5-15].

On the other hand, pc-Si solar cells can be manufactured using several less complicated means, such as, Directional Solidification (DS), casting, and other more specialised techniques [16]. The nature of these techniques is relatively more accessible when compared to the Czochralski (C.Z.) growth process, hence the domination of poly-Si solar cells in the early 2000s. Nonetheless, this results in lower cell performance and high variability in the quality of the manufactured cells that can reach up to 20%. This is due to the ability of these methods to tolerate lower quality starting material, accompanied by higher production yields which presents variability and poorer control over outcome [17].

Solar cell efficiencies are continuously updated with new generation solar cells reaching improved efficiencies [18]. However, there is a constant effort in exploring solutions for improving further the efficiency of the mature technology of crystalline Silicon cells. Crystalline Silicon solar cells, mono-Si, and pc-Si exhibit high External Quantum Efficiency (EQE) in the visible/near-infrared (Vis-NIR) region (430–1000 nm) of the incident solar radiation [14], [19]. Their spectral response peaks between 850 and 950 nm at >95%, while it is reduced between 20–55% in the range of 300–500 nm [20], [21], [22] as shown in Figure 1.4. With the largest portion of spectral irradiance ranging between 300–700 nm (at sea level AM1.5), it is bound to lose more than half of the incident 1000 W/m2; for reference, the usable fraction of the solar spectrum by Si solar cells amounts to less than half at 468 W/m^2 [23].
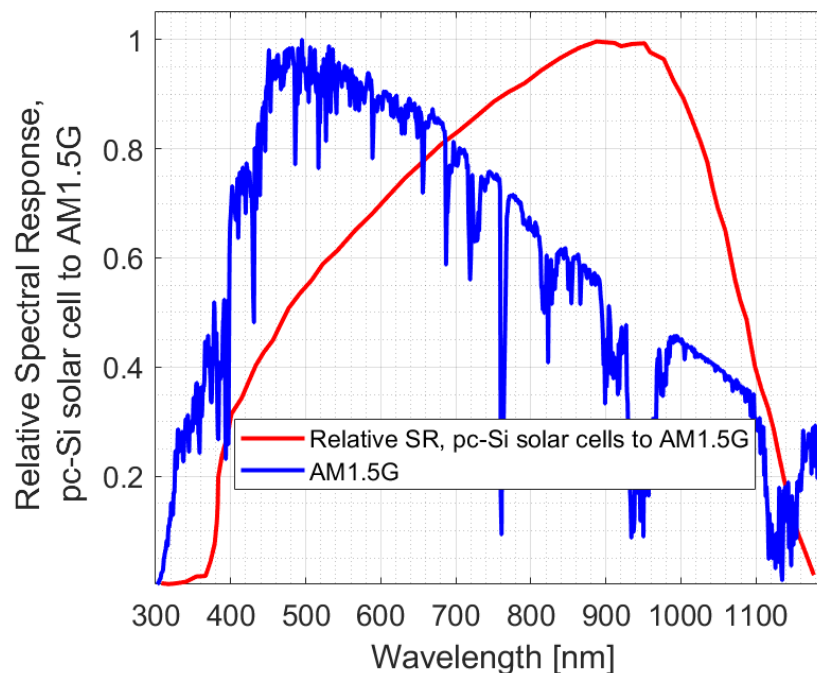
Figure 1.4 Relative spectral response for pc-Si solar cells against normalised AM1.5 Global spectrum (IEC 60904) [21], [22].

Advanced solutions including the use of additives such as luminophores, and solar converters, such as dyes, Luminescent Downshifting (LDS), and upshifting devices have been proposed, including the application of Quantum Dots (QDs), and luminescent solar concentrators, to better match the spectral response of pc-Si solar cells to that of the solar spectrum [24], [25], [26].

LDS involves the conversion of one high-energy photon into a lower-energy one where the spectral response of the solar cell is higher and can be more efficiently absorbed by the solar cell. LDS is considered a subcategory of the quantum process called Down-Conversion (DCon).

The first attempt in exploring the use of DCon to split a high-energy UV photon into two visible light photons was carried out by Dexter in 1957 [27]. DCon can be achieved by the use of host materials (lattices or ions) to achieve quantum efficiencies (QE) bigger than unity [28], as discussed, demonstrated, and modelled by researchers in the literature [29], [30], [31], [32], [33].

The difference between DCon and LDS is the QE achieved by either process; in LDS, a high-energy photon is cut down to a singular low-energy photon and losses due to thermalisation [34], and thus QE below unity.

One of the earliest uses of LDS materials to improve solar cells was performed by Hovel et al. in 1979 [35], where plastic fluorescent materials were implemented for cells with sharp cut-offs in spectral response, and ruby for cells with more gradual cut-offs; efficiency improvements were measured at 0.5–2%. Several different approaches have been used to introduce LDS material to solar cells, with the general trend being adding a transparent host layer that houses the LDS materials on top of the cells. The most used materials were polymethylmethacrylate (PMMA), clear glass, and ideal plastics. These hosted LDS materials such as organic dyes, QDs, and organometallic complexes [36], [37].

This has been used on c-Si cells [24], [34], [37], CdTe [38], GaAs [39], InGaP[40], CIGS [41], DSSC [42], OPV [43], PSC [24]. QDs used for the purposes of PCE improvements can include a variety of commonly used QDs for biological and chemical uses, such as: SiQDs, CQDs, CdS, CdSe, CdTe, $CuInS_2$, CuS, PbS, PbSe, CdSe/ZnS, ZnS, InP, InAs, Ag_2S, Bi_2S_3, Sb_2S_3, $CuInS_2/ZnS$, [28], [39], [40], [44], [45], [46]. Deposition techniques varied and were dependent on the host material. Simple techniques consisted of Spin Coating (SC) [47], [48], Drop Casting (DC) [49], inkjet printing [50], plasma-enhanced chemical vapour deposition (PECVD)[51], [52], and spin-on-glass (SOG) [53]. An in-depth investigation is carried out in Chapter 2, the Literature Review.

As this thesis investigates the utilisation of the LDS phenomenon to enhance the electrical performance of pc-Si solar cells, it is essential to define relevant parameters.

In accordance with the IEC 61215 and the IEC 61853 standards (IEC: International Electrotechnical Commission), the Short Circuit Current (I_{SC}) is the current that flows through a solar cell or module when it is short-circuited, meaning that the current is at its maximum value. While the Open Circuit Voltage (V_{OC}) is the voltage across a solar cell or module when it is open-circuited, meaning that the voltage is at its maximum value. And subsequently, the Maximum Power Point (P_M or MPP) is, as the name states, the maximum power output of a solar cell or when it is operating under specific conditions. It is the product of the voltage (V) and current (I) at the point where the power output is the highest, and can be used to calculate the PCE.

Following that up, another significant parameter is the Short Circuit Current Density (J_{SC}), calculated as the flow of current per unit area under short-circuit conditions. This parameter is particularly important as it normalises the current to the surface area of each cell, allowing for a standardised comparison regardless of size. Hence, it is very useful when simulating electrical enhancements in solar cells.

Moreover, the External Quantum Efficiency (EQE) of a solar cell calculates how efficiently a cell converts incident photons into excited electrons across a spectrum of different wavelengths. By plotting this parameter across the solar radiation spectrum, one can deduce the spectral response of the solar cell technology. Understanding this parameter bases the use of the SCHOTT BG42 bandpass filter in this thesis, where it was used to assess the performance of pc-Si solar cells at its specific operating range from 300-700 nm.

The Photoluminescence Quantum Yield (PLQY) of a semiconductor material quantifies the efficiency of light emission. It is defined by the ratio of the number of photons emitted to the number of photons absorbed. This metric is pivotal in assessing the radiative recombination efficiency of luminescent downshifting (LDS) materials. High PLQY values indicate a material's potential effectiveness in enhancing the performance of solar cells by efficiently converting higher-energy photons to wavelengths more optimally absorbed by the solar cell.

The overall efficiency of a solar cell is denoted as the PCE and is the ratio of electrical power output to the power of incident sunlight, evaluated under standard test conditions that specify light intensity, temperature, and air mass. It incorporates various individual metrics, including I_{SC}, V_{OC}, J_{SC}, and fill factor (FF), to give a comprehensive assessment of the solar cell's capability to convert sunlight into electrical power.

Finally, these parameters are essential for characterising the LDS phenomenon presented by the QDs and for characterising the electrical enhancements observed in the solar cells. For example, LDS increases the number of favourable photons, thereby enhancing the electrical performance of

pc-Si solar cells by boosting the number of charge carriers and, consequently, the I_{SC}. Further elaboration on this will be provided in Chapter 3, the Methodology.

1.2.   Research Aim and Objectives

This doctoral research is characterised by its focused investigation on the direct implementation of LDS Silicon QDs (SiQDs) and Perovskite QDs (PQDs) on pc-Si solar cells as optical planar LDS enhancement devices.

The research methodology is designed to comprehensively investigate QDs in terms of size, structure, chemical composition, surface functionalization, and photoluminescent (PL) properties. This involves both direct chemical synthesis and the acquisition of LDS materials with specified characteristics.

Pc-Si solar cell samples undergo extensive characterisation at various stages of the investigation. At each stage, characterisation includes I-V characterisation, surface reflectance and morphology assessments, and fluorescence microscopy. The process begins with bare cells, progresses through the coating with LDS QDs, and culminates in encapsulation and simulated validation.

Electrical enhancements are evaluated using parameters such as I_{SC}, V_{OC}, and P_M. Graphical plotting is utilised to visualise and investigate the full I-V characteristic profile for each cell at each stage.

Challenges emerge in the direct coating of pc-Si solar cell surfaces with LDS QDs. Experimental factors and variables such as concentration, purity, spread, thickness, host material, environmental degradation, encapsulation, and optical enhancements are systematically altered or controlled. This is to ensure optimal electrical enhancement is achieved as a result of the LDS effect.

Therefore, the overall __aim__ of this doctoral study **is the controlled implementation, engineering, and optimisation of the optical LDS phenomenon presented by SiQDs and PQDs to maximise the efficiency enhancement this phenomenon can bring to pc-Si solar cells.** With consideration to the commercialisation and longevity.

The following key objectives were established to achieve the outlined aim, and ensure optimum results:

1. **To characterise and identify the attributes of the LDS phenomenon of the SiQDs and PQDs.**

The objective involves characterizing LDS QDs prior to their application on pc-Si solar cells. This characterization incorporates assessing the PL profile, chemical composition, morphology, structure and size of the QDs, particularly focusing on their LDS properties.

Concurrently, the pc-Si solar cells are subjected to extensive testing to quantify their electrical and morphological characteristics, aiming to maximise the benefits derived from depositing the LDS QDs.

This dual approach of understanding both the properties of the LDS QDs and the solar cells is crucial for optimising the resultant optical and electrical enhancements. In cases where Phenylacetylene-capped Silicon QDs (PA SiQDs) are synthesized in-house, rigorous characterization and testing are conducted to ensure maximal purity and PL. Similarly, for purchased Caesium-Lead-Iodide ($CsPbI_3$) PQDs, comprehensive characterisation and testing are imperative to confirm the purity and properties of these samples.

The specific choice of these QDs arises from gaps in the literature when assessing them for LDS applications. PA SiQDs have been reported for thermal diffusivity applications [54], but there is no specific focus on their potential for LDS applications, such as enhancing pc-Si solar cells. Additionally, the PA capping functionalization group adds resilience to environmental degradation caused by oxidation and thermal application, which is common in commercial manufacturing settings, which makes them ideal to investigate as LDS devices when considering upscaled commercial application.

On the contrary, $CsPbI_3$ PQDs are well-reported for their outstanding LDS photoluminescent profile. However, they are highly unstable and prone to instantaneous degradation by oxidation and thermal exposure. Therefore, they have not been used in external LDS applications for enhancing pc-Si solar cells but rather in tandem architectures [55]. Investigating both of these LDS quantum dots in the context of electrically enhancing pc-Si solar cells through external applications presents novel endeavours.

2. **To maximise the electrical enhancements resulting from the optical LDS phenomenon.**

Maximising the optical benefits of the LDS effect, as exhibited by QDs, is directly correlated with the electrical enhancements observed in LDS-coated pc-Si solar cells. The research strategy allocates significant time throughout the study period to comprehensively understand and refine

the coating and deposition techniques of LDS QDs. The unique 'inverted pyramids' surface morphology of the pc-Si solar cells [56] presents a notable challenge for achieving uniform depositions. However, devising an effective deposition methodology can exploit this morphology to maximize the LDS optical benefits, thereby enhancing the overall optics of the cells. Distinct methodologies were adopted for SiQDs and PQDs, with the variations and specifics to be extensively discussed in Chapters 4 and 5, respectively. Beyond deposition techniques, this study also delves into encapsulation strategies, intra-cell optical processes, potential commercial applications, and degradation aspects of LDS QDs on solar cells.

3. **To generate reproducible results.**

The established methodology provides detailed, sequential experimental procedures for consistent replication of LDS coated solar cell samples, allowing precise backtracking for adjustments, or troubleshooting. Its design ensures ease of reproduction and accessibility when published. The strict protocol incorporates established techniques, such as the DC method [49], innovatively adapted into the novel LEVA (Liquid EVA: Liquid Ethylene-Vinyl Acetate) coating method, which is introduced in Chapters 3 and 5, that serves as an example of reproducibility and convenience.

Moreover, by actively choosing to focus on pc-Si solar cells, this investigation aims to narrow the performance gap between these cells and their closest, better-performing competitor: mono-Si solar cells. Additionally, this focus allows for higher accessibility to the reproducible methodology due to the fact that pc-Si solar cells are more readily available in the market at a lower price point.

4. **To numerically validate the results with modelling and simulation.**

An adaptable simulation method is employed to utilise characteristic and experimental data of LDS QDs, generating a simulated model that demonstrates LDS electrical enhancements on c-Si solar cells. Aligning simulated and experimental results authenticates the experimental methodology, confirms the LDS effect, and strengthens the outcomes of this doctoral research.

1.3. Thesis Structure

This thesis comprises 8 comprehensive key chapters that delve into the focused investigation conducted during the doctoral research, which centres on the direct implementation of LDS PA SiQDs and CsPbI$_3$ PQDs on pc-Si solar cells as optical planar LDS enhancement devices. The chapters are structured in a chronological sequence, with three primary categories: PA SiQDs, CsPbI$_3$ PQDs, and Simulation.

Chapter 1 sets the stage by revealing the motivation, aims, and objectives of the research. Subsequently, **Chapter 2** conducts a thorough review of the literature, providing insight into the working principles of LDS and its application in solar cell enhancement. It explains the mechanisms behind LDS, the transformation of nanoparticles into LDS QDs via quantum confinement effects, surface engineering of QDs through chemical addition of ligands, and the protective role of these ligands in QD preservation. The chapter delves into optical interactions within deposited LDS layers and presents reported outcomes of utilising LDS SiQDs and PQDs for enhancing pc-Si solar cells. Moreover, it outlines the synthesis processes of SiQDs and PQDs, shedding light on how fabrication methods influence QD size, PL properties, defects, and shelf life.

Chapter 3 outlines the research methodology, experimental procedures, and the instrumentation employed, providing an in-depth understanding of their functionalities. Additionally, it introduces an innovative coating method known as LEVA, designed to enhance the LDS effect delivered by $CsPbI_3$ PQDs in pc-Si solar cells.

Chapter 4 and **Chapter 5** represent the technical heart of the thesis, presenting experimental results derived from the integration of PA SiQDs and $CsPbI_3$ PQDs onto pc-Si solar cells, respectively, with **Chapter 4** delving further into the synthesis of PA SiQDs. Both chapters employ conventional assessment methods, including liquid sample characterisation and solid (pc-Si) sample characterisation through techniques like standardised I-V characterisation, among others. While **Chapter 4** follows a traditional approach involving direct DC and thermal encapsulation, **Chapter 5** employs the novel coating method (LEVA) that optimizes LDS enhancements by extending the active α-phase $CsPbI_3$ PQDs characterized by vibrant PL properties.

Chapter 6 introduces results generated through a simulation model that modifies the AM1.5G solar irradiance based on PL measurements obtained from PA SiQDs and $CsPbI_3$ PQDs using SCAPS-1D software. These simulated outcomes serve to validate the experimental results.

Chapter 7 consolidates and discusses the findings from the preceding technical chapters, providing a comprehensive overview. Finally, **Chapter 8** serves as the conclusion, laying the groundwork for future recommendations and endeavours based on the key discoveries presented throughout the thesis.

2. Literature Review

This chapter comprehensively reviews the literature relevant to the use of LDS QDs and related materials for enhancing the efficiency of solar cell technologies. It specifically focuses on c-Si solar cells, SiQDs, and PQDs.

The review encompasses various aspects including the LDS quantum phenomenon and its working principle, the Quantum Confinement effect in QDs, surface functionalization and capping, LDS application methods and the associated optical processes, reported electrical outcomes and the current State of the Art. Additionally, the chapter delves into the synthesis and fabrication processes of SiQDs and PQDs.

2.1. Luminescent Downshifting (LDS)

2.1.1. LDS, working principle.

As previously introduced, LDS is a form of DCon that converts high-energy photons into lower-energy ones where the spectral response of the solar cell is higher and can be more efficiently absorbed by the solar cell.

DCon is the umbrella term for the conversion of high-energy photons into lower-energy photons through an exciton (electron-hole duo), where the number of converted low energy photons is higher than that of the absorbed photon. This is caused by a combination of LDS and Quantum Cutting (QC), and the continuation of one other photoluminescent quantum process, Upconversion (UC). Quantum cutting is when one high-energy photon is always cut down (converted) into two lower-energy photons. While upconversion is when two lower-energy photons, either absorbed or resulted from LDS and QC, are absorbed, and remitted as one high-energy photon.

Some researchers consider DCon to be LDS [24], while other define LDS as a photoluminescent process that goes under the DCon umbrella as explained above [57], for instance, Jestin et al. (2022) [58] referred to LDS as a DCon process that occurs with an EQE below 100%. The latter umbrella definition was used to base the understanding of LDS in this doctoral research, to draw the difference between LDS and QC. This is illustrated in Figure 2.1.
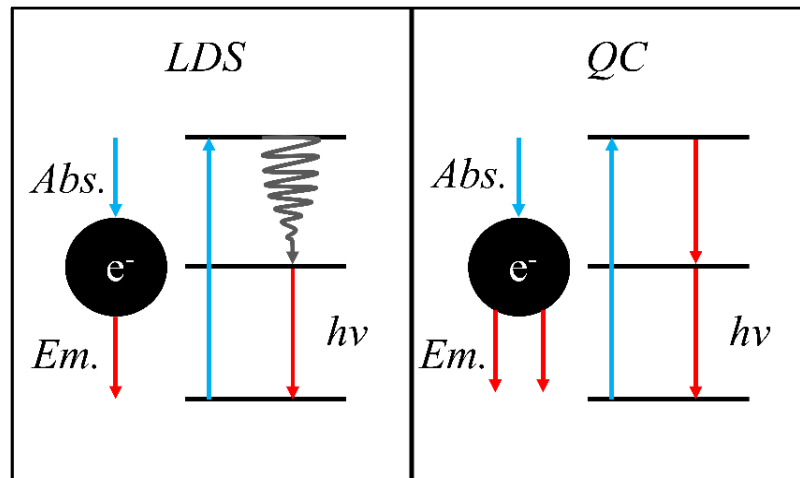
Figure 2.1 Simple electron energy level diagram showcasing the difference between the photoluminescent quantum processes of Luminescent Downshifting (LDS) and Quantum Cutting (QC) [24].

The major difference between LDS and QC is the number of down-converted photons re-emitted, and the wavelengths of these lower-energy photons. In LDS, when a higher-energy photon knocks an electron out of ground state, the electron undergoes non-radiative relaxation processes where a portion of that energy is lost non-radiatively as heat as it relaxes down to ground state. The rest of the energy is radiatively remitted as a lower-energy photon. While for QC, as an electron relaxes, it loses the absorbed energy in two or more lower-energy photons with low-to-none of that energy lost to non-radiative relaxation processes, i.e., heat.

2.1.2. Quantum Confinement effect

Photoluminescent materials, such as dyes, nanoparticles and QDs, can be engineered to perform accurate LDS or QC process where the emitted photons are always within a desired range of wavelengths [59], [60], [61].

It is well constructed in the literature that the PL of nanoparticles is directly dependant on their size [62], [63].

The Quantum Confinement [64] effect is notably significant when the size of a nanoparticle becomes smaller than the exciton Bohr radius of its bulk counterpart [65], [66], [67], [68], hence the term Quantum Dots (QDs). An Exciton is defined as an electron-hole pair [69] and is created by the electron's absorption of energy form an external source, such as a photon. The physical separation between electron and hole in an electron-hole pair is the exciton Bohr radius. For semiconductor, the exciton Bohr radius describes the distance at which an electron can freely roam

from its nucleus as a charge carrier in the bulk of that semiconductor [70], this is also partially represented by the bandgap energy. As a nanoparticle's size falls below the exciton Bohr radius, the exciton gets three-dimensionally confined to a discrete radius, therefore becoming a QD of a specific bandgap. The smaller the QD gets, the stronger quantum confinement affects the crystal, this is reasoned by the increased forced proximity of the electron to its paired hole. This increases the electrostatic Coulomb force which is naturally an inverse square law where the attraction force between two oppositely charged particles dramatically increase as the distance drops [69] as shown in equation 2-1 and Figure 2.2 [71], [72], [73].

$$F = k\frac{|q_1 q_2|}{r^2}$$

(2-1)

Coulomb's law of static attraction, k is Coulomb's constant, q_1 is first point charge, q_2 is second point charge, r is the distance between both charges.
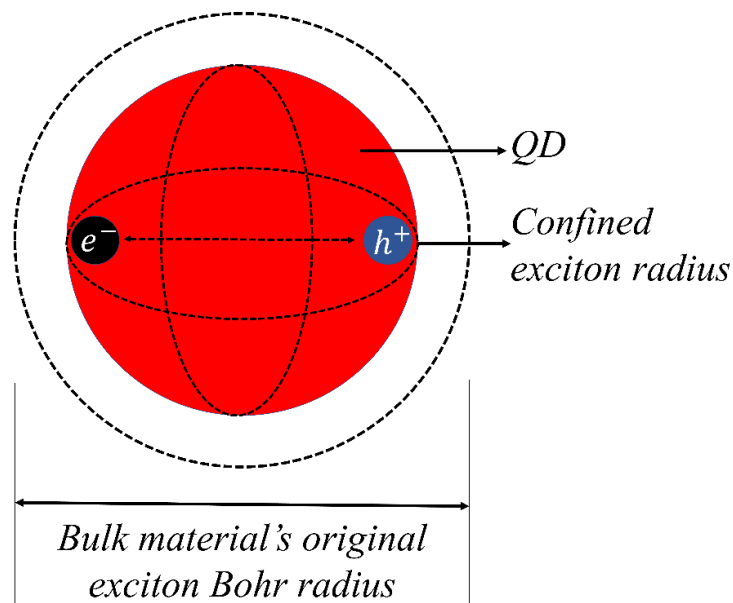
Figure 2.2 Confined exciton radius in a QD resulting from Quantum Confinement [72].

As demonstrated in Figure 2.3 [74-78], as the exciton gets confined in space due to quantum confinement, the electrostatic Coulomb force of attraction increases, which leads to the increase in bandgap energy.

Therefore, an increase in the bandgap is inevitable. These further reasons how smaller QDs possess a significantly larger bandgap than its bigger QD peers made from the same material.

Size reduction below the exciton Bohr radius leads to bandgap increase
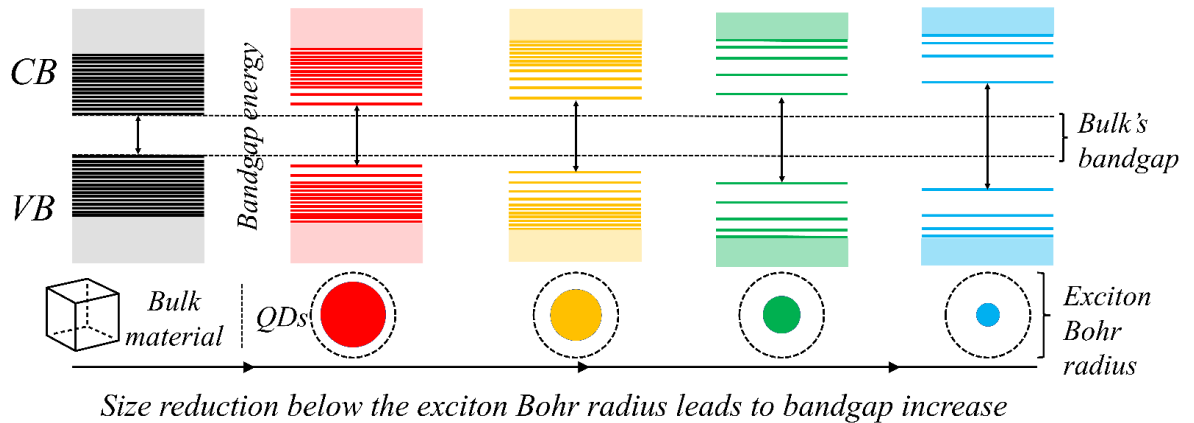
Figure 2.3 Simple illustration of Quantum Confinement effect: effects of reducing a nanoparticle's size below its bulk material's exciton Bohr radius. [72].

Ekimov et al. (1985) [79] have found that Quantum Confinement effects is significant for Silicon nanoparticles smaller than 10 nm in diameter Therefore, as the QDs is synthesised to sizes below 10 nm, the exciton becomes confined in a discrete bandgap. Moreover, Schuppler et al. (1995) [60] have reported an existing but weaker correlation between the quantum confinement effect and PL for particles bigger than 8 nm, where maximum relative PL has been noticed for smaller particles sized at 1 nm and 1.6 nm; measured at 1.85 eV and 1.7 eV respectively. Measurements done by Van Buuren et al. (1998) [80] have shown a maximum direct correlation between size and PL for SiQDs of sizes up to 4 nm. Furthermore, Takagahara et al. (1992) [74] have provided convincing evidence on the quantum confinement effect as evidence of conversion of the indirect bandgaps in Si and Ge (Germanium) bulk semiconductors to discrete, more direct, and bigger bandgaps in 1-3 nm Si and Ge QDs responsible for PL at room temperature.

The reason behind the strong and evident quantum confinement happening for SiQDs below 5 nm is the fact the exciton Bohr radius of Silicon is ~5 nm [81], [82]. However, if the size of a nanoparticle falls on the upper range if its exciton Bohr radius, quantum confinement is still observed and can be relatively strong as, therefore is classified as a QD [75].

Hence, the size of a QD is the main means of controlling the bandgap energy which engineers the photoluminescent properties [83]. By determining size, the desired absorption and emission wavelengths can also be determined. For instance, Kim et al. (2006) [84] have reported the reduction of SiQDs from 4.9 to 2.9 nm in size, thus increasing the bandgap from 1.73 eV to 2.77 eV. This corresponded in the shift of emission PL emission wavelength from ~720 nm down to 460 nm.

Engineering the size holds a key role in deciding the bandgap of the QDs used to enhance pc-Si solar cells by their LDS capability. For pc-Si solar cells with significantly higher solar response

presented at the NIR region, 650-950 nm [20], [21], [22], it is expected that the size of unfunctionalized or pure SiQDs used for this purpose is below 8 nm based on a PL of ~1.37 eV or 905 nm [60].

However, as the quantum confinement effect is only significant on QDs of pure cores, i.e., Si, Ge, C and graphene, and so on. Researchers have also reported the use of external chemical ligands which directly attach to the core shell of the QD. The combination of quantum confinement and ligands extends the customisability of the PL properties.

With the focus of this doctoral thesis on PA SiQDs and $CsPbI_3$ PQDs, it is essential mentioning that the exciton Bohr radius of $CsPbI_3$ PQDs is reported at 6-7 nm [85], [86], [87], [88].

The following subsection will uncover that for QDs with relatively more complicated structures, such as that of the $CsPbI_3$ PQDs, surface and core functionalisation serve a significant role in preserving and altering the physical and PL properties of QDs [86].

2.1.3. Capping ligands and surface functionalisation: bandgap alterations and degradation prevention

Attaching chemical groups to the core of a QD adds extra depth to its bandgap in a way quantum confinement effect cannot. As the size of a nanoparticle drops near or below its bulk material's exciton Bohr radius, quantum confinement proves a direct correlation between the size reduction and the increase in the bandgap. However, this is limited to the type of core element used. Even though the engineering the size can control the PL properties, limitations can apply. Limitations such as fabrication methods, core material, and degradation can limit the precision of the desired size of a QD, hence ligands can be used to overcome these obstacles.

By adding chemical groups as ligands to these QD cores, also known as surface functionalisation, extra electron surface states and defects that function as bridges between existing bandgaps are introduced, illustrated in Figure 2.4. These additional quantum surface states allow the surface electrons to travel between states of specific bandgaps (characteristic to the ligand surface group), thus reemitting photon of specific engineered wavelengths, and enhances the radiative recombination process responsible for emission by elongating its lifetime [68]. In the world of nanoparticles, surface functionalisation serves as means of enhancing biocompatibility of nanoparticles and QDs with living organisms [89]. Nevertheless, it is also useful in specifically engineering the physical and PL properties of QDs, and further protect them for oxidising [90], [91] and environmental degradation [92].

Combining the quantum confinement effect with chemical ligands increases the discreteness of these bandgaps by forcing distinct excitation and emission pathways, also known as exciton recombination routes, in place.
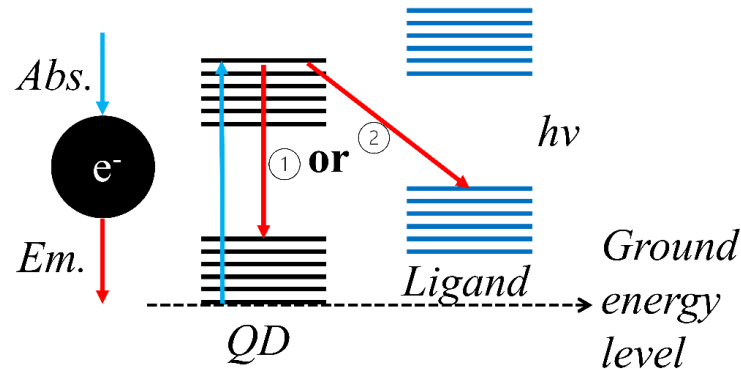
Figure 2.4 Alternative exciton recombination route: one use of chemical surface functionalisation ligands. [93]

For instance, PA SiQDs perform differently to the non-functionalised SiQDs. This was demonstrated by Angı et al. (2016) [94] where the LDS emission of PA functionalised SiQDs, of 3 nm, was observed at 735 nm, with absorption normalised at 300nm. Similarly, Zhou et al. (2015) [93] reported a 70 nm red-shift in LDS emission of 5 nm SiQDs caused by Type-2 surface functionalisation by using MeOTPA. Emission peaked at 749 nm, while to their original sample of decyl-passivated SiQDs peaked at 679 nm. For reference, SiQDs of similar size are expected to perform LDS emission between 400-500 nm [95].

However, adding the same chemical group on a 6 nm sized SiQDs was reported to produce different results. Ashby et al. (2013, 2014, 2015) [54], [96], [97] reported changes in thermal diffusivity on SiQDs by the addition of PA functionalisation group, with focus on thermal applications, such as batteries. These larger SiQDs showed LDS emission peak at 495 nm.

While surface functionalising of QDs is focused on changing the optical properties, it provides protection against oxidation and degradation. Most common means of degradation for QDs differ from one species to the other. For instance, an SiQD core's outer surface tend to fully oxidise within 3 minutes [91]. For CsPb-Halide PQDs, stability at temperatures equal to room temperature or higher has always been a characteristic challenge.

These issues have been successfully solved using specific chemical ligands for surface passivation. Hydrogen termination and Hydrosilylation reactions have been reported as two of the most common chemical processes used for protecting SiQDs by surface functionalization [98]. There is a plenty and numerous methods that can achieve hydrogen-terminated SiQDs, such as, Silane gas plasma synthesis (SiH_4) [84, 99-103], electrochemical etching [104-107], and husk recycling [108]

to name a few. While hydrosilylation reactions, the chemical addition of Silicon hydride (Si-H) [109], tend to be less common for the processing or synthesising of SiQDs, it can be achieved through several methods, such as thermally induced hydrosilylation reactions [50], [110], catalytic hydrosilylation [111], [112], and microwave-assisted hydrosilylation reaction [113-118].

While hydrosilylation preserves SiQDs from oxidation it also enhances dispersion in solvents, especially organic solvents [119-121].

As for $CsPbI_3$ PQDs, oleic acid and oleylamine capping have been the most common chemical surface functionalisation groups used to stabilise these QDs at room temperature and relatively higher [122]. However, density functional theory (DFT) studies have proved these conventional capping ligands contribute to the long-term instability of $CsPbI_3$ PQDs, and were replaced by: lecithin capping ligands [123], thiol capping ligand [124], carboxylic acid and benzylamine capping ligand [125], a novel Sodium Dodecyl Sulphate ligand that enhanced stability and PL properties too [126], a novel oleic-acid only capping that excluded oleylamine [127], a mid-processing treatment (LARP method) [128], and purification method using methyl acetate (MeOAc) [129], [130]. These methods that utilised improved capping ligand and enhanced synthesis procedures extended shelf life from a few days up to 6 months in shelf storage.

2.1.4. LDS QDs and Silicon solar cells enhancement

As previously mentioned, the earliest uses of LDS materials to improve several types of solar cells was performed by Hovel et al. in 1979 [25], [35], [36], where plastic fluorescent materials were implemented for cells with sharp cut-offs in spectral response, and ruby for cells with more gradual cut-offs; efficiency improvements were measured at 0.5–2%.

Crystalline Silicon solar cells, mono-Si, and pc-Si exhibit high EQEs in the Vis-NIR region (430–1000 nm) of the incident solar radiation [14], [19]. Their spectral response peaks between 850 and 950 nm at >95%, while it is reduced between 20–55% in the range of 300–500 nm [20-22]. With the largest portion of spectral irradiance ranging between 300–700 nm (at sea level AM1.5), it is bound to lose more than half of the incident 1000 W/m^2; for reference, the usable fraction of the solar spectrum by Si solar cells amounts to less than half at 468 W/m^2 [23].

Therefore, the employment of the right LDS material to enhance pc-Si solar cells (specifically) will ideally absorb photons in the UV-blue region, 300–500 nm, and boost in the visible/near-infrared (NIR) region, 850-950 nm, where the pc-Si solar cells exhibit the highest solar spectral response [21], [24], [36], [37], [111], [131].

LDS layers not only compensate for direct optical losses, like variations in spectral response at different wavelengths, but also mitigate other optical loss mechanisms affecting electrical performance. These include recombination losses, increased surface reflectance, and heightened non-radiative recombination due to absorption by the Anti-Reflection Coating (ARC) [36], [132]. One way of achieving this is by avoiding non-radiative exciton recombination processes [24], [133] such as Auger [134] and Shockley–Read–Hall [135] recombination.

However, since the LDS layers are externally added onto solar cells, they inflict no physical or chemical changes to the architecture of the solar cells, therefore the maximum the electrical enhancement is capped by the PLQY of the LDS luminophore with a maximum of 100%. Thus, the maximum PCE of any LDS-enhanced cell cannot pass its physical limit; that is the Shockley-Queisser limit of 33.7% for single-junction solar cell operating under AM1.5 solar irradiance [24], [136].

To measure the effectiveness of LDS layers in enhancing the electrical performance of solar cells, researchers focused on measuring the I_{SC}, as it directly correlates to the enhancements presented by the LDS layer.

Simply put, the photocurrent generation in a solar cell is intrinsically linked to the incident light's intensity, as it governs the number of electron-hole pairs created within the cell. The absorption of photons by the solar cell initiates the process of charge carrier generation. In the case of pc-Si solar cells, they exhibit heightened sensitivity to photons within the Vis-NIR region of the electromagnetic spectrum. Consequently, a larger quantity of photons in this range is absorbed, leading to an increased generation of electron-hole pairs, and subsequently a higher magnitude of generated photocurrent.

LDS QDs have collected significant attention as potential enhancements for photovoltaic cells, serving as an alternative to other luminophores like organic dyes and rare-earth complexes/ions. Their wide availability for applications in fields like biochemistry and bioimaging [68], [104] has made them accessible for various purposes. While the specific applications may vary, LDS QDs provide precise tuning of PL characteristics which makes them attractive optical enhancement devices for a variety of solar cell types.

With such tunability, LDS QDs have been used on multiple solar cell technologies for the purpose of PCE improvements. Some of these solar technologies were crystalline-Si (c-Si) cells [24], [34], [37], CdTe [38], [131], [137], [138], GaAs [39], InGaP [40], CIGS [41], [139], DSSC [42], OPV [43], PSC [24], [140], and Perovskite solar cells (PSC) [141].

The literature investigated the use of a wide variety of readily available QDs for solar cell PCE improvements which are commonly used for biological and chemical applications. These QDs were either acquired or synthesised specifically for such investigations and used on numerous solar cell technologies and structures as discussed in the next paragraph.

Beginning with SiQDs, these LDS QDs have demonstrated a PCE increase of 0.4% [53], and 12.4% [142], [143], 4.2% [144] in c-Si, and 1.06% [145], 3-10% [49], 2-3.7% [47], [50] in pc-Si. Subsequently, CQDs achieved a 12% increase in OPV [146]. In contrast, CdS QDs recorded a 33% increase in c-Si [147], 21.52% in GaAs [148], and 1.7% in CdTe [149]. CdO QDs exhibited a 14% increase on mono-Si [150], while CdSe/ZnS QDs achieved 2.87% in GaAs [151]. Furthermore, CdSe/ZnS QDs displayed a 24.65% increase in GaAs [39], 5% on DSSC [42], followed by 3.58% [152] and 5.5% [153] in c-Si solar cells. Continuing, ZnSe QDs showcased a 4.21% increase in PSC [154], and $CuInS_2$/ZnS QDs achieved 3.95% [155], 2.1% [156], and 10.5% [44] in c-Si. Lastly, various Caesium-Lead-Halide ($CsPbX_3$) PQDs achieved diverse results, with $CsPbCl_3$:Mn^{2+} recording a 6.2% increase in pc-Si [157] and 3.34% in PSC with the $CsPbCl_3$:Mn variant. $CsPbBr_3$ achieved 14.06% in GaAs and 4.5% in CIGS [158], while $MAPbBr_3$ achieved 1% in pc-Si [26].

It is apparent that the electrical increases in PCE presented by QDs varies widely based on the type of the solar cell technology used, exact properties of the QDs used, and the exact experimental approach utilised by researchers.

With the focus on c-Si solar cells, a variety of novel, improved, and common LDS materials were used and proposed for the purpose of PCE improvement, such as: QDs, dyes, and rare-earth complexes like lanthanides [24], [36], [37].

Some examples of QDs [142] utilised for this purpose are SiQDs [49, 51, 53, 144, 145, 159-164], PQDs such as $CsPbX_3$ (X=Cl, or Br, or I) [25], [26], [129], [157], [165], [166], ZnO [167], [168], ZnS [169], ZnSe/ZnS Ag [170], CQDs and CdTe [171], [172], CdSe [173], [174], and CdSe/CdS [175].

The list continues for with dyes and organic dyes like LUMOGEN [176], [177], and lanthanides like Eu^{3+} [29, 38, 133, 178-186].

It should be recognised that pioneering research in solar cell enhancement initially focused on dyes and lanthanides; however, QDs have presented substantial advancements. These include exceptional tunability, an elevated Stokes shift that diminishes reabsorption losses, broad absorption bands that extend into the UV spectrum (facilitating a wider range of excitation wavelengths), and an emission peak characterised by a symmetric Gaussian profile [187], [188],

[189], and high quantum efficiencies [190]. Although dyes are more cost-effective and lanthanides exhibit greater thermal stability, the remarkable tunability of QDs with respect to their PL characteristics, coupled with the potential for thermal stabilisation through chemical routes, has rendered them a highly valuable and increasingly popular alternative in LDS applications.

The outlined results in this subsection include diverse experimental scenarios, including ideal ones. It's crucial to explore how host materials enhance the optical properties of certain LDS materials and luminophores when externally applied to various solar cell technologies, especially considering the full encapsulation of commercially available solar panels. Understanding the role of host materials in enhancing the optical processes of an LDS layer holds significant importance in the experimental work presented in this thesis. This significance is emphasised as the research covers two hosting methods: thermal encapsulation in Chapter 4 and the innovative LEVA coating method in Chapter 5.

This discussion is detailed in subsection 2.1.5.

2.1.5. LDS applications methods and optical coupling

It was apparent in the literature that using the right host material and deposition technique is essential to harvest the optimum optical benefit an LDS layer can offer. This is due to the additional optical processes these layers offer.

As Figure 2.5 shows, and assuming the wavelength of incident photon is within the absorption range of the LDS device (QDs), the numbered optical processes are as follows [36], [191]:

1. Incident photon to be absorbed and remitted by LDS.

And assuming isotropic reemission from the QDs:

2. Direct LDS emission into the cell.
3. Total internal reflection at air-layer surface interface.
4. Reabsorption of LDS photon by another QD.
5. A consecutive remission by the second/next QD.
6. An escaping LDS photon, not internally reflected, through top escape cone.
7. An escaping LDS photon through the sides of the LDS layer.
8. Fully transmitted photons that are not absorbed by LDS QDs, any wavelength.
9. Fully or partially reflected photons, reflected by host material. Can be perpendicular or angled.
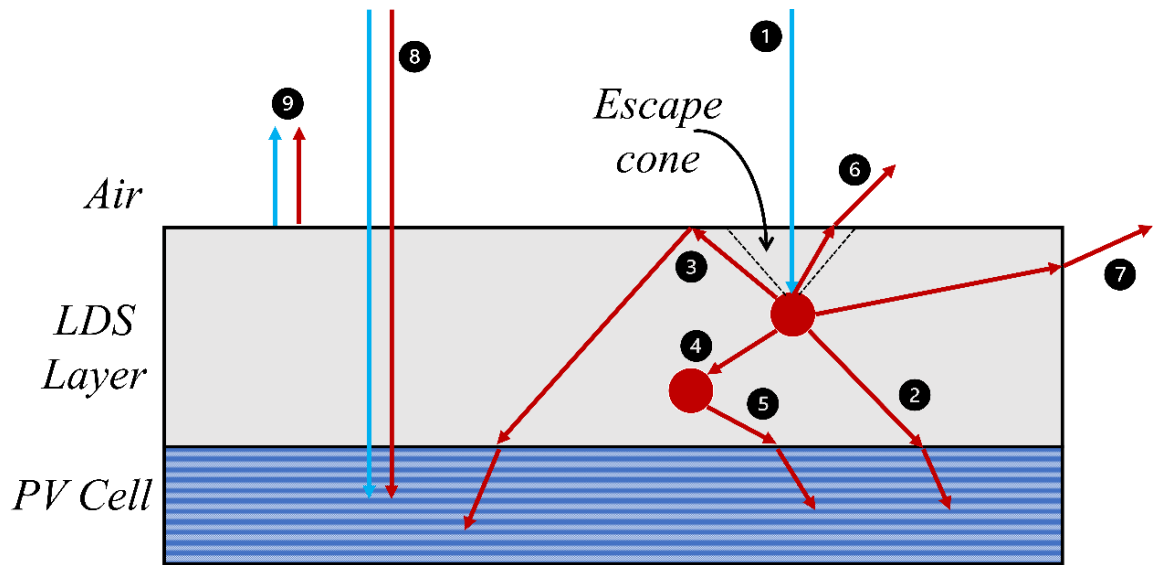
Figure 2.5 LDS layer optical processes on the top of a solar cell. [36], [191]

Processes numbered 2, 3, 4, 5, are perfect examples of light trapping properties LDS layers can introduce to solar cells [192]. These processes are expected to occur within quintessentially thermally encapsulated solar cells [193]. However, unlike encapsulation, these processes are generated by the LDS quantum process making QDs useful in light trapping [194-196] as well spectral conversion.

These processes mark the main means by which LDS enhances solar cells in addition to enhancing the spectral response of these cells by DCon. In fact, encapsulating or hosting LDS materials onto solar cells comes in pairs when considering LDS materials, where researchers have reported the use of host material to be an effective tool in maximising the extraction of electrical benefits from LDS layers. In addition to safeguarding LDS materials from environmental degradation, host layers optimise optical for incident solar radiation (by optimising refractive indices) and reduces optical losses due to scattering as seen in process number 3, which in turned enhances the EQE as reported by González-Díaz et al. (2020) [197] and Ho et al. (2022) [180]. However, Klampaftis et al. 2009 [36] emphasised that adding an LDS layer can also create additional optical interactions that introduces loss mechanism if gains do not compensate for such losses. This occurs if the parasitic absorption from the material is bigger than offered gains, or LDS emission is lower than unity of LQE for the LDS layer (which influenced by PLQY of QDs and other losses), or an overlap of LDS absorption and emission bands which can cause reabsorption losses as portrayed by process number 4 [198], or LDS re-emitted photons escaping out of the layer as shown by processes number 6 and 7 due to isotropic emission [199] where losses occurring through these two processes have been estimated at ~12.5% at air interference with materials of 1.5 refractive index [35], [36], [200], and finally an increase of external reflection that overpower beneficial

internal reflection. Therefore, it is important to produce LDS layers that do not possesses these disadvantageous properties in order to gain enhanced optical coupling and electrical improvements.

Numerous numbers of different host materials have been investigated to introduce LDS material to solar cells, with the general trend being the use of transparent polymers that are capable of housing the LDS materials and optically boosting the LDS phenomenon. Some of the most regular materials were polymethylmethacrylate (PMMA) [34], [138], [149], [169], [201], [202], glass [53], SOG [53], and ideal plastics; PVA [179] and EVA [192].

Some of these materials were temporary and used to only deposit the LDS material onto the cell through direct methods like SC and DC, after which they evaporate. Some of these materials are paint thinners and solvents, such as Toluene, Alcohol, and Dichloromethane (DCM) [145], [203], [204].

Deposition techniques varied and were dependent on the host material and type of deposited layer ranging from simple external layering to active layer addition to solar cells. However, all these methods are based on simple techniques such as of SC [47], [48], [205], DC [49], [206], inkjet printing [50], [207], chemical vapour deposition (CVD) and physical vapour deposition (PVD) [208], plasma-enhanced chemical vapour deposition (PECVD) [51], [52], and spin-on-glass [53], and vacuum lamination [184] or direct application [197], [209] of externally prepared LDS-embedded polymers and plastics.

Following that up, LDS layer thickness is an important parameter for controlling the optical processes for optimum optical coupling as it dictates the optical pathways for incident solar photons. Thickness itself is not the sole factor, as the concentration of LDS material and type of host material are interconnected factors in determining what the optimal thickness should be. For optimal results, host layers need to minimise parasitic and loss mechanisms and optimise the LDS phenomenon, light trapping properties and the overall optical coupling. For externally applied SiQDs LDS layers on c-Si solar cells, the reported literature goes through various thicknesses starting from several nanometres [49], [210] to tens [50] and hundreds [47], [53], [144], [162] of nanometres. In their review, Flores-Pacheco et al. (2020) [142] deducted PMMA-based LDS layers achieved best electrical enhancements at 100 nm. As for PQDs applied to c-Si solar cells, thicknesses averaged at higher values from hundreds of nanometres [211] and up to several microns [26] and even a hundred micron [212].

Ideally, optimum thickness can be estimated based on ideal layer interactions, however the reported literature has shown a repeated theme in using "trial and error" approaches in varying the thicknesses to find the optimum, both experimentally [49], [142] and via simulation [213].

2.1.6. Reported Electrical Results: SiQDs & PQDs on c-Si solar cells.

Given the central focus of this doctoral research on SiQDs and PQDs, this and the upcoming subsections will be dedicated to exploring the relevant research concerning these materials and their applications in enhancing crystalline Si solar cells by LDS.

Furthermore, this subsection focuses on reported results obtained by the direct application of SiQDs and PQDs on c-Si solar cells only, through methods like SC, DC, and host materials (like PMMA or EVA). While subsection 2.1.4 looked into other types of LDS luminophores and materials that were applied to several solar cell technologies, this focused subsection delves into reported research on planned material groups for the PhD project; SiQDs and PQDs.

Starting with SiQDs, Table 2.1 display reported increases in the I_{SC} (or J_{SC}) and PCE of c-Si solar cells resulting from the addition or deposition of SiQDs on the surface of these cells.

Table 2.1 Overview of SiQDs used on c-Si solar cells and enhancements achieved by previous studies.

SiQDs									
Cell Type	Average Size QDs (nm)	λ_{exc} (nm)	λ_{em} (nm)	Surface coating method	J_{SC} (%) Increase	I_{SC} (%) Increase	PCE (%) Increase	LDS layer Thickness (nm)	Ref.
mono-Si	~3	325	660	SC	-	~2.3	3.7 (fresh) / ~1.4 (11-41 days)	~120	[47]
pc-Si	~3 [47]	370	773	Inkjet	-	-	2	27-74	[50]
mono-Si	6.4	300, 400, 500	680	SC with SOG	-	~1.3	0.4 (actual) / 1.2 (model)	130	[53]
pc-Si	1	254 365	328, 410	DC	-	4	~3%	~8	[49]
	2.85		630			~5	7.5-13.5		
mono-Si	2.5	405	~800	DC with SiO$_X$	-	15	~2	400	[214]
mono-Si	2 & 10	-	795-905	SC	-	-	12	50-300	[162]
mono-Si	2.6	<475	525	SC	14.7	-	12.4	-	[143]
mono-Si	4.9	320-400	445-495	Gel-glass	-	6.48	4.2	250	[144]
a-Si	2.85	365	628	SC	-	11.42	-	2-7	[210]
pc-Si	6	415	495	DC & Thermal Encap.	-	DC: 1.06 / Thermal Encap.: 11.86	DC: 0.47 / Thermal Encap.: 11.43	~2	This Thesis & [145]

Pi et al. (2011, 2012) reported electrical increases of ~2.3% and ~2% in the I_{SC} of mono-Si solar cells by SC [47] and of pc-Si solar cells by inkjet technologies [50], or ~3.7% and ~2% in PCE respectively. ~3 nm SiQDs were used in both cases, with emission peak ranging from 660-773 nm. They have concluded that electrical improvements are caused by both LDS and reduction in reflectance in the of ranges of 300-400 nm and 640-1100 nm which maximises at 370 nm and can reach ~33% reduction. It is worth noting that they have reported a decrease in the electrical improvements 11 days after exposure to air due to oxidation of SiQDs, ΔPCE dropped from 3.7% to 1.4%.

Moreover, Švrček et al. (2004) [53] have reported the use of silicate shells, SiO$_2$ specifically, in the application of LDS SiQDs onto the surface of Silicon. This time, the silicate is in liquid form and mixed with dopants, which is also known as Spin-on-Glass (SOG) in the market. They have reported the use of liquid SOG as precursor that hosted the 6.4 nm prior to SC onto mono-Si. A

~1.3% increase in the I_{SC} was reported where the increase in PCE was calculated at 0.4% and modelled at 1.2% (with 100% PLQY). The authors concluded that the electrical enhancements reported was due to LDS (emission at 680 nm).

Stupca et al. (2007) [49] reported electrical increases of 4% and ~5% in the I_{SC} of pc-Si solar cells by DC of 1 nm and 2.85 nm SiQDs, or ~3% and 7.5-13.5% in PCE respectively. The optimum layer thickness found by this report was ~8 nm, given that the SiQDs were deposited by DC using a volatile solvent only with no use of an encapsulating material. Authors concluded that the increase in the electrical performance of the pc-Si solar cell falls to both LDS (emission at 630 nm) and direct charge separation and therefore Schottky-like rectifying junction (between the ~8 nm SiQDs-film to front metal grid), implying chemical "doping-like" changes occurred to the sample solar cell. Such changes are not typically associated with LDS materials in the literature and are researched under the "Schottky junction solar cell" topic [215], [216].

Dorofeev et al. (2014) [214] reported an electrical increase of 15% in the I_{SC} (~2% in PCE) when LDS 2.5 nm SiQDs were deposited on mono-Si solar cells with non-LDS 12 nm SiO_X ($0 \leq x \leq 2$) (silicate) shells. Authors concluded that the measured electrical increases resulted from LDS (emission at 800 nm) and the antireflective properties of the 400 nm thick nanofilm deposited as a significant drop of ~90% was estimated as the weighted average for the drop in specular reflectance. Furthermore, by performing dark I-V characterisation, authors confirm that the nanofilms when applied to solar cells, can enhance performance by decreasing reverse dark currents, presumably through the reduction of unwanted carrier tunnelling in the p-n junction. This was possibly achieved by decreasing the density of electronic energy levels in the band gap, and passivating defect sites of the solar cells using hydrogen atoms from the SiQDs in the films.

Correspondingly, Gribov et al. (2017) [162] have again concluded in a newer publication that the electrical enhancements presented by SiQDs was a combination of LDS, reduced surface reflectance (~90% as mentioned in the previous study), and passivating defect of the solar cells. Only this time pure 2.5 nm and 10 nm LDS SiQDs were deposited by SC to generate nanofilms of varying thickness (50-300 nm) without the non-LDS 12 nm SiO_X, and a 12% increase in the PCE was reported. Interestingly, authors mentioned that the SiQD particle size presented no noticeable effect on the degree of uniformity of deposited films.

Furthermore, using a water-dispersible method, both Lopez-Delgado et al. (2018) [143] and Das et al. (2022) [144] have reported the synthesis of SiQDs through the reduction of APTES by - Sodium L-ascorbate at room temperature in less than an hour. However, this method entails the production of the persistent by product Sodium Silicate (SS), commonly known as "water glass". When dry, it possesses properties of a smooth, shiny, glass-like substrate that exhibits high

adhesion on host surfaces and can withstand temperatures up to 1100°C [217]. It slowly dries, and slowly dissolves in water if presented to again. Both studies showcased a contrast in term of SS, where Lopez-Delgado et al. (2018) [143] deliberately removed SS by immersing the coated solar cell sample in diluted Hydrofluoric Acid (HF) for 120 s, while and Das et al. (2022) [144] chose to keep it a protective and host material for the deposited SiQDs. Results noticeably varied, as SS-free solar cell samples generated a 12.4% increase in PCE (14.7% in J_{SC}) [143], and SS-coated samples generated a 4.2% increase in PCE (6.48% in I_{SC}) [144]. For reference SiQDs size measured at 2.6 nm (emission at 525 nm) and 4.9 nm (emission at 445-495 nm) respectively.

It is worth noting that the number of reports studying the use of LDS SiQDs on mono-Si solar cells outnumber those on pc-Si. By intuition, this can be due to the even surface morphology offered by mono-Si cells in comparison to pc-Si cells. Nonetheless, both types of solar cells undergo surface texturing that introduces V-shaped grooves that boost light trapping [218], [219], [220], [221].

Chowdhury et al. (2016) [210] have reported an 11.42% increase in the I_{SC} of amorphous Si (a-Si) solar cell by SC of 2.85 nm SiQDs with emission peak at 628 nm. Authors concluded that electrical enhancements resulted from LDS, enhanced optical coupling due to overall reduction in reflectance, and finally enhancement in charge separation by the introduction of indirect bandgaps between the cell and the confined SiQDs.

Finally, this thesis investigated the application of 6 nm PA SiQDs with an emission peak of 495 nm. Initially, using direct DC, 0.01 mg and 0.15 mg of PA SiQDs were deposited onto the surface of 39 mm × 39 mm pc-Si solar cells, achieving I_{SC} increases of 1.06% and 0.75%, respectively. A maximum increase in PCE of 0.47% was attained. However, after thermally encapsulating the pc-Si solar cells in a commercially styled solar cell sandwich, an improved I_{SC} increase of 11.86% was achieved, with the maximum PCE increase rising to 11.43%. The PA SiQDs layer thickness was estimated to be ~2 nm after DC. These improvements were attributed to the LDS effect and enhanced optical coupling, and resulted in a publication [145].

As for PQDs, Table 2.2 display reported increases in the I_{SC} (or J_{SC}) and PCE of c-Si solar cells resulting from the addition or deposition of PQDs on the surface of these cells.

Table 2.2 Overview of PQDs used on c-Si solar cells and enhancements achieved by previous studies.

					PQDs				
Cell Type	**Average Size QDs (nm)** *and type*	**λ_{exc} (nm)**	**λ_{em} (nm)**	**Surface coating method**	**J_{SC} (%) Increase**	**I_{SC} (%) Increase**	**PCE (%) Increase**	**LDS layer Thickness (nm)**	**Ref.**
mono-Si	3-5: MAPbBr$_3$	405	531	SC	4.03	-	6.69	1000-4000	[26]
pc-Si					2.07	-	8.43		
pc-Si	8: CsPbCl$_3$:Mn^{2+}	387	405, 600	DC	5.10	-	6.20	-	[157]
c-Si	11.2: CsPbCl$_3$:Mn^{2+}	-	600	LPD	5.17	-	5.14	250	[211]
c-Si	8: CsPbCl$_3$:Mn^{2+}, Er^{3+}	375	600	External EVA Film	-	3.42	4.02	1×10^5	[166]
pc-Si	4.9: CsPbBr$_3$–Cs$_4$PbBr$_6$	200	~500	Doctor-blade in ZnO/EVA	3.63	-	7.93	1×10^5	[212]
pc-Si	12: CsPbI$_3$	<680	690	LEVA	-	1.55	0.43-1.5	240000	This Thesis

It was significantly less popular to use the LDS quality of Caesium-Lead-Halide (CsPbX$_3$) PQDs for the external enhancements of solar cells, and specifically single junction c-Si solar cells. This could be due to the focus on using PQDs as internal active layers within PSCs or other solar cell technologies [222], [223], [224], [225].

Nevertheless, Meng et al. (2020) [26] have reported the electrical enhancements of 4.03% and 2.07% in the I_{SC} of both mono-Si and pc-Si solar cells respectively, or 6.69% and 8.43% ion PCE. This was achieved by SC of the cells using 3-5 nm MAPbBr$_3$ (MA: methylammonium) with thickness varying between 1000 and 4000 nm (emission peak at 531 nm). Authors concluded that enhancement resulted from LDS, and pointed out QDs with high PLQY can lead to a significant increase of the EQE in the UV-blue region of the solar radiation, which is the expected absorption region for LDS QDs specifically designed for solar cell enhancements.

Moreover, the specific integration of CsPbI$_3$ PQDs with pc-Si solar cells is not directly evident in the available literature. However, the use of analogous CsPbCl$_3$ PQDs with Manganese doping (CsPbCl$_3$:Mn^{2+}) was reported a few times for the enhancement of these cells.

Wang et al. (2018) [157] reported the use of 8 nm LDS $CsPbCl_3:Mn^{2+}$ PQDs (emission peak at 405 and 600 nm) for electrical efficiency enhancement of pc-Si solar cells. By DC, the cells were coated with the PQDs at different concentrations varying from 3-18 mg/ml, with no specific mention of the layer thickness. Highest electrical enhancement was reported at 9 mg/ml with 5.1% increase in the I_{SC} and 6.2% in the PCE. Authors concluded that the electrical enhancements resulted from LDS and improved optical coupling due to light trapping capabilities of the LDS PQDs.

Following that up, Sun et al. (2020) [211] reported on the use of LDS 11.2 nm $CsPbCl_3:Mn^{2+}$ PQDs (emission peak at 600 nm) as well where c-Si solar cells were coated using the liquid-phase deposition (LPD) method resulting in a 250 nm thick nanofilm. The highest electrical enhancement was reported at 5.17% for J_{SC} and 5.14% in terms of PCE. Authors concluded these enhancements resulted from LDS.

Similarly, Song et al. (2022) [166] reported the use of Mn^{2+} and Er^{3+} co-doped 8 nm $CsPbCl_3$ PQDs (emission peak at 600 nm). In this case samples were not directly coated, instead, different concentrations of PQDs (0-11.8 wt %) were mixed into 0.1 mm thick EVA films that were then dried and placed on top of c-Si solar cells. PQDs concentration of 0.9% by weight reported the highest electrical enhancement at 3.42% in the I_{SC} and 4.02% in PCE. Authors concluded these enhancements resulted from LDS.

Using the doctor-blade method to coat pc-Si solar cells with 0.1 mm thick LDS ZnO/EVA, Song et al. (2022) [212] have reported on the enhancement of these cells by embedded the encapsulant with 4.9 nm $CsPbBr_3$–Cs_4PbBr_6 joint PQDs (emission peak at ~500 nm). 3.63% and 7.93% were reported for electrical increases in the J_{SC} and PCE respectively. Authors concluded that these enhancements resulted from LDS, and due to a reduction in carrier relaxation energy loss.

Finally, this thesis investigated the application of 12 nm $CsPbI_3$ PQDs with an emission peak at 690 nm. Using a novel room-temperature coating methodology known as LEVA, 0.01 mg of the PQDs was directly deposited onto the surface of twenty-five 39 mm $\times$ 39 mm pc-Si solar cells, achieving a maximum increase in I_{SC} of 1.55% and an average increase of 0.93%. A maximum increase in PCE of 1.5% was also achieved. The PQDs were embedded in LEVA optical films with a thickness of 240 μm, which temporarily protected the PQDs from phase-shifting degradation, enabling reliable and stable LDS-based electrical enhancements for up to two days. The improvements were attributed to the LDS effect and enhanced optical coupling.

This review subsection highlights that the average size of LDS QDs used for c-Si solar cell enhancement is ~3.8 nm for SiQDs and ~7.2 nm for PQDs, with average emission peaks at ~610

nm and ~566 nm, respectively. SiQDs were mainly deposited in open air, while PQDs employed a mix of open-air and hosted deposition techniques. Furthermore, it can be deduced that while size and functionalisation are key in designing the LDS effect of QDs, some variations can arise as a result of differences in synthesis techniques and methodologies. Therefore, when selecting the right QDs for LDS applications, it is vital to assess their LDS performance based on characterisation results and not the chemical structure alone.

2.2.   Synthesis and Fabrication of SiQDs and PQDs

This subsection reviews the reported methodologies used to synthesis SiQDs and PQDs.

2.2.1.   SiQDs

Since Si nanoparticles are based off bulk Silicon, they can be manufactured physically in top-down processes, or chemically synthesised in both top-down and bottom-up fabrication processes [98], [226].

2.2.1.1.   Physical Methods

Physical approaches are top-down nanoparticles fabrication processes that starts with reducing bulk materials and ends with nanoparticles and QDs.

These methods tend be quicker and easier to establish compared top chemical methods as the overall fabrication process usually follows iterative means and uses cheaper bulk starting materials.

1.   Non-Thermal Plasma

Several researchers have successfully synthesised free-standing SiQDs using plasma-based methods: specifically, non-thermal plasma [227].

Pi et al. (2011) [47] successfully demonstrated the use of non-thermal plasma to fabricate free-standing SiQDs from Silane (SiH_4). The average size of SiQDs was measured at 3nm using X-ray Diffractometer (XRD). PL properties were measured at 325 nm for excitation, and 660 nm for emission.

Same fundamental method was utilised by several other researchers with slight differences, for instance Liu et al. (2016) [228] hydrosilylated their free-standing SiQDs by implementing hydrosilylation as the final step of synthesis.

Moreover, it has been reported by several researchers the successful fabrication of SiQDs by non-thermal plasma with Silicon Tetrachloride ($SiCl_4$) as starting substance [229], [230].

2. Laser Ablation

Laser Ablation relies on using high energy laser to sperate Silicon nanoparticles and SiQDs directly from high purity bulk Silicon in the form of thin plates or sheets [226], [231], [232], [233], [234], [235]. Rodio et al. (2016) [236] have produced 4nm SiQDs using laser ablation of 99.999% Silicon (placed in a cuvette and submerged in deionised water) by a 1 MJ/pulse laser.

Xin et al. (2017) [237] conducted a study to investigate the influence of various solvents on the efficacy of laser ablation in the production of SiQDs. Notably, their findings highlighted 1-octyne as the most effective solvent, demonstrating superior performance in several key aspects including size control and photoluminescent properties. Furthermore, the research findings concluded that the utilisation of a carbon-rich solvent for the synthesis of SiQDs via laser ablation provides enhanced control over critical factors such as size, photoluminescent properties, QY, and size distribution.

Similarly, Zhang et al. (2018) [238] conducted a study involving the use of laser ablation to produce SiQDs in a solvent primarily consisting of 1-octene. Notably, 1-octene shares a similar chemical structure with 1-octyne, both having an equal number of carbon atoms. However, a key distinction lies in the presence of a carbon triple bond in 1-octyne compared to a carbon double bond in 1-octene. In their research, the main variable examined was the duration of laser ablation (LAT), with 1-octene serving as the solvent throughout. Their findings indicated that prolonged LAT resulted in smaller SiQDs, subsequently leading to a larger bandgap. Specifically, SiQDs produced after 30 minutes of LAT exhibited an average size of 4.23 nm, while extending the LAT to 120 minutes yielded SiQDs with an average size of 1.42 nm.

3. Milling and Pulverising

Milling and pulverizing represent some of the most straightforward techniques for the top-down synthesis of SiQDs, relying entirely on mechanical processes. The inaugural use of this method was documented in a publication by Gaffet and Harmelin in 1990 [239]. They achieved the successful fabrication of crystal-amorphous Silicon nanoparticles through ball milling, generating SiQDs of differing sizes and exhibiting minimal metallic contamination.

Ray et al. (2009) [240] have reported a successful fabrication method for SiQDs utilising mechanical ball milling. They employed 99.9% pure Silicon powder with an average particle size of 20 μm and subjected it to ball milling at 250 [rpm] with a ball-to-powder weight ratio

of 10:1. This milling process was conducted for different durations, resulting in four samples milled for 25, 50, 75, and 100 hours, respectively. Toluene was employed as a milling medium to provide lubrication, thereby preventing, and reducing undesirable oxidation. The estimated sizes of the SiQDs produced in this manner ranged between 4-10 nm.

One of the concerns associated with physical milling techniques is the potential for contamination, both from metallic impurities introduced by the milling balls and organic contaminants from the milling medium, such as Toluene . To mitigate this issue, the authors employed an etching process on the dry product of the milled SiQDs using an acidic solution consisting of 2:1 of H_2SO_4 and H_2O_2 respectively.

However, it's important to note that milling is considered a less reliable method for fabricating SiQDs. This approach typically offers poor size control with high levels of inaccuracy and carries a risk of introducing both metallic and organic contaminations into the SiQDs samples.

Pulverising is another physical method that relies on the application of mechanical force to crush and grind macro materials into smaller structures on micro and nanoscales. Like milling, this method has its drawbacks, primarily poor size control and the potential for introducing metallic and organic contaminants. However, researchers have devised strategies to mitigate these issues by incorporating an additional step before pulverising by electrochemical etching.

Electrochemical etching is originally a chemical route that can be used to synthesize SiQDs. However, Švrček et al. (2004) [53] and Valenta et al. (2005) [241] applied electrochemical etching to porous Silicon, increasing its porosity and the likelihood of creating nano and micro-scale pores. When pulverising electrochemically etched porous Silicon, researchers achieved promising results with improved size control. Švrček et al. (2004) reported a median average size of 6.4 nm, while Valenta et al. (2005) demonstrated a mean average size of 2 nm. These findings compare favourably to an estimated average size of 2.5-3 nm based on a similar method published by Kanemitsu et al. (1993) [242].

2.2.1.2.   Chemical Methods

Chemical routes primarily employ bottom-up methods, which involve starting materials that are molecular and atomic in nature. These materials undergo chemical treatments and reactions to produce the desired product, typically on a micro and nano scale. However, it's worth noting that some chemical approaches, such as electrochemical etching, are top-down methods [98], [226].

Chemical routes are among the most used methods for synthesizing nanoparticles. This popularity can be attributed to the extensive research conducted on the biological applications of

nanoparticles [89], [104], [190], [243], [244], [245], [246], including SiQDs. Consequently, chemical-based methods have been well-developed and are widely documented in the existing literature on nanoparticle synthesis.

1. Electrochemical Etching

Electrochemical etching stands out as one of the most precise methods for synthesizing SiQDs. This technique offers exceptional control over both the size and size distribution of the SiQDs. Furthermore, it has the capability to produce SiQDs as small as 4.6 nm [246] and even down to 1 nm [49]. Electrochemical etching relies on utilising a Silicon wafer as an electrical component (cathode), where a high current density is applied to create pores and generate nanoparticles within the Si wafer.

The initial successful application of electrochemical etching to Silicon wafers was documented by Canham in 1990 [107]. By employing chemical dissolution, they effectively showcased the creation of a nanowire network within bulk Silicon. Their ground-breaking utilisation of electrochemical etching for Silicon nanowires quickly prompted numerous successful research publications on SiQDs, including works by Wolkin et al. (1999) [91], Sweryda-Krawiec et al. (1999) [247], and Lie et al. (2002) [248], among others.

Stupca et al. (2007) [49] successfully synthesized monodisperse, free-standing SiQDs measuring 1 nm (blue luminescent) and 2.85 nm (red luminescent) using electrochemical etching of crystalline Silicon wafers. The etching process involved a solution of Hydrofluoric acid (HF) and Hydrogen Peroxide (H_2O_2). They produced 1 nm SiQDs by applying a high etching current across the substrate and 2.85nm SiQDs by using a low etching current.

When excited at 254 nm and 365 nm, the 1nm SiQDs emitted light at 328nm and 410nm, respectively. In contrast, the 2.85nm SiQDs emitted at 630 nm for both excitation wavelengths as the energy absorbed of 3.2-3.4 eV, exceeded the bandgap of 2.15 eV resulting in re-emission at the same wavelength. While for the 1 nm SiQDs, the bandgap was approximately 3.6 eV which was lower than absorbed photons.

Similarly, Chen et al. (2019) [249] also employed HF and H_2O_2 as etchant components to etch Silicon wafers and achieved precise fabrication of 2.5 nm SiQDs.

Moreover, Ahire et al. (2012) [246] used a 1:1 HF Ethanol solution as the etchant, and they etched Silicon chips at a high current density of 400 [mA cm^{-2}] for 5 minutes, followed by amine-termination. This process yielded amine-terminated SiQDs with an average size of 7.5 ± 1.0 nm, with emission centring at 450 nm, and a wide absorption curve below 400 nm.

2. Reduction of Silicon Halides

By reducing Si-halides, Si nanoparticles and SiQDs can be produced with precise quantities due to tuneable stoichiometry. Several papers reported the production of SiQDs by reducing $SiCl_4$ [250] using sodium naphthalenide [54], [96], [97], [145], sodium [251], tetraethylorthosilicate, and lithium aluminium hydride [252], [253] as reducing agents.

However, this chemical synthesis method typically yields blue luminescent SiQDs [145] with a wide particle size distribution. Despite this, these SiQDs can exhibit high QY of up to 90% [254].

3. Decomposition of Si Precursors

This method is based on the hydrothermal decomposition of organosilicates such as 3-aminopropyl triethoxysilane (APTES), 3-aminopropyl trimethoxysilane (APTMS), and N-[3-(trimethoxysilyl)propyl]-ethylenediamine (DAMO), by reducing agents such as $LiAlH_4$, sodium citrate, sodium ascorbate, $NaBH_4$, and Thiourea [61], [143], [161], [164], [255], [256], [257], [258], [259], [260], [261].

By varying any reaction parameter, the QY of these SiQDs can jump from 35-40% [164] to 65-85% [262], [263]. This parameter can be temperature, reaction time, reducing agent used or relevant stoichiometry, and Si precursor used or relevant stoichiometry.

2.2.2. PQDs

The synthesis methods of Perovskite QDs are primarily bottom-up chemical methods. These methods are generally characterised by their high accuracy in control over size and morphology, modularity, and high production yields [264].

With the focus on lead halide PQDs, such as $CsPbX_3$ (X=Cl, or Br, or I), the following methods are some of the common fabrication strategies followed for the synthesis of such PQDs [265], [266], [267].

1. Hot-injection synthesis

PQDs synthesised using this method are more uniform in size and show less defects post-production.

To synthesize $CsPbX_3$ PQDs, a meticulous chemical process is undertaken. This involves rapidly injecting a precursor containing the A-site cation (Cs acetate) into a specially equipped flask, all while maintaining an inert atmosphere. Within this flask, a solution containing

dissolved metal halide (PbX_2) and specific ligands, typically oleic acid and oleylamine, resides in a high-boiling-point solvent, often octadecene. The entire setup is meticulously controlled at a specific elevated temperature, typically within the range of 120-150°C [266]. Inside the flask, nucleation and growth of the PQDs occur over a brief period, usually around 5 seconds. Following this growth phase, the process is rapidly cooled, often by immersing the flask in an ice bath, effectively arresting crystal growth. To obtain PQDs with high PLQYs, any excess ligands in the reaction mixture are thoroughly removed through a washing procedure using an antisolvent, typically methyl acetate or ethyl acetate [267], [268], [269].

Song et al. (2022) and Sun et al. (2020) [166], [211] reported on the use of this method to synthesise $CsPbCl_3$ PQDs for the purpose of electrically enhancing c-Si (including pc-Si) solar cells.

2. Ligand-assisted reprecipitation (LARP)

This method is considered to be the most common as it requires no high temperatures, vacuum or inert atmospheres [270]. It can also be used for upscaled production quantities [267].

This synthesis method begins by dissolving metal halides, A-site halides, and ligands (typically oleylamine and oleate) in a polar solvent while employing vigorous stirring. After a specific duration of stirring, the resulting mixture is introduced drop by drop into a counter-solvent [271], [272], [273], room temperature and pressure.

It is worth noting that the LARP can only produce $CsPbI_3$ PQDs by increasing the temperature up to 80°C and excluding polar solvents from the mix. Nevertheless, these PQDs completely decompose by the 120th minute mark [274]. This point is specifically important for this PhD research as rapid decomposition and degradation of deposited LDS QDs is a significant challenge this project aims to address through encapsulation and layered protection.

However, due to the nature of fast reaction kinetics, and rapid crystallisation, LARP produces PQDs with higher deformity compared to the hot-injection method.

3. Microwave-assisted synthesis

The microwave-assisted method involves the synthesis of PQDs by combining reagents like precursors, ligands, and solvents in one contraption with the application of external energy. However, one common drawback is the poor size homogeneity of the synthesized PQDs [275], [276], [277].

4. Laser in situ synthesis

For this method, metal halides, A-site halides, and ligands (typically oleylamine and oleate) are dissolved in a polar solvent (*in situ*) with the presence of an encapsulant like PMMA. This mixture is then SC onto a substrate top form a thin film, which is then pulsated by a pulse laser to produce a pattered form of the PQDs. This was demonstrated by Zhan et al. (2021) [278] where 7.7 nm $CsPbI_3$ PQDs were produced by mixing CsI, PbI_2, and PMMA in DMF (solvent), and then the spun film was pulsated by a focused 405 nm nanosecond pulse-laser beam with a 0.9 NA objective.

2.3. Review conclusions

This literature review investigates the LDS working principle in relation to QDs, quantum confinement effects, size, surface functionalization, external application methods, optical processes, fabrication, synthesis, and the state-of-the-art SiQDs and PQDs used for enhancing c-Si solar cells.

Despite significant interest, gaps in the literature indicate insufficient focus on up-scaling these advancements to commercial pc-Si solar cells. Research often targets photovoltaic technology enhancement under ideal conditions.

Moreover, while many studies use host materials to minimise refractive index mismatches, less attention is given to their role in QD protection. Particularly for thermally sensitive QDs like PQDs, concerns about thermal degradation are often overlooked, with PQDs frequently exposed to degradation accelerators such as open-air deposition or high-temperature thermal hosting.

This project investigates two types of LDS QDs: PA SiQDs, typically used in controlling thermal diffusivity in materials and batteries [54], [96], [97], and $CsPbI_3$ PQDs, mainly used in PQD-based solar cells and hybrid-structured tandem solar cells [25], [55], [268], [279], but with limited application in externally enhancing c-Si solar cells.

Gaps in the literature include lack of consideration for thermal degradation and stability of LDS materials, especially when deposited onto solar cells or when these cells are thermally encapsulated. Additionally, the literature lacks the use of PA as a functional group in LDS SiQDs, and the use of $CsPbI_3$ PQDs in LDS enhancements of c-Si solar cells, particularly regarding thermal stability.

Up to the point of writing this thesis, there has been no specific mention of using $CsPbI_3$ PQDs for non-chemically altering LDS efficiency enhancement of c-Si solar cells.

This doctoral research introduces novel approaches by addressing these gaps, particularly in utilising PA SiQDs as LDS devices for enhancing commercially available pc-Si solar cells, focusing on electrical enhancement, commercial viability, and reproducible deposition and thermal encapsulation methods. It also presents a novel room-temperature methodology for integrating $CsPbI_3$ PQDs onto pc-Si solar cells. This method ensures protection against thermal degradation caused by encapsulation temperatures and air exposure, which can lead to morphological phase shifts in the structure of $CsPbI_3$ PQDs.

3. Methodology and Experimental techniques

3.1. Introduction

The experimental work in this thesis covers the full investigation of the controlled implementation of PA SiQDs and $CsPbI_3$ PQDs onto pc-Si solar cells as optical LDS layers for electrical enhancements. The basis of these experiments was aimed at understanding and optimising LDS QD-coatings to maximise the photogenerated current, measured by the I_{SC}.

This chapter aims at introducing and explaining the analytical techniques, instruments, and methods used throughout the doctoral research. It covers the PL spectroscopy and spectrophotometry, Fourier Transform Infrared Spectroscopy (FT-IR), Scanning and Transmission Electron Microscopy (SEM and TEM), photovoltaic I-V characterisation, fluorescent microscopy, and confocal microscopy on LDS QDs and pc-Si solar cell samples. This included the sample preparations, encapsulations, and data analysis.

3.2. Materials and Deposition

The LDS material utilised for this project consisted of PA SiQDs and $CsPbI_3$ PQDs. PA SiQDs are Silicon quantum dots capped with the chemical group of Phenylacetylene. PA SiQDs for this project were chemically synthesised in-house by reducing $SiCl_4$ using sodium naphthalenide [54], [96], [97]. Average size was measured at 6 nm, with absorption/emission measured at 415/495 nm respectively. As for $CsPbI_3$ PQDs, these QDs were commercially acquired from Quantum Solutions™, dubbed as QDot™ ABX3-685, The company reported emission peak at 692 nm and a broad excitation range below 680 nm, with PLQY of 99%, and an average size of 11 nm ± 1 nm.

With both QD materials showing a favourable LDS behaviour, they were investigated in the form of LDS layers that were directly deposited onto pc-Si solar cells.

To minimise material losses and maximise the harvest of the benefits introduced by LDS, DC [49] was employed as the primary method of deposition; this ensured none of the active LDS material is lost as seen in SC on rectangular and square substrates [280-282].

In the initial stages of the project, SC was tested against DC as deposition methods. Since volatile solvents are used, the QDs were proved to escape the surface of the pc-Si solar cell samples. This was mainly attributed to the high volatility of the solvents used for the QDs and the high roughness of the pc-Si solar cell surface, which features an inverted pyramid shape. The combination of high volatility and surface roughness led to the formation of gas pockets beneath the deposited liquid during centrifugation in the spin-coater, causing a significant portion of the solution to slide away

from the cells. This phenomenon was evident as residual trails of QDs on the cells and the inner walls of the spin-coater.

DC-made depositions yielded improved results, with more uniform and loss-free coatings of the LDS QDs, with visual results presented in Figure 4.4, Chapter 4. Moreover, DC proved very replicable and reproducible, thus making it very reliable [283].

While some of the QDs used, such as the PA SiQDs, were originally intended for applications in batteries and thermal enhancements [54], [96], [97]. The methodology employed in this project ensured the different focus on utilising the PL properties of these QDs. This presented the possibility of using PA SiQDs as an LDS material for the electrical enhancements of pc-Si solar cells.

The DC LDS layering method is executed carefully, employing a pipette to ensure uniform coverage and dispersion within the layer, while maintaining precise control over the quantity of QDs utilised. Additionally, this included the bench used for DC, which was precisely maintained and levelled, guaranteeing that the deposited coatings evaporate uniformly at the same angle, position, and within the same surrounding evaporative environment.

While studying the V_{OC} and P_M is essential to quantify solar cell improvements, the focus of the project will be the I_{SC}, as it directly correlates to the enhancements presented by the LDS layer. In theory, the employment of the right LDS material to enhance pc-Si solar cells (specifically) will decrease the number of the absorbed photons in the UV-blue region and boost in the Vis-NIR region where the pc-Si solar cells exhibit the highest solar spectral response. The optical mechanism behind a QD-based LDS layer was illustrated in Figure 2.5, in Chapter 2, the Literature Review.

Simply put, the photocurrent generation in a solar cell is intrinsically linked to the incident light's intensity, as it governs the number of electron-hole pairs created within the cell. The absorption of photons by the solar cell initiates the process of charge carrier generation. In the case of pc-Si solar cells, they exhibit heightened sensitivity to photons within the NIR region of the electromagnetic spectrum. Consequently, a larger quantity of photons in this range is absorbed, leading to an increased generation of electron-hole pairs, and subsequently a higher magnitude of generated photocurrent. In this case, the direct deposition of LDS materials by DC ensured optimal performance and no material losses.

3.3. Photoluminescence (PL) spectroscopy and spectrometry

PL is phenomenon in which a material emits light after absorbing photons. A photon is emitted by exciting an electron (photocarrier) in the material from its ground energy state to a higher energy state, which then relaxes back down to ground state; by relaxing the absorbed energy is then released as an emitted photon [284], [285], [286]. As described, in most cases this remission of light occurs in a downshifting manner in which the photoluminescent photons are of low-energy compared to the absorbed high-energy photons. Reason behind its emission being a lower energy photon is energy loss by dissipation as vibration and heat by electron-hole recombination. In some cases, some materials can perform upconversion by exciting an electron using two or more low-energy photons which are then released as one higher energy photon as the photocarrier relaxes back into ground state.

In semiconductors, such as Silicon, the electrons occupy specific energy bands. The valence inner band contains electrons that are bound to the atoms and do not contribute to electrical conduction. While the outer conduction band contains free electrons that are responsible for electrical conductivity. The energy gap between these two bands is known as the bandgap. When such materials receive photons with sufficient energy, valence electrons jump the gap from the valence band to conduction band. This distinction in energy levels, by bandgap, causes the material to have identity PL profile for excitation and emission.

By studying the PL through the spectroscopy of luminescence, the bandgap and active energy states can be numerically extracted.

The project covered the use of PL spectroscopy to study the LDS effects of PA SiQDs and $CsPbI_3$ PQDs for purposes of electrical enhancement of pc-Si solar cells. The identification of excitation & emission pair is essential to determine the benefit of the tested luminophore for LDS-based enhancements as pc-Si solar cells typically exhibit low spectral response to light in the blue & UV region, 350-650 nm, but demonstrate considerably higher response in the NIR region, 650-950 nm [20], [21], [22]. This reduced the selection process to QDs that exhibit significant blue & UV light absorption (below 400 nm) that was emitted out towards the NIR region (ideally towards 700 nm) of the solar spectrum.

The Edinburgh Instruments FS5 Spectrofluorometer was utilised to study the PL of PA SiQDs, and $CsPbI_3$ PQDs.

The QD samples are initially measured by weight and dissolved in a suitable solvent to create a base solution with a known concentration, at room temperature. When needed, the concentration was altered to enhance readings, for instance, very high concentrations can oversaturate sensors

by producing relatively high emission intensity. Hellma fluorescence clear cuvette was used to hold the liquid sample. The spectrofluorometer was calibrated prior to each reading to achieve a true photon count by ensuring the overall received fluorescence does not exceed 1.5m counts per second (cps).

3.4.   Reflectance and Transmittance

The project also entailed an investigation into the reflectance and transmittance characteristics of pc-Si solar cells coated with LDS QDs and relevant materials. This examination encompassed an analysis of the LDS PA SiQDs and $CsPbI_3$ PQDs, as well as the encapsulants and encapsulation materials, including EVA and solar encapsulation glass.

The transmittance of the encapsulant EVA was assessed using the Edinburgh Instruments FS5 Spectrofluorometer in various encapsulation configurations. These configurations were intentionally designed to simulate the potential impact on transmittance that EVA might have when employed as an encapsulant in distinct scenarios. These configurations correspond to the varying methodologies applied in coating the cells with PA SiQDs using DC combined with thermal encapsulation, and $CsPbI_3$ PQDs using a novel method called LEVA coating, which is further explained in subsection 3.6 and 3.7. Comprehensive information regarding each LDS material is provided in the relevant chapters, Chapter 4 and 5, respectively. The outcomes of this characterisation can be found in Figure 5.9 of Chapter 5. For configurations, using the 50 mm $\times$ 50 mm Pilkington OptiWhite 3.2 mm encapsulating glass [287], the setup involved measurements of various configurations: a single sheet, a double sheet sandwich with an air gap, a double sheet sandwich bonded with a LEVA film, and finally, a double sheet sandwich adhered with a thermally applied EVA film. A schematic of the transmittance setup is shown in Figure 3.1.
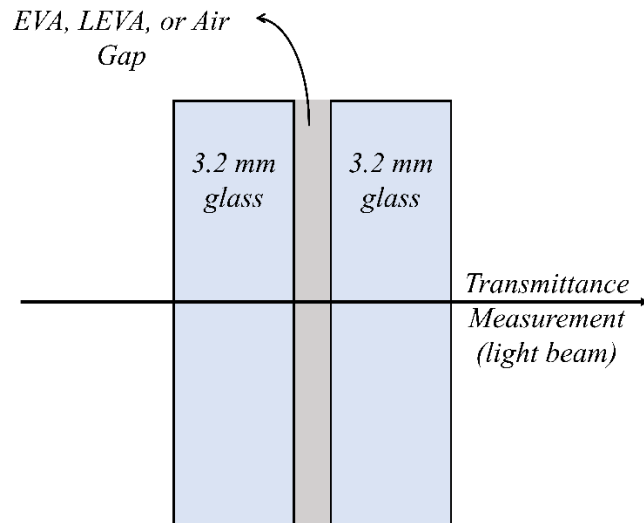
Figure 3.1 Transmittance testing set up, a schematic. Pilkington OptiWhite 3.2 mm encapsulating glass sandwiching EVA, LEVA, or an Air Gap.

As for the LDS coated pc-Si solar cells, a halogen light source (HL-2000-FHSA, with adequate optical fibre) was fitted on the Ocean HDX Spectrometer to test for possible changes in reflectance the LDS materials present. The reflectance set up consisted of the spectrometer itself, adequate optical fibre, Halogen Light Source, and Ocean Insight (formerly Ocean Optics) WS-1 Diffuse Reflectance Standard and STAN-SSH Specular Reflectance Standard. A schematic of the reflectance setup is shown in Figure 3.2. It shows how Specular and Diffuse reflectance measurements are carried at different angles, 0° and 45° respectively.
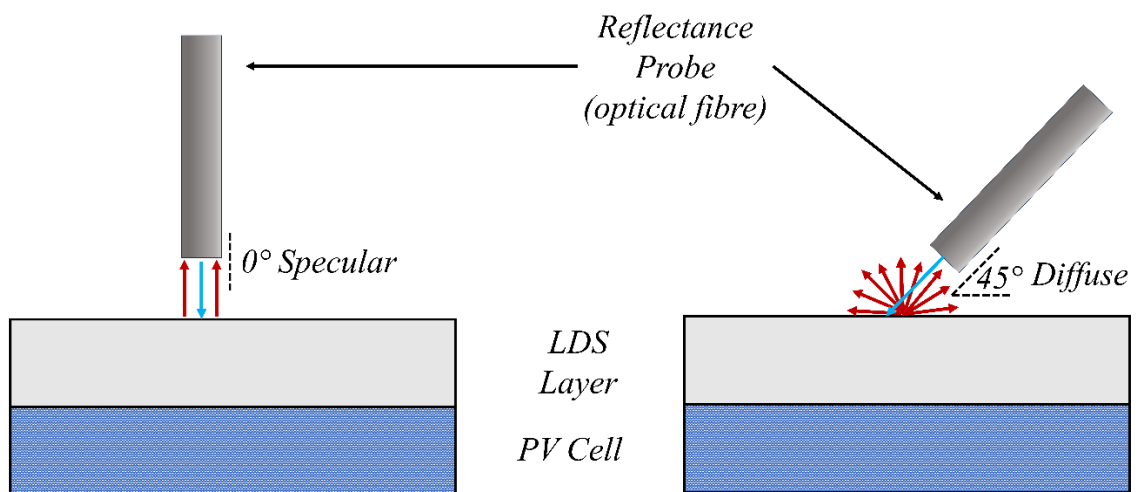
Figure 3.2 Reflectance testing set up, a schematic. Specular measurements carried perpendicularly at 0°, and Diffuse measurements carried angled at 45°. The same setup was used for bare uncoated reference cells.

3.5. Further non-destructive characterisation: SEM, TEM, FT-IR, Fluorescent and Confocal microscopy.

The QDs sample went under SEM & TEM for precise size and morphology measurements. FT-IR was used to determine the chemical composition of the samples.

SEM and TEM, in principle, produce similar measurements outcome with some variation in lateral and depth resolutions, which is directly proportional to the energy of the electrons emitted by each instrument. In the SEM, typical electron energies are 1-30 keV with lateral resolution of 1 nm and depth resolution of 10 nm. While TEM's typical electron energies are 80-300 keV, with lateral resolution of 100 mm and depth resolution of 1 nm [288]. In the SEM, the sample is expected to scatter the electrons back to sensor which then forms an image, while in TEM the higher energy electrons pass through (transmit through) the sample to a sensor. For the purposes of measuring QDs, maximum resolutions provided by the SEM are sufficient, as QDs used in the project vary in sizes from ~1-12 nm only.

For the SEM and TEM, the University of East Anglia provides access to a state-of-the-art Zeiss Gemini 300 SEM, and a JEOL 2010 200 kV TEM.

As for the FT-IR, Perkin Elmer Spectrum BX FT-IR Spectrometer was used to study the chemical composition of LDS QDs. In principle, an FT-IR spectrometer breaks down chemical composition by recording the transmittance spectrum of an InfraRed radiation beam that passes through the designated sample; the wavenumber can vary typically from 4000 and 400 cm^{-1}. The spectrometer then uses Fourier Transform to break down the spectrum into peaks which can singularly or collectively correspond to registered fingerprint values for specific chemical bonds. These values are used to identify chemical composition based on the elements and compounds present in the measured sample [289], [290].

However, samples of synthesised PA SiQDs characteristically presented impurities, such as Naphthalene, that blocked electron transmission in SEM and TEM, or masked resulting measurements obtained on the FT-IR. Therefore, other techniques were used to compensate for this. Details are enclosed within Chapter 4.

Fluorescence microscopy was conducted on solid pc-Si solar cell samples using the ZEISS Axio Scope.A1 microscope at 5× & 10× zoom. The samples were excited using the Excelitas Technologies' X-Cite 120Q spectral excitation light source, which emitted multiple peaks at 335, 370, 410, 440, 550, and 580 nm. The primary objective of this analysis was to reveal the deposition patterns and visually illustrate the existence of the deposited LDS layers on the solar cells. This

was achieved by showcasing the anticipated PL colours that corresponded to the PL measurements of the LDS material, thereby providing a clear visual confirmation of the presence of these layers.

Lastly, the pc-Si solar cell samples were subjected to 3D scanning and imaging using the Olympus LEXT OLS 5000 Confocal microscope. This allowed for the study of roughness profiles and thickness before and after the deposition of LDS layers. Since setups are specific for either LDS QD material, detailed explanations of the testing setup and results will be provided in subsections 4.3.2 for PA SiQDs and 5.3.2 for $CsPbI_3$ PQDs.

3.6. Methodological protocol

This subsection introduces the fundamental experimental protocol employed for the enhancement of pc-Si solar cells. Figure 3.3 delineates the essential steps undertaken to characterize the LDS and encapsulation materials before any processing of solar cells using techniques and instruments outline in subsections 3.3 to 3.5. Subsequently, Figure 3.4 illustrates the steps required to attain high-quality results, commencing with initial cell preparations, and concluding with the final encapsulation of cells.
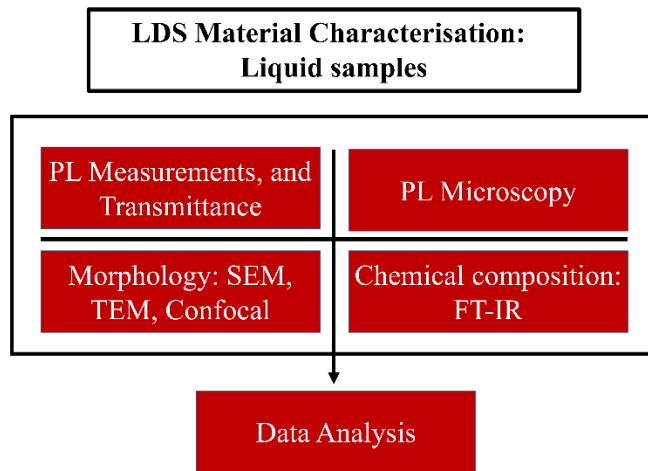
Figure 3.3 Methodology (liquid samples): Experimental components for the characterisation of LDS materials employed, PA SiQDs and CsPbI₃ PQDs, in addition to encapsulation materials like EVA and solar glass.

Figure 3.3 above presents the experimental components employed for the investigation and characterisation of the liquid samples of LDS QDs used throughout this thesis, with results detailed in subsections 4.3.1 and 5.3.1. Additionally, some components were utilised for the characterisation of encapsulation materials, such as EVA and LEVA films, with results outlined in subsections 4.3.2 and 5.3.2.

It is important to note that these systematic investigative components do not follow a specific order and can be applied based on the material being characterized. This contrasts with the methodical approach employed for solid samples, namely the pc-Si solar cells, as outlined in Figure 3.4.
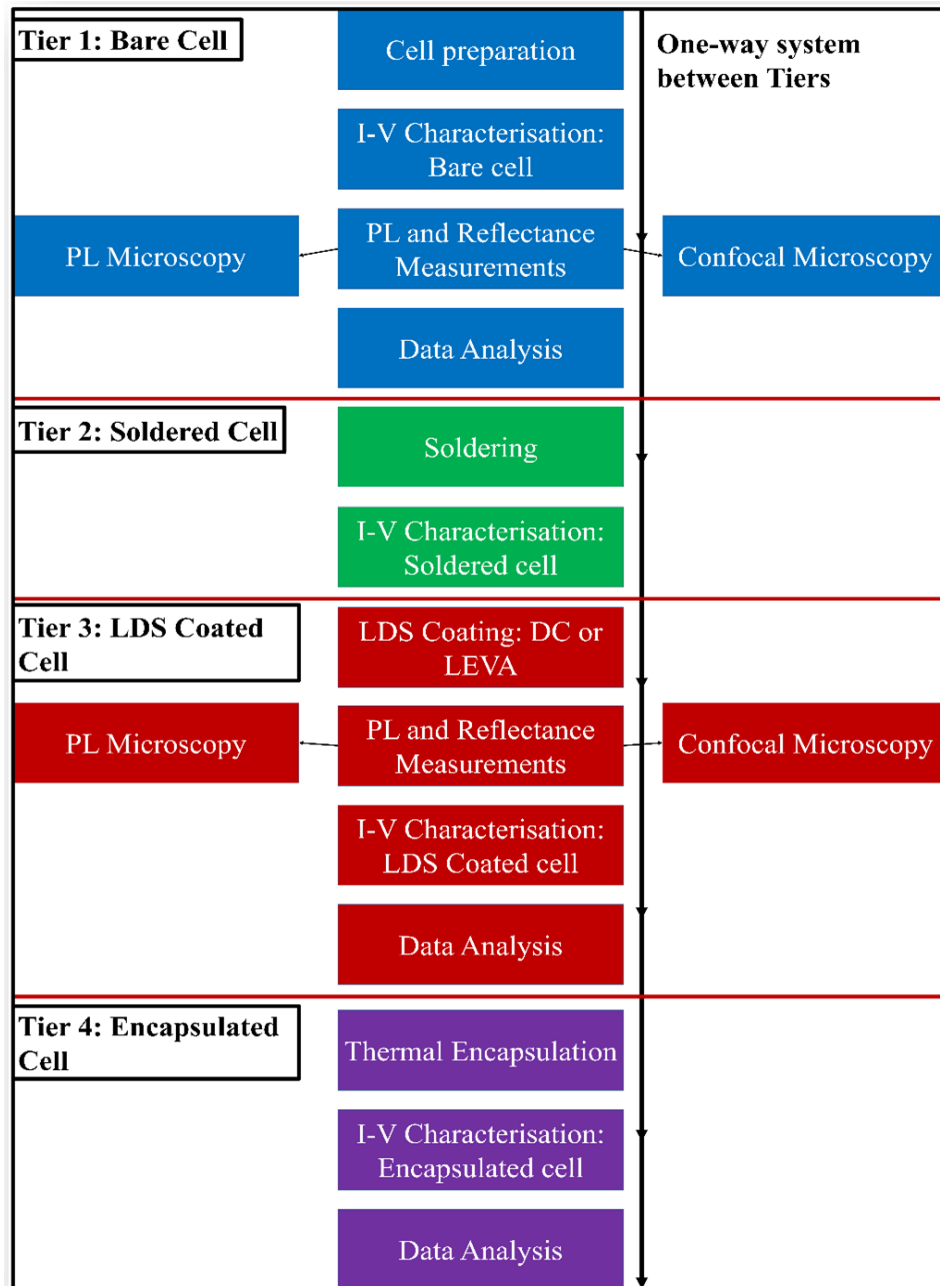
Figure 3.4 Methodology (solid samples): Experimental Protocol for pc-Si solar cells experimental investigation based on a Tier one-way system.

The steps outlined for the solid samples' methodology are divided into 4 Tiers, with each tier focusing on a different state of the solar cell experimentation.

Tier 1, Bare: includes cell preparations, and base reference characterisation. Noting that reference characterisation here refers to all measurements prior to DC coating with LDS QDs, which serves as the basis of data analysis.

Tier 2, Soldered: refers to transitional electrical stage where the sample is soldered with thin ribbon wires and I-V characterised once more. It expected that electrical readings would stabilise and show better consistency after soldering as I-V measuring probes have better surface contact.

Tier 3, LDS Coated: is concerned with coating the solar cells with LDS QDs, which was achieved by direct DC for PA SiQDs and a novel method called LEVA coating for $CsPbI_3$ PQDs (introduced in subsection 3.7). This includes another round of electrical I-V characterisation, PL, and microscopy. Results from this tier serve as evidence of enhancement or degradation in the performance of the pc-Si solar cells, where data is directly analysed and compared to results from Tier 1 and 2.

Tier 4, Encapsulated: this tier ideally investigates encapsulating the solar cells using conventional EVA as an encapsulant, pressed under Pilkington's OptiWhite 3.2 mm solar cell glass. However, $CsPbI_3$ PQDs cannot withstand high encapsulation temperature, so for that the cells were coated using EVA films only resulting from the novel LEVA coating.

To ensure consistency, all cells are processed following the standardized protocol with strict adherence to the specified procedures. This includes using identical tools, instruments, settings, and testing conditions throughout the experiment.

3.6.1. Cell preparations

Figure 3.5 illustrates the cleaning and exposure of busbars using invasive glass fibres, which is a critical step in the experimental process. This step involves removing the oxidized top layer, which can lead to high parasitic electrical resistance, such as series resistance, R_S, and compromise the accuracy of I-V characterisation. By exposing the underlying metal surface, the electrical measurements remain unaffected, ensuring reliable data acquisition.
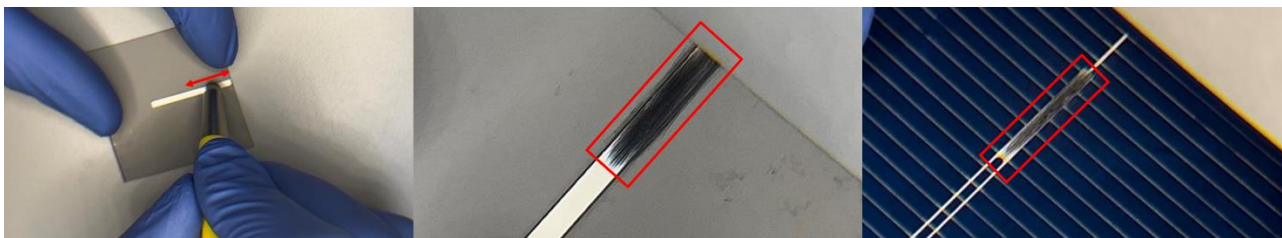
Figure 3.5 Cell preparation: Busbar cleaning using glass fibres.

It is important to note that this cleaning and exposure process is performed as a Tier 1 step, indicating its significance at the initial stage of the experiment to allow for uninterrupted electrical contact by the I-V characterisation probes. The cells are soldered in Tier 2, thus all measurements done from this Tier onwards are for soldered pc-Si solar cells. An example of the soldering process is depicted in Figure 3.6.

During soldering, it is crucial to ensure that the soldering product is thin and flush with the surface of the cell. Any protrusions or unevenness can create points of stress that may lead to cell cracking, particularly when handling and encapsulating the cell under a 3.2 mm glass sheet [287] using thermal encapsulation (also known as thermal lamination) with ethylene-vinyl acetate (EVA) as the encapsulant. Careful attention to these details is essential to prevent damage and maintain the integrity of the solar cell throughout the experimental process.
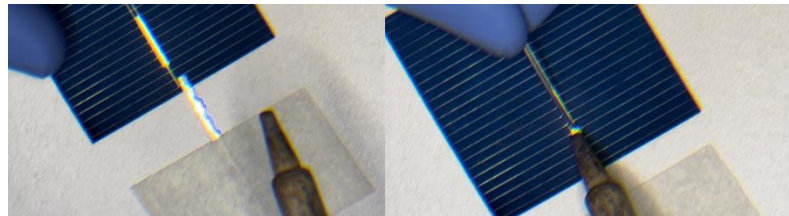
Figure 3.6 Cell preparation: Soldering procedure of pc-Si solar cells.

3.7. Conventional Encapsulation and the novel LEVA coating method

Despite being the final step in the experimental process, the encapsulation of pc-Si solar cells plays a crucial role in elevating the cells to meet industrial standards, closely resembling cells utilised in commercial solar modules. Apart from safeguarding the cells against environmental factors, encapsulation significantly improves the electrical properties by optimizing the optical characteristics of the solar cell sandwich. These optical enhancements manifest as improved optical coupling, enhanced light trapping, and better control over internal reflection, all of which contribute to the overall performance enhancement of the solar cells [193].

The thermal encapsulation of PA SiQDs coated pc-Si solar cells follows a conventional and well-established method that involves thermal lamination [291], [292]. The cells, sized 39 mm × 39 mm, are encapsulated using a sandwich structure consisting of a Tedlar white backsheet, EVA film, and a Pilkington OptiWhite glass with a thickness of 3.2 mm. All components of the sandwich have dimensions of 50 mm × 50 mm. This is shown in Figure 3.7, as a layer illustration (a), and a real image of a fully encapsulated pc-Si solar cell sample (b).

The thermal encapsulation (lamination) process is carried out by heating the sandwich using a hot-air gun, raising the temperature up to 100°C. The EVA film, present in both the thin layer on the Tedlar backsheet and as the top layer itself, melts during the process. The melted EVA acts as an adhesive, effectively bonding the glass to the cell.

Careful execution of the encapsulation process is crucial to ensure optimal results. Sufficient pressure is applied to remove any trapped air bubbles, while avoiding excessive pressure that could damage the cell. When performed correctly, the EVA forms a seamless bond between the glass and the cell, resulting in improved optical coupling and reduced internal reflection [291], [292]. These enhancements contribute to the overall performance improvement of the solar cell. Furthermore, this process forms a weather-proofing system that protects the cells from external weather-related damages, thus improving the overall lifespan of the cell.

Detailed analysis and discussion of the electrical results obtained from this encapsulation process will be presented in the PA SiQDs chapter, Chapter 4, providing further insights into the effectiveness of the encapsulation method.
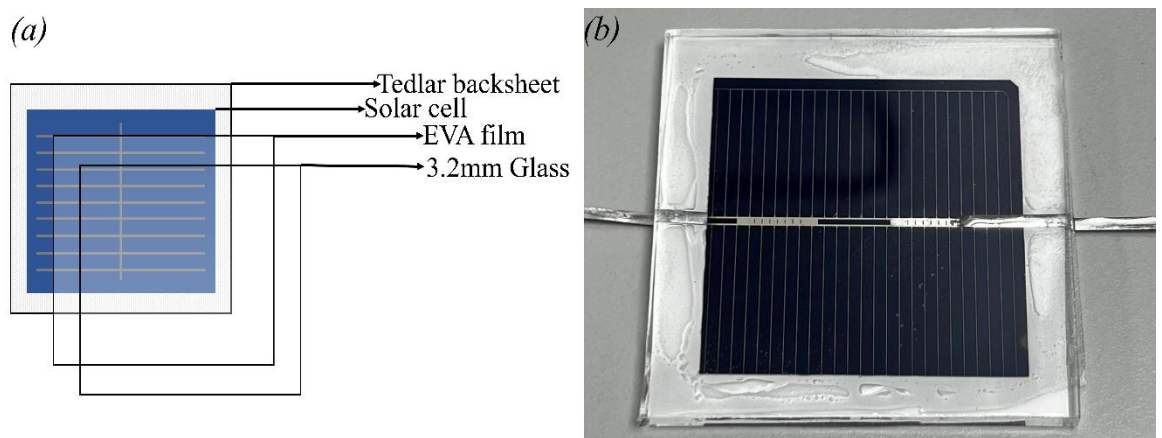
Figure 3.7 Thermal Encapsulation of a pc-Si solar cell, (a) a breakdown illustration of the lamination layers, and (b) an image of a fully thermally encapsulated pc-Si solar cell sample.

Certainly, the practical implementation and optimization of PQDs for enhancing pc-Si solar cells involve a protocol similar to that of SiQDs. However, due to the differences in the properties of these materials, variations arise in the handling and implementation procedures. PQDs have certain limitations, such as lower tolerance to high temperatures and rapidly degraded upon exposure to air [293], [294], [295], [296], [297] compared to SiQDs [96] which were shown to retain 96% of their PL intensity even when kept in 80°C hot water for 12 days [298]. Therefore, due to the oxygen-sensitive and highly degradable nature of PQDs ($CsPbI_3$) under thermal encapsulation

(lamination) temperatures exceeding 100°C, an alternative coating and coating method was developed to completely avoid direct heat application.

The new coating method was achieved by using EVA in a liquid form. Liquid EVA (LEVA) was prepared by dissolving 10 g of the encapsulant EVA in 3 ml of Toluene with the aid of a hot air gun at 145°C, inducing thorough mixing by convection. The resulting Liquid EVA mixture, referred to as LEVA hereafter, was then mixed with PQDs of a known concentration using a needle and vortex mixer. In the same manner as DC, 1 ml of the LDS LEVA mixture was then evenly poured over solar cells and allowed to dry by fully evaporating Toluene, resulting in a very thin LDS EVA host layer (denoted as LEVA film or LEVA coating henceforth), this process is shown in Figure 3.8.

This technique, drawing inspiration from the literature [184] represents a novel approach, previously unreported in such a manner. While the literature suggested limited use of dissolved EVA for LDS applications, particularly employing Toluene-dissolved EVA to create external LDS films formed on encapsulating glass before the thermal encapsulation of a Silicon solar cell [184], the LEVA method distinguishes itself by introducing an intermediate characterisation stage. In this method, the electrical enhancements in the cells are attributed to the LDS effect of the $CsPbI_3$ PQDs, isolated from the optical benefits caused by the encapsulation process. Further details are discussed and presented in subsection 5.2.1.

LEVA coating enabled the partial encapsulation of solar cells carrying PQDs as LDS frontal layers, while excluding the conventional 3.2 mm Pilkington OptiWhite glass and Tedlar backsheet. LEVA films act as a protective layer for the PQDs, prolonging their active shelf life by slowing down morphological degradation induced by exposure to air and high temperatures exceeding 100°C [130], [293], [299]. Since the resulting dry EVA layer is very thin, it does not add major optical benefit (full thermal encapsulation level) by itself to the solar cell and is effective only when combined with the LDS PQDs. Therefore, results are comparable to direct application of QDs by DC, and not conventional encapsulation. Hence, the LEVA coating will be treated as an alternative to the direct DC method used with PA SiQDs in Tier 3 results.

All LDS electrical and optical enhancements of the pc-Si solar cells, in addition to the properties of the LEVA layer, will be extensively explored and discussed in Chapters 4 and 5.
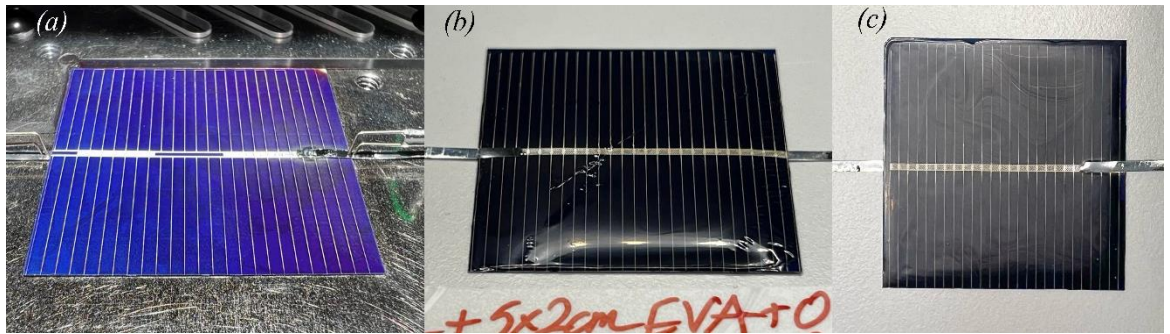
Figure 3.8 Novel LEAV coating: (a) is Bare cell, (b) LEVA coated wet cell showing meniscus before drying, (c) fully dried LEVA film coated cell showing streaks of CsPbI₃ PQDs.

3.8. Photovoltaic I-V Characterisation

I-V characterisation of the pc-Si solar cells was performed using a calibrated ABET Technologies' model 11002 SunLite Solar Simulator (USA) and KEITHLEY Tektronix 2450 SourceMeter (UK). The sample was placed on a temperature-controlled vacuum chuck and tested under standard test conditions (STC), which include a simulated solar irradiance of 1000 W/m^2 at AM1.5 and a cell temperature of 25°C. The position of the samples is fixed for identical light intensity each test. This is shown in Figure 3.9.

This step is iterated at least 6 times for each tier of the protocol, resulting in a minimum of 24 readings. The repetition of readings facilitates the application of robust statistical metrics, such as standard deviation, ensuring the systematic monitoring of accuracy and precision in the results. Additionally, it aids in identifying any anomalies or irregularities in the readings.

The accuracy specifications provided by the KEITHLEY Tektronix 2450 SourceMeter are detailed as follows [300]: for the current range of 1 A, the accuracy is 0.067% + 900 μA with a resolution of 50 μA. Regarding the voltage range of 2 V, the accuracy is 0.020% + 300 μV with a resolution of 50 μV. These accuracies are specified at a temperature of 23° ±5°C. As an example, from the laboratory, when Sample P23 was measured in its bare state at 25°C, it yielded an I_{SC} of 0.50071 A and a V_{OC} of 0.61996 V. Consequently, readings are accurate to the third decimal place for the I_{SC} (0.50071 ±0.0013 A) and to the fourth decimal place for the V_{OC} (0.61996 V ±0.00047 V).

Given that LDS optical enhancement primarily aims to increase the electrical photogenerated current without physically altering the pc-Si solar cell, fluctuations in the I_{SC} are expected to occur more frequently. This characteristic explains the lower accuracy observed in I_{SC} when compared to V_{OC}.

The results will be presented with precision to the third decimal place in the subsequent Chapters 4, 5, and 6 to maintain clarity and consistency.

To evaluate the precision and accuracy and consistency of the measurement system, two pc-Si solar cells, S1 and S2, were specifically prepared for this purpose. The I-V characterisation of these cells was conducted using the SunLite Solar Simulator in conjunction with the KEITHLEY 2450 SourceMeter, as previously mentioned. Each cell was subjected to 15 measurements, with a subtle variation between S1 and S2. For S1, all 15 measurements were taken continuously, without any replacement of the I-V probes during the process. On the other hand, for S2, the I-V probes were replaced for each of the 15 measurements, with the probes temporarily removed from the cell and then carefully repositioned. This approach was employed to thoroughly assess the reliability and reproducibility of the readings, taking into account the potential impact of probe placement on the measurement precision. The results from this rigorous testing will provide valuable insights into the accuracy and consistency of the system, thus validating its suitability for precise photovoltaic performance analysis. The results are shown in Table 3.1.

Table 3.1 Electrical parameters of samples S1 and S2 after 15 readings, continuous and discontinuous respectively.

Sample	Electrical Parameters	Average for 15 readings	Standard deviation (STD)
S1	I_{SC} (A)	0.514	0.00119
	P_M (W)	0.209	0.00042
	V_{OC} (V)	0.612	0.00012
S2	I_{SC} (A)	0.515	0.00272
	P_M (W)	0.209	0.00070
	V_{OC} (V)	0.613	0.00017

As seen in Table 3.1, electrical measurements are accurate to the 3rd decimal place for the I_{SC} as proved by an STD of 0.00119 A, and 4th decimal place for the P_M and V_{OC} as proved by STDs of 0.0007 W and 0.00017 V respectively. This reflects the high precision and accuracy the setup can achieve. This is true under condensed testing conditions of 15 readings in a short amount of time, in addition to the condition of cell being constant throughout the readings; unlike actual cells which will go under 4 different tiers of experimental testing, accounting for 24 total readings.

As these readings are well spread over a day of experimental work, the overall accuracy of the measurements, taking into account the temporal stability of the light source (Class ABA), precise positioning, temperature control, and controlled environmental conditions, can be confidently reported up to the third decimal place.

A blue bandpass filter, SCHOTT BG42 [301], was also used in some of the experiments to examine performance mainly in the blue-green light region between 300-700 nm (details are discussed later in Chapter 4, Figure 4.14).
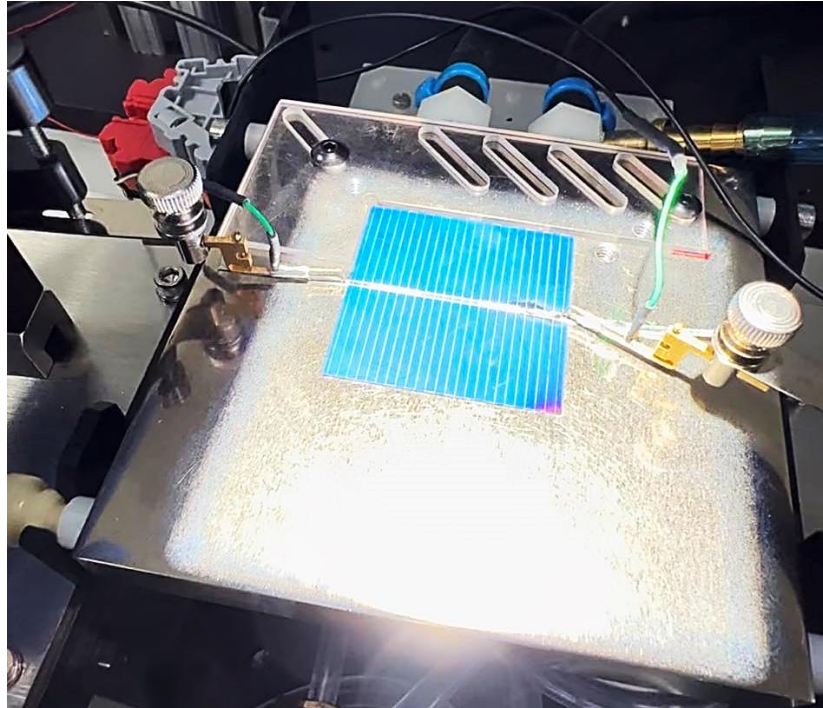
Figure 3.9 I-V characterisation of a Bare Soldered pc-Si solar cell.

Data analysis of I-V readings were based on calculating the I_{SC}, V_{OC}, P_M as main analytical parameters. The aim in increasing the performance of the solar cells can be justified by an increase in the I_{SC} mainly, and an increase in the 3 parameters overall. An increase in the I_{SC} dictates an increase in the maximum current generated by the cell which is directly proportional to the increase in received photons that are downshifted towards the red-light region. Moreover, While the literature has demonstrated increases in the V_{OC}, as displayed in Table 2.1 in subsection 2.1.6, these marginal increases are often attributed to the enhanced P_M resulting from the increased I_{SC} and also by enhanced charge separation and lower recombination losses. This enhancement is facilitated not only by the improved optical coupling but also by enhanced light trapping mechanisms. For detailed references on the specific studies supporting these findings, please refer to the literature cited in the respective subsection 2.1.6.

Reference samples were prepared throughout the whole project for measurements at each Tier. These samples ensured that I-V measurements were consistent throughout the life of each cell: this covered all stages from Tier 1 (bare) to Tier 4 (encapsulated; where applicable). In some cases, these cells also were used as references for reflectance measurements.

Figure 3.10 illustrates an electrical I-V characterisation curve of a pc-Si solar cell sample. This figure exhibits points for parameter extraction, crucial for both electrical performance measurements and analysis, including the I_{SC}, V_{OC}, and P_M. Additionally, other parameters are extracted to assess the cell's physical characteristics. For instance, the shunt resistance (R_{Sh}) can be monitored to examine the cell's physical integrity, revealing the presence of cracks, microcracks, or breakages. The series resistance (R_S) can indicate changes in electrical connections, such as contact issues with soldered wires.

As depicted in Figure 3.10, I_{SC} and V_{OC} are directly extracted by identifying the two points where the curve intersects with the axes. The y-intercept corresponds to I_{SC}, while the x-intercept denotes the V_{OC}.

P_M is found by calculating the highest power value, determined by the simple power equation, equation (3-1), expressed as:

$$P_M = I_{MP} \times V_{MP}$$

<div align="right">(3-1)</div>

Where I_{MP} and V_{MP} represent the current and voltage values that yield the maximum power (P_M), as indicated on Figure 3.10.

Subsequently, R_{Sh} is calculated by determining the negative inverse of the gradient of tangent 1 in Figure 3.10, while R_S is computed using the same equation but with tangent 2.

While all the parameters mentioned are employed to evaluate the performance of solar cells, the only anticipated change is in the I_{SC}. This is attributed to the fact that LDS films enhance the electrical characteristics of the solar cells externally by offering optical enhancements without causing any chemical or physical alterations. Consequently, LDS enhancements function by amplifying the photogenerated current, as measured by I_{SC}. This specific parameter will be the primary focus throughout this thesis.
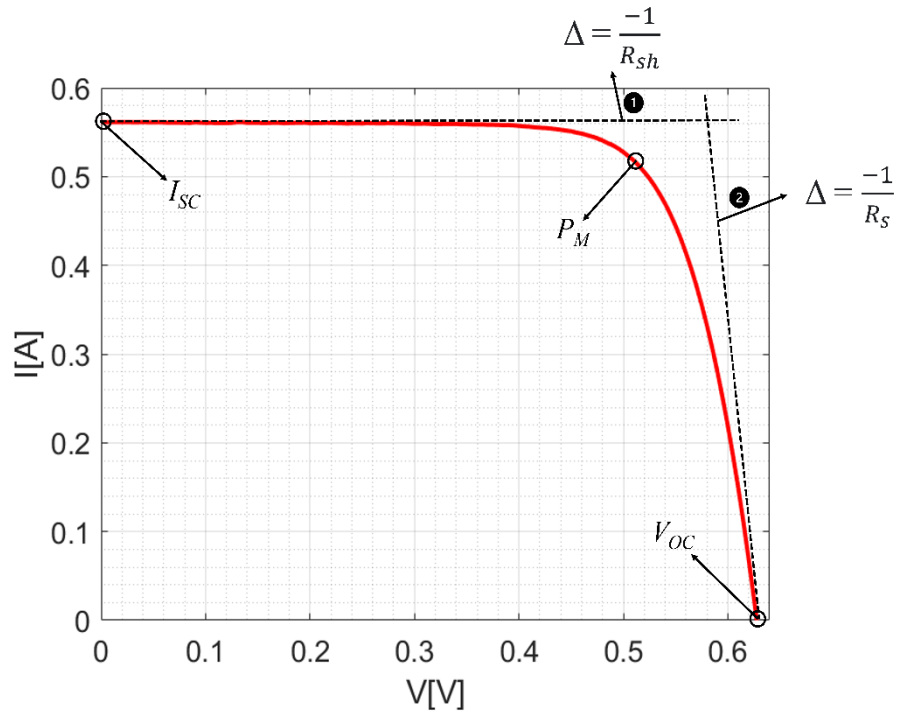
Figure 3.10 Electrical I-V characterisation curve of a pc-Si solar cell: extraction of parameters.

3.9.   Chapter Conclusion

In this chapter, the methodological protocols established for investigating PA SiQDs and CsPbI$_3$ PQDs as LDS devices to enhance pc-Si solar cells were comprehensively outlined, explained, and demonstrated. This included the introduction of the LDS QDs, characterisation techniques for both liquid and solid samples, accuracy and precision, sample preparation, and the depiction of the expected final coated product of LDS pc-Si solar cells.

The chapter emphasised the importance of characterising the LDS QDs before their implementation onto pc-Si solar cells and adapting these characterisation techniques to the coated solar cell samples. Furthermore, it clarified how the protocol set for the solid solar cell samples followed a sequenced, one-way 4-tier system that thoroughly investigated these cells from their initial preparation state to LDS coating and thermal encapsulation.

In light of this, a novel coating process addressing the high sensitivity of CsPbI$_3$ PQDs to phase shifting (degradation) was introduced. Named after one of its main components, LEVA, this process investigates these PQDs as LDS electrical enhancement devices externally deposited at room temperature. The utilisation of CsPbI$_3$ PQDs in these settings represents a novel endeavour, as the literature typically suggests the use of more stable analogous CsPbX$_3$ PQDs in higher temperature settings.

Further details regarding the methodologies and techniques introduced in this chapter will be provided for each material, alongside results, in their respective chapters.

4. PA SiQDs: Enhancing the efficiency of pc-Si solar cells by LDS.

4.1. Introduction

In this chapter the use of LDS PA SiQDs for the enhancements of pc-Si solar cells will be fully investigated and analysed.

Batches of PA SiQDs were freshly synthesised for the project. The fabrication process followed a bottom-up Si-halide reduction chemical method [226] previously reported in the literature for the synthesis of PA SiQDs by Ashby et al. in 2013, 2014, and 2015 [54], [96], [97] for thermal enhancements, and batteries.

This project investigated the specific use and novelty of PA SiQDs as LDS quantum devices to enhance the performance of pc-Si solar cells, which resulted in a publication [145]. These QDs have been reported for stable low thermal diffusivity [54] which can reduce the overall thermal diffusivity in solar cells, thus improving longevity by reducing thermal stress. However, the project focuses on the benefit of using the LDS properties of the QDs to specifically enhance the power conversion efficiency of pc-Si solar cells by externally altering the absorbed solar irradiance. As pc-Si solar cells typically exhibit low spectral response to light in the blue & UV region, 350-650 nm, and demonstrate considerably higher response in the Vis-NIR region, 650-950 nm [20-22], LDS QDs are added onto the surface of the solar cells to downshift shorter wavelength into longer wavelengths.

Following that up, this chapter fully investigates and discusses the employment of PA SiQDs in enhancing pc-Si solar cells by showcasing physical properties of the QDs and presenting optical and electrical characterisations for the cells at different Tiers of the experiments: Tier 1 where the cells are fully bare, Tier 2 where the cells are soldered, Tier 3 where the cells are LDS coated by PA SiQDs, and Tier 4 where the LDS-coated cells are thermally encapsulated in a 3.2 mm Pilkington OptiWhite glass, commercial EVA sheet, and Tedlar white backsheet sandwich.

4.2.   Experimental Procedure

4.2.1.   Synthesis of PA SiQDs

The synthesis method was precisely followed as reported in the literature [54], [96], [97], with some improvements made to the apparatus used, such as the Schlenk line's vacuum and air tightness.

The synthesis procedure is as follows:

In this synthesis method, 1 g of sodium (Na) and 4.2 g of Naphthalene were sonicated in 70 ml of tetrahydrofuran (THF) for 2 hours. This mixture was then added to a dispersion of 1 ml of Silicon chloride in 200 ml of THF, resulting in a brown suspension.

To this suspension, a solution of 2 ml of phenylacetylene (PA) in 20 ml of THF, which had been stirred for 30 minutes, was carefully added. Subsequently, 4.8 ml of n-butyllithium in THF was slowly added dropwise to the PA/n-butyllithium-THF solution. The PA/n-butyllithium-THF solution was then carefully added to the Na/Naphthalene-THF solution, and the mixture was refluxed for 8 hours at an appropriate temperature.

After the refluxing period, the mixture was washed with deionized water and diethyl ether. The solution was transferred to a separating funnel and allowed to settle for separation. This washing process was repeated several times. The diethyl ether portion was then reduced and dried using a rotary evaporator at 50°C until a dry orange/brown powder, referred to as the PA SiQDs product, was obtained.

The mean diameter of the PA SiQDs was reported to be 6 nm, with a standard deviation of 1 nm [97]. Further characterisation of the PA SiQDs, including FT-IR, TEM, NMR, and XPS measurements, can be found in previous studies conducted by Ashby et al. (2013, 2014, 2015) [54], [96], [97].

4.2.2.   Purification of PA SiQDs

Prior to the characterisation process, the PA SiQDs sample underwent a series of methodically designed purification steps to minimize the presence of parasitic impurities, particularly Naphthalene, which was expected to constitute a significant portion (approximately 97% or more) of the final product, as reported in the literature [54], [96], [97]. A visual representation of a freshly synthesised and pre-purified PA SiQDs sample is shown in Figure 4.1, where the expected deep orange-brown colour is diluted down to milky-orange by the excessive Naphthalene.

To enhance the yield, a comprehensive upgrade was implemented on the Schlenk line used for the reaction. The upgrade involved incorporating high-pressure Silicone grease, moisture traps, liquid traps, and a high-end vacuum pump [302]. These enhancements ensured a superior level of airtightness within the system, effectively preventing the access of oxygen and air. Consequently, allowing for higher partial vacuums and increased presence of inert gas (Nitrogen). The primary objective of this step was to maximize the consumption of Naphthalene, which served as the reductant in the reaction, thereby leading to an overall improvement in the final yield. This crucial upgrade acted as an intermediate purification precursor, setting the stage for subsequent purification processes.

Figure 4.1 Fresh PA SiQDs sample (pre-purification from Naphthalene) showing milky-orange colour that indicates varying concentrations of PA SiQDs within the impurity's waxy crystals.

Following the Schlenk line upgrade, three post-synthesis processes were employed to effectively eliminate residual Naphthalene and enhance the quality of the PA SiQDs. These processes were specifically designed to utilise direct heat application, aiming to induce the evaporation of Naphthalene, which possesses a theoretical melting point of 80.26°C.

The first process involved the use of a vacuum-assisted rotary evaporator, commonly known as a rotavapor. In this method, the final PA SiQDs sample was dissolved in ethanol, which exhibits a lower affinity for dissolving Naphthalene compared to the PA SiQDs themselves. The sample was then subjected to a partial pressure of 200 mbar and gradually heated to 100°C while being slowly rotated. The application of vacuum resulted in rapid evaporation of the melted Naphthalene at a considerable rate, effectively purifying at least 90% of the sample by mass. The evaporated

Naphthalene crystallized on the walls of the system and the round-bottom flask, allowing for easy clean-up through an acetone wash. The purified and dried sample was subsequently collected using a spatula. By redissolving the sample and repeating the process, an additional 5% on average could be removed from the initial total weight, thus achieving a higher level of purification. This method was similarly utilised by the reported researchers Ashby et al. in 2013, 2014, and 2015 [54], [96], [97].

The effects of removing 95% of the white and waxy Naphthalene can be seen in Figure 4.2 below; where the sample size greatly decreased, and the colour deepened from milky-orange to orange-brown.
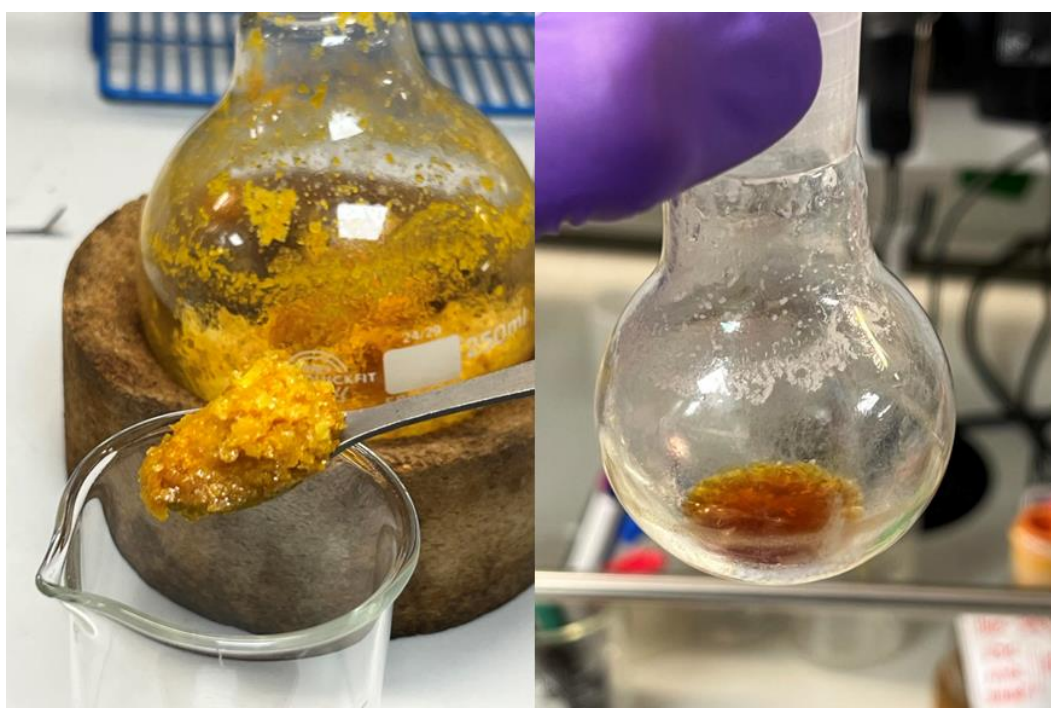
Figure 4.2 Pre-purification (left) and post-purification (right) of the November 2022 PA SiQDs sample using rotavapor only.

The second purification process was an approach involving direct application of heat using a heat-gun, Figure 4.3, and a hot-plate (within a fume cupboard). The heat-gun application at 145°C for 14 minutes resulted in visible reduction of Naphthalene, with the by-product crystallizing on the vial walls. This duration was found to be optimal, allowing Naphthalene to evaporate effectively while still providing enough time for it to cool and crystallize. Beyond the 14-minute mark, the residual Naphthalene ceased significant evaporation, as the air surrounding the sample at the vial's bottom became saturated. This procedure was repeated multiple times, yielding consistent results each time.

Although the heat-gun approach successfully removed a considerable portion of Naphthalene, it was insufficient to achieve complete removal (100%). The remaining sticky and highly viscous sample hindered complete extraction, and only a portion was collected for the purpose of enhancing pc-Si solar cells. The extracted sticky PA SiQDs were dissolved in DCM, known to dissolve both substances effectively, and then DC onto the cells. This method achieved further 2% reduction of Naphthalene; 97% of the impurity removed.

The stickiness and increased viscosity observed in the sample, which was not initially present after synthesis, resulted from the complete dissolution of Naphthalene into the sample. This dissolution led to weak attractive forces between the components, a phenomenon absent in the initial PA SiQDs product during drying. Fresh samples still exhibited Naphthalene associating with the QDs, though the majority of the waxy material tended to favour itself, creating two distinct coloured clusters. One cluster contained a higher concentration of PA SiQDs within Naphthalene crystals, while the other clusters exhibited significantly less PA SiQDs, appearing also milky-orange but whiter in colour.

With the gradual clearance of Naphthalene from the sample, a noticeable change in colour was observed as it transitioned to a darker hue, specifically a dark orange-brown shade, attributed to the presence of Phenylacetylene (PA).

Figure 4.3 The formation of Naphthalene crystals (at the top of the vial) as the main sample (in orange-brown at the bottom of the vial) was heated at 145°C for 14 minutes.

In order to address the incomplete removal of the unwanted substance in the previous two purification processes, an alternative, more rudimentary third approach was tested. The vial

containing the sample was subjected to a 250°C heated hot-plate for a duration of 5 minutes, with the process being repeated multiple times. During this treatment, the Naphthalene component was observed to evaporate, yet the sample retained its waxy consistency, with remnants of the impurity still present within the sample.

Certainly, upgrading the Schlenk line and implementing the two direct purification processes resulted in a remarkable 97% reduction in Naphthalene content. As explored in PL results shown in subsection 4.3.1, this substantial improvement played a crucial role in enhancing the PL quality of the PA SiQDs, making them more suitable for their intended application in solar cell enhancement.

It is crucial to acknowledge degradation as a potential byproduct of these refinement and purification processes. The PA SiQDs are subjected to prolonged exposures at relatively high temperatures of 100°C and 145°C, followed by a brief exposure to an even higher temperature of 250°C. This matter is elaborated upon in subsection 4.3, where results are discussed and analysed.

4.2.3. Sample Preparation of pc-Si solar cells

As detailed in the Methodology, Chapter 3, the solar cells go through 4 Tiers of experimental testing and measurements, where Tier 3 is concerned with LDS layer addition. Pc-Si solar cells samples were coated with LDS PA SiQDs by directly DC. To harvest the maximum benefit from the LDS effect, the highly volatile solvent DCM was chosen to dissolve the QDs for the DC process. This ensured the deposition of uniform and well spread LDS layers on all experimental solar cells. DC solutions were prepared by dissolving specific concentrations of PA SiQDs in 1 ml of DCM.

DCM, known for high volatility, was chosen as it dries up very quickly, but just in time for the liquid solution of DCM and PA SiQDs to spread evenly on the surface of the 39 mm × 39 mm solar cells, leaving uniform LDS layer of the QDs. Other layering methods were tested with the solution, such as SC, but DC have proved superior for creating even layers and lossless depositions. Visual results for both coating methods are presented in Figure 4.4, where two cells were coated using the same concentration of PA SiQDs using 1ml of DCM as a solvent: 0.01 mg/ml.
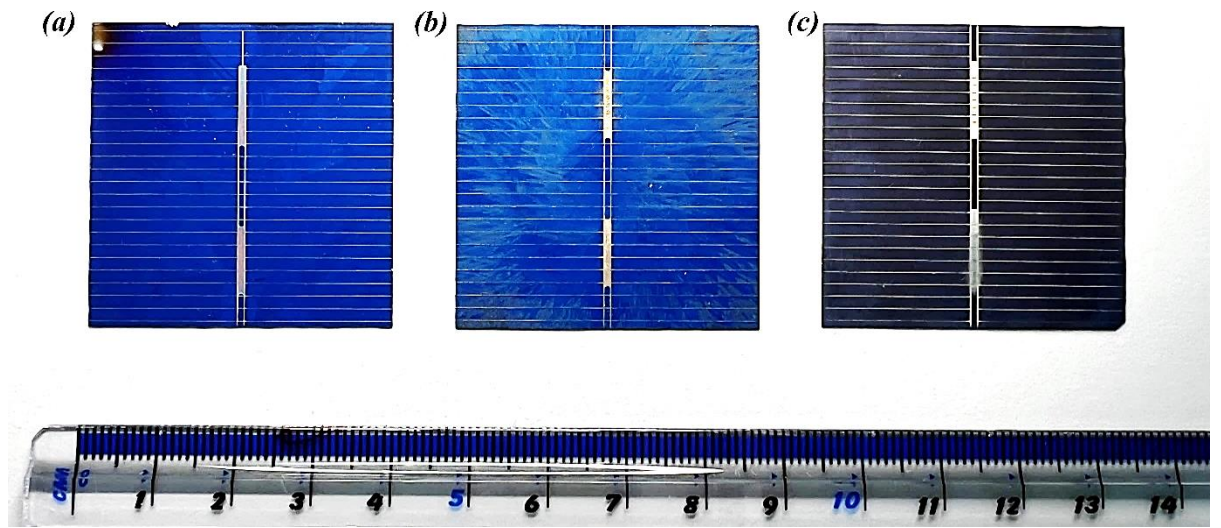
Figure 4.4 LDS PA SiQDs coating uniformity by method on pc-Si solar cells: (a) reference bare cell, (b) Spin Coated cell, (c) Drop Casted cell.

Figure 4.4 illustrates the differences in coating quality between SC and DC methods as previously introduced in subsection 3.2. SC resulted in a poor, non-uniform LDS coating characterized by outward white streaks of PA SiQDs at various concentrations, leaving gaps of non-coated solar cell surface (sample b). Additionally, high-concentration points were observed on the four corners of the cells. In contrast, DC produced a fully and evenly coated pc-Si solar cell (sample c). This is evident from the darker and uniform surface colour, a strong indicator of an even PA SiQDs LDS coating. Notably, allowing the PA SiQDs/DCM solution to dry more slowly using the DC method visually altered the surface, eliminating any streaks of PA SiQDs visible to the naked eye, further confirming the even layering achieved.

Through testing, DCM took less than 5 minutes to dry off completely, leaving uniform and well spread LDS layers. To ensure this uniformity stays controlled between different cells, all tested cells underwent DC and dried in the same experimental conditions. Uniformity has been tested by roughness measurements using a confocal microscope as seen under subsection 4.3.2 in Figure 4.8.

Following that up, pc-Si solar cells went under thermal encapsulation (Tier 4) that thermally laminated the cells into a sandwich of weather-proof system. The solar cell sandwich tends to have improved optical coupling and light trapping as a result of the EVA encapsulant tightly binding the cell to the frontal glass sheet. This further enhances the electrical properties of the cell.

4.3. Results and Analysis

4.3.1. Liquid samples: PA SiQDs characterisation

This subsection presents, analyses, and discusses the results obtained from characteristic measurements performed on liquid samples of PA SiQDs dissolved in DCM, specifically designed for DC onto pc-Si solar cells.

4.3.1.1. Photoluminescence (PL)

Results shown here follow the protocol for liquid sample characterisation shown in subsection 3.6.

Figure 4.5 below demonstrates the significant improvements achieved in the performance of PA SiQDs through the implementation of an upgraded Schlenk line and purification processes. The enhancements are evident in both the emission intensity and the emission wavelength of the samples.
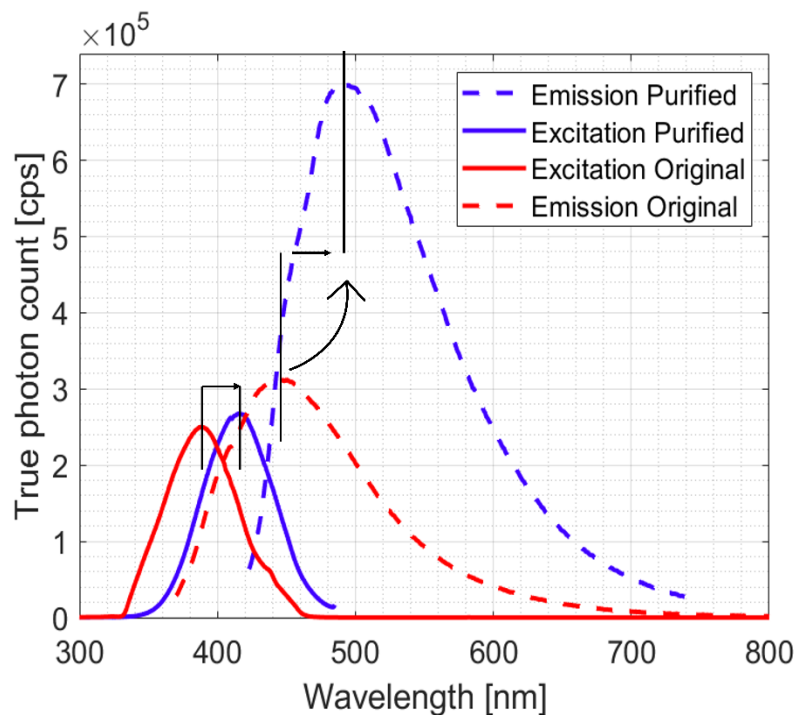
Figure 4.5 PA SiQDs: Excitation & Emission PL measurements for March 2022 original batch (388nm, 447nm) (Schlenk line 1) and November 2022 purified batch (415nm, 495nm) (upgraded Schlenk line 2). Liquid samples in DCM measured using Edinburgh Instruments FS5, true Excitation wavelengths.

Firstly, one purification cycle of the three thermal processes carried out on the November 2022 sample resulted in a substantial increase in emission intensity compared to the March 2022 sample

(original), despite both samples being excited by the same intensity excitation beam. The emission intensity of the November 2022 sample measured at $7x10^5$ cps, while the March 2022 sample exhibited an intensity of $3x10^5$ cps. This improvement clearly indicates the effectiveness of the upgraded Schlenk line and purification procedures in enhancing the PL performance of PA SiQDs.

Secondly, the use of the upgraded Schlenk line, which ensured better airtightness and minimized moisture through the incorporation of traps, led to the production of higher quality PA SiQDs that emitted light in the expected and desired wavelengths above 450 nm for LDS applications suited for Si solar cell electrical enhancements. Specifically, the November 2022 batch emitted light at 495 nm (Excitation: 415 nm), while the March 2022 batch emitted at 447 nm (Excitation: 388 nm). The emission wavelength of the PA SiQDs in the November 2022 batch aligns well with reported data in the literature especially for SiQDs synthesised chemically which is expected to fall between 400-500 nm [144], [226], and serves as a direct indication of the higher quality synthesis process achieved through the upgraded setup.

Furthermore, previous research on SiQDs and their PL behaviour has consistently shown the best PL emission responses to be around 500 nm [303]. Interestingly, the LDS shift between the excitation and emission wavelengths was found to be larger for the higher-quality November 2022 batch compared to the March 2022 batch: 80 nm and 59 nm, respectively. A similar effect was reported by Ji et al. (2019) [243].

4.3.1.2.   FT-IR readings

Using the Perkin Elmer Spectrum BX FT-IR Spectrometer introduced in subsection 3.5, the synthesised samples were tested for chemical composition. This is done by passing infrared light through the sample, which is transformed into a spectrum, using Fourier transform, representing chemical bonds as fingerprints [289]. Peaks or flat parts (absence of peaks) of the curve can singularly or collectively represent specific bonds present in the material.

Figure 4.6 demonstrates lab synthesised PA SiQDs samples: March 2022 batch, November 2022 batch, and the reported batch Ashby et al. (2014) [97] that serves as a baseline.
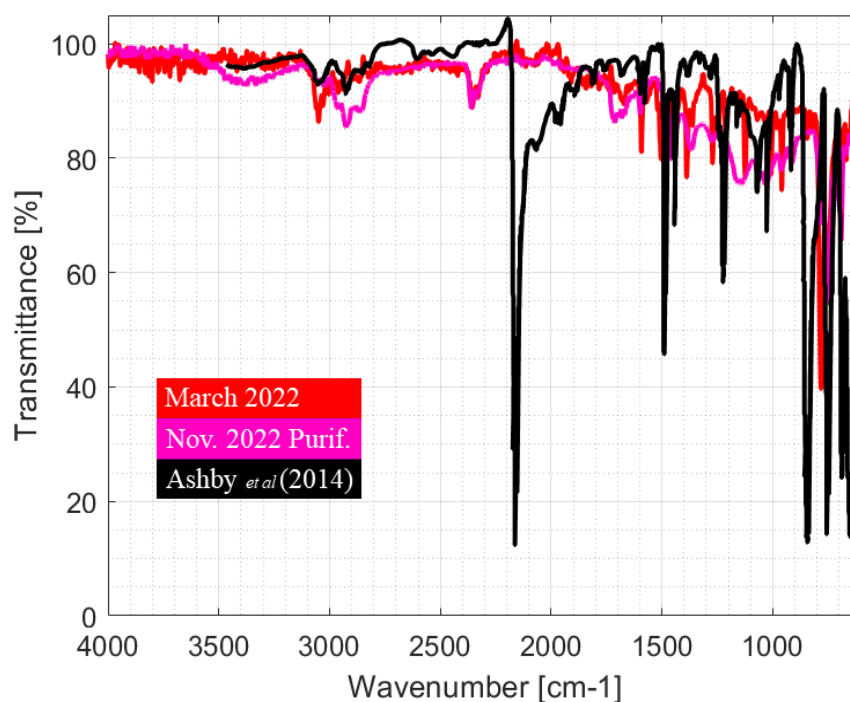
Figure 4.6 FT-IR readings for two PA SiQDs: March 2022 and latest purified sample of November 2022. Purified Nov22 sample is via both rotavapor and hot-plate. Reported sample measured by Ashby et al. (2014) [97] *shown in black.*

According to Ashby et al. (2014) [97], the strong and sharp peak observed at 2161 cm^{-1}, corresponds to the characteristic C≡C bond.

Its presence, coupled with the absence of a sharp peak at 3300 cm^{-1}, suggests the attachment of the C≡C bond to Silicon. This peak is evidently missing in the fabricated samples whether purified or not.

However, it has been noted that the presence of medium sharp peaks at 1441 cm^{-1} and 1221 cm^{-1} provides support for the existence of the C≡C bond to Silicon. Although the evidence in this region is weak, it is deemed acceptable as an indication of the Silicon core's presence, which clearly aligns with the reported sample described by Ashby et al. (2014) [97].

Furthermore, it is worth mentioning that there is evidence of the presence of PA, as proven by peaks at 1068 and 1026 cm^{-1}.

These findings highlight the challenge of characterizing the presence of SiQDs cores within the PA SiQDs samples due to the masking effect of Naphthalene. Further investigation and refinement of the synthesis and purification processes may be necessary to achieve the desired confirmation of the SiQDs core in future iterations of the research.

Nevertheless, the FT-IR readings were sufficient to identify the target PA SiQDs.

4.3.2. Solid samples: PA SiQDs coating characterisation (on pc-Si solar cells)

This subsection presents, analyses, and discusses the results obtained from characteristic measurements performed on solid samples of PA SiQDs coated pc-Si solar cells as per the protocol presented in subsection 3.6.

4.3.2.1. Reflectance

Using an Ocean Insight OceanHDX Spectrometer reflectance setup, diffuse and specular reflectance of the LDS coated pc-Si solar cells were performed.

The presented data in Figure 4.7 showcases the diffuse (45°) and specular (0°) reflectance measurements of a bare pc-Si solar cell and one coated with PA SiQDs. The direct DC of PA SiQDs on the cell surface resulted in a significant reduction in reflectance within specific wavelength ranges, notably between 340-480 nm and 700-920 nm. Conversely, there was a slight increase in reflectance between 500-700 nm.
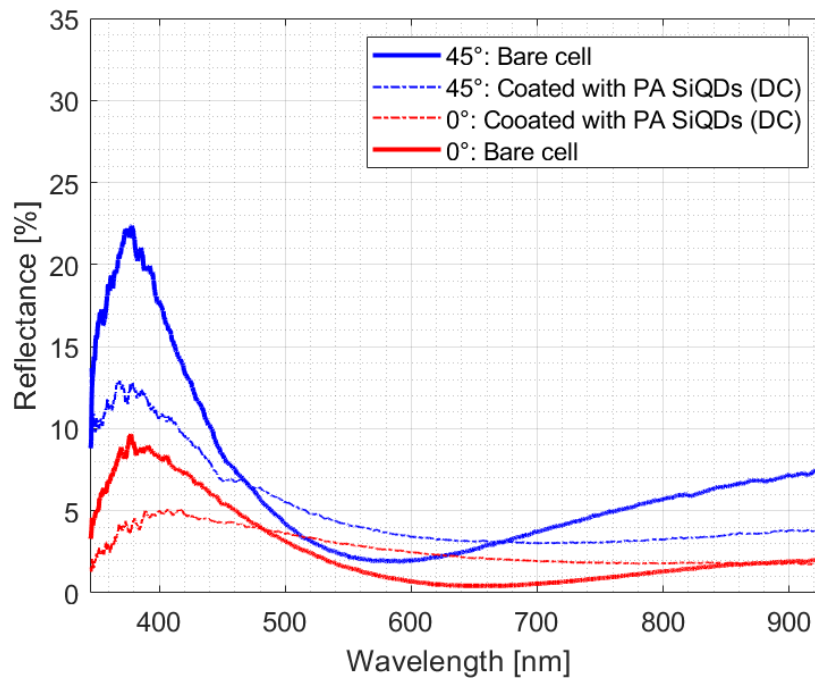
Figure 4.7 Diffuse and specular reflectance measured at 45° and 0°, respectively, for the bare and PA SiQDs coated pc-Si solar cell sample, 0.01 mg of PA SiQDs by DC.

Noteworthy reductions of 61.8% in specular reflectance and 44.4% in diffuse reflectance were observed at a wavelength of 377 nm.

These observations are consistent with the findings presented in the reviewed literature, which have documented analogous decreases in reflectance within the absorption spectrum ranging from

350-450 nm. Such reductions were reported in scenarios where SiQDs were utilised to enhance the efficiency of Si solar cells through LDS. The authors of these studies attributed the decreased reflectance to the effective implementation of LDS [144], [162], [214]. Notably, previous studies have indicated a dominant decrease of ~20% between 300-400 nm [50], ~33% at 370 nm [47], and an 8.5% reduction at 360-370 nm [210].

The significant antireflective behaviour of PA SiQDs can also be attributed to the porous nature of the coating achieved during the DC and drying process [47], [50]. This porosity appears to enhance overall light absorption while diminishing the reflection of incident light in the absorption region from 350-450 nm and past 680 nm (for diffuse reflectance) and past 850 nm (for specular reflectance), thus contributing to improved optical coupling. The literature suggests that utilising porous nanoparticle aid in reducing the refractive index mismatch between the solar cell layers and air and consequently enhance efficiency of the cells [304], [305].

It is noteworthy that pc-Si solar cells inherently possess a V-shaped rough surface as texturing is a part of its manufacturing process. Interestingly, literature suggests that reducing or eliminating these V-shaped features on the cell surface can lead to increased reflection [306]. While the amount of deposited PA SiQDs may not be sufficient to fill these grooves, the excess Naphthalene present within the sample can effectively fill the V-grooves, creating a waxy and flat reflective layer which is characteristic of this material as seen in Figure 4.8. This explains the increase in diffuse reflectance between 480-660 nm and 500-820 nm for specular reflectance. Moreover, the literature indicates that Naphthalene does not absorb wavelengths above 300 nm [307]. Coupled with its refractive index, which is similar to that of glass (1.4003 at 24°C) [308], the incorporation of a Naphthalene layer is expected to increase surface reflection.

Nonetheless, there have been reports in the literature of increased reflectance in the wavelength ranges of 400-650 nm [50] and 540-900 nm [157]. These increases have been attributed to optical LDS losses, a phenomenon arising from the formation of an escape cone. This cone allows a portion of the emitted LDS light to escape from the cell, as previously illustrated in Figure 2.5.

These results suggest that with the right amount of Naphthalene, it could theoretically serve as an optical host layer for PA SiQDs. Although this theory was not further pursued in this chapter, it is elaborated upon in Chapter 7 (Discussion), where the investigation of a host layer carried in Chapter 5 (LEVA coating) was discussed in conjunction with Naphthalene. This was illustrated and explained in Figure 5.8 Chapter 5.

Nevertheless, the observed improvements in light absorption and reduction in reflection in some areas indicate that PA SiQDs offer a promising approach for enhancing the efficiency and

performance of pc-Si solar cells through both LDS and improved optical light trapping and coupling.

4.3.2.2. *Confocal Microscopy*

The Olympus LEXT OLS5000 confocal microscope was utilised to measure several aspects on the solar cell samples. This included the uniformity and roughness changes due direct DC of PA SiQDs as shown in Figure 4.9. A visual example of morphological difference between bare and PA SiQDs coated pc-Si solar cell samples, as a result of Naphthalene filling the V-grooved surface, is shown in Figure 4.8.
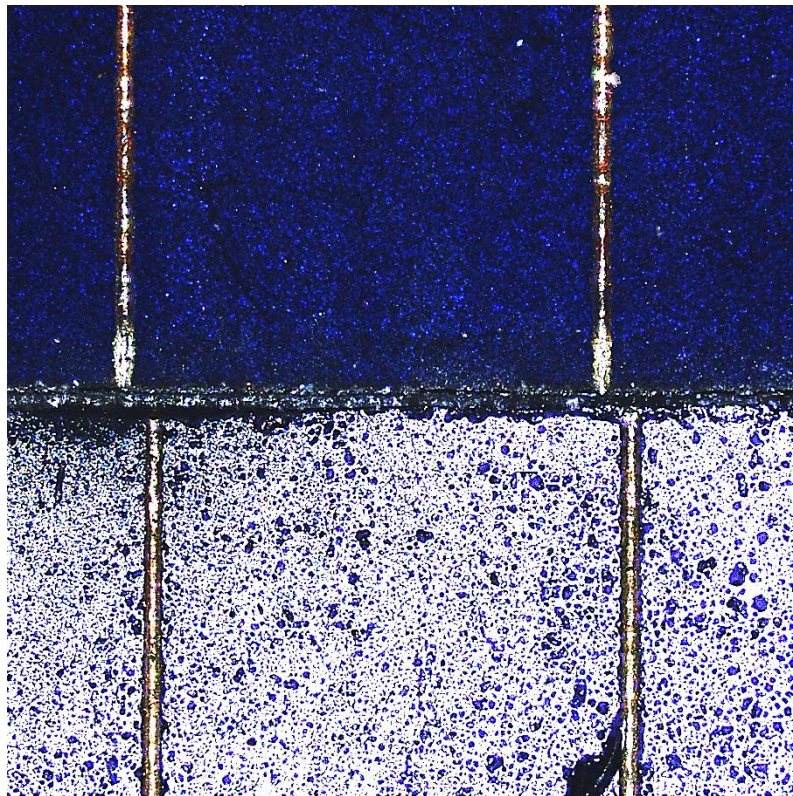
Figure 4.8 Side by side comparison of a Bare pc-Si solar cell (Top) and PA SiQDs DC layered solar cell (Bottom). Perpendicular view of a laser 3D image taken by the Olympus LEXT OLS5000 confocal microscope.
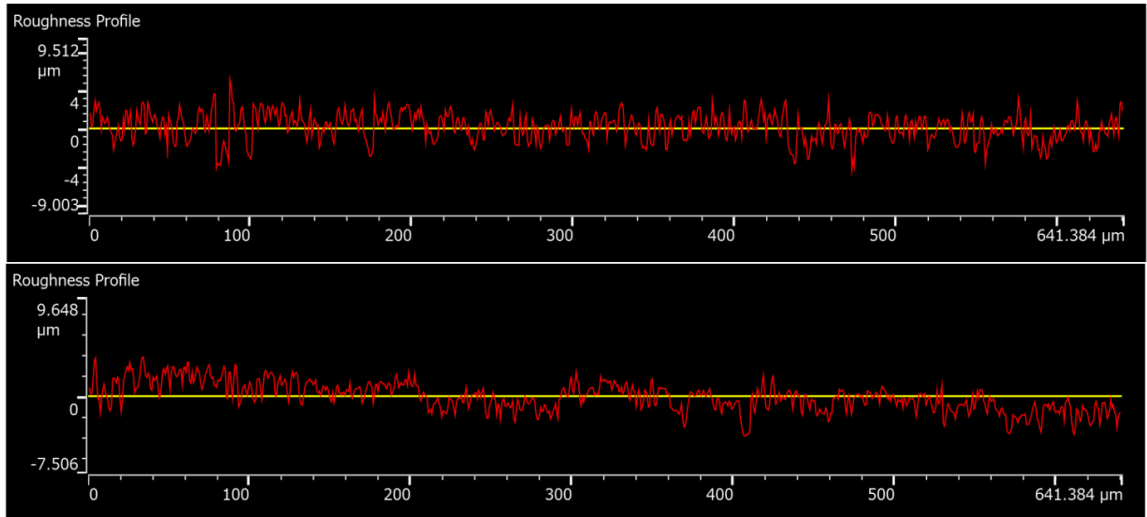
Figure 4.9 Roughness profile extracted from the 3D model generated by the 3D laser image shown above.

It is well shown how the PA SiQDs layer created by direct DC changes the roughness of the pc-Si solar cells, making them smoother. This can be concluded from the roughness profile as the layered cell (shown bottom in Figure 4.9) generate a smoother profile with distinguishable levelled plateaus. Visually, this can be seen as the white-reflecting deposition showing in comparison to the original deep blue colour which is a characteristic of a bare pc-Si solar cell. This reduction of roughness is caused by the PA SiQDs and Naphthalene filling in the gaps caused by the inverted pyramids morphology of the pc-Si solar cells.

4.3.2.3.   Fluorescence Microscopy

Using the ZEISS Axio Scope.A1 fluorescence microscopy setup, fluorescence microscopy of the LDS coated pc-Si solar cells was performed.

The PL spectrum of the PA SiQDs displays a distinct cyan colour with a peak at 495 nm, as detailed in subsection 4.3.1, encompassing a range from 490-506 nm. To excite the sample, the X-Cite 120Q spectral excitation light source [309] was employed, which offers a broad spectrum of wavelengths spanning from 300 to 740 nm. Noteworthy peaks within this range include 335, 370, 410, 440, 550, and 580 nm.

The PL of the PA SiQDs is visually manifested as a distinctive cyan hue, as observed in the right pictures in Figures 4.10 and 4.11. The presence of these quantum dots fills in the V-shaped rough surface of the pc-Si solar cell, and when excited, the emitted LDS cyan light illuminates the entire structure of the cell under the X-Cite 120 Q spectral excitation light. This results in a clearer and more defined image of the solar cell, revealing finer details which serves as a visual proof of the LDS emission by the PA SiQDs.

As depicted in Figures 4-10 and 4-11, a cell was imaged using the fluorescence microscope both in its Bare state (Tier 1) and after being coated with LDS PA SiQDs (Tier 3). To ensure a valid and unbiased comparison, the identical location was marked and measured both before and after the coating process. As previously emphasized, the application of PA SiQDs results in surface illumination of the cells through LDS.
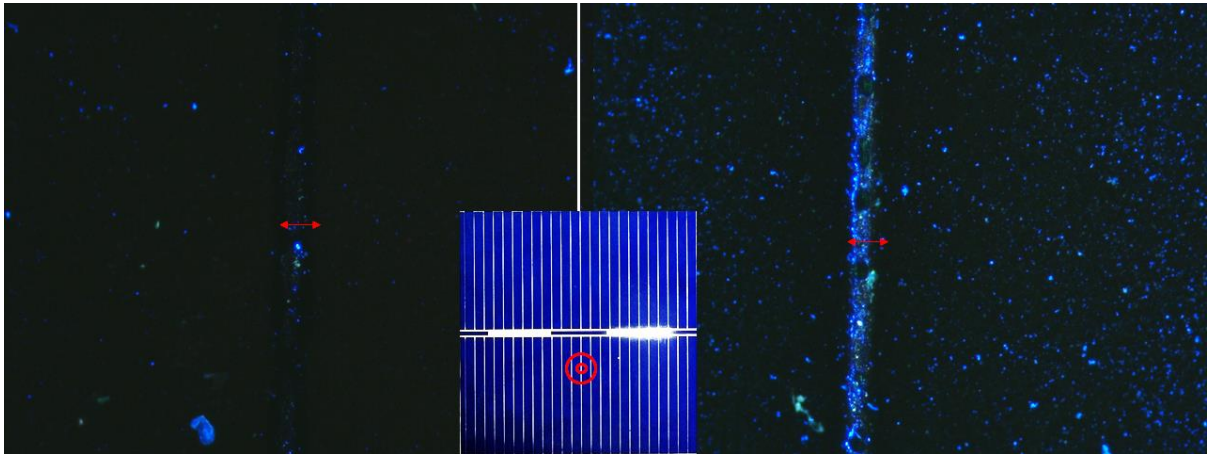
Figure 4.10 Fluorescence microscopy of a pc-Si solar cells at same settings: on the left, the fluorescence image of the Bare cell (Tier 1), and on the right the fluorescence image after applying LDS PA SiQDs coating by DC (Tier 3). In the middle is a picture of the whole solar cell with double red circle showing the region of the x10 microscopy, which is the lower quarter of the central silver finger. The arrows showing the position of the silver finger.
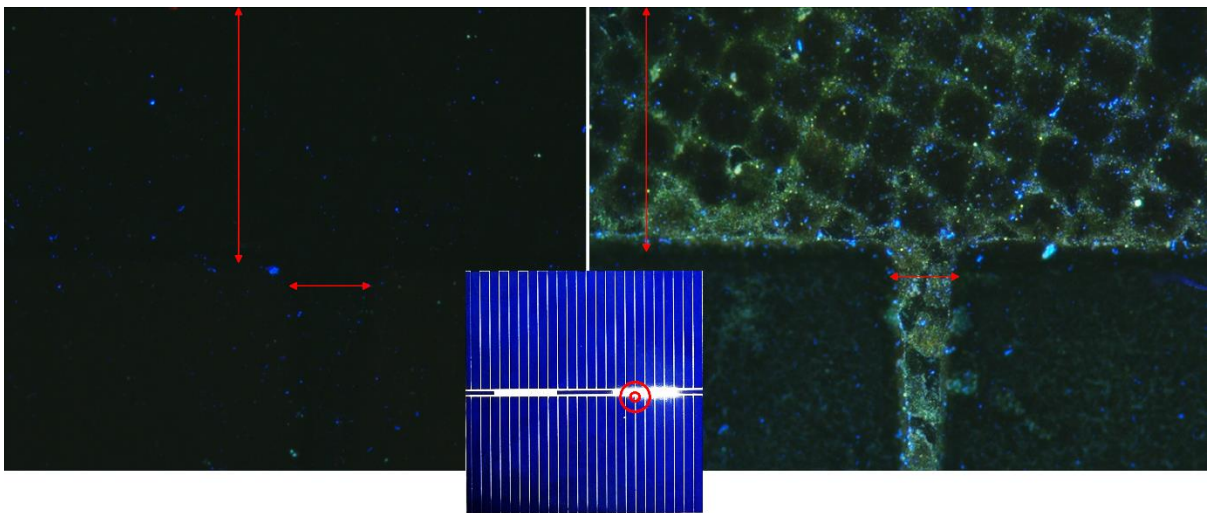
Figure 4.11 Fluorescence microscopy of a pc-Si solar cells at same settings: on the left, the fluorescence image of the Bare cell (Tier 1), and on the right the fluorescence image after applying LDS PA SiQDs coating by DC (Tier 3). In the middle is a picture of the whole solar cell with double red circle showing the region of the x10 microscopy, which is the conjunction between the central-right busbar and a silver finger. The arrows showing the positions of the busbar and silver finger.

Due to LDS, the silver fingers and busbar, exhibits improved visibility and contrast under the influence of the emitted cyan light. This enhanced visualization of the silver finger and the cell structure indicates the effective light-trapping and light-conversion properties of the PA SiQDs, which contribute to the overall improvement in the cell's performance.

The agreement between the expected PL and the measured PL readings further validates the accuracy and reliability of the experimental setup in producing even and well-spread PA SiQDs LDS coatings. This data provides valuable insights into the PL behaviour of the PA SiQDs and their potential application in improving the efficiency and performance of solar cells by effectively converting higher-energy photons into lower-energy ones, thus enhancing light absorption and overall solar cell efficiency. This is fully investigated in the following subsection 4.3.3, which will go into the electrical enhancements generated by the application of LDS PA SiQDs coatings.

4.3.3. Electrical Characterisation of PA SiQDs coated pc-Si solar cells.

4.3.3.1. Direct DC of PA SiQDs

Three samples have been prepared to showcase the LDS enhancements the PA SiQDs can offer, first two samples being Q1 and Q2, where third sample being Q3 which specifically served as a reproducibility proof which will be highlighted later in this section. These samples, alongside 3 reference samples, have led to a publication that strictly investigated the use of PA SiQDs to enhance pc-Si solar cells by LDS [145]. These sets of experiments were performed using the March 2022 batch, while the November 2022 batch was investigated separately later in this chapter in subsection 4.3.3.2.

Samples were coated with PA SiQDs by DC at room temperature with 2 different concentrations. Samples Q2 and Q3 were coated with 0.01 mg of <u>March 2022 batch PA SiQDs</u> dissolved in 1 ml of DCM, while sample Q1 was coated with 0.15 mg using the same parameters.

Difference in concentrations were determined by selecting samples with the most uniform deposition, which yielded consistent electrical results. As discussed earlier in this chapter, the presence of Naphthalene in unpredictable and inconsistent clusters within the synthesised PA SiQDs sample posed challenges in controlling their behaviour during deposition. Analogously coated cells were intended to be coated with varying amounts of PA SiQDs by DC: 0 mg (Reference), 0.01 mg (Q2, Q3), 0.05 mg, 0.1 mg, and 0.15 mg (Q1).

Samples Q1, Q2, Q3 went through all 4 Tiers of experimentation explained in Chapter 3: Bare cell (Tier 1), Soldered cell (Tier 2), LDS Coated cell by DC (Tier 3), and full thermal Encapsulation (Tier 4).

Since Tier 1 results are intended for quality assurance, results of the following 3 Tiers are shown and discussed as appropriate: Soldered cell (Tier 2), LDS Coated cell by DC (Tier 3), and full thermal Encapsulation (Tier 4).

The 3 reference samples were created to create a baseline for the results, and to ensure proper precision of the measurements. Since these cells are not coated (thus skipping Tier 3), they serve as the ground-state to validate increases resulting from PA SiQDs LDS coatings and thermal Encapsulation.

As discussed in the Methodology, Chapter 3, all results are reported to the 3rd decimal place.

The electrical parameters extracted from the I-V characteristics for the two samples Q1 and Q2 before and after the deposition of PA SiQDs by DC are displayed in Table 4.1. Both samples showed an increase in the I_{SC} of 0.75% for Q1 and 1.06% for the Q2 sample. There is a negligible effect of the coating on V_{OC} in Q1. The V_{OC} in Q2, although slightly increased, lies within the range of the standard deviation as discussed in the Chapter 2 and shown in Table 4.1. The increase in P_M for the Q2 sample of 0.51% is attributed to the increase in the current. The I-V characteristics for the Q1 and Q2 samples before and after coating are displayed in Figure 4.12.

Table 4.1 Electrical parameters of samples Q1 and Q2 before and after coating with PA SiQDs by DC, including Standard Deviation (STD).

Samples	Electrical Parameters	Soldered Solar Cell (Tier 2)	STD	Coated with PA SiQDs by DC (Tier 3)	STD	% Increase
Q1	I_{SC} (A)	0.531	0.00071	0.535	0.00032	0.75
	P_M (W)	0.224	0.00035	0.224	0.00086	0.00
	V_{OC} (V)	0.603	0.00019	0.603	0.00025	0.00
Q2	I_{SC} (A)	0.472	0.00005	0.477	0.00046	1.06
	P_M (W)	0.193	0.00013	0.194	0.00058	0.51
	V_{OC} (V)	0.582	0.00012	0.583	0.00063	0.17
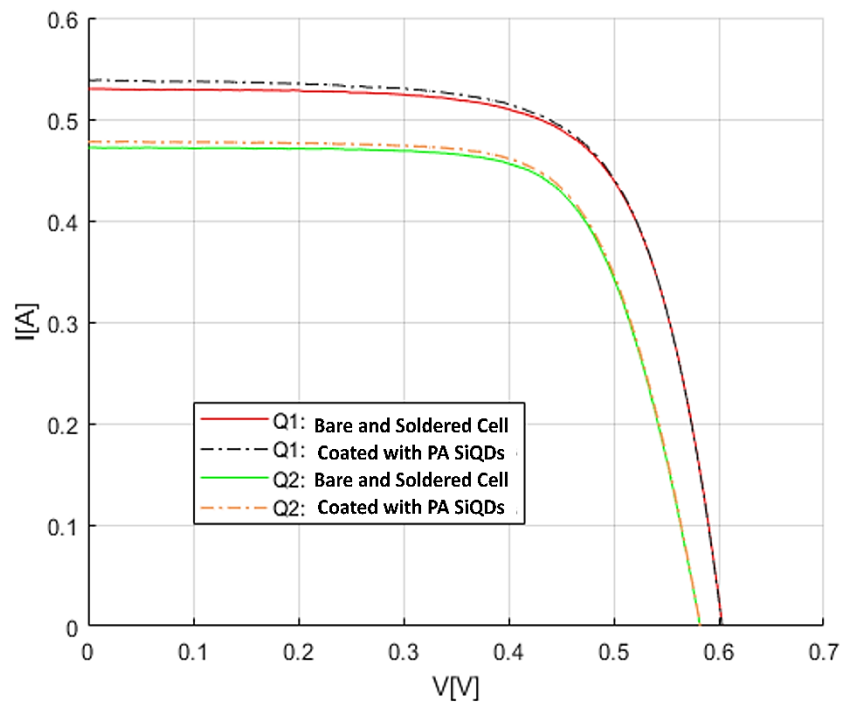
Figure 4.12 I-V characteristic of Q1 and Q2 samples before (Tier 2 soldered cell) and after coating with PA SiQDs by DC (Tier3).

As per the methodical protocol explained in subsection 3.6, the Tier 3 DC coated Q2 sample was further thermally encapsulated (Tier 4) in a sandwich structure consisting of a Pilkington OptiWhite glass with a thickness of 3.2 mm, ethylene-vinyl acetate (EVA) film, and a Tedlar white backsheet; refer to Figure 3.5.

The electrical characteristics of pc-Si solar cell sample Q2 before (Tier 2) and after coating and encapsulation (Tier 4) are shown in Table 4.2. A significant increase in the I_{SC} of 11.86% and the P_M of 11.39% is observed mainly attributed to the increase in the current and the effect of encapsulation.

As previously stated in subsection 3.7, in addition to providing protection against environmental factors, encapsulation plays a pivotal role in enhancing the electrical properties of solar cells by optimizing the optical characteristics within the solar cell sandwich structure. These optical enhancements are evident through improvements in optical coupling, enhanced light trapping, and more effective control over internal reflection. Collectively, these enhancements contribute significantly to the overall improvement in the performance of the solar cells [193] as evident in Table 4.2.

 The I-V characteristic curves of the soldered (Tier 2) and encapsulated (Tier 4) solar cell sample Q2 and reference sample R1 are shown in Figure 4.13.

Table 4.2 Electrical parameters of Q2 sample before coating (Tier 2) and after coating with PA SiQDs and encapsulation (Tier 4).

Electrical Parameters	Q2 Soldered Solar Cell (Tier 2)	Q2 Coated and Encapsulated Cell (Tier 4)	% Increase
I_{SC} (A)	0.472	0.528	11.86
P_M (W)	0.193	0.215	11.39
V_{OC} (V)	0.582	0.586	0.69
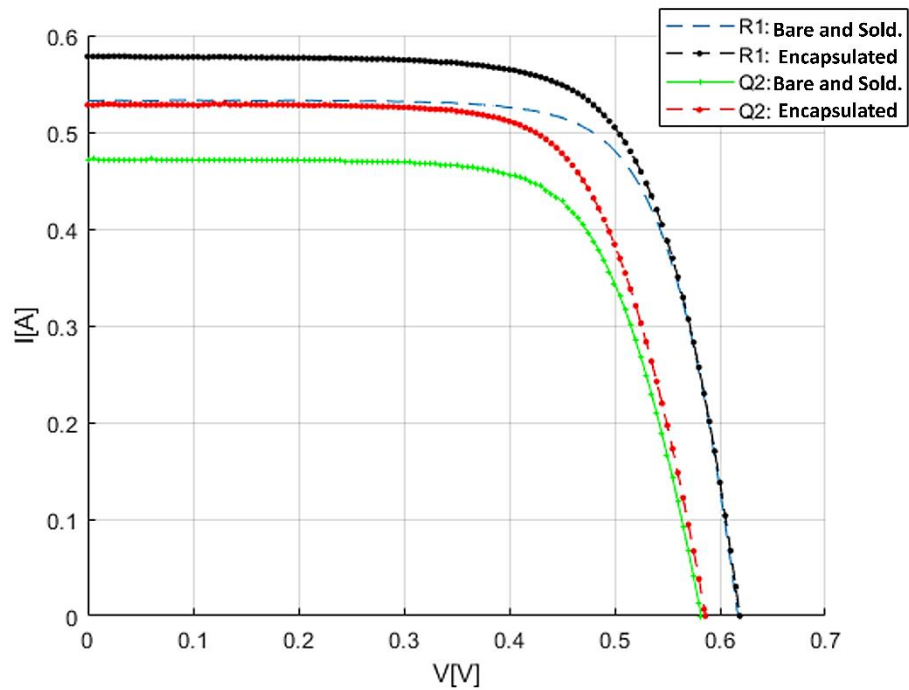
Figure 4.13 I-V characteristic of Q2 sample (coated by DC of PA SiQDs) and reference R1 sample before (Tier 2) and after encapsulation (Tier 4).

To assess the impact of thermal encapsulation, three reference solar cell samples were examined both before (Tier 2) and after the encapsulation process (Tier 4). The results of the electrical parameters are presented in Table 4.3. Following encapsulation, there was a notable increase in the range of 8.26%-8.58% in the I_{SC}. This significant increase can be attributed to a combination of factors, including internal back reflections occurring at the interface with the glass substrate, which possesses high optical characteristics, leading to an improved light trapping capability. Additionally, there was a corresponding increase of up to 8.7% in the P_M. In contrast, the Q2 sample, which was coated with PA SiQDs and subsequently encapsulated, exhibited approximately 3.4% higher enhancement in I_{SC} and approximately 4.1% in P_M when compared to the performance increase observed in the encapsulated reference samples. This increase includes a 1% improvement in I_{SC} attributed to the PA SiQDs coating, while the remaining enhancement is

attributed to improved optical coupling and light trapping resulting from the encapsulation process.

Table 4.3 Electrical parameters of three reference samples before (Tier 2) and after encapsulation (Tier 4).

Reference Cell Sample	Electrical Parameters	Soldered Solar Cell (Tier 2)	Encapsulated Cell (Tier 4)	% Increase
R1	I_{SC} (A)	0.533	0.577	8.26
	P_M (W)	0.240	0.253	5.42
	V_{OC} (V)	0.616	0.619	0.49
R2	I_{SC} (A)	0.548	0.595	8.58
	P_M (W)	0.229	0.249	8.73
	V_{OC} (V)	0.612	0.614	0.33
R3	I_{SC} (A)	0.543	0.589	8.47
	P_M (W)	0.243	0.262	7.81
	V_{OC} (V)	0.620	0.622	0.32

In a further experiment, the incident simulated solar light was selectively filtered through a bandpass filter, specifically the SCHOTT BG42 filter. This filter is designed to predominantly transmit light in the region between 300-700 nm, as demonstrated in Figure 4.14. Its transmission range spans approximately 300-700 nm, with peak transmittance occurring at 511 nm, reaching a high transmittance rate of 92.9% [301]. The utilisation of this filter effectively isolates the impact of PA SiQDs on enhancing pc-Si solar cells to its LDS characteristics. This works by weakening the transmitted solar radiation wavelength at 377 nm where a significant drop in reflectance was observed (Figure 4.7), and relatively allowing in more of the excitation wavelength responsible for LDS. Therefore, testing whether sufficient and effective LDS is presented by PA SiQDs to enhance the performance of pc-Si solar cells. This is further explained in the upcoming subsection 4.3.3.2.

Under the SCHOTT BG42 filter, the increase in I_{SC} for the encapsulated Q2 sample coated with PA SiQDs reached 13.68% compared to 11.57% for the reference uncoated cell R1, as shown in Table 4.4. This enhancement can be attributed to the improved light trapping and optical coupling of the solar cell sandwich, which was further boosted for sample Q2 by the LDS phenomenon.

However, it is worth noting that the corresponding increase for both encapsulated cells were higher in the SCHOTT BG42 filtered (Q2: 13.68% & R1: 11.57%) than that for the full unfiltered simulated solar light (Q2: 11.86% & R1:8.26%). The higher performance in this region is attributed to the effect of encapsulation with higher internal reflections at blue wavelengths.

Moreover, in addition to the electrical enhancements facilitated by the luminescent downshifted light, the presence of PA SiQDs in the solar sandwich further enhances light trapping by acting as absorption focal points for reflected or stray photons that would have otherwise escaped the cell.

However, it is important to note that EVA characteristically absorbs UV light up to 400 nm. Specifically, it blocks 350 nm and allows approximately 75% of light at 388 nm to pass through (Figure 5.9), which is the absorption wavelength for the March 2022 batch. This observation motivated the investigation into purification and higher quality samples, leading to the development of the November 2022 sample that exhibited a shifted absorption wavelength to 415 nm, as previously illustrated in Figure 4.5.

The I-V characteristics for the Tier 2 (soldered) and Tier 4 (encapsulated) coated Q2 sample and reference R1 sample for simulated solar light passing through the blue filter are presented in Figure 4.15.
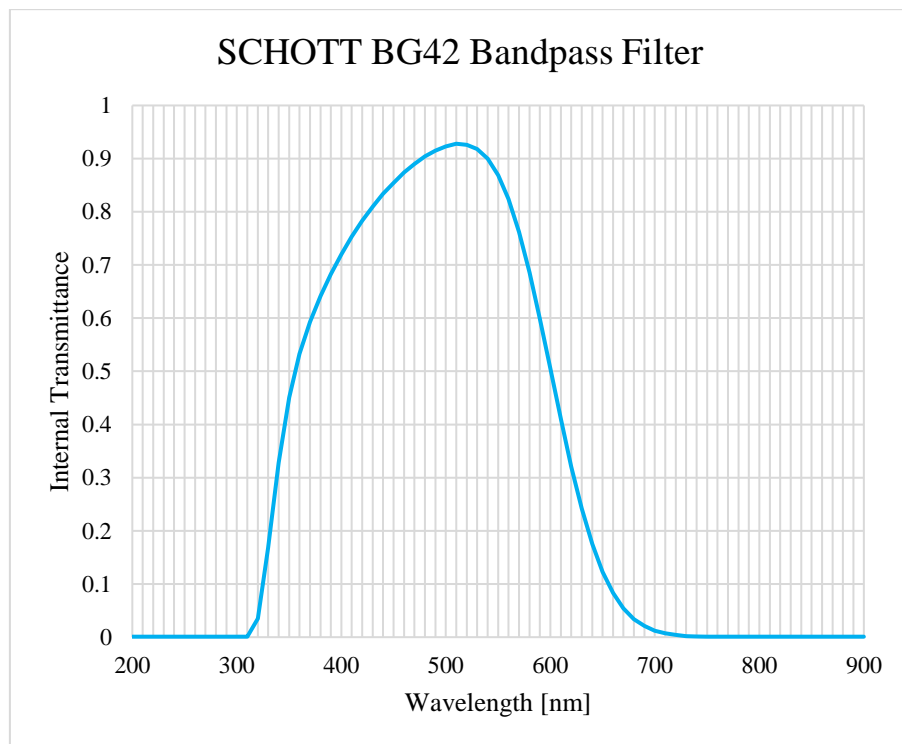
Figure 4.14 Transmittance: SCHOTT BG42 Bandpass NIR-cut filter, Thickness 1.0 mm, Reflection factor 0.9135. [301]

Table 4.4 Electrical parameters of sample Q2 before LDS coating (Tier 2 soldered cell) and after LDS coating (by DC) and encapsulation (Tier 4 cell), compared to reference sample R1 before (Tier 2) and after encapsulation (Tier 4). The incident simulated solar light was reduced and selectively filtered by the blue filter SCHOTT BG42.

Sample	Electrical Parameters	Soldered Solar Cell (Tier 2)	Encapsulated Cell (Tier 4)	% Increase
	I_{SC} (A)	0.117	0.133	13.68
Q2	P_M (W)	0.044	0.051	15.91
	V_{OC} (V)	0.524	0.527	0.57
	I_{SC} (A)	0.121	0.135	11.57
R1	P_M (W)	0.051	0.055	7.84
	V_{OC} (V)	0.574	0.57	−0.70
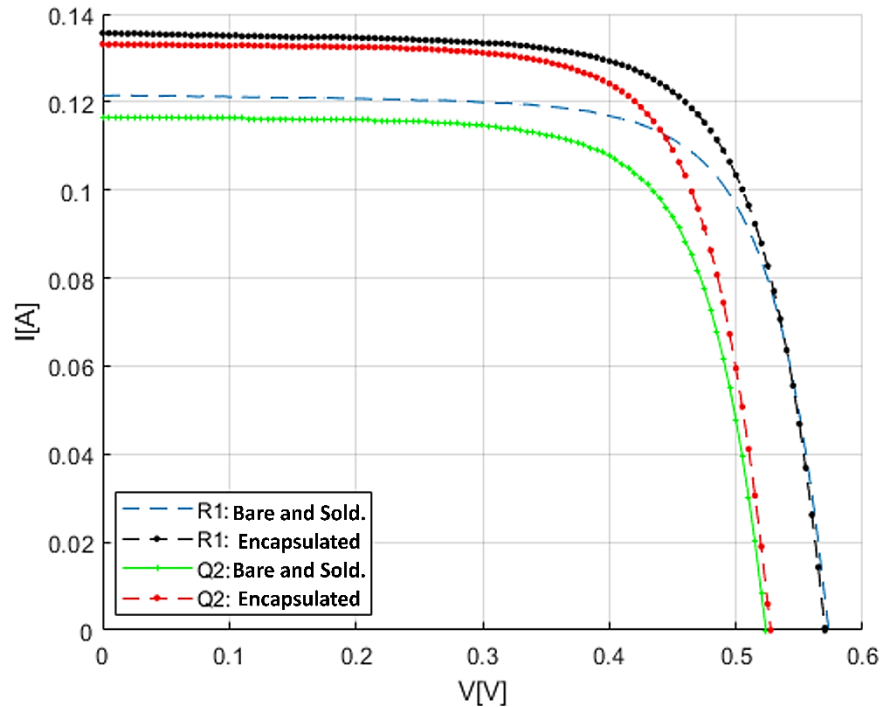
Figure 4.15 I-V characteristic for coated sample Q2 (by DC of PA SiQDs) and reference R1 sample with incident simulated solar light passing through SCHOTT BG42 bandpass filter. The before coating (Tier 2) and after encapsulation (and coating for Q2; Tier 4) curves are displayed.

Finally, the difference in the increase in I_{SC} between the LDS-coated samples of different concentrations (Q1 & Q2) is attributed to the reduction in the porosity of the PA SiQDs films created. According to Pi et al. (2012) [50], an increase in the thickness of SiQDs film from 16 nm to 74 nm led to a decrease in porosity from 84% to 69%. The estimated thicknesses of the deposited layers on the Q2 sample (0.01 mg) and the Q1 sample (0.15 mg) are 2.02 nm and 30.27 nm, respectively. This correlates with an increased reflectance and shading, resulting in a reduction in the expected improvement by depositing higher thickness layers of PA SiQDs on pc-Si solar cells.

The layer thickness was estimated based on the uniformly deposited mass of PA SiQDs times the density of PA and Si over the solar cell area.

The experimental results obtained for the increase in I_{SC}, 1.06% for sample Q2 and 0.75% for sample Q1 (QD size: 6 nm), are consistent with increases reported in the literature for the use of SiQDs to enhance the PCE of Si solar cells: 1.3% [53] (QD size: 6.4 nm) and 2.3% [47] (QD size: 3 nm) in I_{SC}. Moreover, the significant increase in the performance of the encapsulated pc-Si solar cell may be primarily attributed to the improved optical coupling and light trapping capabilities resulting from LDS, eliminating air gaps, and increasing internal reflections. Mohan et al. (2020) [310] tested the improvements in encapsulation introduced to Si solar cells; interpreted from the graphs, it was shown that a drop of 55.5% in reflectance observed at 300 nm was the main contributor to electrical enhancement by encapsulation.

4.3.3.2.   *Further Investigation*

This subsection delves deeper into the investigation of PA SiQDs, exploring aspects such as the LDS phenomenon, sample purification, degradation, and reproducibility.

1.   Electrical enhancement: LDS or Rayleigh Scattering?

The significant drop in reflection at 377 nm (Figure 4.7) may be partly due to Rayleigh Scattering which is maximised in the UV range, especially if the QDs are smaller than 1/10 of the incident wavelength [311]; 37.7 nm in this case, where the average reported size of the PA SiQDs is 6 nm [97], thus acting as an antireflective layer. A blue bandpass filter, SCHOTT BG42, was used for an extra set of I-V characterisation. As shown in Figure 4.14, transmittance at 377 nm reaches 63% and maximises at 511 nm with it reaching 92.9% [301]. Table 4.5 shows the I_{SC} for the Q2 sample before and after coating with PA SiQDs (by DC) when the incident light was passed through the bandpass filter. The standard deviation of the measurements in this case, under filtered light, is much smaller than that under the full simulated solar light (shown in Table 4.1) and lies in the fourth decimal place, as shown in Table 4.5. The relative increase in the I_{SC} after coating with PA SiQDs is 1.2% with uncertainty estimated at ±0.4%.

Table 4.5 Electrical parameters of sample Q2 before coating (Tier 2 soldered cell) and after coating with PA SiQDs (Tier 3). The incident simulated solar light was reduced by the SCHOTT BG42 bandpass filter.

Sample	Electrical Parameters	Soldered Solar Cell (Tier 2)	Coated with PA SiQDs by DC (Tier 3)	% Increase
Q2	I_{SC} (A)	0.1168	0.1182	1.2
	STD of I_{SC} (A)	0.0001	0.0005	N/A

As the filter blocks >37% of the light at wavelength 377 nm and 7.1% at the highest permissible wavelength of 511 nm, it would be expected that the increase in the I_{SC} would drop significantly below 1.06%, which was at the full solar light exposure. Nevertheless, an increase of 1.2% in the I_{SC} is measured, which further proves the LDS behaviour of the PA SiQDs, where UV and near-UV light is downshifted to higher wavelengths. Pc-Si solar cells possess low EQEs in the UV region of the solar spectrum; with EQE dropping below 60% [57], [312]. The low spectral response in the region below 400 nm indicates that the reduction in reflectance around 377 nm cannot be of much benefit to the solar cell itself thus a measurable increase in the I_{SC} due to antireflection alone may not be well supported to defend that the phenomenon is due to backscattering only. This indicates that the downshifting effects carried out by the PA SiQDs are associated with the reduction in the reflection at 377 nm. With EQEs passing 90% past the 400 nm mark, downshifting to 447 nm is the main reason for the increase in the I_{SC}.

2. Degradation and Reproducibility

A follow-up I-V characterisation of the encapsulated sample Q2 has been carried out 74 and 91 days after the first measurement to check on the stability of the sample over time, as shown in Figure 4.16. All PA SiQDs coated pc-Si solar cells, including encapsulated samples like Q2, are stored in a dark, dry place when not in use.
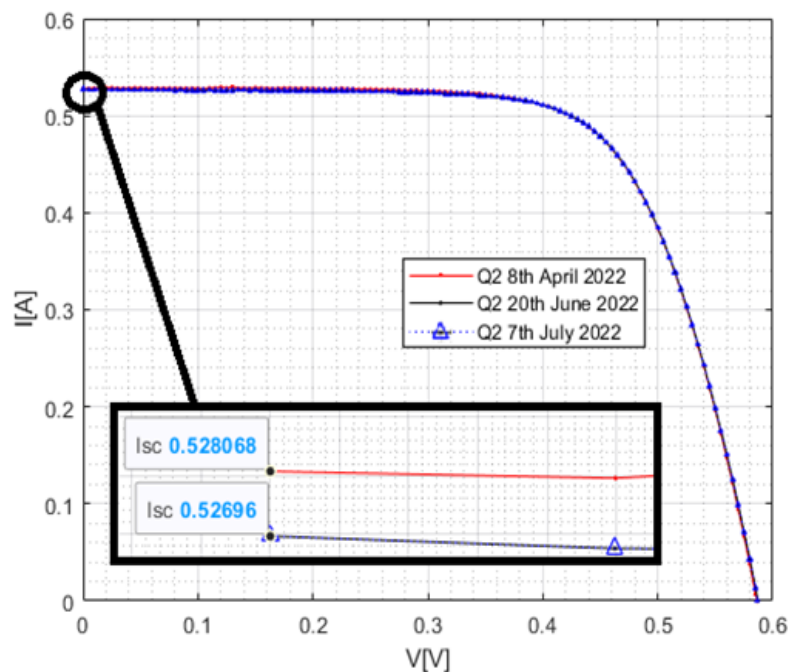
Figure 4.16 I-V characteristic for encapsulated and PA SiQDs coated Q2 sample carried 74- and 91-days post encapsulation (overlapping).

A slight decrease in the I_{SC} of the encapsulated Q2 sample was observed at the 74th and 91st days after the initial characterisation of the fresh sample. The electrical parameter values presented in Table 4.6 represent the average values obtained from measurements conducted six times. The standard deviation of these measurements is further detailed in Table 4.7. As mathematically detailed in subsection 3.8, the I-V measurements performed using the KEITHLEY Source Measure Unit (SMU) and are reported to the third decimal place. This also factors in the temporal stability of the light source (Class ABA), positioning accuracy, temperature control, and controlled environmental conditions. This overall precision is reflected in Table 4.7, with an average standard deviation of 0.002 for I_{SC}, V_{OC}, and P_M.

The values of I_{SC}, V_{OC}, and P_M presented in Table 4.6, corresponding to measurements taken at three different time points, do not exhibit significant variations and fall within the error domain defined by the standard deviation, as shown in Table 4.7. This suggests that any reduction in performance is minimal, and the encapsulated sample has not significantly degraded over the span of 3 months. In contrast, when considering the standard deviation values for the original measurement of sample Q2, it becomes evident that the performance enhancement observed is substantial and outside the range of measurement uncertainty, thus providing a secure basis for the findings.

Table 4.6 Electrical parameters of Tier 4 encapsulated and PA SiQDs coated Q2 sample from characterisation carried out 74 and 91 days apart.

Electrical Parameters	8 April 2022	74 Days: 20 June 2022	% Increase	91 Days: 7 July 2022	% Increase
I_{SC} (A)	0.528	0.527	(-0.19)	0.527	(-0.19)
P_M (W)	0.215	0.215	0.00	0.214	(-0.47)
V_{OC} (V)	0.586	0.587	0.17	0.585	(-0.17)

Table 4.7 Standard deviation (STD) of I_{SC}, P_M, and V_{OC} for Q2 sample after coating with PA SiQDs and encapsulation (Tier 4).

Date	08-Apr-22	74 Days: 20 June 2022	91 Days: 7 July 2022
STD of I_{SC} (A)	0.002	0.003	0.002
STD of P_M (W)	0.002	0.003	0.002
STD of V_{OC} (V)	0.002	0.002	0.002

The slight decrease in the I_{SC} after 74 and 91 days highlights the crucial role of encapsulation when working with air-sensitive QDs like the PA SiQDs. Encapsulation serves as a protective barrier,

preserving the properties of the LDS sample by isolating it from the detrimental effects of air exposure. However, the observed drop in I_{SC} over time also raises the possibility that exposure to air between QD deposition in Tier 3 and encapsulation in Tier 4 may trigger an ongoing oxidation process. This oxidation process might only become quantifiable months after the initial measurements. Further investigations are required to comprehensively study the degradation of PA SiQDs, which can be accomplished through thermogravimetric analysis (TGA) that can be adapted to quantify oxidation.

To validate and ensure the reproducibility of the results, a new sample, Q3, was created 85 days after Q2, using a similar process. Q3 was subsequently coated with 0.01 mg of the PA SiQDs batch initially fabricated in March 2022, Utilising the direct DC method in Tier 3. The I-V characteristic for sample Q3, both before (Tier 2) and after being coated with PA SiQDs (Tier 3), is illustrated in Figure 4.17, and the extracted electrical parameters are presented in Table 4.8.
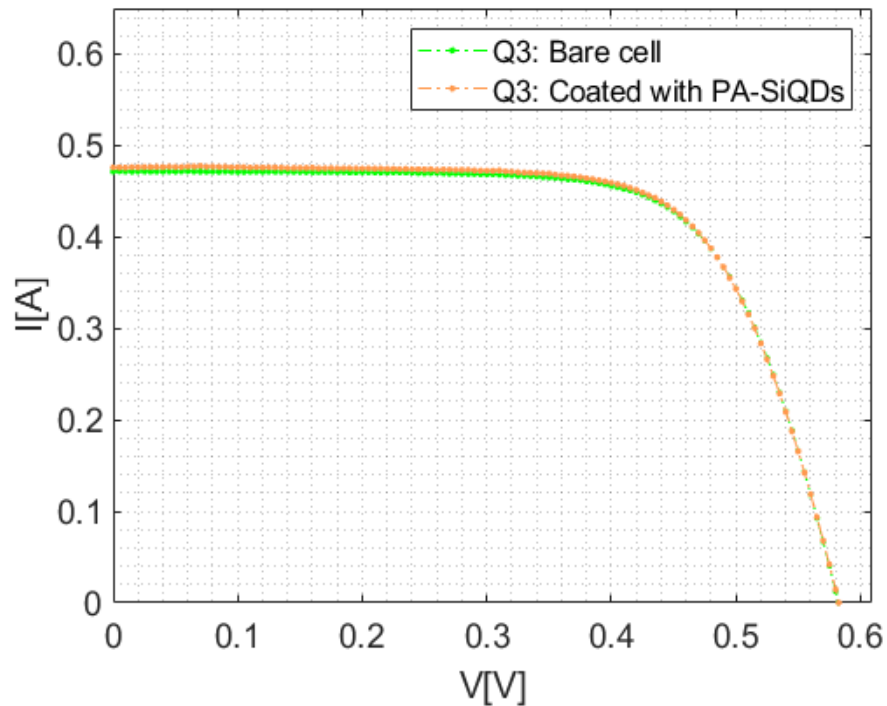
Figure 4.17 I-V characteristic sample Q3 before (Tier 2 soldered cell) and after coating by DC of PA SiQDs (Tier 3).

Table 4.8 Electrical parameters of sample Q3 before coating (Tier 2 soldered cell) and after by DC of PA SiQDs (Tier 3) 85 days later.

Electrical Parameters	Q3 Soldered Solar Cell (Tier 2)	Q3 Coated with PA SiQDs (Tier 3) 85 Days Later	% Increase
I_{SC} (A)	0.509	0.512	0.59
P_M (W)	0.212	0.211	−0.47
V_{OC} (V)	0.602	0.600	−0.33

The deposition of PA SiQDs onto sample Q3, carried out 85 days after the synthesis of the QDs, resulted in a 0.59% increase in the I_{SC}. This smaller increase in I_{SC} for sample Q3, compared to the 1.06% increase observed for sample Q2, suggests degradation in the batch of PA SiQDs that had been stored at room temperature since their synthesis in <u>March 2022</u>. This highlights the importance of using freshly deposited and encapsulated PA SiQDs to maintain their effectiveness. Conversely, the increase in I_{SC} for sample Q3 demonstrates the reproducibility of using PA SiQDs to enhance the performance of pc-Si solar cells, showcasing their potential for consistent results.

The drop in V_{OC}, and hence the P_M, may have been caused by a physical abnormality in the pc-Si solar cell itself and is not related to the LDS effects of PA SiQDs. Such drop may be due microcracks that occur when soldering, and propagated as the cell was moved around for measurements. It is worth noting that the electrical contacts used for the 4-wire I-V characterisation exerts a slight pressure on the cell to maintain electrical contact, which could have stressed the cracks further or created mechanical stress points.

3. Purification effects on LDS Electrical enhancement

After conducting purification processes on the <u>November 2022 batch</u> of PA SiQDs to remove impurities, concerns arose about the thermal stability and potential degradation of the SiQDs under extended exposure to high temperatures above 100°C. To investigate the effects of thermal degradation, two pc-Si solar cells were coated with PA SiQDs using DC. Sample <u>Q4</u> was coated with the PA SiQDs that was purified through <u>one</u> purification cycle, while sample <u>Q5</u> was coated after applying the purification cycle <u>three times</u> to the November 2022 batch of PA SiQDs.

The repetition of the purification processes was carried out to emulate a refinery-style purification system, aimed at achieving the highest level of sample purity. This approach mimics industrial practices where multiple purification steps are employed to produce the cleanest and most refined product. This was achieved by repeating all three purification processes (mentioned in the *Purification of PA SiQDs* subsection 4.2.2) all together exhaustively until no Naphthalene was leaving. This approach ensures the acceleration and magnification of thermal degradation if present.

It was estimated that the fresh November 2022 batch of PA SiQDs contained approximately 90% Naphthalene impurity by weight, where >97% of that was removed by performing multiple cycles of purification.

As stated in subsection 4.2.2, the purification cycle involved three distinct processes. The first process utilised a rotavapor at a partial pressure of 200 mbar and a temperature of 100°C. The second and third processes employed direct heat through a hot-air gun at 145°C for 14 minutes

and a hot-plate at 250°C for 4 minutes, respectively. The first process, conducted at a relatively safe temperature of 100°C and aided by partial pressure to speedup Naphthalene evaporation and minimize oxidation, is unlikely to be the cause of thermal degradation. Additionally, it has been reported in the literature that blue SiQDs can retain up to 94% of their original PLQY after 12 days at 80°C in water [298]. However, the second and third purification processes, which involved direct heating of the PA SiQDs sample in open air at temperatures exceeding 100°C for extended periods, likely led to degradation. This degradation explains the reduced electrical enhancements observed in the extensively purified sample Q5 compared to sample Q4 as seen in results in Table 4.9.

To highlight the impact of thermal purification, the concentration of deposited PA SiQDs was increased fivefold, from 0.01 mg to 0.05 mg.

Table 4.9 Electrical parameters of samples Q4 and Q5 before (Tier 2) and after coating with PA SiQDs by DC (Tier 3), one purification cycle, and exhaustive purification cycles respectively.

Sample	Electrical Parameters	Soldered Solar Cell (Tier 2)	Coated with PA SiQDs by DC (Tier 3)	% Increase
Q4 0.05mg	I_{SC} (A)	0.514	0.518	0.78
	P_M (W)	0.209	0.209	0.00
	V_{OC} (V)	0.612	0.612	0.00
Q5 0.05mg	I_{SC} (A)	0.501	0.503	0.40
	P_M (W)	0.188	0.188	0.00
	V_{OC} (V)	0.611	0.611	0.00

Sample Q4 showed an increase in the I_{SC} by 0.78%, while sample Q5 showed a lower increase of 0.40%. The reduced increase in the I_{SC} shown by sample Q5 can be attributed to thermal degradation of the PA SiQDs, thus lower LDS effect.

To quantify the thermal degradation and give a depth to the damage a refinery-style purification system can present onto these PA SiQDs, the PL (Excitation and Emission) was measured once again for the November 2022 sample when purified <u>once</u> in a full cycle, and after applying <u>three</u> exhaustive purification cycles as shown in Figure 4.18.
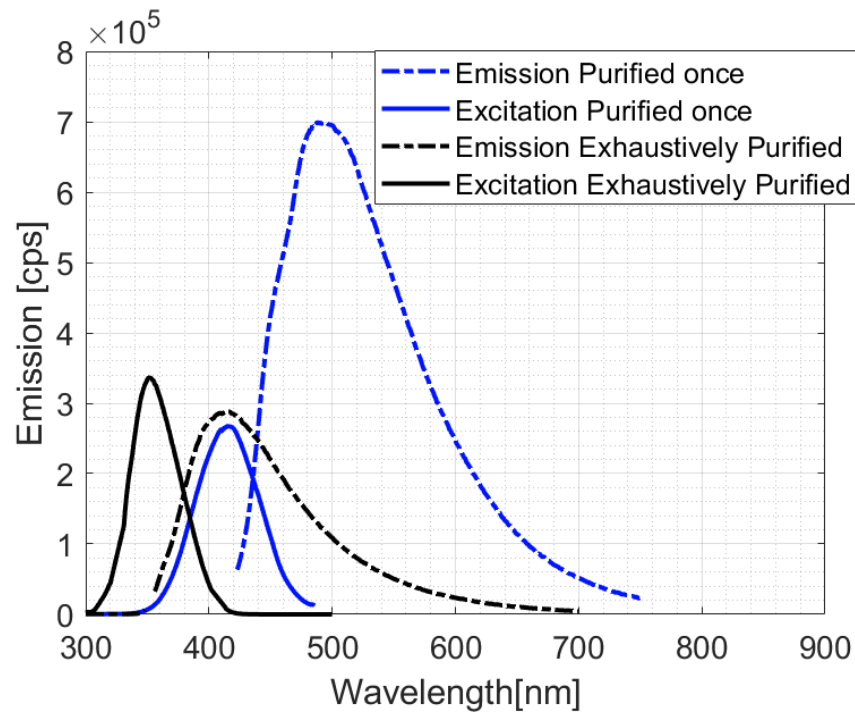
Figure 4.18 PA SiQDs: Excitation & Emission PL measurements for the November 2022 batch with one purification cycle and multiple and exhaustive purification cycles of 3 repetitions.

As clearly stated by Figure 4.18, the PA SiQDs PL profile shifted massively to the left, towards the UV region. With a drop in emission from 495 nm to 417 nm and excitation from 415 nm to 351 nm, the PA SiQDs can still perform useful LDS explaining the increase in I_{SC} by 0.40% on Q5. The shifted PL is closer to that of the March 2022 batch with emission peak at 447 nm and excitation at 388 nm.

Electrical enhancement of 0.40% in the I_{SC} of sample Q5 provided by the degraded and exhaustively purified sample falls short of the enhancement achieved by the original March 2022 and November 2022 batches as seen on samples Q1, Q2, Q3, and Q4 with respective I_{SC} increases of 0.75%, 1.06%, 0.59%, and 0.78%. This is clearly caused by thermal degradation which induced oxidation.

However, it is important to note that a single purification cycle did not lead to the expected increase in the I_{SC} of a pc-Si solar cell sample, despite the improved PL observed in Figure 4.5. This is evident when comparing sample Q4, which showed a 0.78% increase after one purification cycle, with sample Q1, which achieved a 0.75% increase without any purification. To delve deeper into this issue, further extensive experiments should be conducted to ensure the removal of Naphthalene impurities without degrading the quality or performance of PA SiQDs.

One full purification cycle introduced the need to increase the concentration used fivefold, in comparison to the March 2022 batch, to achieve the same level of electrical enhancements. While directly comparing the performance of both PA SiQDs batches is not methodologically rigorous, it was expected for both samples to require similar deposition concentrations. One potential cause for this difference in performance might have been a change in the equilibrium of the ground state of the PA SiQDs when stored. The purification process might have led to an accelerated rate of environmental degradation (oxidation) between the characterisation of liquid and solid samples, which typically occurs over a span of several days.

More details on how to address this topic will be provided in the "*Future Work and Recommendations*" subsection 8.3 in Chapter 8.

4.4.   Chapter Conclusion

This chapter outlined the novel use of PA SiQDs as an LDS material to enhance the performance of pc-Si solar cells. The observed improvement is attributed to the LDS properties of the PA SiQDs, which exhibit a PL emission peak at 495 nm when excited at 415 nm, as well as their anti-reflective properties, shown by a 75.7% reduction in specular reflectance and a 43.1% decrease in diffuse reflectance between 350 nm and 450 nm.

The I-V characterisation of samples Q1 (0.15 mg PA SiQDs) and Q2 (0.01 mg PA SiQDs) before and after coating with PA SiQDs revealed an average increase in I_{SC} by 0.75% and 1.06%, respectively. A further improvement was observed in fully encapsulated samples, showing an overall I_{SC} increase of 3.4% and a P_M increase of 4.1% compared to reference encapsulated samples. This demonstrates that the optical coupling effect due to encapsulation increased the I_{SC} of the PA SiQD-coated solar cells by approximately 2.2%.

The advantage of using PA SiQDs as an LDS material, compared to other SiQDs and QDs, lies in the phenylacetylene (PA) capping ligand. This ligand grants the Si core properties similar to those of bulk silicon but with improved electrical conductivity due to the ligand overlap, as documented in references [96] and [97]. Additionally, PA-capped SiQDs have a longer shelf life compared to non-capped SiQDs, with reduced oxidation rates due to valence electrons being occupied by the capping material. Overall, the straightforward preparation of PA SiQDs samples, as demonstrated in this chapter, shows their potential for enhancing the performance of pc-Si solar cells.

5. CsPbI$_3$ PQDs: Enhancing the efficiency of pc-Si solar cells by LDS.

5.1. Introduction

PQDs have been a trend to study under the field of photovoltaic enhancements, it is being researched as standalone solar cells structures or as LDS enhancers and materials [25, 55, 265, 313-315].

This chapter examines the application of a specific type of PQDs as LDS materials to improve the electrical efficiency of pc-Si solar cells. Literature indicates that Caesium-Lead-Halide (CsPbX$_3$) PQDs are preferred due to their distinct sharp emission peaks and broad absorption peaks, particularly in the UV region of the solar spectrum [157], [316].

Although the use of these PQDs, CsPbI$_3$, in enhancing the efficiency of Si solar cells, particularly as an externally applied LDS layer, was limited in the literature, several analogous versions have been reported to significantly improve cell performance. For instance, the SC application of 3-5 nm MAPbBr$_3$ [26] led to an increase of 4.03% in the J$_{SC}$ of mono-Si solar cells and 2.07% in pc-Si solar cells. Additionally, the DC of 8 nm CsPbCl$_3$:Mn^{2+} boosted the J$_{SC}$ of pc-Si solar cells by 5.1%, while the LPD of 11.2 nm CsPbCl$_3$:Mn^{2+} enhanced the J$_{SC}$ of c-Si solar cells by an identical margin. Furthermore, EVA-hosted depositions of 4.9 nm CsPbBr$_3$–Cs$_4$PbBr$_6$, applied using the doctor-blade method, achieved a 7.93% increase in the J$_{SC}$ of pc-Si solar cells. In comparison, 8 nm (CsPbCl$_3$:Mn^{2+}, Er^{3+}) enhanced the I$_{SC}$ of c-Si solar cells by 3.42%.

The emission peaks of the reviewed PQDs span a range of 531-600 nm. Based on these spectral characteristics, CsPbI$_3$ PQDs were selected for this project due to their favourable emission peak at 692 nm. This peak aligns more effectively with the spectral response of c-Si solar cells, which is most sensitive within the 650-950 nm range [20], [21], [22]

However, CsPbI$_3$ PQDs are susceptible to thermal degradation through phase shifting, as evidenced in prior studies [130], [293], [296], [299]. Therefore, it was crucial to develop an innovative method for depositing these quantum dots at room temperature to circumvent this challenge.

With that in mind, this chapter showcases the full investigation undertaken to research the use of CsPbI$_3$ PQDs as LDS layer aimed at enhancing the electrical performance of pc-Si solar cells. This

includes the utilisation and creation of the room-temperature novel coating method of LEVA, as introduced in Chapter 3.

At the time of writing this thesis, it appears that the exploration of $CsPbI_3$ PQDs as an externally applied LDS layer on pc-Si solar cells is a novel endeavour. To the best of the author's knowledge, this application has not been previously reported in such manner.

5.2. Material and Experimental Procedure

For this project, 100 mg of colloidal Caesium-Lead-Iodide ($CsPbI_3$) PQDs have been purchased from Quantum Solutions™, dubbed as QDot™ ABX3-685, and characterised by their oleic acid and oleylamine capping [317]. The technical specifications provided by manufacturer for these deep red PQDs reported emission peak at 692 nm and a broad excitation range, primarily below 680 nm, with PLQY of 99%, and an average size estimation of 11 nm ± 1 nm.

5.2.1. LEVA vs DC

As previously presented in Chapters 3 and 4, direct DC of LDS QDs has been the main and only deposition method utilised through the entirety of the project. Due its ideal benefit in depositing QDs directly and evenly onto pc-Si solar cell with 0% sample losses, it was deemed the best way to study the LDS effects of the investigated QDs while keeping sample concentration known and controlled. Although direct DC and thermal encapsulation (lamination) have been used to investigate PQDs as LDS layers, it was quickly concluded that these QDs rapidly degrade when exposed to air and high temperatures especially when performing thermal encapsulation. Shi et al. (2020) [295] reported that the PL intensity of $CsPbBr_3$ PQDs (analogous $CsPbX_3$ PQDs) drop from 100% at room temperature down to ~0% at 89.85°C, with this steady thermal degradation starting by heating the sample just above room temperature. Wang et al. (2023) [296] reported that $CsPbI_3$ PQDs completely degrade when heated up to ~130°C. Similarly, Iso et al. (2022) [297] reported a ~34% drop in PL intensity of $CsPbI_3$ PQDs after 1 hour of continuous heating at 100°C, and a 90% drop after 4 hours for a high concentration sample of 43.25 mg/ml. It is deductible from the reported literature that $CsPbI_3$ PQDs start gradually degrading at temperatures above room temperature, with significant PL reduction passing 90°C, and full degradation around 130°C. Therefore, conventional thermal encapsulation, typically operating between 80-100°C or higher, of pc-Si solar cells cannot be performed on PQDs coated sample. Experimental work on thermally encapsulating (laminating) $CsPbI_3$ PQDs coated pc-Si solar cells indicated a full thermal degradation (full loss of PL) of the PQDs coating after a 5-minute exposure to a hot air gun set at 80°C.

Degradation of these PQDs occurs by transformation of the morphology of the PQDs into a degraded yellow state called the δ phase; this happens when the QDs shift phase from the photoluminescent black α phase to the thermodynamically stable and non-PL yellow δ phase (orthorhombic crystal) [130], [293], [296], [299]. In this case, it was thermally induced by exposure to the high encapsulation temperatures.

The original supplied sample has a 3-month handling shelf life from the time of exposure to air and light. By practice, it was confirmed that the original sample in the supplied sealed vial showed no signs of degradation if remained sealed, while all exposed samples (diluted batches in Toluene, 1 mg/ml) degraded in 3-5 months.

This led to the improvisation of a room-temperature novel coating method which was based on using EVA in a liquid form. This was thoroughly explained in the subsection 3.7 and was described as an alternative to conventional full thermal encapsulation (Figure 3.5) in terms of environmental protection and optical coupling.

LEVA was prepared by dissolving 10 g of the encapsulant EVA in 3 ml of Toluene. This was achieved by employing a hot air gun at 145°C, which facilitated thorough mixing through convection. Subsequently, the resulting LEVA mixture was blended with PQDs of a known concentration using a needle and a vortex mixer. Subsequently, 1 ml of the CsPbI₃ PQDs LEVA mixture was uniformly applied (in the same manner as DC) over the solar cells and allowed to dry by complete evaporation of the Toluene, resulting in the formation of a thin LDS EVA host film, referred to as the LEVA film.

This method, inspired by the literature, is a novel approach as it was not previously reported in such manner. Similarities in the literature arise from mixing LDS materials with encapsulants (such as EVA) to form an externally managed dry LDS host layer [315] or heat-dependant flowable LDS host layer deposition [212], composite solar cell structures [318], [319], [320], [321], or by applying these modified encapsulants onto solar cell in a full laminated sandwich using heated vacuum lamination [184].

The innovative LEVA method distinguishes itself by the room-temperature direct application of the LDS LEVA mixture onto the solar cell surface, without the inclusion of encapsulating glass or other solar sandwich components, ensuring uniform coverage. This method establishes an intermediate testing phase that falls between the direct LDS coating on bare cells (Tier 3) and full encapsulating lamination (Tier 4) as seen in Chapter 4 for the PA SiQDs.

By permitting the layer to dry at room temperature and form a consistent host LEVA film, this approach enables the investigation of the LDS-based enhancements of the PQDs in isolation,

separate from the optical improvements brought to the cell by encapsulation, such as enhanced optical coupling and light trapping. Concurrently, it safeguards the PQDs from oxidation and phase shifting due to the high temperatures associated with thermal encapsulation.

As later demonstrated in subsection 5.3.3, the dry LEVA film, when formed, contributes little to no benefit to the cell by itself, rendering it a non-active host layer. Consequently, a PQDs-coated solar cell via the LEVA method is categorized as an LDS-only coated solar cell, aligning with Tier 3 experimentation, as outlined in the Methodical protocol flowchart presented in Figure 3.2, Chapter 3.

As of the time of writing this thesis, LEVA has only been subjected to initial trials investigating the complete encapsulation of pc-Si solar cells using LDS LEVA. Results of these trials will be discussed and demonstrated in Chapter 7.

However, it is reasonable to infer that extended encapsulation is feasible through vacuum lamination, given the adhesive characteristics of dried LEVA. The resultant LEVA film exhibits a smoother texture compared to commercially available EVA sheets, rendering it an excellent candidate for vacuum lamination. However, the reported literature, particularly by Klampaftis et al. (2011) [184], emphasises the use of high temperatures throughout the whole process, such as 90°C through mixing, 100°C for pressing moulds, and 155°C when vacuum laminating the cells for encapsulation. These temperatures are not suitable for the use with these CsPbI₃ PQDs, as they were proven to degrade rapidly under such relatively high temperatures [295], [296], [297]. This issue can be overcome by lightly spraying the LEVA film with small amounts of Toluene. This process smoothens the texture further, resulting in improved surface contact. By spraying the surface with Toluene, the adhesion of the LEVA film to the front encapsulating solar glass is enhanced, enabling vacuum lamination to be utilised for the complete encapsulation of LEVA-coated pc-Si solar cells without subjecting them to high temperatures, while still allowing Toluene to evaporate under vacuum.

5.2.2. Sample preparation of pc-Si solar cells

As detailed in Chapter 3, the solar cells go through 4 Tiers of experimental testing and measurements, where Tier 3 is concerned with LDS layer addition.

To establish a fair comparison between the CsPbI₃ PQDs and PA SiQDs used in Chapter 4, direct DC of PQDs was still performed to create a baseline of results which can be used as a starting point for the full investigative experiments carried out in this chapter. Direct DC results can also aid in constructing a general idea of how LEVA compares to it, and what benefit this novel coating method brings forward.

Following that up, pc-Si solar cells were prepared by uniformly depositing PQDs of known concentrations, 1 and 2 mg, onto the cells' 39 mm × 39 mm surface. Toluene was used as the solvent in for both direct DC and the LEVA methods. For direct DC, 1 ml of Toluene was used. While for LEVA, 1 ml of the prepared PQDs LEVA solution was poured over.

In either case, Toluene takes relatively longer to fully evaporate when compared to more volatile solvents like Ethanol or DCM. By practice, samples needed 10-15 minutes on average to fully dry out, leaving uniform and well spread LDS layers, where repeatability between samples is ensured by the strict experimental protocol. Layer roughness and evenness for LEVA coated samples is show in subsection 5.3.2, while roughness and evenness of DC coated samples have been previously demonstrated and checked in subsection 4.3.2 which is still a valid representation for DC results in this chapter.

The direct DC layered pc-Si solar cells went under thermal encapsulation (Tier 4) that thermally laminated the cells; this is to show the rapid degradation of the PQDs caused by exposure to high temperatures.

Details will be discussed with results later in this chapter in subsection 5.3.3.

5.3. Results and Analysis

5.3.1. Liquid samples: CsPbI₃ PQDs characterisation

This subsection presents, analyses, and discusses the results obtained from characteristic measurements performed on liquid samples of CsPbI₃ PQDs dissolved in Toluene, specifically designed for DC and LEVA coatings onto pc-Si solar cells.

5.3.1.1. *Photoluminescence (PL)*

Results shown here follow the protocol for liquid sample characterisation shown in subsection 3.5.

The CsPbI₃ PQDs showcase an excellent photoluminescent emission response to any exciting wavelength that is set before the emission peak. As seen in Figure 5.1, it possesses the ability to absorb any photon with a wavelength below its emission peak of 690 nm. The figure showcases a wide and broad absorption peak that extends primarily from 420 nm and to the borders of the emission peak starting at 680 nm.

Investigated as LDS materials for enhancing pc-Si solar cells, these PQDs can effectively convert absorbed UV and near-UV photons into longer wavelengths in the Vis-NIR region of the spectrum, specifically around 690 nm, they hold significant potential for enhancing pc-Si solar cells because these cells typically exhibit low spectral response to light in the UV-Vis region, 350-650 nm, but

demonstrate considerably higher response in the NIR region, 650-950 nm [20], [21], [22]. The spectral response of pc-Si solar cells was explained in subsection 1.1 and shown in Figure 1.4. Theoretically, employing PQDs could increase the number of red photons available for absorption, ultimately enhancing the photovoltaic (PV) performance of the solar cells.
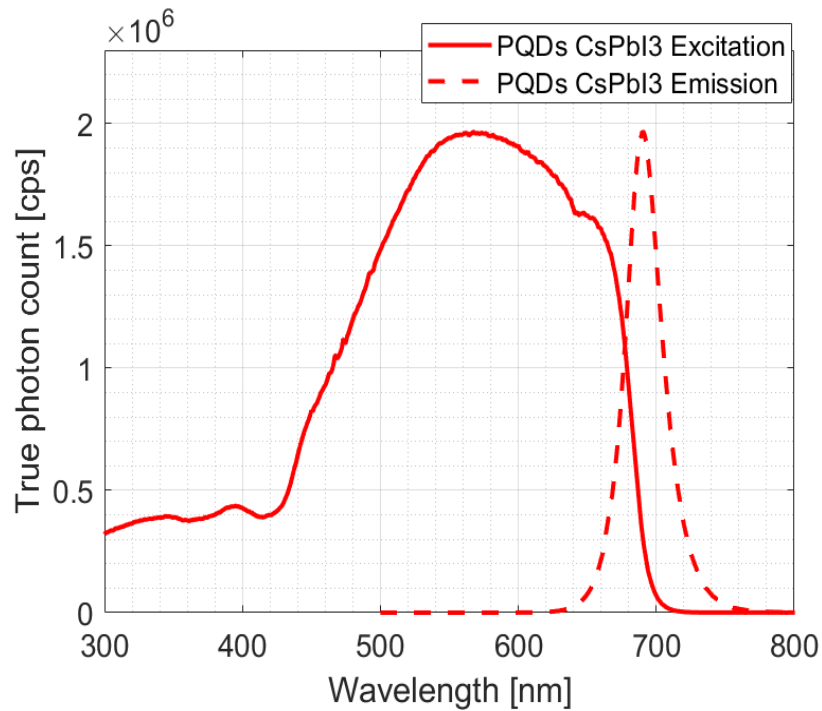
Figure 5.1 Excitation (filled lines), Emission (dotted lines), PL reading for PQDs CsPbI₃ (<680nm, 690nm) liquid sample measured on the Edinburgh Instruments FS5; true Excitation wavelength.

It is noteworthy that the measured PL of the PQDs closely aligned with the provided data by the manufacturer, exhibiting a minimal difference of only 3 nm for the emission peak. The measured peak emission was recorded at 690 nm, while the reference value was indicated as 692 nm [317]. This indicates a strong agreement between the measured and supplied data for the emission characteristics of the PQDs.

Moreover, the manufacturer's provided excitation profile displayed a matching pattern, spanning from 620 nm to 720 nm, which, notably, was the sole range provided for excitation measurements. This alignment reinforces the reliability and consistency between the measured excitation profile and the manufacturer's provided information.

Figure 5.2 serves as additional evidence supporting the conclusions drawn in Figure 5.1. It demonstrates the consistent emission wavelength of the sample, even when excited at seven distinct wavelengths. The resulting emission consistently falls within the range of 690-693 nm.

This outcome aligns with both the measurements conducted in-house and the specifications provided by the manufacturer.
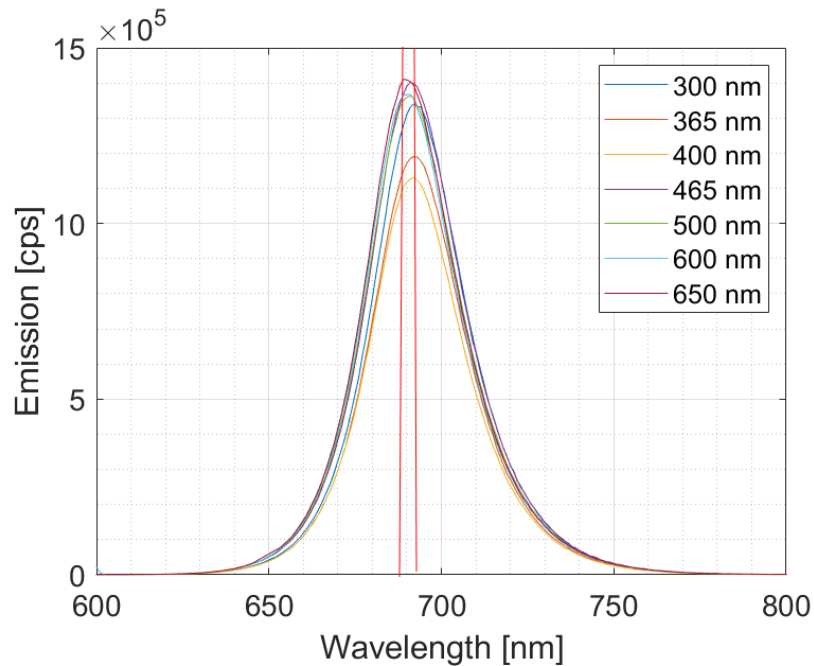
Figure 5.2 Emission PL reading for PQDs CsPbI₃ liquid sample measured on the Edinburgh Instruments FS5; at a range of excitation wavelengths (300, 365, 400, 465, 500, 600, 650 nm).

The consistency in the emission wavelength across multiple excitation wavelengths reinforces the reliability and accuracy of the measurements. It affirms that the emission characteristics of the sample are stable and reproducible. This confirms once again the reliability of using the CsPbI₃ PQDs as LDS entities to specifically enhance pc-Si solar cells and highlights its advantageous LDS behaviour in absorbing a wide range of wavelengths.

5.3.1.2. SEM and TEM

Using the Zeiss Gemini 300 SEM and JEOL 2010 200 kV TEM, a nanoscale imaging was carried out to characterise the CsPbI₃ PQDs. By allowing the host solvent, Toluene, to evaporate on a copper mesh grid, clusters of suspended PQDs were left behind, ready to be imaged. Figure 5.3, 5.4 and 5.5 presents the outcomes obtained from both SEM and TEM offering a comprehensive view of the PQDs' morphology and physical attributes.

For SEM imaging, Figure 5.3 showcases the clusters of coagulated CsPbI₃ PQDs dispersed, with a closer look in Figure 5.4 showcasing the cubic structure of CsPbI₃ PQDs which strongly agrees with the reported morphology in the literature [279, 322-324] and further validates the reliability of the acquired sample.
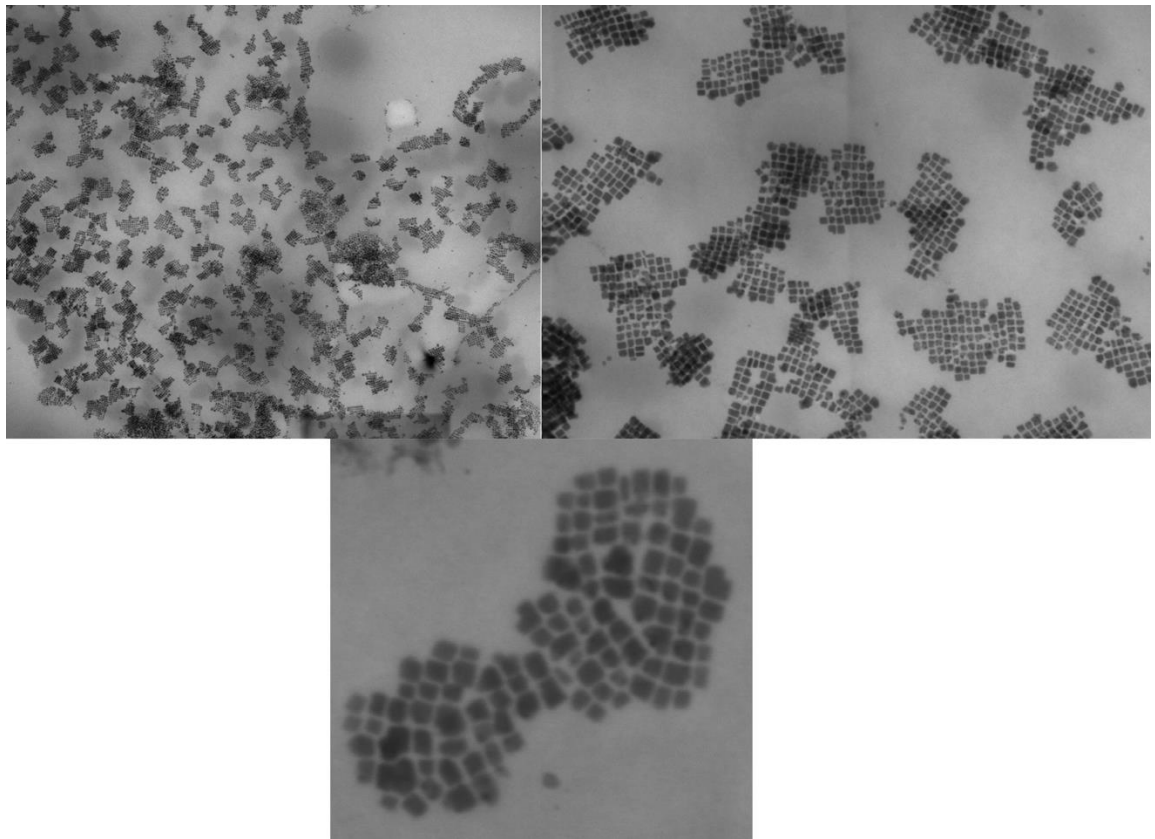
Figure 5.3 SEM imaging of CsPbI₃ PQDs.
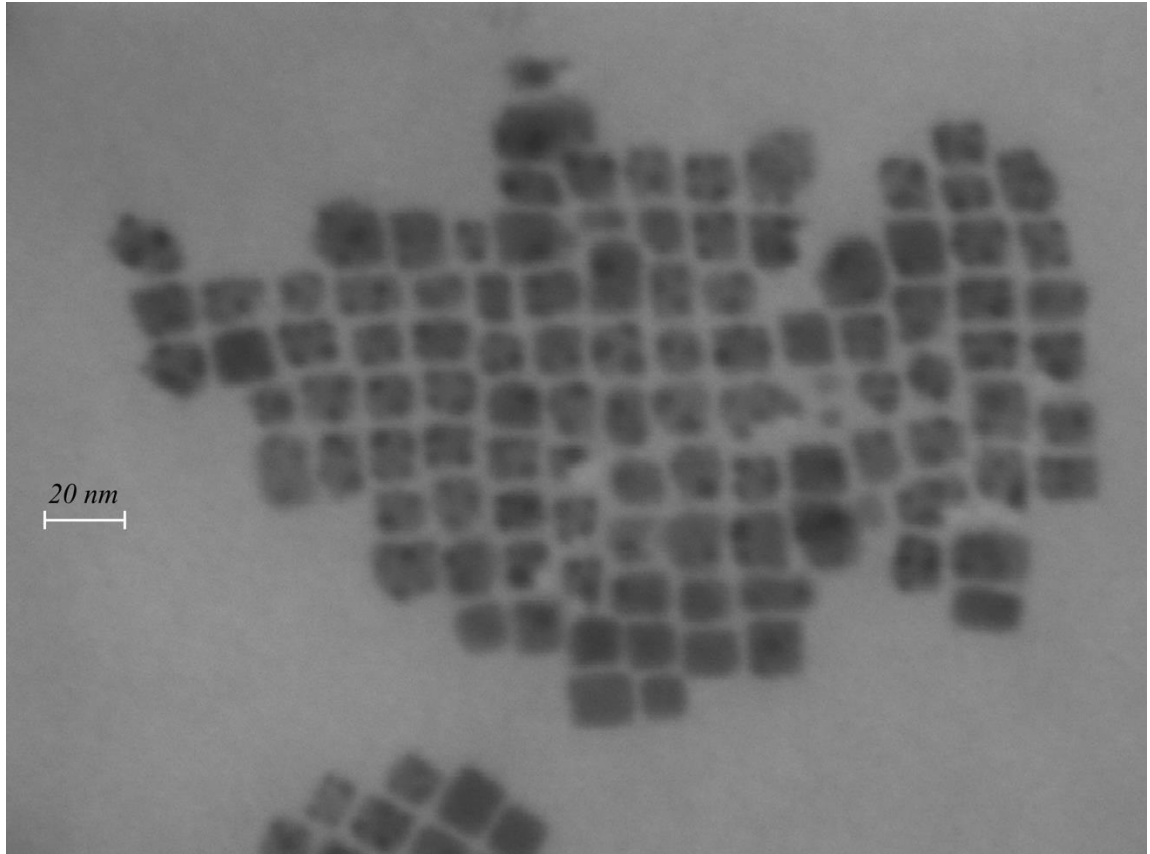
Figure 5.4 SEM imaging of CsPbI₃ PQDs, a closer look.
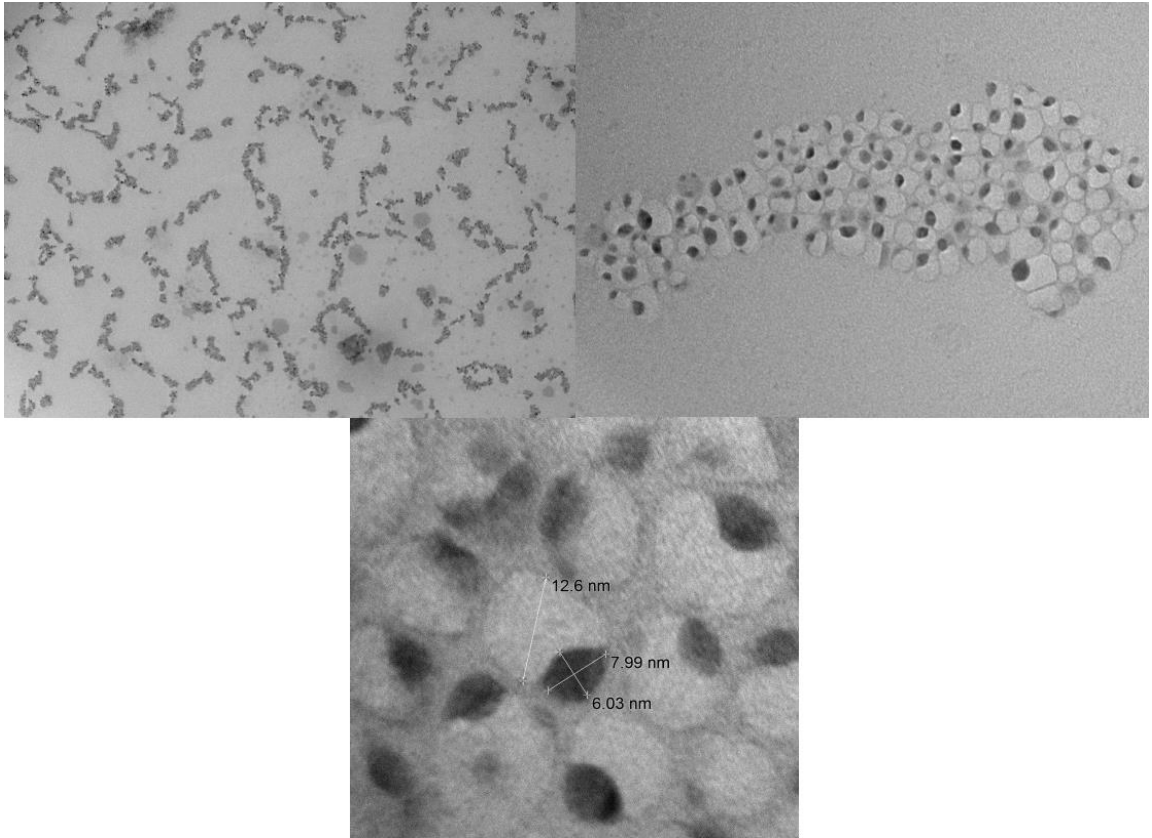
Figure 5.5 TEM imaging of CsPbI₃ PQDs.

In both instances, the image quality obtained from the instruments was exceptional. They were capable of capturing details with a high level of precision, reaching a resolution of 10 nm. Notably, features as small as 2 nm were clearly discernible in the captured images. The average size of the CsPbI₃ PQDs measured around 12 nm which was slightly larger than the manufacturer provided measurement of 11 nm [317]. This measurement falls within the range reported in the literature with average CsPbI₃ PQDs size measured by SEM or TEM was reported at ~10.05 nm [322], 10.07 nm [324], 10.4 – 12.1 nm [126], ~13 nm [129], and 12.7 nm [279].

5.3.2. Solid samples: CsPbI₃ PQDs coating characterisation on pc-Si solar cells and LEVA films

This subsection presents, analyses, and discusses the results obtained from characteristic measurements performed on solid samples of CsPbI₃ PQDs coated pc-Si solar cells as per the protocol presented in subsection 3.6.

5.3.2.1. Reflectance

Using an Ocean Insight OceanHDX Spectrometer reflectance setup, diffuse and specular reflectance of the PQDs LEVA coated pc-Si solar cells were performed.

The presented dataset in Figure 5.6 illustrates the outcomes of diffuse (45°) and specular (0°) reflectance measurements conducted on both a bare pc-Si solar cell and a counterpart coated with PQDs-incorporated LEVA (sample P28). As the LEVA layering methodology adheres to strict reproducibility criteria which ensured all cells are processed the same regardless the used QDs concentration, it can be reasonably assumed that all LEVA coated cells possess uniform LEVA films in terms of thickness, uniformity, and smoothness. This can be seen in Figures 3.6 and 5.11, with measurements displayed in Figures 5.12 and 5.13.
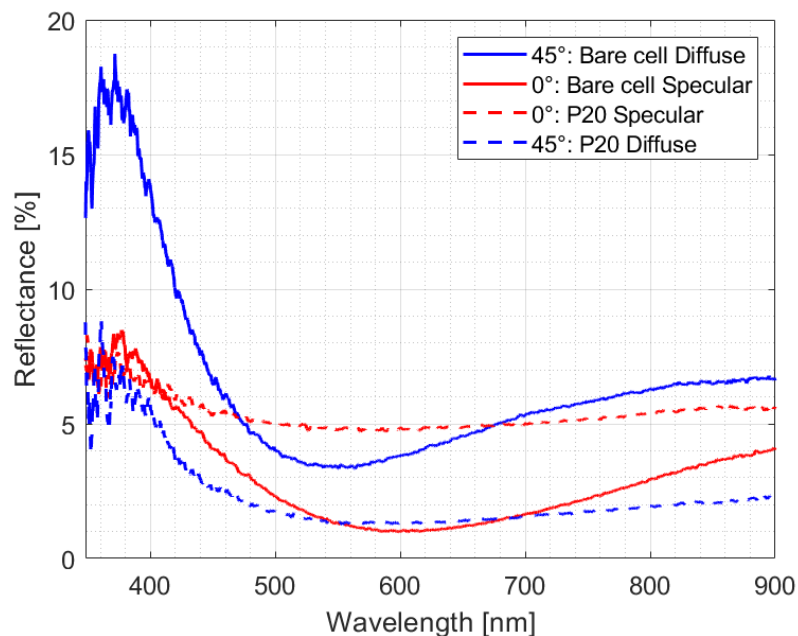
Figure 5.6 Diffuse and specular reflectance measured at 45° and 0˚, respectively, for the bare and PQDs coated (P28) pc-Si solar cell sample, 0.01 mg of PQDs by LEVA method.

The PQDs LEVA film applied to the pc-Si solar cell surface has resulted in a substantial reduction in <u>diffuse</u> reflectance across the measured wavelength spectrum of 350-900 nm. The most significant reductions are observed in the UV-blue region, where the weighted average reflectance dropped from 17.4% for the Bare reference cells to 6.32% for the PQDs LEVA coated sample P28 between 371-388 nm, amounting to a reduction of 63.7%. Additionally, there was a substantial reduction in the Vis-NIR region, with a 67.8% drop at 848 nm, reducing from 6.58% (Bare) to 2.12% (P28).

The smallest reduction was observed at 526 nm in the green-yellow region, where reflectance decreased from 3.45% (Bare) to 1.47% (P28), resulting in a 57.4% reduction.

These reductions hold significant importance as they are a direct product of the absorption of UV-blue photons by the LDS PQDs, addressing the low solar response of pc-Si solar cells in this range, 350-500 nm. This, in turn, maximizes the generation of downshifted photons from PQDs, thereby amplifying the emission of red photons at 690 nm.

Furthermore, the sustained reduction in reflectance starting at 600 nm onwards contributes to absorbing more of the incident solar irradiance naturally, leading to an increased absorption of red photons. This can be observed in Figure 5.6, where the weighted average reflectance for the PQDs LEVA coated sample P28 was 1.82% between 600-900 nm, compared to 5.31% for the Bare reference cell in the same region of the spectrum, representing a reduction of 65.7%. It is worth noting that the reduced reflectance profile of the PQDs LEVA coated solar cell (P28) closely aligns with that of its bare counterpart.

Reduction in <u>specular</u> reflectance is observed at 377 nm with a decrease of 22% from 8.45% (Bare) to 6.59% (P28). This observation is particularly significant, as it further proves the PQDs' absorption of targeted incident photons within the 350-377 nm wavelength range.

The observations coherently with the results found in the literature reviewed. Notably, similar patterns of decreased reflectance within the 350-450 nm absorption spectrum have been well-documented. These reductions in reflectance are observed in cases where PQDs are employed to enhance the efficiency of c-Si solar cells via LDS. Researchers in these studies have consistently attributed the decreased reflectance to the to the effective implementation of LDS [26], [157], [166], [212].

The specular reflectance profile initially demonstrates a reduction, followed by a plateau beyond 422 nm, maintaining a consistent pattern until the end of the measured wavelength range at 900 nm. The initial reduction is due to the combination of PQDs-based LDS light trapping and UV-blocking characteristics of the LDS LEVA film (inherent characteristic of EVA, shown later in

Figure 5.9). However, since the surface of pc-Si solar cells is inherently V-shaped, the reported literature has suggested that reducing or eliminating these V-shaped grooves on the cell surface can lead to increased reflection [306]. Therefore, the resulting PQDs LEVA film, fills these V-shaped grooves and therefore creates a flatter surface which increases the overall specular reflectance. This explains the plateau of increased specular reflectance appearing beyond the 422 nm mark in Figure 5.6. This is illustrated in Figure 5.8. Additionally, it is important to acknowledge findings in the literature that report an increase in reflectance within specific wavelength ranges, notably 400-650 nm [50] and 540-900 nm [157]. These observed increases in reflectance have been attributed to optical losses associated with LDS. This phenomenon is theorized to originate from the formation of an 'escape cone,' a construct that permits a fraction of the LDS-emitted light to escape from the solar cell, thereby increasing reflectance at that region.

While the noticeable increase in specular reflectance is evident, the combination of localized reduction between 350-377 nm, assisted by the substantial decline in diffuse reflectance spanning the full measured wavelength range of 350-900 nm, profoundly contributes to the optical enhancement conferred by the integration of LDS PQDs.

To substantiate this assertion and validate the role of PQDs in reducing reflectance by enhancing light trapping because of LDS, Figure 5.7 provides a direct comparison for reflectance measurements between the PQDs LEVA coated pc-Si solar cell (sample P28) and a reference cell (sample R6) with an identical LEVA film but devoid of PQDs.

While in Figure 5.6, it is evident that the LEVA film increased specular reflectance at 605 nm from 1% (Bare) to 4.8% (P28). Figure 5.7 clearly illustrates the significant role played by CsPbI₃ PQDs in reducing this increased specular reflectance. The addition of CsPbI₃ PQDs to sample P28 using the LEVA coating method led to a reduction in specular reflectance at 605 nm from 6.49% (R6) to 4.8% (P28). This represents a decrease of 26% attributed to the LDS effect of the PQDs, which reduced reflectance by absorbing more photons than the non-LDS LEVA film, and therefore improving the optical coupling and light trapping in the cell. Thus, toning down some of the inevitable increase in specular reflectance caused by the LEVA film at that wavelength.
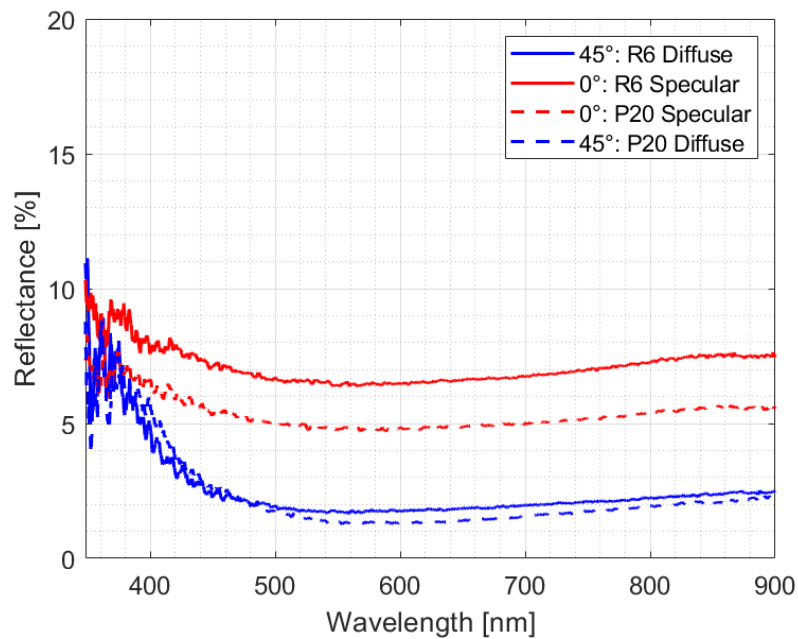
Figure 5.7 Diffuse and specular reflectance measured at 45° and 0°, respectively, for the Reference (R6) and PQDs coated (P28) pc-Si solar cell sample, 0.01 mg of PQDs by LEVA method.

The overall attenuation of reflectance ensuing from the incorporation of CsPbI₃ PQDs into the innovative LEVA film, substantiates the ability of the optical host in employing the LDS phenomenon to generate reliable and reproducible reflectance reductions.

Dispersing clusters of CsPbI₃ PQDs into a three-dimensional optical host, the LEVA film, allows them to act as "focal points" for the light trapping phenomena caused by their LDS behaviour, refer to Figure 2.5. This is true as PQDs will be allowed to interact with LDS photons leaving neighbouring ones and stray photons that are either internally reflected or leaving the cell. Hence, it can be assumed that this effect is amplified by the optical host which explains the reduced reflection (diffuse and specular) in the LDS coated cell P28 compared to the reference cell R6 as proved in Figure 5.7.

Furthermore, this enhanced LDS optical environment complements the inherent light-trapping capabilities of these pc-Si cells, resulting from their V-shaped grooves. This contributes to a significant reduction in diffuse reflectance. However, Figures 5.6 and 5.7 clearly show a notable increase in specular reflectance, primarily caused by the enhanced surface evenness of the LEVA-coated cell. Although surface roughness does not exhibit significant improvement (as measured in the next subsection 5.3.2.3), the smooth surface of LEVA films creates a relatively more even and shiny surface. This smoothness reflects perpendicular incident light more efficiently than the

native rough surface of the V-grooved pc-Si solar cells. Therefore, causing a specific increase in the specular reflectance while reducing diffuse reflectance.

The mechanism behind these two analogous yet opposite phenomena is illustrated in Figure 5.8.
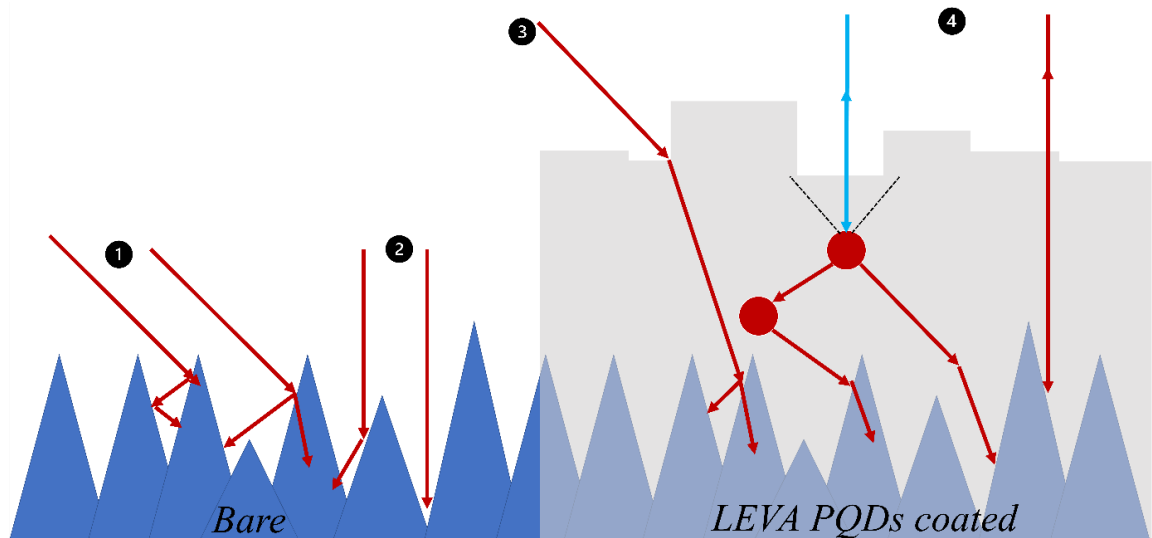
Figure 5.8 Illustration: Changes in Diffuse and Specular reflectance behaviour introduced by the LEVA PQDs film. With light interactions numbered 1 to 4.

Figure 5.8 visually illustrates the process behind the ability of the LEVA film in decreasing diffuse reflectance while adversely increasing the specular reflectance. Assuming the ARC layer acts equally on both the bare and coated cells, the characteristic V-shaped grooves of pc-Si solar cells are very effective at light trapping from all angles of incidence as they act as geometrical trapping protrusions that would favour reflection into the cell rather than outward reflection as seen by light interactions numbered 1 and 2. Once the cell is coated by the LEVA method, the resulting dry LEVA film produces a more even and smoother surface that introduces an extra reflection stage for incident light before it reaches the V-shaped grooves of the cells as seen by light interactions numbered 4. Nevertheless, as the film is not perfectly even, possessing a slightly geographical surface influenced by the V-shaped grooves, it introduces points of geometrical traps that work similarly to the cell's grooves but with lower effectiveness due to the smoother surface. This effect is illustrated in light interaction number 3. The presence of light-trapping LDS PQDs, in conjunction with the V-shaped grooves, contributes to trapping incident light, reducing diffuse reflectance but increasing specular reflectance in the process.

It is worth noting that the literature advocates that diminishing or eradicating these V-shaped features on the cell surface can result in increased reflection [306], directly contributing to the observed increase in specular reflectance.

In addition to enhancing the overall light trapping capabilities of the coated cells through the LDS phenomenon presented by the CsPbI$_3$ PQDs, analogous halide CsPbBr$_3$ PQDs [225] and Silicon QDs (SiQDs) [47] were reported to introduce anti-reflective behaviour when deposited onto solar cells, attributed to their inherent porosity. This porosity encourages light absorption while minimizing the reflection of incident light, contributing to overall improved optical properties.

5.3.2.2. *Transmittance*

Moving on to transmittance, the effects of liquefying EVA in the LEVA process were studied using the Edinburgh Instruments FS5 Spectrofluorometer.

A LEVA film was sandwiched between two 3.2 mm Pilkington OptiWhite solar glass pieces and measured for transmittance. The same sandwich was reconstructed using a commercially available EVA sheet that was thermally applied to adhere the two solar glass squares together. For reference, a single solar glass sample, and an air-gapped solar glass sandwich were also measured for transmittance.

As demonstrated by in Figure 5.9, it is clear how commercially available EVA (for solar cells and panels applications) characteristically blocks UV light blow 350 nm. This is shown by both the thermally applied EVA sheet and LEVA film. This serves as a first proof on the how liquefying EVA by Toluene (LEVA) does not change the optical characteristics of EVA. A further proof was extracted on the chemical stability of LEVA films by obtaining FT-IR readings on two EVA films: commercially available EVA versus a dry LEVA film, shown in Figure 5.10. The readings for the film show a nearly perfect overlap especially in the sharp and strong peaks between 1700 cm^{-1} to 4000 cm^{-1}, with a matching but slightly misaligned silhouette below 1700 cm^{-1} which is acceptable.

This is strong evidence of the preservation of the LEVA method for the chemical, physical and optical properties of EVA.
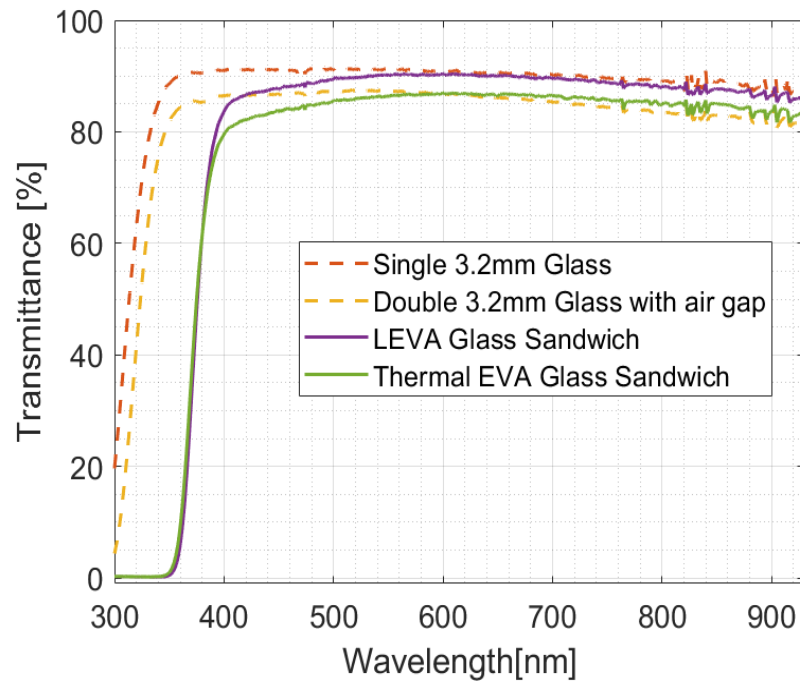
Figure 5.9 Transmittance: LEVA film vs a commercially available EVA sheet, both sandwiched between two 3.2 mm Pilkington OptiWhite solar glass [287].
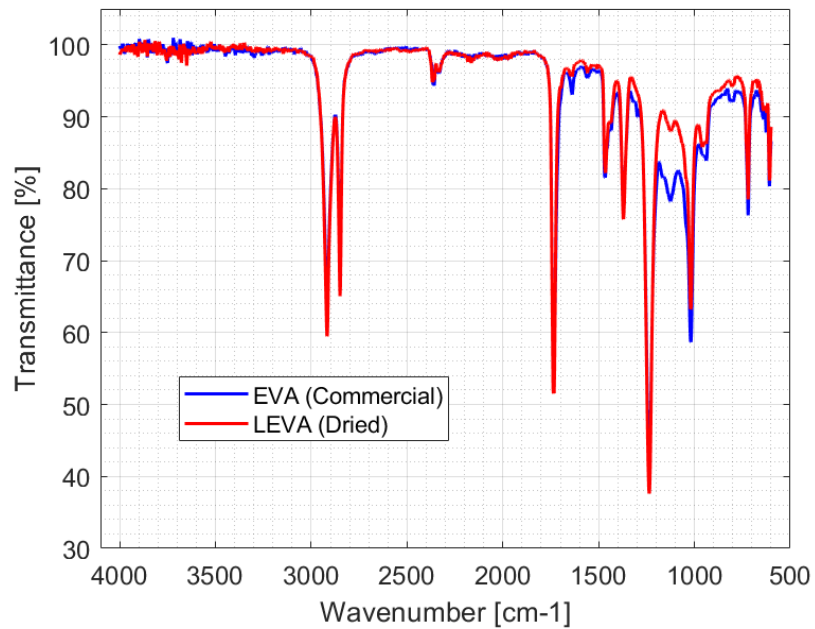
Figure 5.10 FT-IR measurements of EVA films: LEVA film (red) vs commercially available EVA sheet (blue).

Moreover, since the LEVA film generated very smooth surfaces that increases surface contact, it adheres significantly better to glass than thermally applied EVA sheet. This is evident by the outstanding near-overlap in transmittance of 90.4% shown by the LEVA glass sandwich (of two

glass sheets) to that of only one glass sheet, specifically after 580 nm. This setup surpassed the transmittance of the air-gapped sandwich starting early at 410 nm.

Furthermore, the same figure indicates the poorer surface contact resulting from thermally applying the EVA sheet in a glass sandwich and how this made it perform, on average, like the air-gapped sandwich. It only slightly overcomes the air-gap contraption's transmittance by 2.4% at 860 nm, with transmittance of 84.8% compared to 82.8%. Additionally, while the transmittance silhouette of the thermally applied EVA sheet matches that of the LEVA film, the highest measured transmittance at 600 nm drops from 90.4% (LEVA) to 87% (thermal), amounting to a 3.8% drop. This gap started emerging at 393 nm and consistently continued from 405 nm until the upper limit of the measurement at 930 nm, resulting in a weighted average drop of 3.9%.

The advancement of the LEVA film compared to the thermally applied EVA sheet can be attributed to morphological changes that occur on the surface of the EVA sheet. Figure 5.10 demonstrated no chemical changes to the Toluene -liquefied EVA. However, when liquefying the commercial EVA sheet, it loses its rough texture, which is a cause of bubbling when thermally applied. Despite taking precautions to avoid visible bubbling in the process of thermal encapsulation, microbubbles resulting from the rough texture of the EVA sheet were inevitable. When thermally applying EVA as an encapsulant between two impermeable sheets of materials, microbubbles have no means of escape, thus getting trapped. This also applies to the thermal encapsulation of solar cells. The presence of these bubbles reduces the transmittance of light and disrupts the quality of light-trapping properties of the EVA-glass combination by introducing points of refraction within the contraption, which eventually increases scattering. Although this issue is not common in commercially thermally encapsulated solar panels, the method followed here mirrored the same steps taken to thermally encapsulate a PA SiQDs coated pc-Si solar cell, as seen in Chapter 4, which ensured minimal exposure of these QDs to high temperatures to avoid accelerated degradation.

It is relevant to note that LEVA films will be investigated solely as a direct incorporation method for CsPbI₃ PQDs onto pc-Si solar cells and not for encapsulation, thus falling under Tier 3 experimentation, and therefore is considered as a direct coating method. This implies that LEVA films will not be combined with the upper 3.2 mm Pilkington OptiWhite solar glass. Further details on this will be expanded upon in subsection 5.3.3.

5.3.2.3. Confocal Microscopy

The Olympus LEXT OLS5000 confocal microscope was utilised to measure several aspects on the solar cell samples. This included the roughness changes and overall thickness of the PQDs LEVA film created by the novel LEVA coating method. Additionally, it was used to study the patterns of the poured PQDs LEVA film.
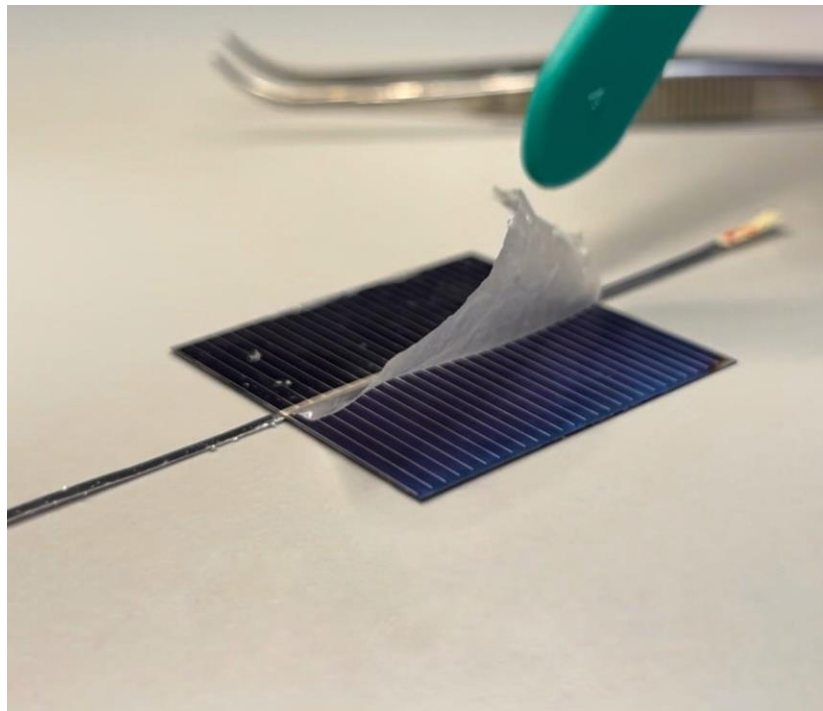
Figure 5.11 A visualization of the dried LEVA film created by the novel LEVA coating method. In this case half of the film was peeled while the other left intact.

Through the utilisation of the confocal microscope's advanced 3D laser scanning capabilities, comprehensive profiling and quantification of both thickness and surface roughness were possible, as depicted in Figure 5.12 and 5-13.
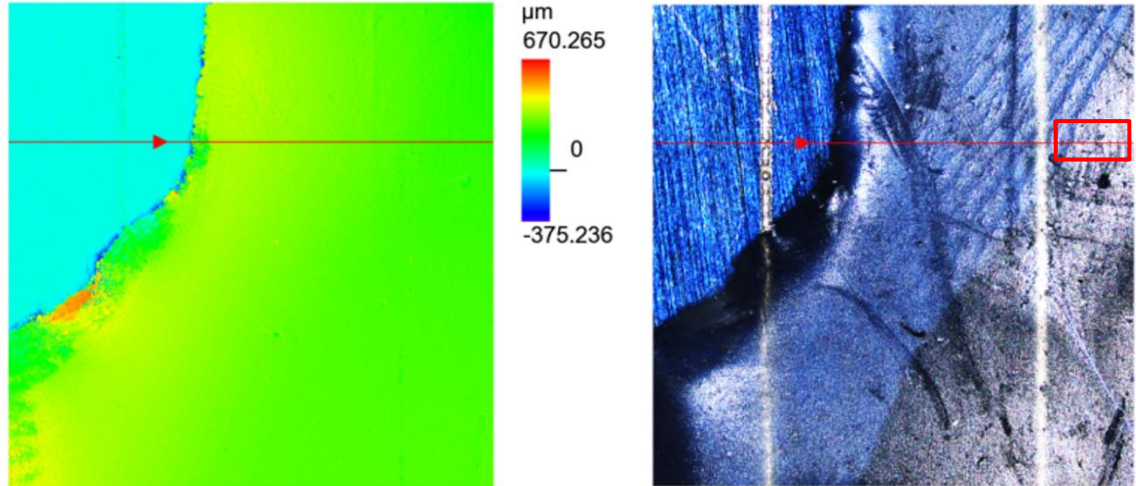
Figure 5.12 Overview of LEVA coating pc-Si solar cell. Left: Depth heatmap indicating coating thickness with the solar cell as the zero point. Right: Coloured image revealing the bare area on the left top of the cell, while the rest is coated with the PQDs LEVA film.

Both images showcase the same cell, the left being a heatmap of depth with zero point being the bare solar cell, while the right figure is a coloured image that shows three regions of the measured cell, bare, peeled LEVA film, and intact LEVA film. The LEVA film was peeled and cut to be measure under the confocal microscope for thickness and roughness. The peeled region was kept to prevent any pulling out of the intact film, thus preserving its adhesion to the cell.
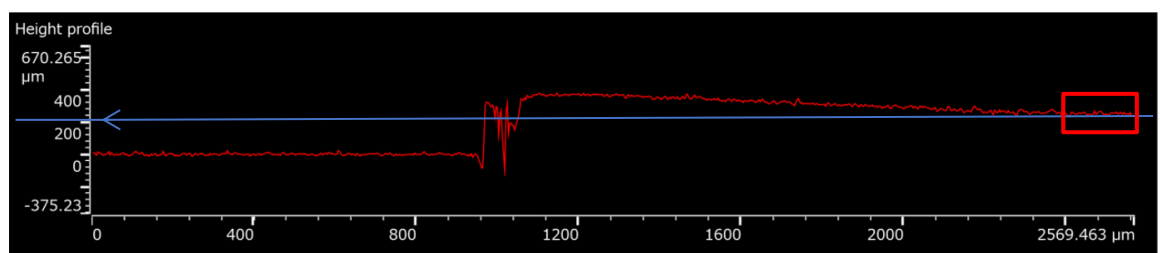
Figure 5.13 Profilometer profile measuring thickness and roughness, extracted from the 3D model generated by the 3D scan shown in Figure 5.12.

The thickness of the intact LEVA film measures at 240 μm, as indicated by the red rectangle at the conclusion of the profile. To provide a point of reference, the thickness of commercially acquired EVA sheet, conventionally employed for thermal encapsulation, stands at 460 μm [325], which in ensured to stays consistent after the thermal encapsulation process. The LEVA film demonstrates a 47.8% reduction in thickness when compared to its commercial counterpart.

Furthermore, when assessing roughness, the surface characteristics of the LEVA film closely align with those of the pc-Si solar cell as it masks the V-shaped grooves.

The subsequent coloured analysis of the PQDs LEVA film has been undertaken, adding further dimensions to the investigation. Starting with Figure 5.14.
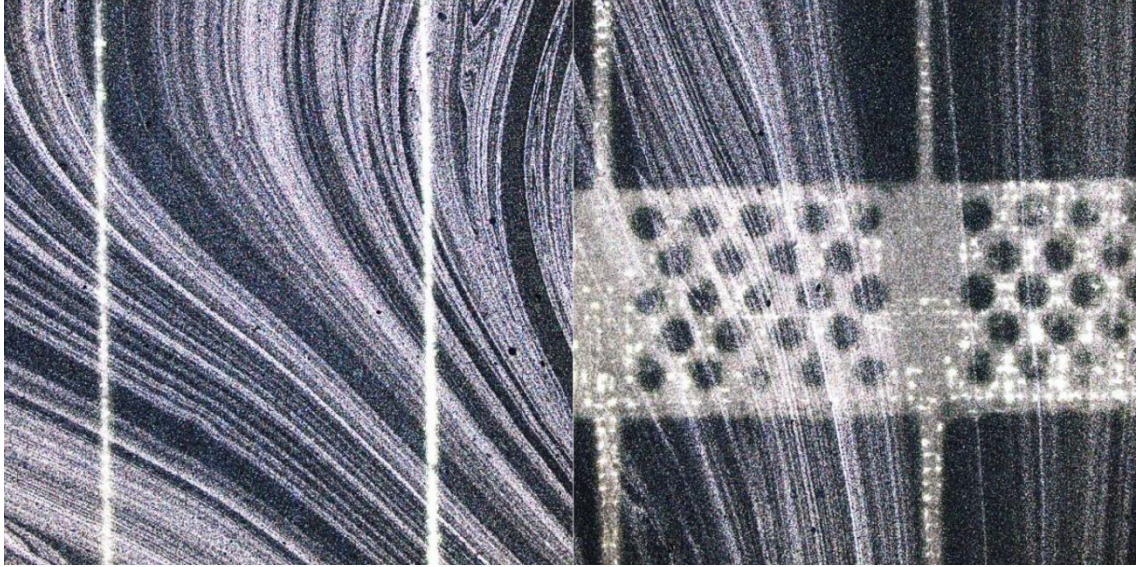
Figure 5.14 Confocal coloured microscopy of sample P28, processed and coated by the LEVA method. 1 ml of 0.01 mg PQDs LEVA poured and allowed to dry forming a film. Left x5, right x10.

As depicted in Figure 5.14, observable refraction streaks of higher concentration PQDs are represented in grey, while areas of lower concentration appear in a darker blue, which looks directly into the surface of the solar cell itself. These patterns correspond to the mixing process, where the LEVA and PQDs solution is blended using a sterile needle and a vortex mixer. The origin of these streaks can be attributed to the viscosity of the formed LEVA: as the liquified EVA cools after the dissolution of EVA in Toluene, its viscosity increases. Although this effect could be mitigated by elevating the Toluene content, it is more advantageous for LEVA to exhibit higher viscosity, as this aids in controlling its flow. By elevating the viscosity, drying patterns generated by the evaporation of Toluene, such as "coffee stains" and other similar effects, are less likely to impact the uniformity of the film. This ensures a consistent and uniform PQDs LEVA film is generated.

While the variation between the streaks in grey and darker blue might initially appear indicative of uneven mixing and consequently uneven concentration distribution, it is important to note that this effect is somewhat exaggerated by the bright images captured during the construction of the 3D model using the confocal microscope. To provide a clearer understanding of this phenomenon,

further insight can be gained through the results obtained from fluorescence microscopy, which is elaborated upon in the subsequent subsection.

5.3.2.4.   Fluorescence Microscopy

Using the ZEISS Axio Scope.A1 fluorescence microscopy setup, fluorescence microscopy of the LDS coated pc-Si solar cells was performed as seen in Figure 5.15.
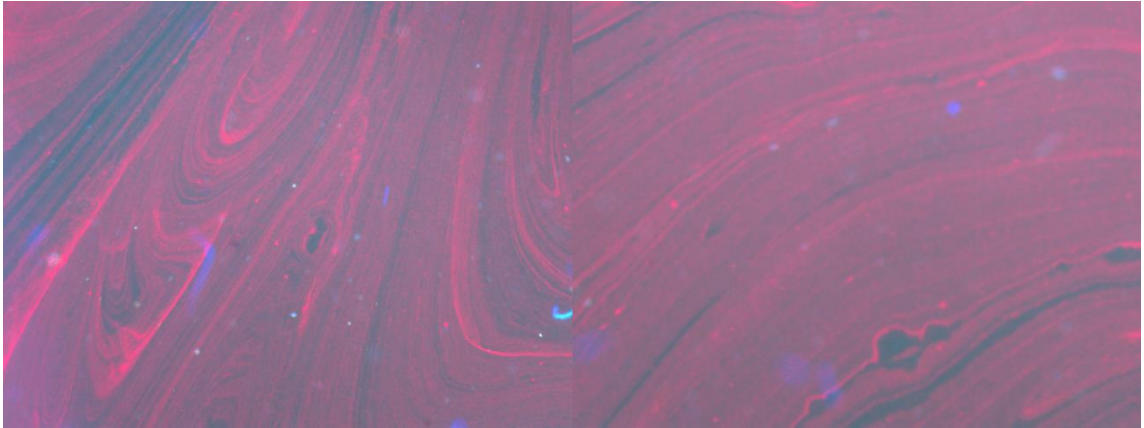
Figure 5.15 Fluorescence microscopy was employed to examine PQDs LEVA-coated sample P28, captured at x5. This analysis encompassed two randomly selected regions on the cell.

Correlating Figure 5.15 with Figure 5.14, it becomes apparent that the streaks of CsPbI₃ PQDs within the LEVA film are of well distribution across the solar cell area with coverage exceeding 95% of the cell's surface, and minimal appearance of low-concentration regions where the blue surface of the pc-Si solar cell can be seen peeking through.

As outlined in the Chapter 3, the excitation process utilised the X-Cite 120 Q spectral excitation light source, which encompassed a broad spectrum of wavelengths spanning from 300 to 740 nm. Notable peaks were evident at 335, 370, 410, 440, 550, and 580 nm. This excitation range is consistent with the data presented in Figures 5.1 and 5.2, which demonstrate the capacity of CsPbI₃ PQDs to absorb wavelengths up to 680 nm and proficiently downshift these absorbed wavelengths to the 690-693 nm range. This phenomenon accounts for the uniformity in the observed PL imaging, depicted by a single dominant colour. It is pertinent to note that any visual presence of blue lines or specs is attributed to reflections off dust particles.

As the PL spectrum of the PQDs exhibits a distinctive red colour at a wavelength of 690 nm, the images visually agree with the measured PL readings of the liquid sample.

The agreement between the expected visual PL as seen in Figure 5.15 and the measured PL readings in Figure 5.1 further validates the accuracy and reliability of the LEVA experimental

setup in incorporating CsPbI$_3$ PQDs onto pc-Si solar cells and preserving them from immediate oxidation and phase shifting. The showcased data provides valuable insights into the PL behaviour of the PQDs and their potential application in improving the efficiency and performance of solar cells by effectively converting higher-energy photons into lower-energy ones, which is fully investigated in following subsection 5.3.3.

Henceforward, a comprehensive exposition and interpretation of the electrical characterisation and resulting enhancements will be presented and discussed.

5.3.3. Electrical characterisation of CsPbI$_3$ PQDs coated pc-Si solar cells.

5.3.3.1. *Direct DC of PQDs*

It was emphasised throughout the chapter that the novel LEVA coating method was the successful method of incorporating PQDs onto pc-Si solar cells. However, this was preceded by a series of tests utilising the use of direct DC as the main method. As already discussed, the addition of PQDs onto bare solar cells in open air starts an unmeasurable degradation in PL activity which takes place relatively fast; usually a DC coated cell will visibly stops reacting to UV light stimulant within 2 days or shorter. Another issue was raised when thermally encapsulating solar cells with a CsPbI$_3$ PQDs coating, and that is direct and near-instant degradation of these QDs by morphologically shifting from the black α phase (PL active) into a dormant yellow δ phase [130], [293], [299].

To highlight the potential LDS enhancements that CsPbI$_3$ PQDs can provide, two samples, P1 and P2, were carefully prepared. These samples were coated with CsPbI$_3$ PQDs using the DC method at room temperature, and notably, they were prepared with significantly higher concentrations compared to the PA SiQDs discussed in Chapter 4. This strategic choice allowed for a detailed study of the dispersion and uniformity of the PQD coating when employing the DC method while minimising the effects of degradative phase shifting.

In contrast to the optimal concentration of 0.01 mg/ml found for PA SiQDs in Chapter 4, samples P1 and P2 were coated with 2 mg and 1 mg of PQDs, respectively, suspended in 1 ml of Toluene. These samples were systematically subjected to all four Tiers of experimentation as explained in Chapter 3, progressing from the initial Bare state (Tier 1), then through the Soldered state (Tier 2), followed by DC Coating (Tier 3), and finally culminating in Thermal Encapsulation (Tier 4), with the PQDs DC coating intact.

The decision to substantially increase the PQDs' concentration from 0.01 mg to 1 and 2 mg was multifaceted. Besides addressing concerns of PQD loss due to induced thermal degradation during

the encapsulation process, the primary motivation was to counteract the instantaneous degradation observed in lower concentration PQD coatings when exposed to air. The experiments revealed that lower concentrations, typically ranging from 0.01 to 0.1 mg/ml, experienced a rapid transition from the photoluminescent (PL active) black α phase to an inert yellow δ phase upon drop casting onto the flat, air exposed surface of the 39 mm × 39 mm pc-Si solar cells.

To benefit from cross referencing, the same 3 reference samples used in the publication and the previous PA SiQDs (Chapter 4) were used as a baseline for the results of this subsection, refer to Table 4.3. Since these cells are not LDS coated (thus skipping Tier 3), they are used to prove increases by DC and thermal Encapsulation.

As discussed in the Methodology, Chapter 3, all results are reported to the 3rd decimal place.

The electrical parameters extracted from the I-V characteristics for the two samples P1 and P2 before and after the deposition of PQDs by DC are displayed in Table 5.1. Both samples showed a significant decrease in the I_{SC} of 18.80% % for P1 and 10.26% for the P2 sample. There is a negligible effect of the coating on V_{OC} in P1 and P2, with a reduction of 1.58% and 0.5% respectively. These results are caused by optical losses as explained throughout in this subsection.

The decrease in P_M for both samples are unmistakably substantial as a result of the substantial decrease in the I_{SC}. This is visualised by the I-V characteristic curve shown in Figure 5.16.

Table 5.1 Electrical parameters of samples P1 and P2 before and after coating with PQDs by DC.

Samples	Electrical Parameters	Bare and Soldered Solar Cell	Coated with PQDs by DC	% Increase
P1	I_{SC} **(A)**	0.548	0.445	-18.80
	P_M **(W)**	0.244	0.204	-16.39
	V_{OC} **(V)**	0.624	0.614	-1.60
P2	I_{SC} **(A)**	0.536	0.481	-10.26
	P_M **(W)**	0.238	0.213	-10.50
	V_{OC} **(V)**	0.607	0.604	-0.49
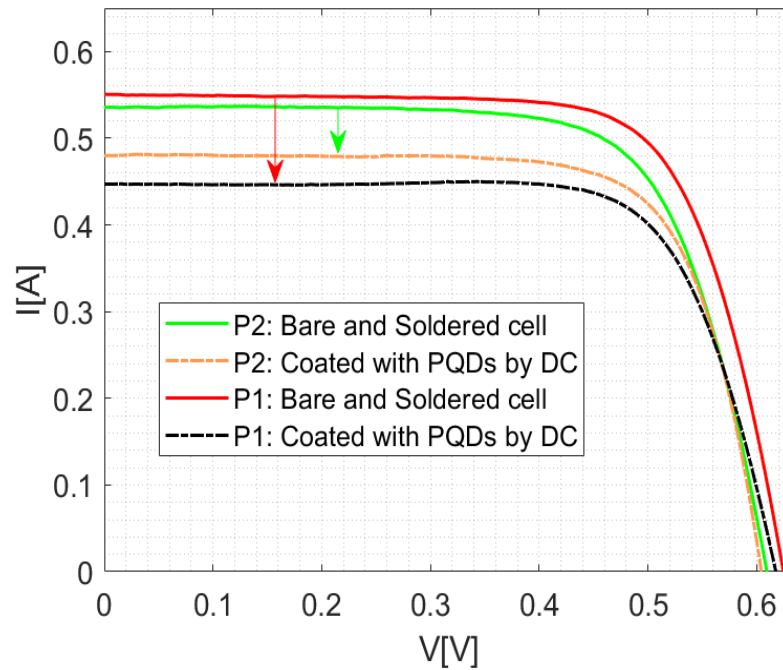
Figure 5.16 I-V characteristic of P1 and P2 samples before (Tier 2 soldered cell) and after coating with PQDs by DC (Tier3).

Referring to Figure 5.1, the broad absorption band of these PQDs is evident, allowing them to absorb most wavelengths below 680 nm. Although absorption intensity varies across wavelengths, this broad characteristic absorption band enables them to serve effectively as a long-pass filter when evenly deposited at high concentrations, in addition to boosting photons in the range of 690-693 nm by LDS. This characteristic also accounts for their distinctive deep red colour.

At elevated concentrations, these PQDs are capable of absorbing a significant portion of incident photons below 680 nm, while still permitting longer wavelengths to pass through, along with the LDS re-emission at 690-693 nm. However, when deposited at significantly high concentrations, their high PLQY of 99% leads to a partial blockage of the solar spectrum, affecting approximately one-third of the useful spectrum. While an LDS PQDs coating can effectively increase the quantity of downshifted red photons, which Si solar cells respond to more effectively, excessively high concentrations of PQDs can result in a shading effect. This shading effect, in turn, may disrupt the normal operating conditions of the coated pc-Si solar cells, preventing them from absorbing most of the incident solar radiation below 680 nm.

Furthermore, one of the key factors to the electrical losses lies in the intrinsic nature of QDs as quantum symmetric systems, leading to isotropic emission [199]. In the absence of a suitable host

material or thermal encapsulation combined with glass (as in the case of 3.2 mm glass), the PQDs-coated solar cells can theoretically experience a loss of up to 50% of the re-emitted red light at 690-693 nm; assuming that up to 50% of the LDS re-emitted light is facing upward or away from the surface of the cell. While the V-shaped grooves on the pc-Si surface can aid in containing the PQDs within the cell, and reducing reflectance, the results indicate that this approach alone is insufficient. This was also reported in the literature where increased deposited concentrations of PQDs can decreases PCE of pc-Si solar cells due to the filling up of the inverted-pyramids with PQDs cluster which reduces light trapping [157].

In the absence of a host material, crucial optical phenomena such as enhanced light trapping, total internal reflection, and optical coupling are absent. This realization underscores the significance of developing the novel coating method using LEVA.

To further analyse the effect of thermal encapsulation, sample P2 was thermally encapsulated.

As indicated in Table 5.2 and illustrated in Figure 5.17, the encapsulation of sample P2 successfully restored the cell's performance to a level slightly surpassing its original state at the experiment's outset. This enhancement was primarily achieved through the physical enhancement of light trapping, alongside improvements in optical coupling and internal reflection.
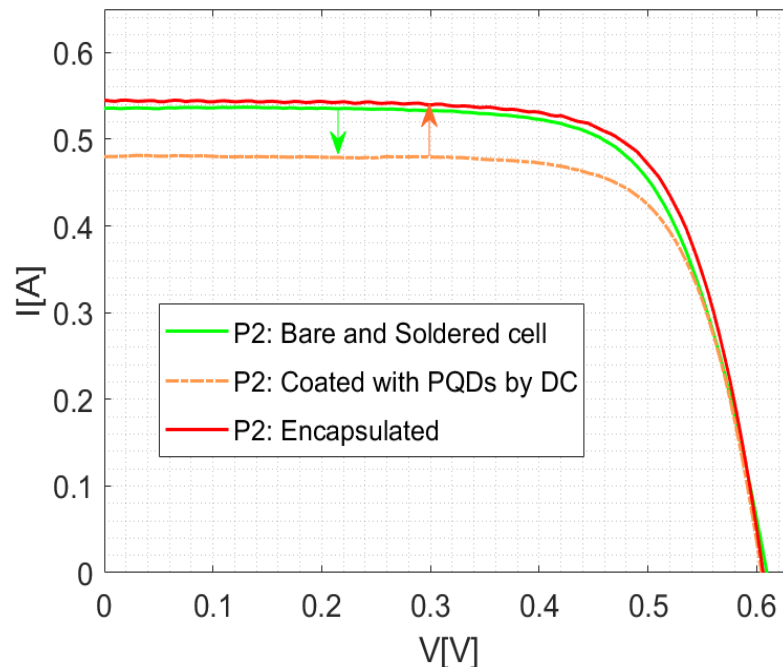
Figure 5.17 I-V characteristic of coated P2 sample (by DC of PQDs) before (bare and soldered cell), after DC, and after full thermal encapsulation.

Table 5.2 Electrical parameters of P2 sample before coating (bare cell) and after coating with PQDs and encapsulation.

Electrical Parameters	P2 Bare and Soldered	P2 Coated with PQDs by DC	% Change	P2 Coated and Encapsulated	Total % Change
I_{SC} (A)	0.536	0.481	(- 10.26)	0.543	+1.31
P_M (W)	0.238	0.213	(-10.05)	0.237	(-0.42)
V_{OC} (V)	0.607	0.604	(-0.49)	0.606	(-0.16)

Table 5.2 clearly shows the substantial drop in the performance of the pc-Si solar cells due the high concentration of CsPbI₃ PQDs deposited by DC, and how thermal encapsulation recovered that culminating in a total increase of 1.31% in the I_{SC} of the solar cell. Under typical conditions, thermal encapsulation is expected to elevate the ground-state I_{SC} by an average of 8.44%, as evidenced by the results from samples R1, R2, and R3.

Moreover, the cell visibly stops reacting to external UV light stimuli, and the PQDs layer show no sign of red emission. Further investigation of this phenomenon is conducted through fluorescent microscopy, as presented in Figure 5.18. The results indicate that the red LDS emission is significantly reduced, diminishing almost entirely following the process of thermal encapsulation.
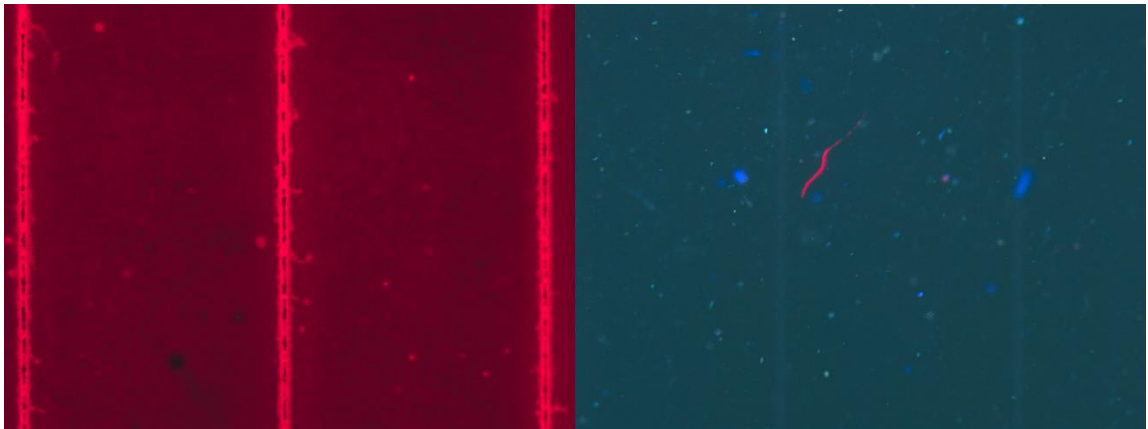
Figure 5.18 CsPbI₃ LDS coated Sample P2: before (left) and after (right) thermal encapsulation.

As briefly mentioned before, the reason behind this is the full thermal degradation of the CsPbI₃ PQDs under encapsulation temperature exceeding 100°C; morphologically shifting from the photoluminescent black α phase state into a dormant yellow δ phase [130], [293], [295], [296], [297], [299].

Therefore, it can be concluded that there was a need to create a method that protects PQDs from oxidation and thermal degradation, while providing substantial optical benefits. PQDs LEVA films will benefit from enhanced light trapping, total internal reflection, and optical coupling, as

well as elevation from the V-shaped grooves of the pc-Si cell which leads to enhanced angular responses. Simultaneously, it will protect the PQDs from oxidation, and skips thermal degradation by skipping thermal encapsulation (lamination) completely.

5.3.3.2.   *Novel method: PQDs coating by the LEVA method.*

Following the experimental procedures of incorporating CsPbI₃ PQDs onto pc-Si solar by direct DC, the novel LEVA coating method was specifically designed to overcome the shortcomings of the DC method, while harnessing the LDS phenomenon of these QDs. The useful LDS properties of these PQDs are characterised by emission peak of 692 nm, a broad excitation range primarily below 680 nm, and PLQY of 99%.

To ensure a complete understanding of how LEVA enhances a solar cell, 25 cells were coated using the novel method. Using LEVA, each cell was coated with a LEVA film hosting CsPbI₃ PQDs of a controlled and known concentration.

To establish a baseline for the results, three LEVA reference samples were fabricated. These samples aimed to determine any optical advantages that a pure LEVA film might introduce to pc-Si solar cells.

Following the substantial decline in I_{SC} and performance witnessed with the usage of higher concentrations (2 and 1 mg/ml) as discussed in the preceding subsection, a reduced concentration of 0.01 mg/ml was chosen for subsequent tests on all cells. This concentration choice was influenced by the same concentration utilised to enhance sample Q2 in the PA SiQDs chapter.

The electrical parameters extracted from the I-V characteristics for the seven samples (P3, P23-P28) before and after the incorporation of PQDs-incorporated LEVA are presented in Table 5.3, alongside an illustrative I-V characteristic curve in Figure 5.19. These samples showcase the best results.

Concentrating on I_{SC}, the integration of PQDs through the LEVA process yielded notable outcomes. The highest recorded increase in I_{SC} was observed in samples P3 and P28, with increments of 1.55% and 1.40% respectively, ten samples passing the 1% threshold. However, the coating exhibited minimal influence on V_{OC} for all samples, resulting in incremental enhancements ranging between 0.02% and 0.28%. This outcome aligns with expectations, as the elevation in generated photocurrent (I_{SC}) due to LDS and improved light trapping directly corresponds to amplified charge separation and radiative recombination.

The range of P_M increases spanned from 0.15% to 1.53%, a phenomenon attributed mainly to the increase in current. While the quantitative consistency in V_{OC} and P_M increases might not be

uniform, the remarkable consistency in positive electrical enhancements arising from the effective incorporation of PQDs through the LEVA coating method is undeniable. The capacity of PQDs LEVA film to enhance red light intensity, facilitate light trapping, and elevate radiative recombination is evident in the incremental enhancement of V_{OC}, even though V_{OC} enhancement is inherently linked to solar cell physics, such as bandgap alteration or doping concentration modification.

Table 5.3 Electrical parameters of seven samples (P3, P23-P28) before coating (bare cell) and after coating with PQDs LEVA film. 0.01 mg/ml.

Samples	Electrical Parameters	Soldered Solar Cell (Tier 2)	Coated with PQDs by LEVA (Tier 3)	% Increase
P3	I_{SC} (A)	0.517	0.525	1.55
	P_M (W)	0.212	0.213	0.47
	V_{OC} (V)	0.617	0.617	0.00
P23	I_{SC} (A)	0.504	0.510	1.19
	P_M (W)	0.212	0.214	0.94
	V_{OC} (V)	0.614	0.615	0.16
P24	I_{SC} (A)	0.504	0.510	1.19
	P_M (W)	0.202	0.205	1.49
	V_{OC} (V)	0.615	0.616	0.16
P25	I_{SC} (A)	0.503	0.509	1.19
	P_M (W)	0.220	0.220	0.00
	V_{OC} (V)	0.610	0.611	0.16
P26	I_{SC} (A)	0.502	0.509	1.39
	P_M (W)	0.215	0.216	0.47
	V_{OC} (V)	0.614	0.614	0.00
P27	I_{SC} (A)	0.505	0.511	1.19
	P_M (W)	0.209	0.212	1.44
	V_{OC} (V)	0.613	0.614	0.16
P28	I_{SC} (A)	0.500	0.507	1.40
	P_M (W)	0.208	0.210	0.96
	V_{OC} (V)	0.618	0.618	0.00

Referring to Table 5.4, three LEVA reference samples were prepared to serve as a baseline for measurements. The table clearly illustrates how the LEVA film possesses the capacity to marginally enhance the electrical performance of pc-Si solar cells by engendering an increase in I_{SC}. This enhancement can be attributed to the anticipated effect of improved optical coupling within the cells. EVA's potential to enhance total internal reflection and light trapping, though perceptible, remains considerably modest when compared to the notable enhancements observed

in PQDs-incorporated samples, as indicated in Table 5.3. The I-V characteristic curve in Figure 5.19 provides a comparative illustration between sample P25 and R4.

It is relevant to highlight that in two out of the three instances, a reduction in V_{OC} was observed, accompanied by a distinct decrease in P_M across all cells. The I_{SC} increased 0.2% for all three measurements, while variations in V_{OC} ranged from a decrease of 0.33% to an increase of 0.33%.

Given the marginal nature of these alterations in electrical characteristics, the overarching inference suggests that the LEVA film tends to marginally decrease the performance of pc-Si solar cells. However, these effects are counterbalanced by the integration of PQDs. The synergy between these highly photoluminescent quantum dots and the 240 μm thick host LEVA film lays the groundwork for an efficient light trapping system, empowered by the principle of LDS. Consequently, the LDS LEVA system emerges as an efficacious strategy for enhancing the performance of pc-Si solar cells.

Table 5.4 Electrical parameters of three reference samples before and after LEVA coating (film).

Samples	Electrical Parameters	Bare and Soldered Solar Cell	Coated with pure LEVA film only	% Change
R4	I_{SC} (A)	0.505	0.506	0.20
	P_M (W)	0.220	0.219	(-0.45)
	V_{OC} (V)	0.616	0.615	(-0.16)
R5	I_{SC} (A)	0.501	0.502	0.20
	P_M (W)	0.190	0.189	(-0.53)
	V_{OC} (V)	0.613	0.615	0.33
R6	I_{SC} (A)	0.501	0.502	0.20
	P_M (W)	0.209	0.208	(-0.48)
	V_{OC} (V)	0.615	0.613	(-0.33)
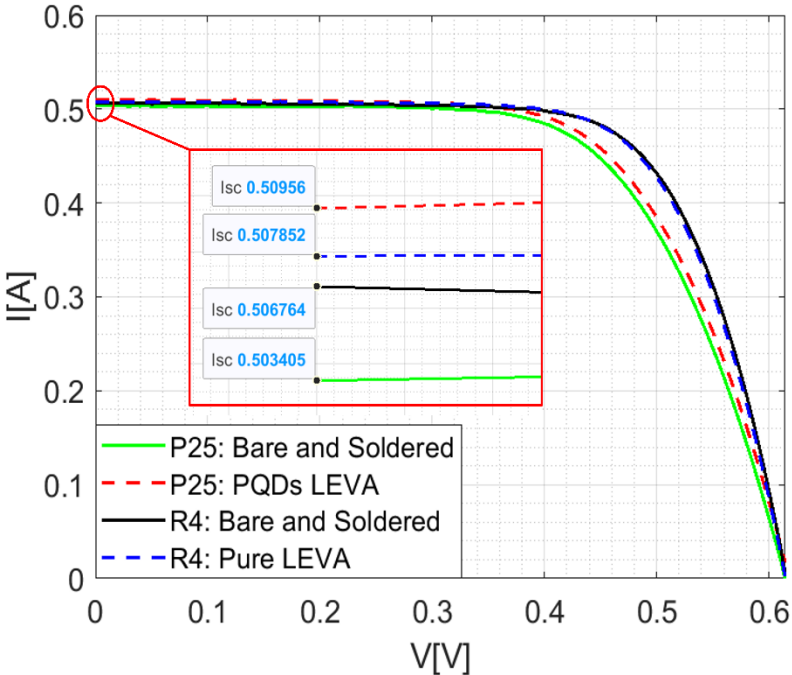
Figure 5.19 I-V characteristic for PQDs LEVA coated P25 sample and referenced LEVA sample R4.

5.3.3.3.   Reproducibility and Degradation

With the original purchased CsPbI₃ PQDs sample tightly sealed away from air, light, and temperature, it was relatively straightforward to recreate LEVA-coated samples that strictly incorporate PQDs at 0.01 mg/ml of Toluene.

Table 5.5 showcases the percentage change in the I_{SC} of 25 PQDs LEVA-coated pc-Si solar cell sample. All twenty-five samples generated a positive increase in the I_{SC} in a standardised manner, where 15 samples exceeded 0.9% average increase. 10 samples exceeded the 1% mark.

Table 5.5 Electrical parameters of all samples (P3-P16, P18-P28) before coating (bare cell) and after coating with PQDs LEVA film. 1 mg/ml.

Sample cell	I_{SC} % Increase	Sample cell	I_{SC} % Increase
P3	1.55	*P16*	0.76
P4	0.64	*P18*	0.34
P5	0.72	*P19*	0.94
P6	0.43	*P20*	0.92
P7	0.96	*P21*	0.49
P8	0.90	*P22*	1.11
P9	0.95	*P23*	1.19
P10	1.09	*P24*	1.19
P11	0.44	*P25*	1.19
P12	0.39	*P26*	1.39
P13	0.77	*P27*	1.19
P14	1.20	*P28*	1.40
P15	0.78		

Degradation concerns will be addressed through repeated I-V characterisations of some of the cells listed in Table 5.3, conducted after 10 days from initial LDS LEVA coating. This will evaluate the effectiveness of the LEVA film in extending the shelf life of CsPbI₃ PQDs. Specifically, it aims to assess film's role in shielding the PQDs from oxidation-based degradation.

Table 5.6 Electrical parameters of samples P23-P27 after fresh coating of PQDs LEVA films and 10 days later.

Samples	Electrical Parameters	Coated with PQDs by LEVA (Tier 3)	10 days later	% Change	Total % Change 10 days from Tier 2 (original state)
P23	I_{SC} (A)	0.510	0.506	(-0.78)	0.40
	P_M (W)	0.214	0.212	(-0.93)	0.00
	V_{OC} (V)	0.615	0.614	(-0.16)	0.00
P24	I_{SC} (A)	0.510	0.503	(-1.37)	(-0.20)
	P_M (W)	0.205	0.201	(-1.95)	(-0.50)
	V_{OC} (V)	0.616	0.615	(-0.16)	0.00
P25	I_{SC} (A)	0.509	0.504	(-0.98)	0.20
	P_M (W)	0.220	0.213	(-3.18)	(-3.18)
	V_{OC} (V)	0.611	0.611	0.00	0.16
P26	I_{SC} (A)	0.509	0.508	(-0.20)	1.20
	P_M (W)	0.216	0.215	(-0.46)	0.00
	V_{OC} (V)	0.614	0.612	(-0.33)	(-0.33)
P27	I_{SC} (A)	0.511	0.509	(-0.39)	0.79
	P_M (W)	0.212	0.212	0.00	1.44
	V_{OC} (V)	0.614	0.614	0.00	0.16

As demonstrated in the presented data of Table 5.6, LEVA films exhibited limitations in preserving PQDs from oxidation over extended periods. It is noteworthy that these PQDs, under typical conditions, would have undergone degradation within just two days if deposited in open air. Although their visible PL attributes endured beyond expectations, their capacity to maintain effective LDS characteristics remained, albeit to varying degrees. This is exemplified by the enhancement in I_{SC} observed in several samples, such as P26, P27, P23, and P25, showcasing total percentage increases of 1.2%, 0.79%, 0.40%, and 0.20%, respectively. Only one cell, sample P24, exhibited a reduction in I_{SC} of 0.20% after ten days of LDS LEVA coating.

5.4. Chapter Conclusion

This chapter outlined the novel use of 12 nm CsPbI₃ PQDs as an LDS material to enhance the performance of pc-Si solar cells through a novel room-temperature deposition method known as LEVA. In this chapter, 0.01 mg of the PQDs was deposited onto the surface of twenty-five 39 mm × 39 mm pc-Si solar cells, achieving a maximum increase in I_{SC} of 1.55% and an average increase of 0.93%. A maximum increase in PCE of 1.5% was also observed.

The improvement in performance is attributed to the LDS properties of the CsPbI₃ PQDs, which exhibit a PL emission peak at 690 nm when excited at 680 nm or below, down to 420 nm.

Additionally, the PQDs demonstrate anti-reflective properties, reducing diffuse reflectance by 58.2% and specular reflectance by 9.2% between 350 nm and 400 nm, with a further 64.5% reduction in diffuse reflectance between 400 nm and 930 nm.

The LEVA coating method has proven effective in utilising the LDS properties to improve pc-Si solar cell performance. This improvement is achieved through light trapping, enhanced optical coupling, and total internal reflection. However, while LEVA temporarily mitigates phase-shifting degradation due to air exposure and high encapsulation temperatures, it does not consistently protect the CsPbI₃ PQDs beyond 10 days. Therefore, to maximise the benefits of using LEVA to integrate PQDs onto pc-Si solar cells, further development is needed. This includes combining LEVA films with full encapsulation. One promising approach involves modified vacuum lamination techniques, leveraging LEVA film properties before drying to facilitate full encapsulation without high temperatures.

The advantage of using CsPbI₃ PQDs over other CsPbX₃ PQDs or QDs lies in their sharp 690 nm emission peak, a result of LDS from any absorbed excitation wavelength below 680 nm. This characteristic makes them ideal for LDS applications on pc-Si and other semiconductor solar cells. However, to fully realise their potential for enhancing pc-Si solar cells, the stability challenges must be resolved.

6. Simulation

6.1. Introduction

This chapter aims to the exploration of an effective simulation methodology that computes the LDS phenomenon and its effects on the electrical performance of pc-Si solar cells.

It will focus on the numerical modification of solar irradiance through the LDS phenomenon, facilitated by the utilisation of PA SiQDs and $CsPbI_3$ PQDs as LDS photonic enhancers for solar cells.

Simulating the LDS effect of dyes and QDs is a well-researched area, often relying on ray-tracing and optical layer interaction models [37], [131], [138], [213], [326], [327]. Ray tracing models excel in providing highly accurate representations of photonic interactions within optical layers, particularly when dealing with LDS materials of known and well-defined characteristics, such as the refractive indices and extinction coefficients of the materials, the total layer thickness, the particle volume concentration, and the average size and size distribution of the LDS particles [213].

The existing models, while valuable, encounter limitations when applied to impure materials such as the PA SiQDs discussed in Chapter 4 or materials requiring a host medium for environmental protection, as exemplified by the development of LEVA to deposit $CsPbI_3$ PQDs on pc-Si solar cells, acting as an optical host in Chapter 5.

Moreover, as detailed in Chapters 4 and 5, a range of deposition methods and encapsulation techniques were explored, resulting in different material combinations. Utilising a ray-tracing-based simulation model could introduce errors arising from these material variations, some of which might be unknown or uncontrollable. For example, while EVA was the primary encapsulant, it was applied using two different techniques, leading to varying levels of adhesion between the EVA films and the pc-Si solar cells. The transmittance results presented in Figure 5.9, Subsection 5.3.2, underscored how the innovative LEVA method led to the production of EVA films with enhanced transparency, attributed to improved adhesion. This was demonstrated by an enhanced transmittance of 90.4% achieved by a LEVA film dual glass sandwich, compared to 87% from its thermally applied EVA counterpart. This improvement, observed at maximum peaks around 600 nm, accounted for a 3.4% increase in transmittance. The improved adhesion of the glass sheets in the LEVA method resulted in a smoother surface without the bubble formation typically induced by the texturing on the surface of thermally applied EVA sheets.

Given the challenges encountered in extracting isolated ray-tracing simulations for the parameters of the employed LDS materials, a different approach was adopted involving LDS simulation models where the LDS phenomenon is mathematically represented as a macro effect. One approach involves directly modifying the incident solar irradiance to simulate the red-shifted effect induced by LDS and utilising it to model the electrical performance of solar cells [174], [191], [328]. Additionally, to create an accurate ray-tracing model capturing the optical enhancement introduced by LDS QDs, it is imperative to account for the V-shaped grooves on the pc-Si solar cells. This necessitates the development of a dedicated model tailored to represent these specific structural features on their own [329].

Given the challenges and diverse parameters involved in the project, the chosen method for simulation was the direct modification of solar irradiance. This method was preferred as it provides a more representative simulation model and allows for the direct consideration of LDS and optical enhancements induced by PA SiQDs and CsPbI$_3$ PQDs, along with their respective encapsulation methods and impurities (for PA SiQDs). This approach facilitates a comprehensive understanding of the impact of these materials on the optical and electrical performance of solar cells within the project's specific context. Hence, the aim is to validate the experimental results rather than optimise the characteristics of the LDS layer, such as thickness and concentration, or to predict an ideal one.

The approach draws substantial inspiration from the reported work of Abderrezek et al. (2013) [328]. To conduct this simulation, SCAPS-1D one-dimensional solar cell simulation software [330] was employed, which is known for its robust capabilities in solar cell performance analysis.

The subsequent sections will delve comprehensively into the adopted methodology and the underlying assumptions.

6.2. Simulation procedure

6.2.1. Simulation Methodology

The methodology outlined in the referenced work [328] relied on the mathematical integration of the LDS effect [35] produced by three distinct organic dyes (BASF Lumogen violet 570, yellow 083, and orange 240) doped within PMMA, which served as an LDS encapsulant in a simulated GaInP solar cell system and thickness computed at 3 mm. In the context of this PhD project, this approach aligns with the experimental investigations conducted on the enhancement of pc-Si solar cells through the application of PA SiQDs by DC and CsPbI$_3$ PQDs using the innovative LEVA method.

The incorporation of the LDS encapsulant PMMA in the referenced work [328] highlights how the model considers the suspension of LDS components in an optical layer. This is a critical factor in simulating the LDS effect for the used LDS QDs. As demonstrated in Chapter 4 and 5, the outcomes underscore the significance of optical hosting in optimizing the optical benefits derived from the LDS QDs. This matter will be further discussed in Chapter 7, where the impurity Naphthalene is regarded as a beneficial optical host material with characteristics comparable to those of the LEVA film.

Nevertheless, the methodology adopted in this study differs by treating the modified solar irradiance as the consequence of the LDS phenomenon facilitated by the QDs and their optical hosts as an integrated system. Consequently, the direct integration of the thickness of the LDS coating on pc-Si solar cells into the mathematical model was not pursued. Instead, adjustments to solar irradiance were implemented by integrating the LDS profiles of the liquid QD samples, specifically the PL spectra (Excitation and Emission) [327], [328], [331], into the solar irradiance spectra. This approach also assumes the cuvette's path length (1000 μm) as a multiple of the LDS coating thickness. For example, to simulate the LEVA film thickness of 240 μm on $CsPbI_3$ PQDs coated pc-Si solar cells, the concentration of the measured liquid sample would be reduced by a factor of 2.74. Theoretically, this approach accounts for uniform distribution of PQDs throughout a unit of thickness regardless of the scenario and is explained by the second assumption in subsection 6.2.2.

Subsequently, the modified AM1.5G solar irradiance data was integrated into the SCAPS-1D software, enabling the simulation of the resultant electrical enhancements exhibited by the Si solar cell model. It is important to highlight that the utilised Si solar cell model is designed to simulate a fundamental crystalline solar cell in a one-dimensional context. The focus of this model is exclusively directed towards evaluating the overall light interaction in a singular direction and potential alterations in electrical parameters. As such, the model does not explicitly account for specific factors such as surface roughness, variations within individual layers, localized points of light interaction (including internal reflection) across layers or LDS entities (i.e., LDS QDs).

Consequently, the simulation method adopted here aligns with the broader project theme, as it effectively explores the macro-scale impact of QD-induced LDS on pc-Si solar cells through the modification of solar irradiance. Further elaboration on the interplay between mathematical methodologies and the underlying assumptions can be found in subsection 6.2.2, where the relationship is elucidated.

6.2.2. Assumptions, and mathematical approaches.

The model's underlying assumptions are informed by a blend of factors encompassing the attributes of the SCAPS-1D software [330], as well as real-world measurements. SCAPS-1D functions as a solver for diverse solar cell models within a one-dimensional context. As elucidated earlier, the Si solar cell model contained within the software's library conceptualizes solar cells as unidirectional and one-dimensional layered constructs, essentially analogous to electrical sandwiches with varying electrical properties and capacitances across layers. Consequently, this perspective prioritizes electrical characteristics and omits considerations of substrate roughness and internal reflection points. However, the modified solar irradiance accounts for these effects, as the modification captures the macro-level outcomes stemming from various phenomena introduced by LDS QDs coatings, encompassing LDS, light trapping, and total internal reflection.

With this foundation, the following points are the assumptions made:

1. **First assumption** entails considering the quintessential crystalline Si solar cell model provided in SCAPS-1D under the name "example Si" as an accurate representation of the experimental pc-Si solar cells adopted throughout the project. Achieving precision in modelling each individual cell is desirable; however, practical constraints arose due to the utilisation of over a hundred pc-Si cells sourced from two different manufacturers. Additionally, the manufacturers did not provide parameters related to the physical characteristics of the cells which are essential for the simulation, including conduction band, valence band, electron and hole mobility, donor and acceptor density, etc. Consequently, characterizing these in-depth parameters proved challenging to incorporate fully into the project. Therefore, by utilising the I-V characteristics curve, the provided example was assumed to be accurately representative given the available information and constraints.

2. **Second assumption** hinges on the complete equivalence between the measured PL profiles of PA SiQDs and PQDs liquid samples and the PL profile exhibited by the LDS coated solar cells. To achieve this alignment, adjustments were made to the concentration of liquid samples to mirror that present on the enhanced solar cells. For instance, when considering 0.01 mg of PQDs applied to pc-Si solar cells measuring 39 mm × 39 mm with a host thickness of up to 240 μm (LEVA film), the concentration within the measurement cuvette was calibrated to 0.0037 mg/ml. This calibration accounted for the cubic 10 mm 10 mm × 10 mm cuvette light pathway, which is volumetrically 2.74 times larger than the

EVA film produced through the LEVA process. A parallel adjustment was also set in place for the 0.01 mg of PA SiQDs drop-casted onto pc-Si solar cells.

It is worth noting that the distribution of QDs within host materials (such as EVA or Naphthalene) diverges from their distribution in liquid solvents. Despite this, this assumption postulates a uniform distribution of LDS QDs across coated solar cells. This uniformity is assumed to extend to photon interactions, encompassing processes like absorption, emission, trapping, and reflection. Therefore, by keeping the number of PQDs consistent, it can be assumed that these optical interactions are occurring at the same rate and intensity.

By treating the PL profiles in this manner, the assumption aims to bridge the gap between dissolved and deposited states of QDs, ultimately facilitating a consistent representation of LDS effects in the simulation.

3. **Third assumption** posits complete absorption (as indicated by excitation) of incident solar irradiance [328], followed by full emission back into the solar cell with zero losses (0%) by reflection [332], refraction [333], optoelectrical losses [334], [335]. This assumption is based on the one-directional setup allowed by SCAPS-1D for illuminated and simulated cells. In this context, the cells receive solar irradiance that is already modified, inherently considering optical losses within the LDS layer, as demonstrated by the second assumption. Introducing externally calculated losses would potentially interfere with the LDS effect. Therefore, the only losses considered in this simulation are those provided by the "example Si" solar cell model on SCAPS-1D.

4. **Fourth assumption** considers the intensity of the Xenon-based light source utilised by the Edinburgh Instruments FS5 Spectrofluorometer as matching the AM1.5G solar irradiance. This correspondence is considered acceptable, given that the 150 W continuous-wave (CW) Ozone-free Xenon arc lamp consistently aligns with the AM1.5G solar irradiance. Despite not achieving a perfect overlap between both spectra, the spectrum of the light source was considered satisfactory and reported as such in the literature [336] [337].

5. **Fifth assumption** deems the temperature of the solar cells and the physical states of the QDs (regarding degradation) irrelevant for the simulated outcomes. The default testing temperature in SCAPS-1D is set to 26.85°C (300 K), while all in-lab characterisation took place at a localized 25.00°C. For the simulation, the slight difference of 1.85°C was

assumed to be acceptable, and it was not changed to keep the default material properties of the "example Si" solar cell model unchanged.

These assumptions collectively underpin the simulation's framework and allow for an exploration of the broader impacts of LDS QDs on pc-Si solar cells within a macro-scale context. Further interpretation on the relationship between mathematical methodologies and the assumptions employed is explored below.

The modified AM1.5G solar irradiance was calculated in accordance with the following equation:

$$\varphi_M = \varphi_O - \varphi_A + \varphi_E$$

<div align="right">(6-1)</div>

- $\varphi_M = Modified\ AM1.5G\ solar\ irradaiance$
- $\varphi_O = Original\ AM1.5G$
- $\varphi_A = LDS\ Absoprtion$
- $\varphi_E = LDS\ Emission$

Since it was assumed that 100% incident irradiance is absorbed and remitted by QDs [328], [334], [335], and PL was measured in true photon count, the equation can be rewritten as ratios of both:

$$\varphi_M = \varphi_O - \left(\varphi_O * \frac{\varphi_A}{\varphi_{AMax}}\right) + \left(\varphi_O * \frac{\varphi_E}{\varphi_{EMax}}\right)$$

<div align="right">(6-2)</div>

This implies that the original irradiance was gradually absorbed until reaching full absorption at the wavelength that presented with the highest absorption intensity. Areas of modification are expected to align with the PL spectra (absorption and emission) taken for both PA SiQDs and PQDs.

Example of modification of the AM1.5G solar irradiance based on the PL profile of LDS CsPbI$_3$ PQDs is shown below in Table 6.1. Figure 5.1 was used to extract absorption (solid line) and emission (dotted line) data in count per second (cps).

Following this, for the LDS PA SiQDs, the PL profile of the original batch from March 2022 was utilised for parameter extraction. This is illustrated by the red curves (both solid and dotted lines) in Figure 4.5. The reason for choosing the original PA SiQDs sample is that the pc-Si solar cell

sample with the optimum concentration of 0.01 mg, sample Q2, was enhanced using this March 2022 batch.

Table 6.1 AM1.5G Solar irradiance modification by LDS using PL profile: CsPbI₃ PQDs.

a	b	c	d	e	f	g	h	i
530	1.54E+00	1.83E+06	1.16E+07	1.57E-01	2.87E+02	2.44E+06	1.18E-04	1.30E+00
680	1.40E+00	1.59E+06		1.36E-01	2.38E+06		9.78E-01	2.57E+00

* a- Wavelength (nm), b- AM1.5G Global (Wm⁻²nm⁻¹),

c- Absorption (cps), d- Max Absorption (cps), e- Absorption ratio,

f- Emission (cps), g- Max Emission (cps), h- Emission ratio,

i- Modified AM1.5G Global (Wm⁻²nm⁻¹)

Referring to values shown in Table 6.1, the modified AM1.5G solar irradiance at 680nm is calculated as follows:

$$\varphi_M = 1.40 - \left(1.40 * \frac{1587746}{11647043}\right) + \left(1.40 * \frac{2382643}{2437113}\right) = 2.57$$

(6-3)

The example shown in equation 6-3 portrays the effects of LDS as shown by the employment of CsPbI₃ PQDs for the purpose of enhancing pc-Si solar cells by the generation of extra red photons in the visible/near-infrared (NIR) region of the visible light, which is of a heightened response by this specific type of solar cells as discussed in Chapters 1-5.

6.3.   Results and Analysis

As mentioned earlier, SCAPS-1D provides a one-dimensional approach to calculate electrical changes in solar cell models. In this context, the integration of PL profiles directly into the simulation allowed for the incorporation of the complex sum of outcomes resulting from LDS and optical enhancements brought about by the direct implementation of LDS QDs layers. This modification of the solar irradiation permitted the inclusion of optical changes within the confines of the strictly electrical Si solar cell simulation model [330], [338], [339].

The simulated electrical outcomes exhibit a remarkable concordance with the actual experimental results, as will be demonstrated below.

In line with the simulation methodology outlined in subsection 6.2.1 and assumptions in subsection 6.2.2, the AM1.5 Global solar irradiance was modified to replicate the LDS effects

induced by PA SiQDs and CsPbI$_3$ PQDs on the incident solar irradiance received by the pc-Si solar cells. As previously detailed, the assumption was made that the cells fully absorb the modified spectrum (with 0% losses), in addition to the full absorption of the irradiance by the QDs, resulting in a 100% LDS efficiency [328], [334], [335].

Based on the PL spectra of both QDs, as presented in their respective chapters, it was expected that both QDs would generate the modified profiles illustrated in Figure 6.1, in accordance with their PL behaviours. PA SiQDs were projected to modify the spectrum with nearly sharp peaks at 415 nm for absorption and 495 nm for emission. Conversely, PQDs exhibited a peak modification at 690 nm for emission and a broader profile spanning from 300 nm to 660 nm for absorption, with a significant alteration occurring between 450 nm and 660 nm.
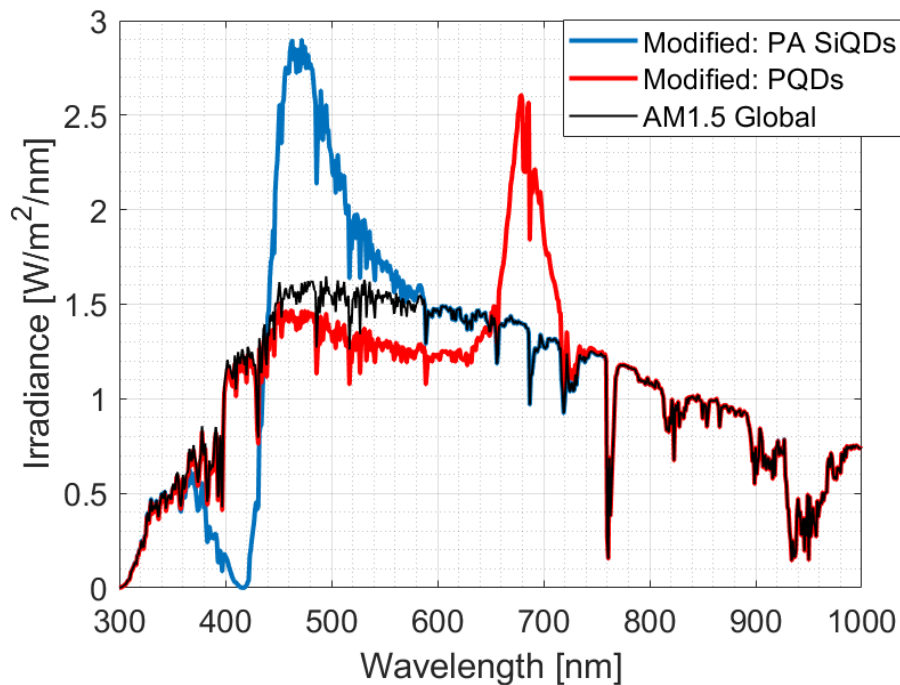
Figure 6.1 AM1.5 Global solar irradiance: Original spectrum, and modified spectra by PA SiQDs and PQDs (separately).

The J$_{SC}$ electrical parameter has been extracted from the J-V (current-voltage) characteristics for the two simulated Si solar cell samples and the best performing experimental samples Q2, P3, and P28 both before and after the application of PA SiQDs and PQDs. This is displayed in Table 6.2.

The corresponding J-V characteristics for all five samples before and after the application of QDs for LDS are presented in Figures 6.3 and 6.4.

Table 6.2 SCAPS-1D: Simulated and Real J_{SC} electrical results.

Si solar cell	Concentration (mg/ml)	Bare	LDS coated	% Increase
		J_{SC} (mA/cm²)		
PA SiQDs				
Simulated	0.01	35.762	36.173	**1.15**
Q2	0.01	31.031	31.360	**1.06**
CsPbI$_3$ PQDs				
Simulated	0.01	35.762	36.390	**1.76**
P3	0.01	33.979	34.504	**1.55**
P28	0.01	32.855	33.362	**1.40**

Table 6.2 presents results from the simulated Si solar cell model using SCAPS-1D, expressed in terms of J_{SC}. J_{SC} is a density reading that is independent of the cell area and focuses solely on irradiance intensity. Experimental results were initially obtained as I_{SC} (area-specific short circuit current) for each cell, as depicted in Table 4.1 for Q2, and Table 5.3 for P3 & P28. Subsequently, these values were converted to J_{SC} by dividing the I_{SC} by the pc-Si solar cell's area of 39 mm $\times$ 39 mm. Therefore, J_{SC} is expressed in mA/cm².

The results show a significant alignment between the simulated and experimental outcomes of best performing cells, indicating a reasonable agreement. For PA SiQDs modified AM1.5G solar irradiance, the simulated Si solar cell exhibited a 1.15% increase in J_{SC} based on a simulated LDS layer concentration of 0.01 mg/ml. This is slightly higher than the experimental sample Q2 by 0.09% (absolute percentage difference).

For PQDs modified AM1.5G solar irradiance, the simulated Si solar cell demonstrated a 1.75% increase in JSC based on a 0.01 mg/ml simulated LDS layer. This is again slightly higher than the experimental samples P3 and P28, by 0.21% and 0.36% respectively (absolute percentage difference). The increase in the simulated results can be attributed to the superior distribution of PQDs in the liquid PL sample used for irradiance modification compared to the direct results obtained from cells where, in LEVA, clustering occurs, resulting in streaks of PQDs, as observed in Figure 5.14. Other causes can be due to losses, like optical losses (reflection, escaping light by re-emission) which were not accounted for as explained by the assumptions.

The J-V characteristics curves, shown in Figures 6.3 and 6.4, visually illustrate the close agreement between the experimental and simulated samples in terms of expected electrical enhancements in the J_{SC} on each cell. This confirms the effectiveness of both the direct DC and LEVA deposition

methods in harnessing the LDS characteristics of PA SiQDs and PQDs, respectively, to enhance the electrical performance of pc-Si solar cells.

These enhancements are achieved by downshifting incident solar irradiance photons from the UV-blue region to the Vis-NIR region of the spectrum, increasing the number of photons that match the higher spectral response of pc-Si solar cells in the visible region of 450-550 nm for PA SiQDs, and the NIR region of 650-950 nm for $CsPbI_3$. This phenomenon was explained in detail in the Methodology chapter (Chapter 3) and is based on the typical spectral response of pc-Si solar cells [20], [21], [22]. The spectral response of the "example Si" solar cell is preregistered and provided by SCAPS-1D.

As expected, $CsPbI_3$ PQDs performed relatively better than SiQDs due to their more favourable LDS emission peak at 692 nm which is better absorbed by Si solar cells.

However, it is crucial to elucidate the distinctions in the form of the I-V curves between simulated ideal cells and real-life lab-measured ones, as depicted in Figures 6.3 and 6.4. The imperfections present in the Silicon used and the physical structure of pc-Si are more common when compared to its direct competitors, especially mono-Si solar cells, let alone ideal cells. This is directly caused by the manufacturing process of pc-Si solar cells, where Silicon ingots are melted together, resulting in a crystal formation with a higher defect density [340]. In contrast, the Czochralski (C.Z.) growth process is used for mono-Si solar cells, where Silicon ingots are grown into high-purity uniform crystals. Therefore, mono-Si solar cells exhibit higher quality and efficiency, as discussed in Chapter 1.

To visualize these differences, Figure 6.2 showcases an I-V curve of an ideal solar cell (red curve) and how parasitic series and shunt resistances, and characteristic defects affect its performance. With an ideal cell's I-V curve stretching towards the upper right corner of the graph, defects and errors can manifest on the curve [136]. If the upper half of the I-V curve shifts downward (as indicated by blue curve 1), this signifies a decrease in the shunt resistance (R_{Sh}) of the cell. Such a decrease can be attributed to manufacturing defects in the crystal or the cell surface, or variations in material quality and purity [341]. This results in each cell being unique and typically deviating from the ideal "example Si" cell demonstrated in simulations. A reduced R_{Sh} leads to increased surface leakage currents or junction leakage across the cell.

Conversely, a lateral shift of the curve's right side towards the left (represented by black curve 2) indicates an increase in the total series resistance (R_S) of the cell. This increase is due to cumulative ohmic resistances, including the base semiconductor material (Si), the contact resistance at the metal-semiconductor junctions on the grid fingers, the grid fingers themselves, and the busbar

resistance [341]. The combination of these factors elevates the overall resistance, a phenomenon discussed in Chapter 3 and illustrated in Figure 3.8.
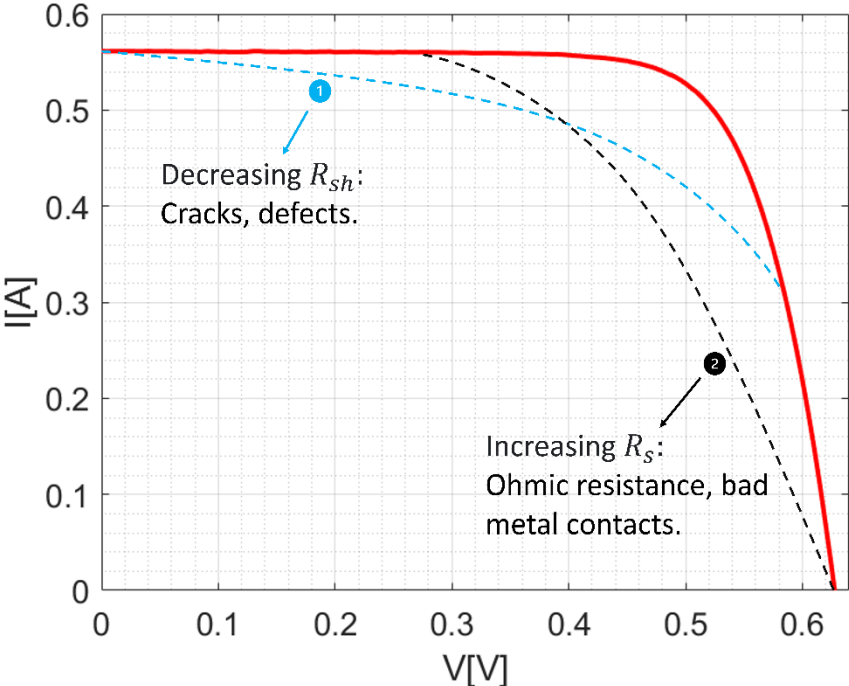
Figure 6.2 Ideal Si solar cells and physical defects: R_{Sh} and R_S.
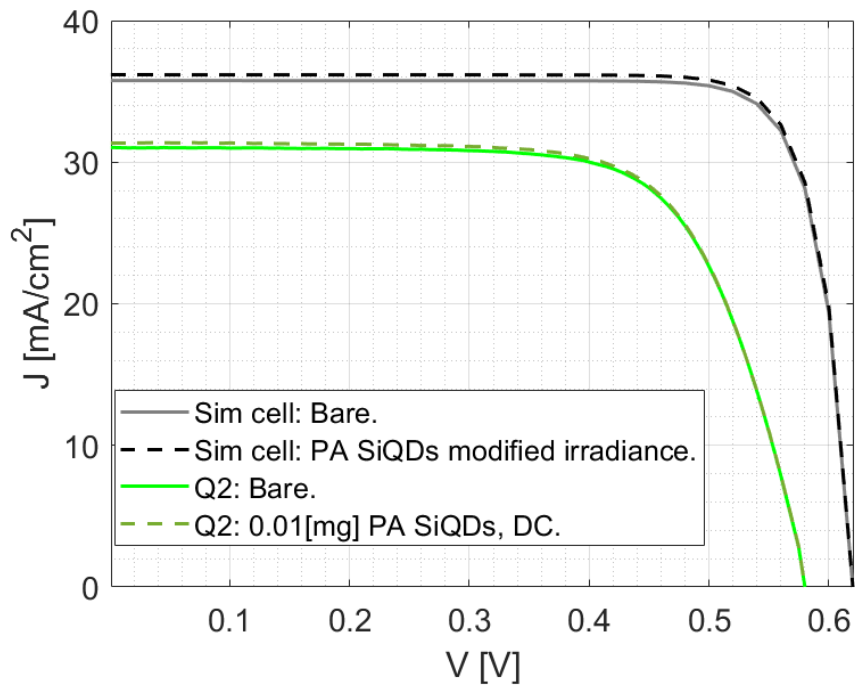
Figure 6.3 SCAPS-1D: J-V characteristic of Si simulated solar cell, sample Q2. Before (solid line) and after (dotted line) application of PA SiQDs.
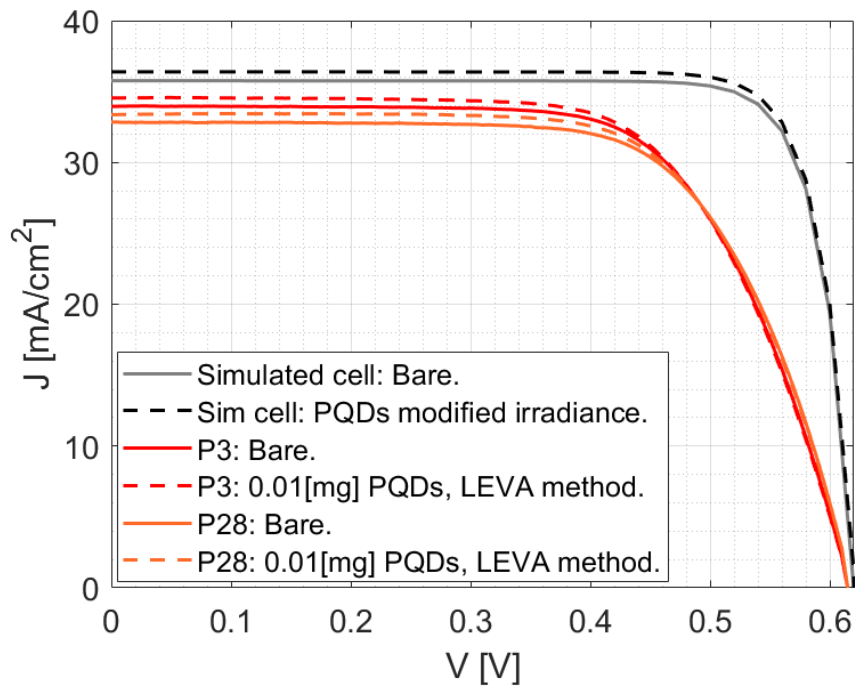
Figure 6.4 J-V characteristic of Si simulated solar cell, samples P3 and P28. Before (solid line) and after (dotted line) application of PQDs.

Patterns in electrical enhancements in both simulated Si solar cells and best performing experimental cells show further similarity in terms of V_{OC}, this is presented in Table 6.3.

Table 6.3 SCAPS-1D: Simulated and Real V_{OC} electrical results.

Si solar cell	concentration (mg/ml)	Bare	LDS coated	% Increase
PA SiQDs				
		V_{OC} (V)		
Simulated	0.01	0.620	0.621	**0.16**
Q2	0.01	0.582	0.583	**0.17**
CsPbI$_3$ PQDs				
Simulated	0.01	0.620	0.621	**0.16**
P3	0.01	0.617	0.617	**0.00**
P28	0.01	0.618	0.618	**0.00**
P25	0.01	0.610	0.611	**0.16**
P27	0.01	0.613	0.614	**0.16**

Both simulated Si solar cells demonstrated a 0.16% increase in V_{OC} due to the implementation of LDS QDs. In contrast, their experimental counterparts showed varying results, with two cases (P3, and P28) displaying no increase in V_{OC}, and the other case (Q2) exhibiting a slight increase of 0.17%.

Other samples discussed in Chapter 5, P25 & P27, related to PQDs coated pc-Si solar cells, exhibit a closer agreement with the simulated results for V_{OC}. These results offer further validation of the simulation methodology's reliability in constructing an accurate electrical model for LDS-coated Si solar cells.

The consistency between the 0.17% increase observed in experimental sample Q2 and the identical 0.16% increase observed in samples P25 and P27, when compared to the 0.16% increase in the simulated cells, provides strong evidence for the accuracy of the simulated model in predicting real-world experimental outcomes. This alignment extends to specific details and patterns of electrical enhancements, including the significant increases in J_{SC} across all cases and the relatively smaller increase in V_{OC}.

In both simulation and real experimentation, it was anticipated that the change in V_{OC} would be considerably lower than that of J_{SC} (or I_{SC}). This expectation arises from the fact that the introduction of LDS QDs as external layers on top of the pc-Si solar cells does not alter the electronic properties of the semiconducting Si or its resistive characteristics [36].

This alignment provides compelling evidence of the capacity of LDS QDs layers to enhance the performance of pc-Si solar cells through LDS and improved light trapping and improved optical

coupling. It confirms the role of LDS in increasing charge separation, which directly correlates with an increased V_{OC}.

The causes behind the unexpected increase in the V_{OC} were explored in the Literature Review subsection 2.1.4. It is stated that LDS layers not only compensate for direct optical losses, such as variations in spectral response at different wavelengths, but also mitigate other optical loss mechanisms affecting electrical performance. These mechanisms include recombination losses, increased surface reflectance, and heightened non-radiative recombination due to absorption by the ARC [36], [132]. One method of achieving this is by avoiding non-radiative exciton recombination processes [24], [133], such as Auger [134] and Shockley–Read–Hall [135] recombination. By mitigating losses through minimizing non-radiative recombination, LDS can indirectly increase the V_{OC} by enhancing the effective lifetime of the charge carriers, contributing to voltage generation.

However, it is noteworthy that previous work, reported at the beginning of the chapter and similarly utilising the modification of incident solar irradiance, presented contrasting results. One study reported that the V_{OC} remained unchanged [328], while another reported an increase of 0.32% when using 1mM of CdSe/ZnS LDS QDs [174].

Additionally, the heightened charge separation can be directly linked to the increased number of photons aligning with the higher spectral response of pc-Si solar cells in the Vis-NIR region, as well as the effects of enhanced light trapping and increased radiative recombination [180], as shown by the significantly increased J_{SC}.

6.4.   Model Accuracy and Economical Feasibility

It is important to assess how the simulated results compare to the whole array of experimental results and not only the best performing LDS coated pc-Si solar cells. To visualise that, Figure 6.5 showcases all experimentally generated electrical enhancement results for 28 pc-Si solar cells

driven by the LDS of PA SiQDs and CsPbI$_3$ PQDs, compared to their simulated counterparts, expressed as a percentage increase of the I$_{SC}$.
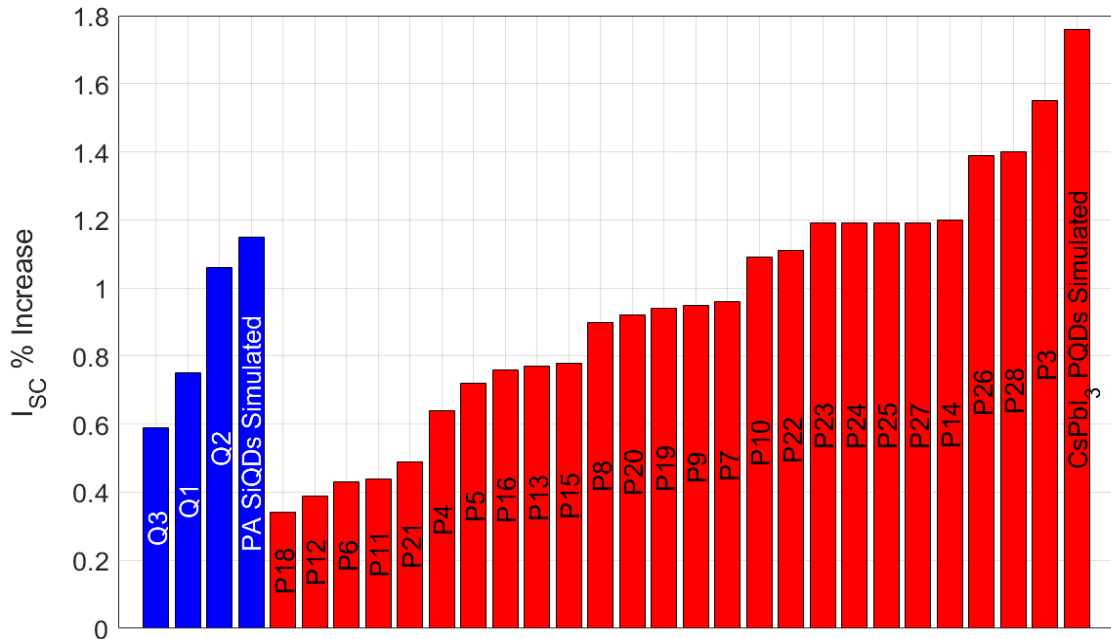
Figure 6.5 Percentage increase of I$_{SC}$ in 28 experimental pc-Si cells against their 2 simulated counterparts from the SCAPS-1D model; 3 PA SiQDs coated cells and simulated cell in <u>blue</u>, and 25+1 CsPbI$_3$ PQDs coated cells (by LEVA) and simulated in <u>red</u>.

It is noteworthy that all cells showed consistent V$_{OC}$ increases ranging from 0% to 0.17%, except for Q3, which exhibited a 0.33% decrease due to degradation in the PA SiQDs used for this sample (refer to subsection 4.3.3).

However, regarding I$_{SC}$, which is dependent on LDS, it is evident that increases in the electrical parameters varied across the samples. For PA SiQDs-coated pc-Si solar cells, the increases ranged between 0.55% and 1.06%, while for CsPbI$_3$ PQDs-coated ones (by LEVA), the range was 0.34% to 1.55%. The Relative Error (RE), based on the Absolute Error (AE), ranged from 7.83% to 48.70% for PA SiQDs-coated cells and from 11.93% to 80.68% for CsPbI$_3$ PQDs-coated cells, with Mean Absolute Error (MAE) of 0.35 and 0.84, respectively.

This indicates that the simulated results did not closely match the entire range of results for either LDS QD material.

Nevertheless, considering the highest-performing cells, the model closely matched the experimental results, with an AE of 0.21 between the simulated solar cell results for both materials and their corresponding highest-performing experimental cells: Q2 for PA SiQDs and P3 for CsPbI$_3$ PQDs, with RE of 7.83% and 11.93%, respectively. Bearing this in mind, it can be

reasonably concluded that, since the simulation model assumed no optical losses compared to those occurring in real-world experimental pc-Si cells, the simulated results likely represent the upper limit for the experimental electrical enhancements that LDS-coated pc-Si solar cells could have achieved under ideal conditions. This also concludes that while no experimental cells reached this threshold, the implemented experimental methodology successfully approached it, as evidenced by the highest-performing solar cells.

One possible reason for the model closely matching the experimental results is the alignment of the number of active LDS QDs in the liquid sample used for PL spectrometry with the number of LDS QDs deposited on the pc-Si solar cells. This created a realistic PL profile, which was directly used to produce the simulated results through SCAPS-1D. However, since SCAPS-1D is one-dimensional, it is challenging to draw definitive conclusions from it, making it important to investigate three-dimensional models that can accurately account for the optical interactions between incident light and LDS QDs, such as ray tracing.

Finally, regarding cost-effectiveness, calculating the LCOE can aid in assessing the economic feasibility of incorporating QDs as LDS devices onto commercial pc-Si solar cells. For example, with the commercial cost of acquiring $CsPbI_3$ PQDs being £3.5/mg (4.375 USD/mg), this adds £33.6 (42 USD) to an average solar panel containing 60 156 mm solar cells. The PCE of one of the coated solar cells (sample P24) was calculated at 1.5%. Assuming the current LCOE is 0.049 USD/kWh and the PQDs last for over assumed operational lifetime of a panel with no degradation, the new LCOE can be estimated at 0.07 USD/kWh. As this higher LCOE indicates, it is presently not feasible to use CsPbI3 PQDs to improve the performance of pc-Si solar cells. However, if the cost of these QDs were assumed to be negligible due to the commercialisation of the LDS material's synthesis process, the increased PCE could potentially reduce the LCOE to 0.048 USD/kWh. Thus, with a 2.1% reduction in the LCOE, it would be economically beneficial and advantageous to introduce QDs as LDS devices on commercial solar cells.

6.5.   Chapter Conclusion

To conclude this chapter, the developed simulation method has demonstrated its reliability for assessing the robustness of experimental techniques and validating the obtained results. Both simulated and laboratory-derived data have been effectively employed for mutual validation.

Nonetheless, the minor disparities between the simulated and experimental outcomes can be attributed to the assumptions made during the construction of the simulation. For example, the second assumption suggested that the distribution of QDs in solvents tends to be more uniform

than that on solar cells. This difference in uniformity may be explained by drying patterns observed in solvent-based experimental setups.

However, even with the incorporation of significant assumptions, the close alignment of real-life experimental results with the simulated model underscores the reliability of the simulation. It further reaffirms the authenticity of the experimental results obtained in the Solar Energy Lab. While ray tracing simulation models were considered, the developed experimental-numerical model employed throughout this chapter has demonstrated its robustness in representing real experimental conditions, which are otherwise difficult to quantify at the time of experimentation. The use of the Edinburgh Instruments FS5 spectrofluorometer for obtaining readings from the LDS QDs "mimicking" solutions (as detailed in the second assumption) was a significant step toward accurately modelling the LDS layer.

The agreement observed in the J_{SC} results and the notable alignment in V_{OC} measurements offer compelling evidence of the success achieved in the experimental endeavours. The investigation into the utilisation of QDs as LDS devices for enhancing the electrical performance has yielded results characterized by reliability, reproducibility, and repeatability.

7. Discussion

In this chapter, Chapter 7, the results generated in the preceding technical Chapters 4, 5, and 6 will be further discussed, connected, and analysed.

7.1. PA SiQDs and CsPbI$_3$ PQDs: Cross Comparison

The general outcome for this doctoral research supports the use of LDS QDs to electrically enhance the performance of pc-Si solar cells through optical and chemically non-altering means which was characterised by adding LDS layer on top of these cells.

The LDS PA SiQDs used in Chapter 4 exhibited a 415/495 nm excitation/emission PL profile, they still proved useful in enhancing pc-Si solar cells. This is a straightforward example of how an LDS material that has any downshifted emission wavelength that falls within the Vis-NIR region proves useful in enhancing pc-Si solar cells. The closer the emitted wavelength to the spectral response peak in near-infrared (NIR) region (850-950 nm), the more effective LDS becomes in enhancing these cells, refer to Figure 1.4. This was shown later in the following chapter, Chapter 5, which is aimed at the usage of CsPbI$_3$ PQDs that possess a higher PL LDS profile of (<680nm)/690 nm. With the presented LDS profile, it is evident that LDS CsPbI$_3$ PQDs proved to be significantly more effective than PA SiQDs in generating higher quality results, surpassing the 0.9% increase in I$_{SC}$ 62.5% of the time, compared to 20% with PA SiQDs.

However, in terms of the application of LDS coatings, CsPbI$_3$ PQDs were straightforward in concentration control compared to PA SiQDs. This discrepancy can be attributed to variations in the chemical synthesis techniques employed for both QD groups. As discussed in subsection 2.2, PQDs tend to exhibit more efficient synthesis processes, resulting in a notably purer product in comparison to SiQDs. These differences in synthesis methods and their implications were elaborated upon in Chapter 2, where various fabrication approaches for each QD group were discussed in detail.

Nonetheless, for the PA SiQDs in specific, the employed Si-halide reduction chemical method [226], [54], [96], [97] generated varied amounts of the by-product Naphthalene, which is used as a reduction agent, and allowed it to bind to the target product of PA SiQDs. The final PA SiQDs product before purification consisted of 90% Naphthalene, where 97% of that was successfully removed using a purification cycle that consisted of three thermally-dependant processes. However, subsection 4.2.2. detailed how extended exposure to high temperatures, up to 250°C,

made it challenging to quantify and measure the level of thermal degradation and determine the concentration of affected PA SiQDs.

In subsection 4.3.3, the study investigates the use of a PA SiQDs sample from the November 2022 batch, which underwent a single purification cycle, to enhance pc-Si solar cells. This sample showed improved PL properties, with an emission peak at 495 nm compared to the 447 nm peak of the March 2022 batch. Despite this improvement, a fivefold increase in sample concentration was needed to maintain sufficient electrical enhancement. This is evident when comparing samples Q4 and Q5, treated with 0.05 mg from the November 2022 batch, to Q2 and Q3, coated with 0.01 mg from the March 2022 batch. Although direct comparison is challenging due to the eight-month synthesis gap, both were expected to need similar deposition concentrations for equivalent electrical enhancement. Contrary to expectations, the November 2022 batch required a higher concentration despite its higher PL intensity and better emission peak.

The results imply that a single thermal purification cycle may degrade the PA SiQDs. This degradation wasn't clear in Figure 4.18, which compared PL of PA SiQDs after one and multiple purification cycles. However, this difference may stem from a change in the ground-state equilibrium of PA SiQDs during storage. The purification process might have accelerated environmental degradation, such as oxidation, which is generally slow, as observed in the March 2022 sample (85 days: sample Q3). Accelerated degradation likely occurred between the characterisation of liquid and solid samples, spanning a few days to up to a week.

Therefore, it is with no doubt that the purity of the acquired $CsPbI_3$ PQDs is one of biggest factors behind the multiple successful reproducible results when compared to the in-house synthesised PA SiQDs.

It is worth noting that the novel LEVA methodology was investigated as potential coating method for PA SiQDs. With its success in employing $CsPbI_3$ PQDs as LDS layer, which was resulted by hosting the PQDs in light-trapping LEVA films, LEVA was also tested to coat pc-Si solar cells with PA SiQDs.

However, results were inconclusive and showed no trend or reproducibility. This raised the question on the compatibility of LEVA with PA SiQDs, and after careful consideration it was narrowed down to two causes. First being the degradation caused by the purification cycle as only the November 2022 batch was included in these tests given that the March 2022 batch was old and unreliable at that stage of experimental work.

Consequently, LEVA's incompatibility in hosting PA SiQDs was further justified by the second cause, which is Naphthalene. It was emphasised in Chapter 5 that the LEVA generated EVA thin

film managed to effectively harvest the electrical enhancements by enhancing the optical trapping environment for the PQDs and therefore setup a fully-fledged LDS ecosystem, which was visually represented in Figure 2.5 and further explained in Figure 5.8.

Given this, it is highly probable that Naphthalene acted as an optical trapping environment for PA SiQDs, similar to the LEVA films with PQDs. This explains why the direct DC of PA SiQDs was effective, as Naphthalene suspended the QDs in a three-dimensional optical system like LEVA. In contrast, the LEVA method worked well with pure PQDs but faced difficulties with impure PA SiQDs. Naphthalene interfered optically with LEVA due to poor mixing, creating random refraction points and leading to inconclusive results.

Thus, Naphthalene, though an impurity, might have enhanced the LDS effect of PA SiQDs. However, since it was abundant and of unknown concentration in the final PA SiQDs product, it remains an impurity that must be eliminated or avoided by modifying the synthesis procedure. Theoretically, the LEVA method should enhance the LDS effect of PA SiQDs if the sample were as pure as CsPbI$_3$ PQDs. This observation forms the basis for some recommendations discussed in subsection 8.3.

Following up, Table 7.1 and 7.2 display the differences in generated electrical results by the coated pc-Si solar cells as products of using the DC/Thermal Encapsulation method and the LEVA coating method with both LDS QDs materials, the PA SiQDs or CsPbI$_3$ PQDs.

Table 7.1 Thermally Encapsulated pc-Si solar cells: LDS coating by the DC method. Soldered (Tier 2), LDS QDs Coated (Tier 3), and Thermal Encapsulation (Tier 4).

* *This % increase value is only indicative of the enhancements presented by thermal encapsulation **only** and not LDS coating.*

Samples	Electrical Parameter	Soldered Cell (Tier 2)	Coated with QDs by DC (Tier 3)	Tier 2 to Tier 3 % Increase	Encapsulated Cell (Tier 4)	Tier 2 to Tier 4 % Increase	Tier 3 to Tier 4 % Increase*
			SiQDs coated				
Q2	**I$_{SC}$ (A)**	0.472	0.477	1.06	0.528	11.86	10.69*
			PQDs coated				
P2	**I$_{SC}$ (A)**	0.536	0.481	(-10.26)	0.543	1.31	12.89*
			Thermal Encapsulation Reference Cell				
R2	**I$_{SC}$ (A)**	0.548	N/A		0.595	8.58	N/A

Table 7.2 LEVA coated pc-Si solar cells: Soldered (Tier 2), and LDS QDs coated in LEVA film (Tier 3).

Samples	Electrical Parameter	Soldered Cell (Tier 2)	LEVA coated (Tier 3)	Tier 2 to Tier 3 % Increase
PQDs coated				
P3	I_{SC} (A)	0.517	0.525	**1.55**
P26	I_{SC} (A)	0.502	0.509	**1.39**
P28	I_{SC} (A)	0.500	0.507	**1.40**
SiQDs coated				
Q6	I_{SC} (A)	0.501	0.506	**1.00**
Q6b	I_{SC} (A)	Equal to Q6: reused cell	0.502	**0.20**
Q7	I_{SC} (A)	0.499	0.500	**0.20**
LEVA Reference Cells				
R4	I_{SC} (A)	0.505	0.506	**0.20**
R5	I_{SC} (A)	0.501	0.502	**0.20**
R6	I_{SC} (A)	0.501	0.502	**0.20**

Direct DC of PA SiQDs yielded positive results, with reproducible increases in the I_{SC} of pc-Si solar cells ranging from 0.59% to 1.06%. However, this method faced challenges with $CsPbI_3$ PQDs, resulting in a significant 10.26% reduction in sample P2, primarily due to the use of a much higher 1 mg/ml concentration. Subsection 5.3.3 explains that while the optimal mass for PA SiQDs and PQDs (in LEVA) was 0.01 mg, the higher masses of 1 and 2 mg aimed to counter the rapid phase shift of $CsPbI_3$ PQDs at lower concentrations during DC deposition.

A 0.01 mg $CsPbI_3$ PQD coating deposited directly via DC degraded before I-V characterisation on the vacuum chuck. High-intensity solar simulator light may have also accelerated this phase shift. This rapid shift made DC deposition of PQDs challenging and their characterisation nearly impossible, as each cell needed roughly 20 minutes for full I-V characterisation. Additionally, higher concentrations might form radiant LDS coatings under UV light, but it does not guarantee that a portion of the PQDs does not degrade, which is unquantifiable in this case.

Moreover, it was discussed in subsection 5.3.3 how these relatively very high concentrations create a highly active LDS layer that mimics shading and significantly increases reflectance on the coated solar cells by trapping and reflecting more photons than needed, thus significantly reducing the electrical performance of the cell [157].

On the other hand, it is shown in Table 7.2 how the LEVA method was used to deposit $CsPbI_3$ PQDs in a protective and transparent host layer. Although the method was developed for the use with $CsPbI_3$ PQDs, it was also employed to be used with PA SiQDs.

Nevertheless, when the one-cycle purified November 2022 PA SiQDs sample was used in conjunction with LEVA, no consistent outcomes were observed. Instead, the results exhibited significant variations, with some solar cells demonstrating an increase in I_{SC} of nearly 0.2% and up to 0.99%, in a seemingly random and unpredictable manner. Consequently, the data collected from these trials could not yield a meaningful and conclusive outcome, except for identifying Naphthalene as a potential factor contributing to the inconsistent results. For instance, sample Q6 showcased two results, one being 0.99% increase in the I_{SC} and the other being 0.2% when redeposited (cell reused) using the same concentration. This was followed by 0.2% by sample Q7, where in all three scenarios 0.01 mg of $CsPbI_3$ PQDs was deposited in 1 ml of LEVA.

Recommendations for potential improvements in the utilisation of LEVA with PA SiQDs will be deliberated in subsection 8.3.

The LEVA method showcased an outstanding consistency in harvesting the LDS of $CsPbI_3$ PQDs, but not at all for PA SiQDs due to the Naphthalene impurity that interferes with the light trapping properties of the optical EVA host layer created by LEVA.

It is noteworthy that even after subjecting sample P2, of degraded electrical performance, to thermal encapsulation at 100°C, mimicking the standard encapsulation process performed on sample Q2, it displayed a remarkable increase caused by the optical enhancement presented by lamination layers themselves and not LDS. This I_{SC} increase for sample P2 was calculated at 12.89% and occurred between LDS coated (Tier 3) and encapsulated (Tier 4) states. For reference, sample Q2 exhibited a 10.69% increase between the same Tiers. While the primary focus is on the overall increase in the I_{SC} caused by the LDS phenomenon from the soldered state at Tier 2 to full thermal encapsulation in Tier 4, it is essential to highlight how thermal encapsulation optically aided both sample P2 and sample Q2 in this specific context.

As established in Chapter 5, it was anticipated that most of the PQDs would transition from the PL-active black α phase to an inert yellow δ phase when exposed to temperatures exceeding 80°C [295], [296], [297].

The results presented in Table 7.1 suggest that the remaining PL-active $CsPbI_3$ exhibited LDS activity within the encapsulated solar cell structure. While visually in the laboratory, the cell appeared unresponsive to UV light, the similarity of the outcomes achieved by sample P2 in this context to that of Q2 provides credible evidence of LDS activity, as observed in encapsulated Q2.

However, it was not feasible to quantify or measure PL parameters on the encapsulated P2 cell in this case since the concentration of PQDs in either phase remained unknown, and encapsulated solar cell samples are irretrievable after thermal encapsulation (lamination). PL measurements were still conducted on the solid solar cell sample P2; however, the intensity of the LDS light was too faint to be recorded.

Interestingly, the literature reports that a $CsPbI_3$ PQDs sample with a significantly higher concentration (43.25 mg/ml) required 4 hours for the PL of these QDs to decrease by 90% when exposed to a temperature of 100°C [297]. This suggests that PQDs may undergo a more prolonged phase transition under thermal influence when they are clustered together. Nonetheless, the experimental measurements were insufficient to definitively confirm this hypothesis, as a significantly lower concentration of 1 mg of $CsPbI_3$ PQDs was used on samples P2. Furthermore, as mentioned earlier, the PL measurements on sample P2 yielded no results. It is noteworthy that the duration of the thermal encapsulation process varied between 15-20 minutes per cell, ensuring no bubble formation in the EVA layer between the 3.2 mm Pilkington OptiWhite glass and the pc-Si solar cell. An illustration of the solar cell sandwich (Glass-EVA-Cell-Tedlar) resulting from the thermal encapsulation process (Tier 4) was presented in Figure 3.5.

These results underscore the distinct challenges posed by PA SiQDs and $CsPbI_3$ PQDs. PA SiQDs presented challenges related to sample purity, while $CsPbI_3$ PQDs posed challenges in safeguarding against degradative phase shifting. Despite both QD groups operating on the same underlying principles, the challenges they presented led to two different approaches for their implementation while maintaining consistent outcomes.

For PA SiQDs, achieving sample purity posed a significant challenge. The purification cycle, involving three thermal processes, notably enhanced the sample's purity by effectively removing Naphthalene, achieving a purification rate of 97%. However, challenges emerged concerning the thermal stability of these SiQDs, as prolonged exposure to high temperatures did lead to sample degradation. While the literature did not extensively mention similar issues related to LDS QDs sample purity, one of the thermal processes (rotary evaporator) within the purification cycle followed the procedures outlined in the referenced work [54], [96], [97]. This work, however, did not delve into investigating the effect of temperature on the thermal stability of PA SiQDs.

7.2. Reported vs Experimental Outcomes: Novelty, Challenges, and Solutions

The electrical enhancement results demonstrated by PA SiQDs in this PhD thesis align well with reported literature findings. The investigation took a step further by introducing thermal

encapsulation as a separate step, demonstrating the feasibility of utilising LDS QDs in a commercially reproducible and up-scalable setup. The experimental results obtained for the increase in I_{SC}, 1.06% for sample Q2 and 0.75% for sample Q1 (QD size: 6 nm), are consistent with increases reported in the literature for the use of SiQDs to enhance Si solar cells: 1.3% [53] (QD size: 6.4 nm) and 2.3% [47] (QD size: 3 nm).

Concerning CsPbI$_3$ PQDs, the challenge of safeguarding against degradative phase shifting due to exposure to air and high temperatures presented hurdles in depositing these QDs onto pc-Si solar cells followed by thermal encapsulation. The LEVA coating method protected CsPbI$_3$ PQDs from air exposure, extending the lifespan of the PL-active black α phase and enabling experimental characterisation of PQDs coated pc-Si solar cells. Chapter 5 explains how the LEVA film improves optical properties, enhancing the LDS effect through better optical coupling and light trapping.

The electrical enhancement results demonstrated by CsPbI$_3$ PQDs align well with reported literature findings, where out of the 25 generated samples, all demonstrated a positive increase in I_{SC}. Notably, the average increase was 0.93%, with 10 samples surpassing the 1% mark. In the literature, analogous CsPbCl$_3$:Mn^{2+} PQDs were reported to achieve increases of 3.42% [166], 5.10% [157], and 5.17% [211] in the I_{SC} of Si solar cells. Similarly, MAPbBr$_3$ PQDs were reported to achieve increases of 2.07% and 4.03% [26]. It is worth noting that CsPbI$_3$ PQDs were not specifically reported in the literature for LDS-only enhancement of Si solar cells through direct surface deposition. Instead, they were documented in doping hybrid-structured tandem solar cells, where they were chemically included in the cells' architecture. This approach can also apply to other analogous PQDs, as solar cell surface modification and doping to host these QDs are recommended to stabilize their photochemical and chemical characteristics [25].

While depositing CsPbI$_3$ PQDs through the LEVA method allowed for the direct harvest of PL, achieving full encapsulation of the cell in the thermal encapsulation fashion shown in PA SiQDs-coated cells while keeping the PQDs intact proved challenging. Instead, a mechanical pressure approach was tested. In this method, a freshly LEVA-coated pc-Si solar cell (LEVA film not fully dried) was pressed in a solar cell sandwich between the 3.2 mm Pilkington OptiWhite glass and Tedlar white backsheet using a clamp. The cell was then left to allow the LEVA film to dry by the evaporation of the solvent Toluene.

However, this method did not succeed in creating a fully encapsulated solar cell. Toluene's only escape path was the side of the solar cell sandwich, creating evaporation pathways that ultimately delaminated the LEVA film completely off the cell. Figure 7.1 displays the results of this mechanical encapsulation approach, showcasing full delamination that occurred first from the sides of the sandwich and then slowed down towards the centre. It is important to note that the

darker central spots may appear in full contact with the cell, but they are fully delaminated. The reason behind these spots is the slowing down of the Toluene evaporation rate at the end of the process, caused by the central force point of the clamp being in that spot. An ideal example was displayed in Figure 3.5, represented by thermal encapsulation.
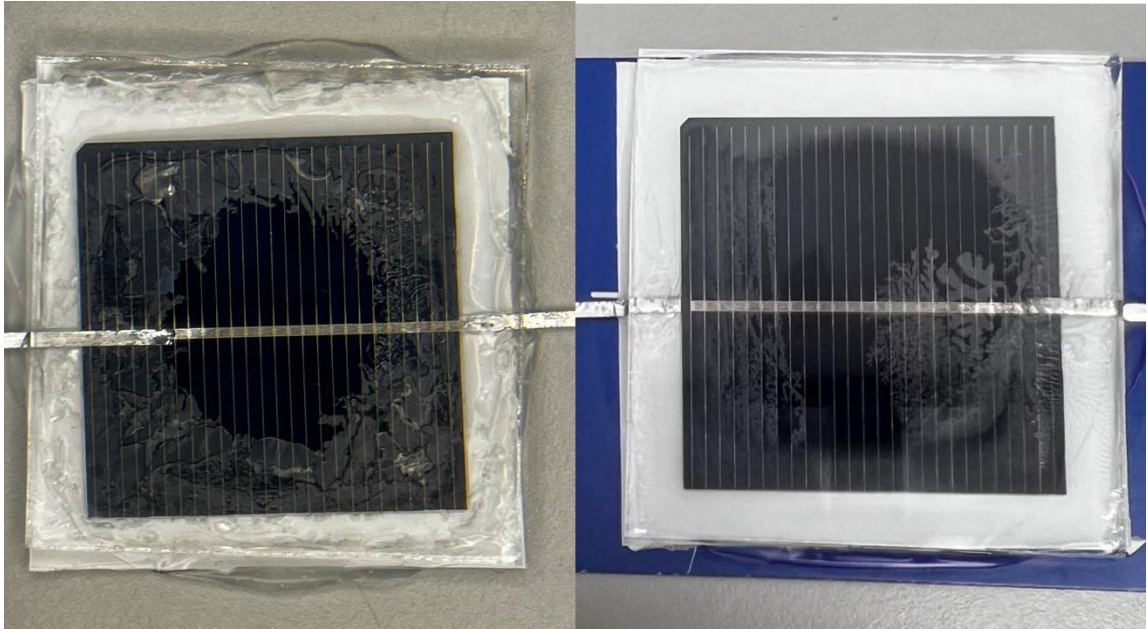
Figure 7.1 Mechanical solar cell encapsulation using LEVA as an encapsulant. Mechanical pressure applied using a clamp.

Subsection 5.2.1 detailed the application of a modified vacuum lamination process that eliminates the need for high temperatures, relying instead on vacuum pressure to create the solar cell sandwich. This method is essentially a variation of the mechanical solar cell encapsulation shown in Figure 7.1. The key difference in setting up vacuum lamination and mechanical encapsulation lies in the state of the LEVA film. Instead of using a fresh LEVA coating, an almost dry LEVA film (around 20% Toluene remaining) can be employed to hold the solar cell sandwich together through temporary adhesion. The sandwich is then processed in a vacuum laminator, where the vacuum maintains the structure while expelling Toluene. This approach was inspired by the work reported by Klampaftis et al. (2011) [184], with the main distinction being the avoidance of high temperatures, as the process in this study does not exceed 155°C. It is worth noting that the LEVA method shows similarity to the reported work by Song et al (2022) [166], but the EVA films are externally generated and applied to the outer layer of an unconventionally constructed cell sandwich, layered as Cell-Glass-Film and held together with aluminium tape with no encapsulant between the Si solar cells and glass. While it was possible to apply an external approach using the LEVA method, the focus is on investigating an alternative to thermal encapsulation. This alternative should be capable of both safeguarding the CsPbI$_3$ PQDs and maximising the optical

benefits of encapsulation. Such benefits include enhanced optical coupling and reduced refractive index mismatch between the solar cell layers and air. These enhancements are particularly pronounced when using solar glass as the top encapsulation layer. This was demonstrated in cells Q2 (LDS), R1, R2, and R3, which exhibited significant increases in I_{SC} of 11.86%, 8.26%, 8.58%, and 8.47%, respectively, as a result of thermal encapsulation with 3.2 mm Pilkington OptiWhite solar glass. While LEVA films themselves were effective in enhancing optical coupling, their impact was not as significant as that of thermal encapsulation. The limited enhancement is substantiated by the reflectance measurements presented in Figure 5.7. There, sample R6 demonstrates a reduction in reflectance, while sample P28 exhibits a further reduction, attributable to the incorporation of LDS PQDs. This observation highlights the necessity for situating LEVA films between the glass and solar cells, as opposed to their external application atop the glass, to optimise the benefits conferred by LDS.

Furthermore, with the assistance of mathematical modelling, Chapter 6 provided a simulation of results that exhibited high resemblance between the modelled and LDS-coated (Tier 3) experimental results concerning the electrical enhancements of pc-Si solar cells. These encompassed enhancements achieved through direct DC coating with PA SiQDs and via LEVA coating with $CsPbI_3$ PQDs. Although certain assumptions were made, the model validated the successful application of different QDs, accommodating their distinct characteristics.

Taking these considerations into account, it is crucial to highlight the limitations introduced by these assumptions. The five assumptions formulated for the simulation model in subsection 6.2.2 aimed to standardise the characteristics of instruments used and align obtained parameters. For example, the first assumption posited that the electrical parameters of the real and simulated Si solar cells are equal. This approach implies that the model, while not a fully comprehensive representation of the apparatus used, is accurate enough to illustrate how the optical effects introduced by the LDS QDs can enhance the electrical performance of pc-Si solar cells. It is important to note that these assumptions were necessary to address challenges related to measuring discrete parameters crucial for a more comprehensive model. Some of these challenging parameters include the refractive indices and extinction coefficients of materials, the total layer thickness, the particle volume concentration, and the average size and size distribution of the LDS particles within the layer [213].

The adopted methodology effectively addressed this gap by portraying the LDS phenomenon as a macro effect, akin to a filter, modifying the incident solar irradiance of AM1.5G. Utilising the optically-sensitive Si solar cell model "example Si" provided by SCAPS-1D [330], the extracted electrical parameters effectively capture the optical enhancements introduced by LDS. Since the

assumptions are general and do not specifically manipulate the input or output of the simulation, the results offer a relatively accurate representation of how the optical LDS phenomenon can enhance the electrical performance of Si solar cells.

It is crucial to acknowledge that the original work documented in the literature [328] and similar models [174], [191], which served as inspiration for the simulation method outlined in Chapter 6, reported more favourable results, some of which are significant. In Chapter 6, the reported increases in the I_{SC} were 1.76% and 1.15% for two simulated samples enhanced by $CsPbI_3$ PQDs and PA SiQDs, respectively. These values differ from the reported substantial increases of 13.13% on a GaInP solar cell [328] and 10% on a pc-Si solar cell [174].

This discrepancy arises from the incorporation of optoelectrical interactions within the layers of the solar cell architecture itself, including an LDS layer. This would have been feasible in this thesis if the material parameters of the experimental pc-Si solar cells were known or provided by the manufacturers. Unfortunately, this information was not available, necessitating the establishment of the first assumption, which assumed the full equivalence between the SCAPS-1D provided solar cell "example Si" and the actual pc-Si solar cells used in the experiments.

The work presented in this research delves into the innovative and novel use of PA SiQDs and $CsPbI_3$ PQDs for enhancing pc-Si solar cells through LDS. The physical and PL characteristics of these QDs differ from the average values reported in the literature. Specifically, the PA SiQDs measured 6 nm, surpassing the reported average of ~3.8 nm, while the $CsPbI_3$ PQDs were 12 nm, larger than the ~7.2 nm average. It is deduced that size is not the primary factor in choosing the right LDS QDs; rather, their quantum, PL, and surface functionalisation properties take priority. For example, PA SiQDs exhibit greater thermal stability due to PA surface capping, yet they have a lower average emission peak at 495 nm, which is 115 nm below the reported average of ~610 nm. With direct DC application, three cells demonstrated an increase in I_{SC} ranging from 0.59-1.06%. These results align with reported electrical enhancements in similar DC setups, such as ~1.3% [53], ~2.3% [47], 4-5% [49], and 6.48% [144].

Regarding the $CsPbI_3$ PQDs, they exhibited a higher emission peak at 692 nm, compared to the reported average of ~566 nm. Although this emission peak is more favourable for enhancing c-Si solar cells, these PQDs are thermally unstable and degrade rapidly under thermal encapsulation. However, the novel room-temperature LEVA coating method successfully coated pc-Si solar cells without damaging the PQDs, achieving an average increase of 0.93% and a maximum of 1.55% in I_{SC}. Literature reports similar increases with $CsPbCl_3:Mn^{2+}$ PQDs, achieving 3.42% [166], 5.10% [157], and 5.17% [211] in the I_{SC} of Si solar cells. In comparison, $MAPbBr_3$ PQDs reported increases of 2.07% and 4.03% [26].

Furthermore, the significance of the synergistic relationship between encapsulation and the LDS phenomenon deserves emphasis. This combined effect was evident in the thermally encapsulated pc-Si solar cell sample Q2 and its reference counterparts. Notably, the expected average increase of 8.44% in the I_{SC} due to encapsulation was further enhanced to 11.86% with the addition of LDS using PA SiQDs. A similar trend was observed in cells coated with $CsPbI_3$ PQDs using the LEVA method, where reference samples exhibited an average I_{SC} increase of 0.2%, whereas those with LDS coating achieved an average of 0.93%.

In terms of reflectance, both types of LDS QDs demonstrated comparable effects. Samples coated with PA SiQDs using DC showed a remarkable decrease in reflectance, with a 61.8% reduction in specular reflectance and a 44.4% reduction in diffuse reflectance at 377 nm. Likewise, $CsPbI_3$ PQDs LEVA coated cells displayed a 63.7% decrease in diffuse reflectance and a 22% decrease in specular reflectance at the same wavelength. These findings align with previously documented research, which reported similar decreases in reflectance within the 350-450 nm, which is the typical target absorption range for LDS materials chosen to enhance c-Si solar cells. Such reductions, typically observed when SiQDs and PQDs are used to enhance the efficiency of Si solar cells through LDS, are attributed to the effective implementation of LDS [144], [162], [214]. Prior studies have recorded a dominant decrease of approximately 20% in reflectance between 300-400 nm [50], around 33% at 370 nm [47], and an 8.5% reduction between 360-370 nm [210].

Conversely, for both PA SiQDs and $CsPbI_3$ PQDs, an increase in reflectance was observed in the 480-660 nm range. This finding aligns with prior research, which has identified similar increases in the 400-650 nm spectrum [50]. These results are consistent with well-documented trends in the literature regarding the use of LDS materials for enhancing c-Si solar cells' efficiency. Specifically, increases in reflectance have been observed in the broader range of approximately 450-700 nm. Researchers attribute these changes in reflectance to the effective implementation of LDS, a correlation that has been consistently reported across studies [26], [157], [166], [212].

Concluding this chapter, it further discussed, connected, and analysed the results presented in Chapters 4, 5, and 6. Additionally, it laid the groundwork for future work and recommendations aimed at extending the scope of this research. These recommendations will be detailed and explained in the subsequent and final chapter, Chapter 8, which focuses on Conclusion and Future Work.

8. Conclusion, and Future Work

Chapter 8 concludes the doctoral research presented in this thesis and outlines the major findings and recommendations for future work.

8.1. General Conclusion

The primary focus of the PhD thesis revolved around investigating the use of LDS PA SiQDs and $CsPbI_3$ PQDs in enhancing the electrical performance of 39×39 mm pc-Si solar cells. This was achieved through the direct deposition and implementation of LDS PA SiQDs and $CsPbI_3$ PQDs onto the surface of these solar cells, creating active optical enhancement layers. Importantly, this process did not involve any chemical alterations to the cells themselves.

By carefully controlling the concentration of deposited QDs, it was possible to demonstrate the optimal concentrations for enhancing electrical performance. The research revealed that the ideal mass for depositing PA SiQDs and $CsPbI_3$ PQDs was 0.01 mg.

Scalable deposition methodologies, including direct DC and the innovative LEVA approach, were thoroughly explored. Both methods successfully achieved reproducible electrical enhancements while addressing the purity and stability challenges specific to their respective LDS QD materials.

This project introduces a novel approach by investigating PA SiQDs as LDS electrical enhancement devices through direct deposition on pc-Si solar cells using the DC method. The study also effectively addressed scalability and demonstrated commercial viability by thermally encapsulating pc-Si solar cells in an industry-standard process.

The project further breaks new ground by exploring $CsPbI_3$ PQDs as an externally applied LDS layer on pc-Si solar cells at room temperature. Based on the literature, this specific application had not been previously examined, as most research focuses on tandem solar cell architecture or LED applications. The LEVA coating methodology enabled the reliable and reproducible enhancement of electrical performance while protecting the PQDs from rapid phase shifting (degradation) due to exposure to air and light.

Reflectance measurements demonstrated significant reductions in specular and diffuse reflectance for both QD types, confirming the LDS effect. PA SiQDs reduced specular reflectance by 75.7% and diffuse reflectance by 43.1% between 350 nm and 450 nm. $CsPbI_3$ PQDs achieved reductions in diffuse reflectance by 58.2% and specular reflectance by 9.2% between 350 nm and 400 nm, with a 64.5% reduction in diffuse reflectance between 400 nm and 930 nm.

By successfully reproducing results using both PA SiQDs and CsPbI$_3$ PQDs, while considering the different setups and approaches, the set of objectives was effectively achieved. This demonstrated the controlled implementation, engineering, and optimization of the optical LDS phenomenon facilitated by these QDs and their and their potential for electrical enhancement through the introduction of the LDS phenomenon in pc-Si solar cells.

8.2. Major Findings

The major findings of this thesis can be concisely summarized as follows:

1. **Successful demonstration of consistent and reproducible electrical enhancements in pc-Si solar cells using the optical LDS phenomenon offered by PA SiQDs and CsPbI$_3$ PQDs.**

The work presented in Chapters 4 and 5 showcases the precise control of electrical enhancements in pc-Si solar cells through the strategic implementation of LDS QDs at specific concentrations and via reliable methods. The optimal deposition concentration of QDs was determined to be 0.01 mg/ml, ensuring the most significant electrical enhancements when 1 ml of the QD mixture was applied to the commercial pc-Si solar cells.

In Chapter 4, applying PA SiQDs via direct DC to three cells achieved an increase in the I$_{SC}$ by 0.59-1.06%. Challenges in replicating experiments with PA SiQDs, due to Naphthalene content, were mitigated by a purification cycle, which removed 97% of Naphthalene but caused thermal degradation. Still, a fivefold increase in concentration led to a 0.40-0.78% rise in I$_{SC}$, with further discussion in subsection 8.3.

Chapter 5 investigated the application of 100% pure LDS CsPbI$_3$ PQDs for the efficiency enhancements of pc-Si solar cells, for the first time. Using a room-temperature novel LEVA method, a deposition of 0.01 mg/ml concentration resulted in a maximum I$_{SC}$ improvement of 1.55% across twenty-five pc-Si solar cells, with an overall average increase of 0.93%, where 10 samples exceeded the 1% mark.

2. **Demonstration of an LDS-based thermal encapsulation process that is suitable for commercial scaling.**

Chapter 4 involved the lamination of PA SiQDs coated pc-Si solar cells into a solar cell sandwich using a thermal encapsulation process, as illustrated in Figure 3.5. This encapsulation process emulates the method employed in the commercial production of final solar panel products. It serves as an essential evaluation of the potential for upscaling the implementation of LDS QDs in the existing solar cell industry.

For reference purposes, samples denoted as R1, R2, and R3 were created to highlight the successful integration of PA SiQDs into a downscaled, commercially mimicking pc-Si solar cell sandwich. This was proved by the 11.86% increase in the I_{SC} of sample Q2, versus 8.44% for reference samples.

Findings underscore the undeniable potential for introducing enhancing LDS QDs into existing high-temperature commercial production lines.

Regarding degradation, sample Q2, characterised via I-V measurements 74 and 91 days post thermal encapsulation, exhibited a consistent drop of 0.19% in both instances. This suggests that the encapsulation effectively prolonged the shelf life and stabilised the deposited PA SiQDs, despite repeated exposures to the 1000 W/m^2 solar light simulator or storage in open-air.

For reference, encapsulation of solar cells and modules is an ongoing research field that focuses on researching protective materials that also further enhance the electrical properties of the cells and modules especially when considering Cell-to-Module losses [342], [343].

3. **Development of an innovative coating method that is both protective and enhances the optical performance of LDS CsPbI$_3$ PQDs.**

The LEVA film prevented the phase shift (degradation) of the PQDs from their PL-active black α phase to an inert yellow δ phase. It achieved this by avoiding thermal encapsulation and direct exposure to air, which is known to induce phase shifting. Additionally, the LEVA film enhanced the optical performance of the LDS PQDs by improving their light trapping capabilities. This optical enhancement was instrumental in harnessing the electrically enhancing potential of these PQDs.

The LEVA method was devised as a solution to the limitations encountered with the DC method, where PQDs rapidly underwent phase shifting when exposed to air, especially at the low but optimal deposition concentration of 0.01 mg. Higher concentrations were unsuccessful in preventing rapid air-induced phase shifting and made it challenging to determine the exact quantity of LDS-active PQDs. The LEVA method addressed these issues by maintaining a constant amount of LDS-active PQDs. While there is no exact mention of this specific issue in the literature, similar approaches have been employed to address similar challenges with analogous PQDs by incorporating them directly into encapsulants but mixed at relatively high temperatures [166], [212].

Although the LEVA method initially protected CsPbI$_3$ PQDs from immediate phase shifting upon air exposure, this protection lasted only a few days. Subsequently, the coated cells demonstrated

a notable performance decline and the PQDs ceased to illuminate under UV light (almost entirely). Table 5.6 presents this effect, showing an average 0.74% reduction in the I_{SC} of 5 cells, 10 days after the LDS LEVA coating.

4. **Sufficient evidence provided to support that the electrical enhancements facilitated by optically active QDs are driven by LDS, as demonstrated using the SCHOTT BG42 bandpass filter for PA SiQDs and the LEVA method for CsPbI₃ PQDs, and simulation.**

The improved light trapping observed in LDS coated pc-Si solar cells plays a significant role in the electrical enhancements achieved. To comprehend this phenomenon, it is essential to visualize the LDS coatings as a three-dimensional layer in which QDs are suspended at various depths and in different cluster formations. Moreover, even distribution of QDs throughout this layer is crucial. In this thesis, it was established that LDS coatings enhance the electrical performance of Si-based solar cells by optically downshifting photons from the blue region of the solar spectrum to red photons, where the cells exhibit higher spectral response. This improved overall spectral response leads to more efficient photon absorption and increased photocurrent generation (measured by the I_{SC}).

The efficiency of this optical ecosystem benefits from the complexity of QD dispersion within the layer. The QDs act as "focal points" that trap photons within the cells, especially at greater depths within the layer. This light trapping effect is achieved through the isotropic reemission of LDS QDs, where a photon that is outwardly reflected by the cell surface has a chance of being re-emitted back towards the cell if reabsorbed by a QD on the way out of the LDS layer. Consequently, evenly dispersing QD suspensions within an LDS layer significantly enhances light trapping in coated cells.

To further confirm that the observed light trapping is indeed a result of LDS, rather than Rayleigh scattering, a different approach was taken for each material: PA SiQDs and CsPbI₃ PQDs.

In the case of PA SiQDs, as detailed in Chapter 4, there was some challenges introduced by the presence of Naphthalene as an impurity, where it persisted to stay even after exhaustive purification cycles. Chapter 7 suggested that Naphthalene might have contributed to the enhanced QD performance by potentially acting as a host layer. To ensure that the light trapping was LDS-induced, the cells in this chapter, including reference cells, underwent I-V characterisation under a blue bandpass filter, SCHOTT BG42. Using this filter specifically isolates the impact of PA SiQDs on pc-Si solar cells, focusing on their LDS characteristics. It attenuates solar radiation at 377 nm, where a notable reflectance drop was observed (Figure 4.7), while permitting more of the

excitation wavelength for LDS. This approach tests the effectiveness of PA SiQDs in enhancing pc-Si solar cell performance through LDS. This was further explained in subsection 4.3.3.2. The results revealed that the encapsulated sample Q2 (0.01 mg PA SiQDs) displayed a 13.68% increase in I_{SC} compared to reference sample R1, which showed an increase of 11.57%.

The validation process for $CsPbI_3$ PQDs was more straightforward. These PQDs were 100% pure, allowing for a direct comparison between LEVA reference pc-Si solar cells and PQDs LEVA cells. Both sets of cells were coated with the same LEVA film in terms of thickness and material quantity. Any disparities in results could therefore be attributed to the presence or absence of LDS $CsPbI_3$ PQDs. Chapter 5 showed that three reference samples (R4, R5, and R6) exhibited an average I_{SC} increase of 0.2%, while twenty-five PQDs-coated cells achieved an average I_{SC} increase of 0.93%. with the highest-performing cells, P3 and P28, demonstrating 1.55% and 1.40% increases respectively.

8.3. Future Work and Recommendations

Here, a set of recommendations, based on this doctoral thesis, are presented to establish the basis of future research beyond this thesis on the topic of LDS SiQDs and PQDs for performance enhancement of pc-Si solar cells.

1. Improving the synthesis of PA SiQDs to produce a pure sample.

Since the amount of Naphthalene present in the synthesised PA SiQDs samples was unknown, it is recommended to separate the two by improvising a synthesis method that produces pure PA SiQDs samples.

A starting point would be improving on current post-synthesis purification thermal processes such as vacuum-assisted rotary evaporator (rotavapor) which uses damage-free temperatures of below 100°C (safe for PA SiQDs). Improvising the process can be by using a lower partial pressure (below 200 mbar) and the increasing the operation time to allow for as much Naphthalene as possible to be extracted.

Other recommended method would be based on particle size and molecular weight, such as molecular weight cut off (MWCO) where the PA SiQDs will be filtered out of the final sample containing impurities.

Continuing with this line of investigation, upon obtaining a pure sample of PA SiQDs, the systematic addition of Naphthalene can be carried out and examined as an optical host. This approach serves to complement the following recommendation provided in this subsection and

addresses the uncertainty introduced by Naphthalene when present as an impurity of unknown concentration.

2. **Explore the employment of Naphthalene as an optical host layer.**

As discussed in Chapter 7, it is deductible that the direct DC method worked with PA SiQDs and not PQDs due to the presence of Naphthalene. Which hosted the PA SiQDs just like the LEVA film did with the pure CsPbI$_3$ PQDs sample. Therefore, it can be safely assumed that the presence of this impurity was vital for the harvesting of LDS from the PA SiQDs. Hence, further optical analysis is recommended to understand the benefit and the possibility of using Naphthalene as a host for LDS QDs, which also could potentially allow testing the DC method with CsPbI$_3$ PQDs at low concentrations by hosting them in Naphthalene instead of LEVA.

Exploration of the optical benefits and mechanisms in Naphthalene, LEVA, and thermal encapsulation (EVA and solar glass) is recommended through ray-tracing simulations [37], [138], [326], [327] and the methodology set for experimental work for this thesis. With the systematic and methodical addition of these optical hosts to pure LDS QDs coatings, the enhanced light trapping can be quantified and further investigated.

3. **Advance the LEVA method to include full solar cell encapsulation.**

By employing a heat-less modified vacuum lamination process, it is feasible to enhance the LEVA method for full solar cell encapsulation, similar to the thermal encapsulation process.

This involves wetting the surface of a dry LEVA-coated cell with Toluene. Afterward, the treated cell is placed within a solar cell sandwich structure inside a heat-less vacuum lamination process that aids the slow extraction of Toluene. This was inspired by the literature [184] where the vacuum lamination process originally reached temperatures of 155°C.

The tiny amount of Toluene serves to facilitate the adherence of the LEVA film to the frontal solar glass. Meanwhile, the vacuum laminator ensures an even distribution of force and, importantly, promotes the complete evaporation of Toluene. The end result is an encapsulated pc-Si solar cell, and notably, this entire process is accomplished without the application of heat.

4. **Exploration of different commercially available LDS QDs.**

Having effectively employed PA SiQDs and CsPbI$_3$ PQDs to enhance the electrical performance of pc-Si solar cells, it is advisable to consider exploring alternative LDS QDs with desirable traits like heat resistance, high purity, and red LDS emission.

Immediate suggestion for PQDs would be the use of analogous forms, such as $CsPbCl_3:Mn^{2+}$ PQDs [157], [166], [211], and $MAPbBr_3$ PQDs [26] which showcased better resistant to higher temperatures close to the thermal encapsulation temperatures.

As for PA SiQDs, the immediate suggestion would be investigating synthesis processes that produce pure forms of SiQDs, such as electrochemical etching and laser ablation [98], [107].

Furthermore, it is recommended to conduct further investigations involving different variants of SiQDs and PQDs. This expanded research scope can potentially unveil both the advantages and limitations of PA SiQDs and $CsPbI_3$ PQDs, contributing to a more comprehensive understanding of these materials especially for the enhancement of pc-Si solar cells.

5. Long-term planned degradation measurements.

Although short-term degradation results were presented in Chapters 4 and 5, it is advisable to conduct comprehensive degradation experiments encompassing a range of parameters as stipulated by the IEC 61215 and 61646 standards. These parameters include but are not limited to light soaking, UV preconditioning, outdoor exposure, thermal cycling, humidity-freeze, delamination, and more.

An optimal setup would investigate long term degradation on PA SiQDs thermally encapsulated and $CsPbI_3$ PQDs LEVA coated pc-Si solar cells and in different environmental conditions as follows:

a. In normal storage conditions; dark, room-temperature, and open to air.
b. Outdoor storage in enclosed transparent compartments in several testing conditions: dry, dry UV protected, moist (allowing full cycles from evaporation to condensation) and shaded from direct sunlight.
c. Light-soaking according to IEC 61215 and 61646 standards.
d. Delamination according to IEC 61215 and 61646 standards.

Further aspects can be also tested, but these conditions are specifically recommended to investigate the resistance and stability of the LDS QDs in different scenarios, and the longevity of encapsulants.

6. Investigation of three-dimensional simulation models.

Investigating three-dimensional models is crucial, as they can accurately account for the optical interactions between incident light and LDS QDs, such as ray tracing. As shown in Chapter 6, While the alignment of active LDS QDs in the liquid sample used for PL spectrometry with those

deposited on pc-Si solar cells produced a realistic PL profile for SCAPS-1D simulations, the one-dimensional nature of SCAPS-1D has inherent limitations. Thus, it is essential to explore three-dimensional models that provide a comprehensive understanding of light interactions with LDS QDs.

References

[1]   IEA, 'Renewables Information: Overview, IEA, Paris'. Accessed: Sep. 05, 2023. [Online]. Available: https://www.iea.org/reports/renewables-information-overview/supply

[2]   Fraunhofer Institute for Solar Energy Systems, 'Photovoltaics Report', Freiburg, Feb. 2023. Accessed: Sep. 06, 2023. [Online]. Available: https://www.ise.fraunhofer.de/content/dam/ise/de/documents/publications/studies/Photovoltaics-Report.pdf

[3]   SolarPower Europe, 'Global cumulative installed solar PV capacity 2019 | Statista', Global Market Outlook for Solar Power 2020-2024. Accessed: Sep. 06, 2021. [Online]. Available: https://www.statista.com/statistics/280220/global-cumulative-installed-solar-pv-capacity/

[4]   IRENA, 'Renewable Power Generation Costs in 2022', Abu Dhabi., 2022. Accessed: Sep. 06, 2023. [Online]. Available: https://www.irena.org/Publications/2023/Aug/Renewable-Power-Generation-Costs-in-2022

[5]   LONGi, 'At 26.81%, LONGi sets a new world record efficiency for silicon solar cells'. Accessed: Nov. 17, 2023. [Online]. Available: https://www.longi.com/en/news/propelling-the-transformation/

[6]   M. A. Green *et al.*, 'Solar cell efficiency tables (version 62)', *Progress in Photovoltaics: Research and Applications*, vol. 31, no. 7, pp. 651–663, Jul. 2023, doi: 10.1002/pip.3726.

[7]   M. A. Green, E. D. Dunlop, J. Hohl-Ebinger, M. Yoshita, N. Kopidakis, and X. Hao, 'Solar cell efficiency tables (Version 58)', *Progress in Photovoltaics: Research and Applications*, vol. 29, no. 7, pp. 657–667, Jul. 2021, doi: 10.1002/pip.3444.

[8]   M. A. Green *et al.*, 'Solar cell efficiency tables (Version 61)', *Progress in Photovoltaics: Research and Applications*, vol. 31, no. 1, pp. 3–16, Jan. 2023, doi: 10.1002/pip.3646.

[9]   M. A. Green *et al.*, 'Solar cell efficiency tables (Version 60)', *Progress in Photovoltaics: Research and Applications*, vol. 30, no. 7, pp. 687–701, Jul. 2022, doi: 10.1002/pip.3595.

[10]   M. A. Green *et al.*, 'Solar cell efficiency tables (Version 53)', *Progress in Photovoltaics: Research and Applications*, vol. 27, no. 1, pp. 3–12, Jan. 2019, doi: 10.1002/pip.3102.

[11]   M. A. Green, E. D. Dunlop, D. H. Levi, J. Hohl-Ebinger, M. Yoshita, and A. W. Y. Ho-Baillie, 'Solar cell efficiency tables (version 54)', *Progress in Photovoltaics: Research and Applications*, vol. 27, no. 7, pp. 565–575, Jul. 2019, doi: 10.1002/pip.3171.

[12]   M. A. Green, E. D. Dunlop, J. Hohl-Ebinger, M. Yoshita, N. Kopidakis, and A. W. Y. Ho-Baillie, 'Solar cell efficiency tables (Version 55)', *Progress in Photovoltaics: Research and Applications*, vol. 28, no. 1, pp. 3–15, Jan. 2020, doi: 10.1002/pip.3228.

[13]   M. A. Green, E. D. Dunlop, J. Hohl-Ebinger, M. Yoshita, N. Kopidakis, and X. Hao, 'Solar cell efficiency tables (version 56)', *Progress in Photovoltaics: Research and Applications*, vol. 28, no. 7, pp. 629–638, Jul. 2020, doi: 10.1002/pip.3303.

References

[14] M. Green, E. Dunlop, J. Hohl-Ebinger, M. Yoshita, N. Kopidakis, and X. Hao, 'Solar cell efficiency tables (version 57)', *Progress in Photovoltaics: Research and Applications*, vol. 29, no. 1, pp. 3–15, Jan. 2021, doi: 10.1002/pip.3371.

[15] M. A. Green, Y. Hishikawa, E. D. Dunlop, D. H. Levi, J. Hohl-Ebinger, and A. W. Y. Ho-Baillie, 'Solar cell efficiency tables (version 52)', *Progress in Photovoltaics: Research and Applications*, vol. 26, no. 7, pp. 427–436, Jul. 2018, doi: 10.1002/pip.3040.

[16] R. Van Overstraeten, 'CRYSTALLINE SILICON SOLAR CELLS FOR ONE SUN UTILISATION', in *Energy and the Environment*, Elsevier, 1990, pp. 104–111. doi: 10.1016/B978-0-08-037539-7.50013-2.

[17] M. A. Green, 'Materials for solar cells', *Materials for Energy Conversion Devices: A Volume in Woodhead Publishing Series in Electronic and Optical Materials*, pp. 3–34, Jan. 2005, doi: 10.1533/9781845690915.1.3.

[18] NREL, 'Best Research-Cell Efficiency Chart. Photovoltaic Research'. Accessed: Sep. 10, 2023. [Online]. Available: https://www.nrel.gov/pv/cell-efficiency.html

[19] M. A. Green, K. Emery, Y. Hishikawa, W. Warta, and E. D. Dunlop, 'Solar cell efficiency tables (version 48)', *Progress in Photovoltaics: Research and Applications*, vol. 24, no. 7, pp. 905–913, Jul. 2016, doi: 10.1002/pip.2788.

[20] H. Wirth, 'Crystalline Silicon PV Module Technology', in *Semiconductors and Semimetals*, vol. 89, Elsevier, 2013, pp. 135–197. doi: 10.1016/B978-0-12-381343-5.00003-3.

[21] M. Alonso-Abella, F. Chenlo, G. Nofuentes, and M. Torres-Ramírez, 'Analysis of spectral effects on the energy yield of different PV (photovoltaic) technologies: The case of four specific sites', *Energy*, vol. 67, pp. 435–443, Apr. 2014, doi: 10.1016/j.energy.2014.01.024.

[22] M. Aminul Islam, N. M. Kassim, A. Ahmed Alkahtani, and N. Amin, 'Assessing the Impact of Spectral Irradiance on the Performance of Different Photovoltaic Technologies', in *Solar Radiation - Measurement, Modeling and Forecasting Techniques for Photovoltaic Solar Energy Applications*, IntechOpen, 2022. doi: 10.5772/intechopen.96697.

[23] J. M. Nunzi, 'Requirements for a rectifying antenna solar cell technology', in *Nanophotonics III*, D. L. Andrews, J.-M. Nunzi, and A. Ostendorf, Eds., SPIE, Apr. 2010, p. 771204. doi: 10.1117/12.855825.

[24] B. McKenna and R. C. Evans, 'Towards Efficient Spectral Converters through Materials Design for Luminescent Solar Devices', *Advanced Materials*, vol. 29, no. 28, p. 1606491, Jul. 2017, doi: 10.1002/adma.201606491.

[25] A. S. Sadhu, Y.-M. Huang, L.-Y. Chen, H.-C. Kuo, and C.-C. Lin, 'Recent Advances in Colloidal Quantum Dots or Perovskite Quantum Dots as a Luminescent Downshifting Layer Embedded on Solar Cells', *Nanomaterials*, vol. 12, no. 6, p. 985, Mar. 2022, doi: 10.3390/nano12060985.

[26] L. Meng *et al.*, 'Improving the efficiency of silicon solar cells using *in situ* fabricated perovskite quantum dots as luminescence downshifting materials', *Nanophotonics*, vol. 9, no. 1, pp. 93–100, Jan. 2020, doi: 10.1515/nanoph-2019-0320.

References

[27]   D. L. Dexter, 'Possibility of Luminescent Quantum Yields Greater than Unity', *Physical Review*, vol. 108, no. 3, pp. 630–633, Nov. 1957, doi: 10.1103/PhysRev.108.630.

[28]   M. B. De la Mora, O. Amelines-Sarria, B. M. Monroy, C. D. Hernández-Pérez, and J. E. Lugo, 'Materials for downconversion in solar cells: Perspectives and challenges', *Solar Energy Materials and Solar Cells*, vol. 165, pp. 59–71, Jun. 2017, doi: 10.1016/j.solmat.2017.02.016.

[29]   J.-C. G. Bünzli and A.-S. Chauvin, 'Lanthanides in Solar Energy Conversion', in *Handbook on the Physics and Chemistry of Rare Earths*, vol. 44, Elsevier, 2014, pp. 169–281. doi: 10.1016/B978-0-444-62711-7.00261-9.

[30]   R. H. Bartram and A. Lempicki, 'Electron multiplication in scintillators and phosphors', *J Lumin*, vol. 72–74, pp. 734–736, Jun. 1997, doi: 10.1016/S0022-2313(97)80791-0.

[31]   C. Ronda, 'Luminescent materials with quantum efficiency larger than 1, status and prospects', *J Lumin*, vol. 100, no. 1–4, pp. 301–305, Dec. 2002, doi: 10.1016/S0022-2313(02)00456-8.

[32]   B. S. Richards, 'Luminescent layers for enhanced silicon solar cell performance: Down-conversion', *Solar Energy Materials and Solar Cells*, vol. 90, no. 9, pp. 1189–1207, May 2006, doi: 10.1016/j.solmat.2005.07.001.

[33]   A. Shalav, B. S. Richards, and M. A. Green, 'Luminescent layers for enhanced silicon solar cell performance: Up-conversion', *Solar Energy Materials and Solar Cells*, vol. 91, no. 9, pp. 829–842, May 2007, doi: 10.1016/j.solmat.2007.02.007.

[34]   H. Ahmed, S. J. McCormack, and J. Doran, 'External Quantum Efficiency Improvement with Luminescent Downshifting Layers: Experimental and Modelling', *Int J Spectrosc*, vol. 2016, pp. 1–7, Jan. 2016, doi: 10.1155/2016/8543475.

[35]   H. J. Hovel, R. T. Hodgson, and J. M. Woodall, 'The effect of fluorescent wavelength shifting on solar cell spectral response', *Solar Energy Materials*, vol. 2, no. 1, pp. 19–29, Sep. 1979, doi: 10.1016/0165-1633(79)90027-3.

[36]   E. Klampaftis, D. Ross, K. R. McIntosh, and B. S. Richards, 'Enhancing the performance of solar cells via luminescent down-shifting of the incident spectrum: A review', *Solar Energy Materials and Solar Cells*, vol. 93, no. 8, pp. 1182–1194, Aug. 2009, doi: 10.1016/j.solmat.2009.02.020.

[37]   D. Alonso-Álvarez *et al.*, 'Luminescent down-shifting experiment and modelling with multiple photovoltaic technologies', *Progress in Photovoltaics: Research and Applications*, vol. 23, no. 4, pp. 479–497, Apr. 2015, doi: 10.1002/pip.2462.

[38]   B. M. van der Ende, L. Aarts, and A. Meijerink, 'Lanthanide ions as spectral converters for solar cells', *Physical Chemistry Chemical Physics*, vol. 11, no. 47, p. 11081, Nov. 2009, doi: 10.1039/b913877c.

[39]   H.-V. Han *et al.*, 'A Highly Efficient Hybrid GaAs Solar Cell Based on Colloidal-Quantum-Dot-Sensitization', *Sci Rep*, vol. 4, no. 1, p. 5734, Jul. 2014, doi: 10.1038/srep05734.

References

[40] C. Krishnan *et al.*, 'Efficient light harvesting in hybrid quantum dot–interdigitated back contact solar cells *via* resonant energy transfer and luminescent downshifting', *Nanoscale*, vol. 11, no. 40, pp. 18837–18844, Oct. 2019, doi: 10.1039/C9NR04003J.

[41] A. Solodovnyk *et al.*, 'Optimization of Solution-Processed Luminescent Down-Shifting Layers for Photovoltaics by Customizing Organic Dye Based Thick Films', *Energy Technology*, vol. 4, no. 3, pp. 385–392, Mar. 2016, doi: 10.1002/ente.201500404.

[42] H. Ahmed, J. Doran, and S. J. McCormack, 'Increased short-circuit current density and external quantum efficiency of silicon and dye sensitised solar cells through plasmonic luminescent down-shifting layers', *Solar Energy*, vol. 126, pp. 146–155, Mar. 2016, doi: 10.1016/j.solener.2016.01.003.

[43] V. A. Ansi and N. K. Renuka, 'Sucrose Derived Luminescent Carbon Dots as a Promising Bio-Medical Agent', *Mater Today Proc*, vol. 18, pp. 1724–1728, 2019, doi: 10.1016/j.matpr.2019.05.269.

[44] S. Gardelis and A. G. Nassiopoulou, 'Evidence of significant down-conversion in a Si-based solar cell using CuInS2/ZnS core shell quantum dots', *Appl Phys Lett*, vol. 104, no. 18, p. 183902, May 2014, doi: 10.1063/1.4875616.

[45] L. Etgar, 'Semiconductor Nanocrystals as Light Harvesters in Solar Cells', *Materials*, vol. 6, no. 2, pp. 445–459, Feb. 2013, doi: 10.3390/ma6020445.

[46] X. Liu *et al.*, 'Improved device performance of Si-based heterojunction solar cells by using phosphorus doped Si nanocrystals embedded in SiC host matrix', *AIP Adv*, vol. 9, no. 2, p. 025213, Feb. 2019, doi: 10.1063/1.5088022.

[47] X. Pi, Q. Li, D. Li, and D. Yang, 'Spin-coating silicon-quantum-dot ink to improve solar cell efficiency', *Solar Energy Materials and Solar Cells*, vol. 95, no. 10, pp. 2941–2945, Oct. 2011, doi: 10.1016/j.solmat.2011.06.010.

[48] K. Kumar and H. Subramanian, 'Spin coating of Silver Nanoparticles and Silicon quantum dots for enhanced down conversion efficiency', p. 104, 2013.

[49] M. Stupca, M. Alsalhi, T. Al Saud, A. Almuhanna, and M. H. Nayfeh, 'Enhancement of polycrystalline silicon solar cells using ultrathin films of silicon nanoparticle', *Appl Phys Lett*, vol. 91, no. 6, p. 063107, Aug. 2007, doi: 10.1063/1.2766958.

[50] X. Pi, L. Zhang, and D. Yang, 'Enhancing the Efficiency of Multicrystalline Silicon Solar Cells by the Inkjet Printing of Silicon-Quantum-Dot Ink', *The Journal of Physical Chemistry C*, vol. 116, no. 40, pp. 21240–21243, Oct. 2012, doi: 10.1021/jp307078g.

[51] J. Sacks *et al.*, 'Quantum efficiency measurements of down-shifting using silicon nanocrystals for photovoltaic applications', in *2012 38th IEEE Photovoltaic Specialists Conference*, IEEE, Jun. 2012, pp. 000092–000096. doi: 10.1109/PVSC.2012.6317575.

[52] A. Remolina *et al.*, 'Polymorphous silicon thin films obtained by plasma-enhanced chemical vapor deposition using dichlorosilane as silicon precursor', *Nanotechnology*, vol. 20, no. 24, p. 245604, Jun. 2009, doi: 10.1088/0957-4484/20/24/245604.

[53] V. Švrček, A. Slaoui, and J.-C. Muller, 'Silicon nanocrystals as light converter for solar cells', *Thin Solid Films*, vol. 451–452, pp. 384–388, Mar. 2004, doi: 10.1016/j.tsf.2003.10.133.

References

[54]   S. P. Ashby, T. Bian, H. Ning, M. J. Reece, and Y. Chao, 'Thermal Diffusivity of SPS Pressed Silicon Powders and the Potential for Using Bottom–Up Silicon Quantum Dots as a Starting Material', *J Electron Mater*, vol. 44, no. 6, pp. 1931–1935, Jun. 2015, doi: 10.1007/s11664-014-3599-y.

[55]   J. Khan, I. Ullah, and J. Yuan, 'CsPbI $_3$ perovskite quantum dot solar cells: opportunities, progress and challenges', *Mater Adv*, vol. 3, no. 4, pp. 1931–1952, 2022, doi: 10.1039/D1MA01075A.

[56]   S. C. Baker-Finch and K. R. McIntosh, 'One-dimensional photogeneration profiles in silicon solar cells with pyramidal texture', *Progress in Photovoltaics: Research and Applications*, vol. 20, no. 1, pp. 51–61, Jan. 2012, doi: 10.1002/pip.1109.

[57]   W. G. J. H. M. van, A. Meijerink, and R. E. I. Schropp, 'Solar Spectrum Conversion for Photovoltaics Using Nanoparticles', in *Third Generation Photovoltaics*, InTech, 2012. doi: 10.5772/39213.

[58]   Y. Jestin, S. Chandra, B. Cass, H. Ahmed, and S. J. McCormack, 'Down-Shifting of the Incident Light for Photovoltaic Applications', in *Comprehensive Renewable Energy*, Elsevier, 2022, pp. 534–560. doi: 10.1016/B978-0-12-819727-1.00126-6.

[59]   S. Dutta, S. Chatterjee, K. Mallem, Y. H. Cho, and J. Yi, 'Control of size and distribution of silicon quantum dots in silicon dielectrics for solar cell application: A review', *Renew Energy*, vol. 144, pp. 2–14, Dec. 2019, doi: 10.1016/j.renene.2018.06.078.

[60]   S. Schuppler *et al.*, 'Size, shape, and composition of luminescent species in oxidized Si nanocrystals and H-passivated porous Si', *Phys Rev B*, vol. 52, no. 7, pp. 4910–4925, Aug. 1995, doi: 10.1103/PhysRevB.52.4910.

[61]   M. Dasog, Z. Yang, and J. G. C. Veinot, 'Size-controlled solid state synthesis of luminescent silicon nanocrystals using Stöber silica particles', *CrystEngComm*, vol. 14, no. 22, p. 7576, 2012, doi: 10.1039/c2ce25950h.

[62]   F. Pevere, *Optical Properties of Single Silicon Quantum Dots*. KTH School of Engineering Sciences, 2018.

[63]   J.-W. Luo, S.-S. Li, I. Sychugov, F. Pevere, J. Linnros, and A. Zunger, 'Absence of redshift in the direct bandgap of silicon nanocrystals with reduced size', *Nat Nanotechnol*, vol. 12, no. 10, pp. 930–932, Oct. 2017, doi: 10.1038/nnano.2017.190.

[64]   A. P. Alivisatos, 'Perspectives on the Physical Chemistry of Semiconductor Nanocrystals', *J Phys Chem*, vol. 100, no. 31, pp. 13226–13239, Jan. 1996, doi: 10.1021/jp9535506.

[65]   J. Cassidy and M. Zamkov, 'Nanoshell quantum dots: Quantum confinement beyond the exciton Bohr radius', *J Chem Phys*, vol. 152, no. 11, p. 110902, Mar. 2020, doi: 10.1063/1.5126423.

[66]   R. E. Hummel, *Electronic Properties of Materials*. New York, NY: Springer New York, 2011. doi: 10.1007/978-1-4419-8164-6.

[67]   T. V Torchynska and Y. V Vorobiev, *Nanocrystals and quantum dots of group IV semiconductors*. Stevenson Ranch, Calif.: American Scientific (Nanotechnology book series), 2010.

References

[68]   A. S. Karakoti, R. Shukla, R. Shanker, and S. Singh, 'Surface functionalization of quantum dots for biological applications', *Adv Colloid Interface Sci*, vol. 215, pp. 28–45, Jan. 2015, doi: 10.1016/j.cis.2014.11.004.

[69]   S. Wu, L. Cheng, and Q. Wang, 'Excitonic effects and related properties in semiconductor nanostructures: roles of size and dimensionality', *Mater Res Express*, vol. 4, no. 8, p. 085017, Aug. 2017, doi: 10.1088/2053-1591/aa81da.

[70]   Y. Zhang, Y. Liu, C. Li, X. Chen, and Q. Wang, 'Controlled Synthesis of Ag $_2$ S Quantum Dots and Experimental Determination of the Exciton Bohr Radius', *The Journal of Physical Chemistry C*, vol. 118, no. 9, pp. 4918–4923, Mar. 2014, doi: 10.1021/jp501266d.

[71]   B. Uprety and H. Abrahamse, 'Semiconductor quantum dots for photodynamic therapy: Recent advances', *Front Chem*, vol. 10, Aug. 2022, doi: 10.3389/fchem.2022.946574.

[72]   D. Sumanth Kumar, B. Jai Kumar, and H. M. Mahesh, 'Quantum Nanostructures (QDs): An Overview', in *Synthesis of Inorganic Nanomaterials*, Elsevier, 2018, pp. 59–88. doi: 10.1016/B978-0-08-101975-7.00003-8.

[73]   F. S. Riehle, 'The Rational Synthesis of Defect-Free CdE (E=S,Se) Nanocrystals', 2015.

[74]   T. Takagahara and K. Takeda, 'Theory of the quantum confinement effect on excitons in quantum dots of indirect-gap materials', *Phys Rev B*, vol. 46, no. 23, pp. 15578–15581, Dec. 1992, doi: 10.1103/PhysRevB.46.15578.

[75]   G. Ramalingam *et al.*, 'Quantum Confinement Effect of 2D Nanomaterials', in *Quantum Dots - Fundamental and Applications*, IntechOpen, 2020. doi: 10.5772/intechopen.90140.

[76]   F. W. Wise, 'Lead Salt Quantum Dots: the Limit of Strong Quantum Confinement', *Acc Chem Res*, vol. 33, no. 11, pp. 773–780, Nov. 2000, doi: 10.1021/ar970220q.

[77]   B. Delley and E. F. Steigmeier, 'Quantum confinement in Si nanocrystals', *Phys Rev B*, vol. 47, no. 3, pp. 1397–1400, Jan. 1993, doi: 10.1103/PhysRevB.47.1397.

[78]   K. E. Jasim, 'Quantum Dots Solar Cells', in *Solar Cells - New Approaches and Reviews*, InTech, 2015. doi: 10.5772/59159.

[79]   A. I. Ekimov, Al. L. Efros, and A. A. Onushchenko, 'Quantum size effect in semiconductor microcrystals', *Solid State Commun*, vol. 56, no. 11, pp. 921–924, Dec. 1985, doi: 10.1016/S0038-1098(85)80025-9.

[80]   T. van Buuren, L. N. Dinh, L. L. Chase, W. J. Siekhaus, and L. J. Terminello, 'Changes in the Electronic Properties of Si Nanocrystals as a Function of Particle Size', *Phys Rev Lett*, vol. 80, no. 17, pp. 3803–3806, Apr. 1998, doi: 10.1103/PhysRevLett.80.3803.

[81]   S. Lu, B. Wu, Y. Sun, Y. Cheng, F. Liao, and M. Shao, 'Photoluminescence of pure silicon quantum dots embedded in an amorphous silica wire array', *J Mater Chem C Mater*, vol. 5, no. 27, pp. 6713–6717, Jul. 2017, doi: 10.1039/C7TC01117B.

[82]   A. Kole and P. Chaudhuri, 'Growth of silicon quantum dots by oxidation of the silicon nanocrystals embedded within silicon carbide matrix', *AIP Adv*, vol. 4, no. 10, p. 107106, Oct. 2014, doi: 10.1063/1.4897378.

References

[83]   S. Zhu *et al.*, 'Photoluminescence mechanism in graphene quantum dots: Quantum confinement effect and surface/edge state', *Nano Today*, vol. 13, pp. 10–14, 2017, doi: 10.1016/j.nantod.2016.12.006.

[84]   T.-W. Kim, C.-H. Cho, B.-H. Kim, and S.-J. Park, 'Quantum confinement effect in crystalline silicon quantum dots in silicon nitride grown using SiH4 and NH3', *Appl Phys Lett*, vol. 88, no. 12, Mar. 2006, doi: 10.1063/1.2187434.

[85]   Q. Liu *et al.*, 'Exciton Relaxation Dynamics in Photo-Excited CsPbI3 Perovskite Nanocrystals', *Sci Rep*, vol. 6, no. 1, p. 29442, Jul. 2016, doi: 10.1038/srep29442.

[86]   L. Protesescu *et al.*, 'Nanocrystals of Cesium Lead Halide Perovskites (CsPbX$_3$, X = Cl, Br, and I): Novel Optoelectronic Materials Showing Bright Emission with Wide Color Gamut', *Nano Lett*, vol. 15, no. 6, pp. 3692–3696, Jun. 2015, doi: 10.1021/nl5048779.

[87]   S.-T. Ha, R. Su, J. Xing, Q. Zhang, and Q. Xiong, 'Metal halide perovskite nanomaterials: synthesis and applications', *Chem Sci*, vol. 8, no. 4, pp. 2522–2536, 2017, doi: 10.1039/C6SC04474C.

[88]   H. Ebe *et al.*, 'Guanidium iodide treatment of size-controlled CsPbI3 quantum dots for stable crystal phase and highly efficient red LEDs', *Chemical Engineering Journal*, vol. 471, p. 144578, Sep. 2023, doi: 10.1016/j.cej.2023.144578.

[89]   G. Sanità, B. Carrese, and A. Lamberti, 'Nanoparticle Surface Functionalization: How to Improve Biocompatibility and Cellular Internalization', *Front Mol Biosci*, vol. 7, p. 587012, Nov. 2020, doi: 10.3389/fmolb.2020.587012.

[90]   A. Gupta, M. T. Swihart, and H. Wiggers, 'Luminescent Colloidal Dispersion of Silicon Quantum Dots from Microwave Plasma Synthesis: Exploring the Photoluminescence Behavior Across the Visible Spectrum', *Adv Funct Mater*, vol. 19, no. 5, pp. 696–703, Mar. 2009, doi: 10.1002/adfm.200801548.

[91]   M. V. Wolkin, J. Jorne, P. M. Fauchet, G. Allan, and C. Delerue, 'Electronic States and Luminescence in Porous Silicon Quantum Dots: The Role of Oxygen', *Phys Rev Lett*, vol. 82, no. 1, pp. 197–200, Jan. 1999, doi: 10.1103/PhysRevLett.82.197.

[92]   V. Bonu, A. Das, M. Sardar, S. Dhara, and A. K. Tyagi, 'Surface functionalization-enhanced magnetism in SnO$_2$ nanoparticles and its correlation to photoluminescence properties', *J Mater Chem C Mater*, vol. 3, no. 6, pp. 1261–1267, Jan. 2015, doi: 10.1039/C4TC02210F.

[93]   T. Zhou *et al.*, 'Bandgap Tuning of Silicon Quantum Dots by Surface Functionalization with Conjugated Organic Groups', *Nano Lett*, vol. 15, no. 6, pp. 3657–3663, Jun. 2015, doi: 10.1021/nl504051x.

[94]   A. Angı *et al.*, 'Photoluminescence through in-gap states in phenylacetylene functionalized silicon nanocrystals', *Nanoscale*, vol. 8, no. 15, pp. 7849–7853, 2016, doi: 10.1039/C6NR01435F.

[95]   M. Dasog, G. B. De los Reyes, L. V. Titova, F. A. Hegmann, and J. G. C. Veinot, 'Size *vs* Surface: Tuning the Photoluminescence of Freestanding Silicon Nanocrystals Across the Visible Spectrum *via* Surface Groups', *ACS Nano*, vol. 8, no. 9, pp. 9636–9648, Sep. 2014, doi: 10.1021/nn504109a.

References

[96] S. P. Ashby, J. García-Cañadas, G. Min, and Y. Chao, 'Measurement of Thermoelectric Properties of Phenylacetylene-Capped Silicon Nanoparticles and Their Potential in Fabrication of Thermoelectric Materials', *J Electron Mater*, vol. 42, no. 7, pp. 1495–1498, Jul. 2013, doi: 10.1007/s11664-012-2297-x.

[97] S. P. Ashby *et al.*, 'Bridging silicon nanoparticles and thermoelectrics: phenylacetylene functionalization', *Faraday Discuss.*, vol. 176, pp. 349–361, 2014, doi: 10.1039/C4FD00109E.

[98] D. Beri, 'Silicon quantum dots: surface matter, what next?', *Mater Adv*, vol. 4, no. 16, pp. 3380–3398, Aug. 2023, doi: 10.1039/D2MA00984F.

[99] L. Mangolini, E. Thimsen, and U. Kortshagen, 'High-Yield Plasma Synthesis of Luminescent Silicon Nanocrystals', *Nano Lett*, vol. 5, no. 4, pp. 655–659, Apr. 2005, doi: 10.1021/nl050066y.

[100] S. J. Lanham, J. Polito, Z. Xiong, U. R. Kortshagen, and M. J. Kushner, 'Pulsed power to control growth of silicon nanoparticles in low temperature flowing plasmas', *J Appl Phys*, vol. 132, no. 7, Aug. 2022, doi: 10.1063/5.0100380.

[101] N. J. Kramer, R. J. Anthony, M. Mamunuru, E. S. Aydil, and U. R. Kortshagen, 'Plasma-induced crystallization of silicon nanoparticles', *J Phys D Appl Phys*, vol. 47, no. 7, p. 075202, Feb. 2014, doi: 10.1088/0022-3727/47/7/075202.

[102] M. Dworschak *et al.*, 'Silicon nanocrystal synthesis with the atmospheric plasma source HelixJet', *Plasma Processes and Polymers*, vol. 20, no. 2, p. 2200129, Feb. 2023, doi: 10.1002/ppap.202200129.

[103] P. Wollny *et al.*, 'The role of phase transition by nucleation, condensation, and evaporation for the synthesis of silicon nanoparticles in a microwave plasma reactor — Simulation and experiment', *Chemical Engineering Journal*, vol. 453, p. 139695, Feb. 2023, doi: 10.1016/j.cej.2022.139695.

[104] Y. Park, J. Yoo, M.-H. Kang, W. Kwon, and J. Joo, 'Photoluminescent and biodegradable porous silicon nanoparticles for biomedical imaging', *J Mater Chem B*, vol. 7, no. 41, pp. 6271–6292, Oct. 2019, doi: 10.1039/C9TB01042D.

[105] F. K. Başak and E. Kayahan, 'White, blue and cyan luminescence from thermally oxidized porous silicon coated by green synthesized carbon nanostructures', *Opt Mater (Amst)*, vol. 124, p. 111990, Feb. 2022, doi: 10.1016/j.optmat.2022.111990.

[106] N. S. Seroka, R. T. Taziwa, and L. Khotseng, 'Extraction and Synthesis of Silicon Nanoparticles (SiNPs) from Sugarcane Bagasse Ash: A Mini-Review', *Applied Sciences*, vol. 12, no. 5, p. 2310, Feb. 2022, doi: 10.3390/app12052310.

[107] L. T. Canham, 'Silicon quantum wire array fabrication by electrochemical and chemical dissolution of wafers', *Appl Phys Lett*, vol. 57, no. 10, pp. 1046–1048, Sep. 1990, doi: 10.1063/1.103561.

[108] S. Terada, H. Ueda, T. Ono, and K. Saitow, 'Orange–Red Si Quantum Dot LEDs from Recycled Rice Husks', *ACS Sustain Chem Eng*, vol. 10, no. 5, pp. 1765–1776, Feb. 2022, doi: 10.1021/acssuschemeng.1c04985.

References

[109] B. Marciniec, H. Maciejewski, C. Pietraszuk, and P. Pawluc, *Hydrosilylation: A Comprehensive Review on Recent Advances - Google Books*. Springer, 2009. Accessed: Jul. 03, 2020. [Online]. Available: https://books.google.co.uk/books?hl=en&lr=&id=u6bGcegrMgIC&oi=fnd&pg=PR19&dq=hydrosilylation&ots=VqaD8yZntJ&sig=Ifwaleu9bQXFMUh6poS8hVMUDUo&redir_esc=y#v=onepage&q&f=false

[110] J. A. Kelly, A. M. Shukaliak, M. D. Fleischauer, and J. G. C. Veinot, 'Size-Dependent Reactivity in Hydrosilylation of Silicon Nanocrystals', *J Am Chem Soc*, vol. 133, no. 24, pp. 9564–9571, Jun. 2011, doi: 10.1021/ja2025189.

[111] C. Chatgilialoglu, C. Ferreri, Y. Landais, and V. I. Timokhin, 'Thirty Years of (TMS) $_3$ SiH: A Milestone in Radical-Based Synthetic Chemistry', *Chem Rev*, vol. 118, no. 14, pp. 6516–6572, Jul. 2018, doi: 10.1021/acs.chemrev.8b00109.

[112] T. K. Purkait *et al.*, 'Borane-Catalyzed Room-Temperature Hydrosilylation of Alkenes/Alkynes on Silicon Nanocrystal Surfaces', *J Am Chem Soc*, vol. 136, no. 52, pp. 17914–17917, Dec. 2014, doi: 10.1021/ja510120e.

[113] B. F. P. McVey and R. D. Tilley, 'Solution Synthesis, Optical Properties, and Bioimaging Applications of Silicon Nanocrystals', *Acc Chem Res*, vol. 47, no. 10, pp. 3045–3051, Oct. 2014, doi: 10.1021/ar500215v.

[114] Y. Yu and B. A. Korgel, 'Controlled Styrene Monolayer Capping of Silicon Nanocrystals by Room Temperature Hydrosilylation', *Langmuir*, vol. 31, no. 23, pp. 6532–6537, Jun. 2015, doi: 10.1021/acs.langmuir.5b01291.

[115] J. Wang *et al.*, 'A General Route to Efficient Functionalization of Silicon Quantum Dots for High-Performance Fluorescent Probes', *Small*, vol. 8, no. 15, pp. 2430–2435, Aug. 2012, doi: 10.1002/smll.201102627.

[116] M. Simionescu, L. Sacarescu, and G. Sacarescu, 'Microwave-Assisted Synthesis of Functional Polysilanes', *Des Monomers Polym*, vol. 15, no. 2, pp. 127–136, Jan. 2012, doi: 10.1163/156855511X615010.

[117] D. Beri, M. Jakoby, I. A. Howard, D. Busko, B. S. Richards, and A. Turshatov, 'Improved photon absorption in dye-functionalized silicon nanocrystals synthesized *via* microwave-assisted hydrosilylation', *Dalton Transactions*, vol. 49, no. 7, pp. 2290–2299, 2020, doi: 10.1039/C9DT04497C.

[118] D. Beri, D. Busko, A. Mazilkin, I. A. Howard, B. S. Richards, and A. Turshatov, 'Highly photoluminescent and stable silicon nanocrystals functionalized *via* microwave-assisted hydrosilylation', *RSC Adv*, vol. 8, no. 18, pp. 9979–9984, 2018, doi: 10.1039/C7RA13577G.

[119] L. Mangolini and U. Kortshagen, 'Plasma-Assisted Synthesis of Silicon Nanocrystal Inks', *Advanced Materials*, vol. 19, no. 18, pp. 2513–2519, Sep. 2007, doi: 10.1002/adma.200700595.

[120] D. Jurbergs, E. Rogojina, L. Mangolini, and U. Kortshagen, 'Silicon nanocrystals with ensemble quantum yields exceeding 60%', *Appl Phys Lett*, vol. 88, no. 23, Jun. 2006, doi: 10.1063/1.2210788.

References

[121]   J. A. Kelly and J. G. C. Veinot, 'An Investigation into Near-UV Hydrosilylation of Freestanding Silicon Nanocrystals', *ACS Nano*, vol. 4, no. 8, pp. 4645–4656, Aug. 2010, doi: 10.1021/nn101022b.

[122]   S. Mourdikoudis *et al.*, 'Oleic acid/oleylamine ligand pair: a versatile combination in the synthesis of colloidal nanoparticles', *Nanoscale Horiz*, vol. 7, no. 9, pp. 941–1015, 2022, doi: 10.1039/D2NH00111J.

[123]   W. J. Mir *et al.*, 'Lecithin Capping Ligands Enable Ultrastable Perovskite-Phase CsPbI$_3$ Quantum Dots for Rec. 2020 Bright-Red Light-Emitting Diodes', *J Am Chem Soc*, vol. 144, no. 29, pp. 13302–13310, Jul. 2022, doi: 10.1021/jacs.2c04637.

[124]   S. Baek, Y. Kim, and S.-W. Kim, 'Highly photo-stable CsPbI3 perovskite quantum dots via thiol ligand exchange and their polymer film application', *Journal of Industrial and Engineering Chemistry*, vol. 83, pp. 279–284, Mar. 2020, doi: 10.1016/j.jiec.2019.11.038.

[125]   K. Xu *et al.*, 'Room temperature synthesis of cesium lead bromide perovskite magic sized clusters with controlled ratio of carboxylic acid and benzylamine capping ligands', *Solar Energy Materials and Solar Cells*, vol. 208, p. 110341, May 2020, doi: 10.1016/j.solmat.2019.110341.

[126]   J. Zhang *et al.*, 'Highly Luminescent and Stable CsPbI$_3$ Perovskite Nanocrystals with Sodium Dodecyl Sulfate Ligand Passivation for Red-Light-Emitting Diodes', *J Phys Chem Lett*, vol. 12, no. 9, pp. 2437–2443, Mar. 2021, doi: 10.1021/acs.jpclett.1c00008.

[127]   E. Yassitepe *et al.*, 'Amine-Free Synthesis of Cesium Lead Halide Perovskite Quantum Dots for Efficient Light-Emitting Diodes', *Adv Funct Mater*, vol. 26, no. 47, pp. 8757–8763, Dec. 2016, doi: 10.1002/adfm.201604580.

[128]   D. Li, C.-S. Chen, Y.-H. Wu, Z.-G. Zhu, W. Y. Shih, and W.-H. Shih, 'Improving Stability of Cesium Lead Iodide Perovskite Nanocrystals by Solution Surface Treatments', *ACS Omega*, vol. 5, no. 29, pp. 18013–18020, Jul. 2020, doi: 10.1021/acsomega.0c01403.

[129]   F. Liu *et al.*, 'Highly Luminescent Phase-Stable CsPbI3 Perovskite Quantum Dots Achieving Near 100% Absolute Photoluminescence Quantum Yield.', *ACS Nano*, vol. 11, no. 10, pp. 10373–10383, Oct. 2017, doi: 10.1021/acsnano.7b05442.

[130]   A. Swarnkar *et al.*, 'Quantum dot–induced phase stabilization of α-CsPbI$_3$ perovskite for high-efficiency photovoltaics', *Science (1979)*, vol. 354, no. 6308, pp. 92–95, Oct. 2016, doi: 10.1126/science.aag2700.

[131]   D. Alonso-Alvarez, D. Ross, and B. S. Richards, 'Luminescent down-shifting for CdTe solar cells: A review of dyes and simulation of performance', in *2012 38th IEEE Photovoltaic Specialists Conference*, IEEE, Jun. 2012, pp. 000009–000014. doi: 10.1109/PVSC.2012.6317557.

[132]   E.-C. Cho *et al.*, 'Silicon Quantum Dots in a Dielectric Matrix for All-Silicon Tandem Solar Cells', *Adv Optoelectron*, vol. 2007, pp. 1–11, Aug. 2007, doi: 10.1155/2007/69578.

[133] D. Chen, Y. Wang, and M. Hong, 'Lanthanide nanomaterials with photon management characteristics for photovoltaic application', *Nano Energy*, vol. 1, no. 1, pp. 73–90, Jan. 2012, doi: 10.1016/j.nanoen.2011.10.004.

[134] Al. L. Efros and M. Rosen, 'Random Telegraph Signal in the Photoluminescence Intensity of a Single Quantum Dot', *Phys Rev Lett*, vol. 78, no. 6, pp. 1110–1113, Feb. 1997, doi: 10.1103/PhysRevLett.78.1110.

[135] W. Shockley and W. T. Read, 'Statistics of the Recombinations of Holes and Electrons', *Physical Review*, vol. 87, no. 5, pp. 835–842, Sep. 1952, doi: 10.1103/PhysRev.87.835.

[136] W. Shockley and H. J. Queisser, 'Detailed Balance Limit of Efficiency of *p-n* Junction Solar Cells', *J Appl Phys*, vol. 32, no. 3, pp. 510–519, Mar. 1961, doi: 10.1063/1.1736034.

[137] S. Kalytchuk *et al.*, 'Semiconductor Nanocrystals as Luminescent Down-Shifting Layers To Enhance the Efficiency of Thin-Film CdTe/CdS and Crystalline Si Solar Cells', 2014, doi: 10.1021/jp410279z.

[138] B. S. Richards and K. R. McIntosh, 'Overcoming the poor short wavelength spectral response of CdS/CdTe photovoltaic modules via luminescence down-shifting: ray-tracing simulations', *Progress in Photovoltaics: Research and Applications*, vol. 15, no. 1, pp. 27–34, Jan. 2007, doi: 10.1002/pip.723.

[139] E. Klampaftis, D. Ross, S. Seyrling, A. N. Tiwari, and B. S. Richards, 'Increase in short-wavelength response of encapsulated CIGS devices by doping the encapsulation layer with luminescent material', *Solar Energy Materials and Solar Cells*, vol. 101, pp. 62–67, Jun. 2012, doi: 10.1016/j.solmat.2012.02.011.

[140] R. M. Aoki *et al.*, 'Application of heterostructured CdS/ZnS quantum dots as luminescence down-shifting layer in P3HT:PCBM solar cells', *J Lumin*, vol. 237, p. 118178, Sep. 2021, doi: 10.1016/j.jlumin.2021.118178.

[141] S. Ren *et al.*, 'Silicon Quantum Dot Luminescent Solar Concentrators and Downshifters with Antireflection Coatings for Enhancing Perovskite Solar Cell Performance', *ACS Photonics*, vol. 8, no. 8, pp. 2392–2399, Aug. 2021, doi: 10.1021/acsphotonics.1c00550.

[142] A. Flores-Pacheco, M. E. Álvarez-Ramos, and A. Ayón, 'Down-shifting by quantum dots for silicon solar cell applications', in *Solar Cells and Light Management*, Elsevier, 2020, pp. 443–477. doi: 10.1016/B978-0-08-102762-2.00013-6.

[143] R. Lopez-Delgado *et al.*, 'Solar cell efficiency improvement employing down-shifting silicon quantum dots', *Microsystem Technologies*, vol. 24, no. 1, pp. 495–502, Jan. 2018, doi: 10.1007/s00542-017-3405-x.

[144] B. Das *et al.*, 'Spectral conversion by silicon nanocrystal dispersed gel glass: efficiency enhancement of silicon solar cell', *J Phys D Appl Phys*, vol. 55, no. 2, p. 025106, Jan. 2022, doi: 10.1088/1361-6463/ac29e3.

[145] Q. Masaadeh, E. Kaplani, and Y. Chao, 'Luminescent Downshifting Silicon Quantum Dots for Performance Enhancement of Polycrystalline Silicon Solar Cells', *Electronics (Basel)*, vol. 11, no. 15, p. 2433, Aug. 2022, doi: 10.3390/electronics11152433.

References

[146] W. Cao *et al.*, 'One-pot synthesis of double silane-functionalized carbon dots with tunable emission and excellent coating properties for WLEDs application.', *Nanotechnology*, vol. 33, no. 11, p. 115703, Dec. 2021, doi: 10.1088/1361-6528/ac4067.

[147] C. Lin *et al.*, 'Improved efficiency for nanopillar array of c-Si photovoltaic by down-conversion and anti-reflection of quantum dots', A. Freundlich and J.-F. F. Guillemoles, Eds., Feb. 2012, p. 825609. doi: 10.1117/12.908514.

[148] H.-C. Chen *et al.*, 'Enhancement of power conversion efficiency in GaAs solar cells with dual-layer quantum dots using flexible PDMS film', *Solar Energy Materials and Solar Cells*, vol. 104, pp. 92–96, Sep. 2012, doi: 10.1016/j.solmat.2012.05.003.

[149] S. D. Hodgson, W. S. M. Brooks, A. J. Clayton, G. Kartopu, V. Barrioz, and S. J. C. Irvine, 'The impact of quantum dot concentration on the optical properties of QD/PMMA luminescent down-shifting films applied to CdTe photovoltaic devices', *Nano Energy*, vol. 4, pp. 1–6, Mar. 2014, doi: 10.1016/j.nanoen.2013.12.004.

[150] W. Feng, J. Liu, and X. Yu, 'Efficiency enhancement of mono-Si solar cell with CdO nanotip antireflection and down-conversion layer', *RSC Adv.*, vol. 4, no. 93, pp. 51683–51687, 2014, doi: 10.1039/C4RA08328H.

[151] Y. Ahn *et al.*, 'Efficiency Enhancement of GaAs Solar Cell Using Luminescent Down-Shifting Layer Consisting of (CdSe)ZnS Quantum Dots With Calculation and Experiment', *J Sol Energy Eng*, vol. 137, no. 2, Apr. 2015, doi: 10.1115/1.4028700.

[152] B. Sadeghimakki, Z. Gao, and S. Sivoththaman, 'Proof of down-conversion by CdSe/ZnS quantum dots on silicon solar cells', in *2014 IEEE 40th Photovoltaic Specialist Conference (PVSC)*, IEEE, Jun. 2014, pp. 2262–2266. doi: 10.1109/PVSC.2014.6925376.

[153] S.-W. Baek *et al.*, 'Effect of core quantum-dot size on power-conversion-efficiency for silicon solar-cells implementing energy-down-shift using CdSe/ZnS core/shell quantum dots', *Nanoscale*, vol. 6, no. 21, pp. 12524–12531, Aug. 2014, doi: 10.1039/C4NR02472A.

[154] B. Wang, B. Li, T. Shen, M. Li, and J. Tian, 'ZnSe quantum dots downshifting layer for perovskite solar cells', *Journal of Energy Chemistry*, vol. 27, no. 3, pp. 736–741, May 2018, doi: 10.1016/j.jechem.2017.11.021.

[155] M. Hong *et al.*, 'Air-exposing microwave-assisted synthesis of CuInS$_2$/ZnS quantum dots for silicon solar cells with enhanced photovoltaic performance', *RSC Adv*, vol. 5, no. 124, pp. 102682–102688, 2015, doi: 10.1039/C5RA21454H.

[156] Y. Nakamura, Y. Iso, and T. Isobe, 'Bandgap-Tuned CuInS$_2$/ZnS Core/Shell Quantum Dots for a Luminescent Downshifting Layer in a Crystalline Silicon Solar Module', *ACS Appl Nano Mater*, vol. 3, no. 4, pp. 3417–3426, Apr. 2020, doi: 10.1021/acsanm.0c00175.

[157] F. Wang *et al.*, 'Boosting spectral response of multi-crystalline Si solar cells with Mn2+ doped CsPbCl3 quantum dots downconverter', *J Power Sources*, vol. 395, pp. 85–91, Aug. 2018, doi: 10.1016/j.jpowsour.2018.05.066.

References

[158] Y.-C. Kim *et al.*, 'Luminescent down-shifting CsPbBr $_3$ perovskite nanocrystals for flexible Cu(In,Ga)Se $_2$ solar cells', *Nanoscale*, vol. 12, no. 2, pp. 558–562, 2020, doi: 10.1039/C9NR06041C.

[159] Y. Jestin *et al.*, 'Silicon solar cells with nano-crystalline silicon down shifter: experiment and modeling', in *Next Generation (Nano) Photonic and Cell Technologies for Solar Energy Conversion*, L. Tsakalakos, Ed., Aug. 2010, p. 77720B. doi: 10.1117/12.861978.

[160] Z. Ni, S. Zhou, S. Zhao, W. Peng, D. Yang, and X. Pi, 'Silicon nanocrystals: unfading silicon materials for optoelectronics', *Materials Science and Engineering: R: Reports*, vol. 138, pp. 85–117, Oct. 2019, doi: 10.1016/j.mser.2019.06.001.

[161] B. Das *et al.*, 'Tunable dual color emission from the opposite faces of silicon nanoparticle embedded gel-glass', *J Lumin*, vol. 263, p. 120045, Nov. 2023, doi: 10.1016/j.jlumin.2023.120045.

[162] B. G. Gribov *et al.*, 'Production of Silicon Nanoparticles for Use in Solar Cells', *Semiconductors*, vol. 51, no. 13, pp. 1675–1680, Dec. 2017, doi: 10.1134/S1063782617130085.

[163] Z. Deng, X. D. Pi, J. J. Zhao, and D. Yang, 'Photoluminescence from Silicon Nanocrystals in Encapsulating Materials', *J Mater Sci Technol*, vol. 29, no. 3, pp. 221–224, Mar. 2013, doi: 10.1016/j.jmst.2013.01.006.

[164] B. Das, S. M. Hossain, A. K. Pramanick, A. Dey, and M. Ray, 'One-Pot Synthesis of Gel Glass Embedded with Luminescent Silicon Nanoparticles', *ACS Appl Mater Interfaces*, vol. 11, no. 2, pp. 2507–2515, Jan. 2019, doi: 10.1021/acsami.8b17604.

[165] M. F. Abdelbar, M. El-Kemary, and N. Fukata, 'Downshifting of highly energetic photons and energy transfer by Mn-doped perovskite CsPbCl3 nanocrystals in hybrid organic/silicon nanostructured solar cells', *Nano Energy*, vol. 77, p. 105163, Nov. 2020, doi: 10.1016/j.nanoen.2020.105163.

[166] P. Song, S. Hase, S. Zhao, Z. Xu, Y. Iso, and T. Isobe, 'Feasibility of Emission-Enhanced CsPbCl $_3$ Quantum Dots Co-Doped with Mn $^{2+}$ and Er $^{3+}$ as Luminescent Downshifting Layers in Crystalline Silicon Solar Modules', *ACS Appl Nano Mater*, vol. 5, no. 2, pp. 2522–2531, Feb. 2022, doi: 10.1021/acsanm.1c04195.

[167] A. Apostoluk *et al.*, 'Improvement of the solar cell efficiency by the ZnO nanoparticle layer via the down-shifting effect', *Microelectron Eng*, vol. 127, pp. 51–56, Sep. 2014, doi: 10.1016/j.mee.2014.04.025.

[168] A. Apostoluk *et al.*, 'Investigation of luminescent properties of ZnO nanoparticles for their use as a down-shifting layer on solar cells', *physica status solidi c*, vol. 10, no. 10, pp. 1301–1307, Oct. 2013, doi: 10.1002/pssc.201200950.

[169] M. Dai Prè *et al.*, 'Preparation and characterization of down shifting ZnS:Mn/PMMA nanocomposites for improving photovoltaic silicon solar cell efficiency', *Mater Chem Phys*, vol. 139, no. 2–3, pp. 531–536, May 2013, doi: 10.1016/j.matchemphys.2013.02.003.

[170] N. Liu, H. Xue, Y. Ji, and J. Wang, 'ZnSe/ZnS core-shell quantum dots incorporated with Ag nanoparticles as luminescent down-shifting layers to enhance the efficiency of Si

References

solar cells', *J Alloys Compd*, vol. 747, pp. 696–702, May 2018, doi: 10.1016/j.jallcom.2018.03.060.

[171] E. Pelayo, A. Zazueta, R. Lopez, E. Saucedo, R. Ruelas, and A. Ayon, 'Silicon solar cell efficiency improvement employing the photoluminescent, down-shifting effects of carbon and CdTe quantum dots', *Mater Renew Sustain Energy*, vol. 5, no. 2, p. 5, May 2016, doi: 10.1007/s40243-016-0070-4.

[172] A. Z. Kainarbay *et al.*, 'Luminescent down shifting CdTe colloidal quantum dots for enhancing polycrystalline silicon solar cells', *Optik (Stuttg)*, vol. 169, pp. 41–47, Sep. 2018, doi: 10.1016/j.ijleo.2018.05.046.

[173] W. G. J. H. M. van Sark, A. Meijerink, R. E. I. Schropp, J. A. M. van Roosmalen, and E. H. Lysen, 'Modeling improvement of spectral response of solar cells by deployment of spectral converters containing semiconductor nanocrystals', *Semiconductors*, vol. 38, no. 8, pp. 962–969, Aug. 2004, doi: 10.1134/1.1787120.

[174] W. G. J. H. M. van Sark, A. Meijerink, R. E. I. Schropp, J. A. M. van Roosmalen, and E. H. Lysen, 'Enhancing solar cell efficiency by using spectral converters', *Solar Energy Materials and Solar Cells*, vol. 87, no. 1–4, pp. 395–409, May 2005, doi: 10.1016/j.solmat.2004.07.055.

[175] R. Lopez-Delgado *et al.*, 'Enhanced conversion efficiency in Si solar cells employing photoluminescent down-shifting CdSe/CdS core/shell quantum dots', *Sci Rep*, vol. 7, no. 1, p. 14104, Oct. 2017, doi: 10.1038/s41598-017-14269-0.

[176] K. R. McIntosh *et al.*, 'Increase in external quantum efficiency of encapsulated silicon solar cells from a luminescent down-shifting layer', *Progress in Photovoltaics: Research and Applications*, vol. 17, no. 3, pp. 191–197, May 2009, doi: 10.1002/pip.867.

[177] F. Galluzzi and E. Scafé, 'Spectrum shifting of sunlight by luminescent sheets: Performance evaluation of photovoltaic applications', *Solar Energy*, vol. 33, no. 6, pp. 501–507, 1984, doi: 10.1016/0038-092X(84)90004-5.

[178] T. Jin, S. Inoue, K. Machida, and G. Adachi, 'Photovoltaic Cell Characteristics of Hybrid Silicon Devices with Lanthanide Complex Phosphor-Coating Film', *J Electrochem Soc*, vol. 144, no. 11, pp. 4054–4058, Nov. 1997, doi: 10.1149/1.1838135.

[179] S. Marchionna *et al.*, 'Photovoltaic quantum efficiency enhancement by light harvesting of organo-lanthanide complexes', *J Lumin*, vol. 118, no. 2, pp. 325–329, Jun. 2006, doi: 10.1016/j.jlumin.2005.09.010.

[180] W.-J. Ho, J.-J. Liu, and B.-X. Ke, 'Characterization of Luminescent Down-Shifting Spectral Conversion Effects on Silicon Solar Cells with Various Combinations of Eu-Doped Phosphors', *Materials*, vol. 15, no. 2, p. 452, Jan. 2022, doi: 10.3390/ma15020452.

[181] W.-J. Ho, Y.-J. Deng, J.-J. Liu, S.-K. Feng, and J.-C. Lin, 'Photovoltaic Performance Characterization of Textured Silicon Solar Cells Using Luminescent Down-Shifting Eu-Doped Phosphor Particles of Various Dimensions', *Materials*, vol. 10, no. 1, p. 21, Jan. 2017, doi: 10.3390/ma10010021.

[182] J. Zhang, T. Xuan, P. Li, H. Li, C. Wang, and J. Wang, 'Photovoltaic efficiency enhancement for crystalline silicon solar cells via a Bi-functional layer based on

europium complex@nanozeolite@SiO2', *J Lumin*, vol. 215, p. 116708, Nov. 2019, doi: 10.1016/j.jlumin.2019.116708.

[183] G. Katsagounos, E. Stathatos, N. B. Arabatzis, A. D. Keramidas, and P. Lianos, 'Enhanced photon harvesting in silicon multicrystalline solar cells by new lanthanide complexes as light concentrators', *J Lumin*, vol. 131, no. 8, pp. 1776–1781, Aug. 2011, doi: 10.1016/j.jlumin.2011.04.023.

[184] E. Klampaftis, M. Congiu, N. Robertson, and B. S. Richards, 'Luminescent Ethylene Vinyl Acetate Encapsulation Layers for Enhancing the Short Wavelength Spectral Response and Efficiency of Silicon Photovoltaic Modules', *IEEE J Photovolt*, vol. 1, no. 1, pp. 29–36, Jul. 2011, doi: 10.1109/JPHOTOV.2011.2162720.

[185] K. Kawano, K. Arai, H. Yamada, N. Hashimoto, and R. Nakata, 'Application of rare-earth complexes for photovoltaic precursors', *Solar Energy Materials and Solar Cells*, vol. 48, no. 1–4, pp. 35–41, Nov. 1997, doi: 10.1016/S0927-0248(97)00066-4.

[186] J. Day, S. Senthilarasu, and T. K. Mallick, 'Improving spectral modification for applications in solar cells: A review', *Renew Energy*, vol. 132, pp. 186–205, Mar. 2019, doi: 10.1016/j.renene.2018.07.101.

[187] I. Hod *et al.*, 'Dye versus Quantum Dots in Sensitized Solar Cells: Participation of Quantum Dot Absorber in the Recombination Process', *J Phys Chem Lett*, vol. 2, no. 24, pp. 3032–3035, Dec. 2011, doi: 10.1021/jz201417f.

[188] U. Resch-Genger, M. Grabolle, S. Cavaliere-Jaricot, R. Nitschke, and T. Nann, 'Quantum dots versus organic dyes as fluorescent labels', *Nat Methods*, vol. 5, no. 9, pp. 763–775, Sep. 2008, doi: 10.1038/nmeth.1248.

[189] E. G. Moore, A. P. S. Samuel, and K. N. Raymond, 'From Antenna to Assay: Lessons Learned in Lanthanide Luminescence', *Acc Chem Res*, vol. 42, no. 4, pp. 542–552, Apr. 2009, doi: 10.1021/ar800211j.

[190] M. Bruchez, M. Moronne, P. Gin, S. Weiss, and A. P. Alivisatos, 'Semiconductor Nanocrystals as Fluorescent Biological Labels', *Science (1979)*, vol. 281, no. 5385, pp. 2013–2016, Sep. 1998, doi: 10.1126/science.281.5385.2013.

[191] R. Rothemund, 'Optical modelling of the external quantum efficiency of solar cells with luminescent down-shifting layers', *Solar Energy Materials and Solar Cells*, vol. 120, no. PART B, pp. 616–621, Jan. 2014, doi: 10.1016/j.solmat.2013.10.004.

[192] E. Klampaftis and B. S. Richards, 'Improvement in multi-crystalline silicon solar cell efficiency via addition of luminescent material to EVA encapsulation layer', *Progress in Photovoltaics: Research and Applications*, vol. 19, no. 3, pp. 345–351, May 2011, doi: 10.1002/pip.1019.

[193] B. L. Sopori, 'Effects of encapsulation on the performance of silicon solar cells', in *IEEE Conference on Photovoltaic Specialists*, Kissimmee, FL, USA: IEEE, May 1990, pp. 618–623. doi: 10.1109/PVSC.1990.111694.

[194] C. Cho, J. H. Song, C. Kim, S. Jeong, and J.-Y. Lee, 'Broadband light trapping strategies for quantum-dot photovoltaic cells (>10%) and their issues with the measurement of photovoltaic characteristics', *Sci Rep*, vol. 7, no. 1, p. 17393, Dec. 2017, doi: 10.1038/s41598-017-17550-4.

References

[195] Y. Oteki and Y. Okada, 'External-quantum-efficiency enhancement in quantum-dot solar cells with a Fabry–Perot light-trapping structure', *Heliyon*, vol. 9, no. 8, p. e19312, Aug. 2023, doi: 10.1016/j.heliyon.2023.e19312.

[196] Y. Xu and J. N. Munday, 'Light trapping in a polymer solar cell by tailored quantum dot emission', *Opt Express*, vol. 22, no. S2, p. A259, Mar. 2014, doi: 10.1364/OE.22.00A259.

[197] B. González-Díaz, M. H. Saw, C. Hernández-Rodríguez, J. Sanchiz, Y. S. Khoo, and R. Guerrero-Lemus, 'Evolution of the external quantum efficiency of Si-based PV minimodules with encapsulated down-shifters and aged under UV radiation', *Materials Science and Engineering: B*, vol. 261, p. 114763, Nov. 2020, doi: 10.1016/j.mseb.2020.114763.

[198] J. Cho, 'Recent studies of the photovoltaic device enhancement via multifunctional luminescent down-shifting films', *Jpn J Appl Phys*, vol. 62, no. SE, p. SE0802, May 2023, doi: 10.35848/1347-4065/acb77b.

[199] T. Ozel *et al.*, 'Anisotropic Emission from Multilayered Plasmon Resonator Nanocomposites of Isotropic Semiconductor Quantum Dots', *ACS Nano*, vol. 5, no. 2, pp. 1328–1334, Feb. 2011, doi: 10.1021/nn1030324.

[200] W. Viehmann, 'Thin-Film Scintillators For Extended Ultraviolet (UV) Response Silicon Detectors', H. P. Field, E. F. Zalewski, and F. M. Zweibaum, Eds., Nov. 1979, pp. 90–95. doi: 10.1117/12.957960.

[201] L. H. Slooff *et al.*, 'Efficiency Enhancement of Solar Cells by Application of a Polymer Coating Containing a Luminescent Dye', *J Sol Energy Eng*, vol. 129, no. 3, pp. 272–276, Aug. 2007, doi: 10.1115/1.2735347.

[202] H. A. Ahmed, J. Walshe, M. Kennedy, T. Confrey, J. Doran, and Sarah. J. McCormack, 'Enhancement in solar cell efficiency by luminescent down-shifting layers', *Advances in Energy Research*, vol. 1, no. 2, pp. 117–126, Jun. 2013, doi: 10.12989/eri.2013.1.2.117.

[203] T. Maruyama, Y. Shinyashiki, and S. Osako, 'Energy conversion efficiency of solar cells coated with fluorescent coloring agent', *Solar Energy Materials and Solar Cells*, vol. 56, no. 1, pp. 1–6, Sep. 1998, doi: 10.1016/S0927-0248(98)00105-6.

[204] T. Maruyama and J. Bandai, 'Solar Cell Module Coated with Fluorescent Coloring Agent', *J Electrochem Soc*, vol. 146, no. 12, pp. 4406–4409, Dec. 1999, doi: 10.1149/1.1392651.

[205] W. Septina, A. C. Giovanelli, and N. Gaillard, 'Over 10% Efficient CuIn(S,Se)$_2$ Thin Film Solar Cells Fabricated from Molecular Precursor Ink', in *2022 International Conference on Radar, Antenna, Microwave, Electronics, and Telecommunications (ICRAMET)*, IEEE, Dec. 2022, pp. 171–174. doi: 10.1109/ICRAMET56917.2022.9991230.

[206] A. Kaliyaraj Selva Kumar, Y. Zhang, D. Li, and R. G. Compton, 'A mini-review: How reliable is the drop casting technique?', *Electrochem commun*, vol. 121, p. 106867, Dec. 2020, doi: 10.1016/J.ELECOM.2020.106867.

[207] X. Chen *et al.*, 'Balancing the Molecular Aggregation and Vertical Phase Separation in the Polymer: Nonfullerene Blend Films Enables 13.09% Efficiency of Organic Solar

Cells with Inkjet-Printed Active Layer', *Adv Energy Mater*, vol. 12, no. 12, Mar. 2022, doi: 10.1002/aenm.202200044.

[208] M. Musztyfaga-Staszuk, A. Czupryński, and R. Radev, 'Review of the Chosen Methods of Producing Front Contacts to Transparent Conductive Oxides Layers in Photovoltaic Structures', *Energies (Basel)*, vol. 15, no. 23, p. 9026, Nov. 2022, doi: 10.3390/en15239026.

[209] T. Monzón-Hierro *et al.*, 'A new cost-effective polymeric film containing an Eu(III) complex acting as UV protector and down-converter for Si-based solar cells and modules', *Solar Energy Materials and Solar Cells*, vol. 136, pp. 187–192, May 2015, doi: 10.1016/j.solmat.2015.01.020.

[210] F. I. Chowdhury, A. Alnuaimi, N. El-Atab, M. Nayfeh, and A. Nayfeh, 'Enhanced performance of thin-film amorphous silicon solar cells with a top film of 2.85 nm silicon nanoparticles', *Solar Energy*, vol. 125, pp. 332–338, Feb. 2016, doi: 10.1016/j.solener.2015.12.030.

[211] R. Sun *et al.*, 'Highly efficient ligand-modified manganese ion doped $CsPbCl_3$ perovskite quantum dots for photon energy conversion in silicon solar cells', *Nanoscale*, vol. 12, no. 36, pp. 18621–18628, 2020, doi: 10.1039/D0NR04885B.

[212] J. Song *et al.*, 'Performance Enhancement of Crystal Silicon Solar Cell by a $CsPbBr_3 – Cs_4PbBr_6$ Perovskite Quantum Dot @ZnO/Ethylene Vinyl Acetate Copolymer Downshifting Composite Film', *Solar RRL*, vol. 6, no. 11, Nov. 2022, doi: 10.1002/solr.202200336.

[213] B. Lipovšek *et al.*, 'Optical Model for Simulation and Optimization of Luminescent down-shifting Layers in Photovoltaics', *Energy Procedia*, vol. 84, pp. 3–7, Dec. 2015, doi: 10.1016/j.egypro.2015.12.288.

[214] S. G. Dorofeev *et al.*, 'On the application of thin films of silicon nanoparticles for increasing solar cell efficiency', *Semiconductors*, vol. 48, no. 3, pp. 360–368, Mar. 2014, doi: 10.1134/S1063782614030105.

[215] D. Ko, P. R. Brown, M. G. Bawendi, and V. Bulović, 'p-i-n Heterojunction Solar Cells with a Colloidal Quantum-Dot Absorber Layer', *Advanced Materials*, vol. 26, no. 28, pp. 4845–4850, Jul. 2014, doi: 10.1002/adma.201401250.

[216] N. N. Halder, P. Biswas, S. Kundu, and P. Banerji, 'Au/p-Si Schottky junction solar cell: Effect of barrier height modification by InP quantum dots', *Solar Energy Materials and Solar Cells*, vol. 132, pp. 230–236, Jan. 2015, doi: 10.1016/j.solmat.2014.08.035.

[217] S. Ebnesajjad and A. H. Landrock, 'Characteristics of Adhesive Materials', in *Adhesives Technology Handbook*, Elsevier, 2015, pp. 84–159. doi: 10.1016/B978-0-323-35595-7.00005-X.

[218] K. A. Salman, 'Effect of surface texturing processes on the performance of crystalline silicon solar cell', *Solar Energy*, vol. 147, pp. 228–231, May 2017, doi: 10.1016/j.solener.2016.12.010.

[219] S. Nandy, S. Bhattacharya, S. Das, S. Jana, and U. Gangopadhyay, 'Multicrystalline Silicon Texturing By Novel Bi-Component Etching Solution', *Mater Today Proc*, vol. 4, no. 14, pp. 12671–12677, 2017, doi: 10.1016/j.matpr.2017.10.081.

References

[220] S. Belhadj Mohamed, M. Ben Rabha, and B. Bessais, 'Porous silicon/NaOH texturization surface treatment of crystalline silicon for solar cells', *Solar Energy*, vol. 94, pp. 277–282, Aug. 2013, doi: 10.1016/j.solener.2013.04.026.

[221] S. Zhou *et al.*, 'Acid texturing of large area multi-crystalline silicon wafers for solar cell fabrication', in *2013 International Conference on Materials for Renewable Energy and Environment*, IEEE, Aug. 2013, pp. 31–34. doi: 10.1109/ICMREE.2013.6893608.

[222] J.-H. Im, C.-R. Lee, J.-W. Lee, S.-W. Park, and N.-G. Park, '6.5% efficient perovskite quantum-dot-sensitized solar cell', *Nanoscale*, vol. 3, no. 10, p. 4088, 2011, doi: 10.1039/c1nr10867k.

[223] C. Liu *et al.*, 'Efficiency and stability enhancement of perovskite solar cells by introducing CsPbI3 quantum dots as an interface engineering layer', *NPG Asia Mater*, vol. 10, no. 6, pp. 552–561, Jun. 2018, doi: 10.1038/s41427-018-0055-0.

[224] J. Kim *et al.*, 'Alkali acetate-assisted enhanced electronic coupling in CsPbI3 perovskite quantum dot solids for improved photovoltaics', *Nano Energy*, vol. 66, p. 104130, Dec. 2019, doi: 10.1016/j.nanoen.2019.104130.

[225] Y. Cao, D. Wu, P. Zhu, D. Shan, X. Zeng, and J. Xu, 'Down-Shifting and Anti-Reflection Effect of CsPbBr3 Quantum Dots/Multicrystalline Silicon Hybrid Structures for Enhanced Photovoltaic Properties', *Nanomaterials*, vol. 10, no. 4, p. 775, Apr. 2020, doi: 10.3390/nano10040775.

[226] S. Morozova, M. Alikina, A. Vinogradov, and M. Pagliaro, 'Silicon Quantum Dots: Synthesis, Encapsulation, and Application in Light-Emitting Diodes', *Front Chem*, vol. 8, Apr. 2020, doi: 10.3389/fchem.2020.00191.

[227] B. Gelloz, F. B. Juangsa, T. Nozaki, K. Asaka, N. Koshida, and L. Jin, 'Si/SiO2 Core/Shell Luminescent Silicon Nanocrystals and Porous Silicon Powders With High Quantum Yield, Long Lifetime, and Good Stability', *Front Phys*, vol. 7, no. APR, p. 47, Apr. 2019, doi: 10.3389/fphy.2019.00047.

[228] X. Liu *et al.*, 'Optimum Quantum Yield of the Light Emission from 2 to 10 nm Hydrosilylated Silicon Quantum Dots', *Particle & Particle Systems Characterization*, vol. 33, no. 1, pp. 44–52, Jan. 2016, doi: 10.1002/ppsc.201500148.

[229] Y. Ding, R. Yamada, R. Gresback, S. Zhou, X. Pi, and T. Nozaki, 'A parametric study of non-thermal plasma synthesis of silicon nanoparticles from a chlorinated precursor', *J Phys D Appl Phys*, vol. 47, no. 48, p. 485202, Dec. 2014, doi: 10.1088/0022-3727/47/48/485202.

[230] R. Gresback, T. Nozaki, and K. Okazaki, 'Synthesis and oxidation of luminescent silicon nanocrystals from silicon tetrachloride by very high frequency nonthermal plasma', *Nanotechnology*, vol. 22, no. 30, p. 305605, Jul. 2011, doi: 10.1088/0957-4484/22/30/305605.

[231] R. Intartaglia, K. Bagga, and F. Brandi, 'Study on the productivity of silicon nanoparticles by picosecond laser ablation in water: towards gram per hour yield', *Opt Express*, vol. 22, no. 3, p. 3117, Feb. 2014, doi: 10.1364/OE.22.003117.

References

[232] N. G. Semaltianos *et al.*, 'Silicon nanoparticles generated by femtosecond laser ablation in a liquid environment', *Journal of Nanoparticle Research*, vol. 12, no. 2, pp. 573–580, Feb. 2010, doi: 10.1007/s11051-009-9625-y.

[233] P. G. Kuzmin *et al.*, 'Silicon Nanoparticles Produced by Femtosecond Laser Ablation in Ethanol: Size Control, Structural Characterization, and Optical Properties', *The Journal of Physical Chemistry C*, vol. 114, no. 36, pp. 15266–15273, Sep. 2010, doi: 10.1021/jp102174y.

[234] S. Amoruso *et al.*, 'Generation of silicon nanoparticles via femtosecond laser ablation in vacuum', *Appl Phys Lett*, vol. 84, no. 22, pp. 4502–4504, May 2004, doi: 10.1063/1.1757014.

[235] M. Martínez-Carmona and M. Vallet-Regí, 'Advances in Laser Ablation Synthesized Silicon-Based Nanomaterials for the Prevention of Bacterial Infection', *Nanomaterials*, vol. 10, no. 8, p. 1443, Jul. 2020, doi: 10.3390/nano10081443.

[236] M. Rodio, R. Brescia, A. Diaspro, and R. Intartaglia, 'Direct surface modification of ligand-free silicon quantum dots prepared by femtosecond laser ablation in deionized water', *J Colloid Interface Sci*, vol. 465, pp. 242–248, Mar. 2016, doi: 10.1016/j.jcis.2015.11.058.

[237] Y. Xin, T. Kitasako, M. Maeda, and K. Saitow, 'Solvent dependence of laser-synthesized blue-emitting Si nanoparticles: Size, quantum yield, and aging performance', *Chem Phys Lett*, vol. 674, pp. 90–97, Apr. 2017, doi: 10.1016/j.cplett.2017.02.060.

[238] Y. X. Zhang, W. S. Wu, H. L. Hao, and W. Z. Shen, 'Femtosecond laser-induced size reduction and emission quantum yield enhancement of colloidal silicon nanocrystals: effect of laser ablation time', *Nanotechnology*, vol. 29, no. 36, p. 365706, Sep. 2018, doi: 10.1088/1361-6528/aacd75.

[239] E. Gaffet and M. Harmelin, 'Crystal-amorphous phase transition induced by ball-milling in silicon', *Journal of the Less Common Metals*, vol. 157, no. 2, pp. 201–222, Feb. 1990, doi: 10.1016/0022-5088(90)90176-K.

[240] M. Ray, S. Sarkar, N. R. Bandyopadhyay, S. M. Hossain, and A. K. Pramanick, 'Silicon and silicon oxide core-shell nanoparticles: Structural and photoluminescence characteristics', *J Appl Phys*, vol. 105, no. 7, Apr. 2009, doi: 10.1063/1.3100045.

[241] J. Valenta, P. Janda, K. Dohnalová, D. Nižňansky, F. Vácha, and J. Linnros, 'Colloidal suspensions of silicon nanocrystals: from single nanocrystals to photonic structures', *Opt Mater (Amst)*, vol. 27, no. 5, pp. 1046–1049, Feb. 2005, doi: 10.1016/j.optmat.2004.08.060.

[242] Y. Kanemitsu, H. Uto, Y. Masumoto, T. Matsumoto, T. Futagi, and H. Mimura, 'Microstructure and optical properties of free-standing porous silicon films: Size dependence of absorption spectra in Si nanometer-sized crystallites', *Phys Rev B*, vol. 48, no. 4, pp. 2827–2830, Jul. 1993, doi: 10.1103/PhysRevB.48.2827.

[243] Ji, Zhang, Zhang, Quan, Huang, and Wang, 'Fluorescent and Mechanical Properties of Silicon Quantum Dots Modified Sodium Alginate-Carboxymethylcellulose Sodium Nanocomposite Bio-Polymer Films', *Polymers (Basel)*, vol. 11, no. 9, p. 1476, Sep. 2019, doi: 10.3390/polym11091476.

[244] W. C. W. Chan and S. Nie, 'Quantum Dot Bioconjugates for Ultrasensitive Nonisotopic Detection', *Science (1979)*, vol. 281, no. 5385, pp. 2016–2018, Sep. 1998, doi: 10.1126/science.281.5385.2016.

[245] S. Chinnathambi, S. Chen, S. Ganesan, and N. Hanagata, 'Silicon Quantum Dots for Biological Applications', *Adv Healthc Mater*, vol. 3, no. 1, pp. 10–29, Jan. 2014, doi: 10.1002/adhm.201300157.

[246] J. H. Ahire *et al.*, 'Highly Luminescent and Nontoxic Amine-Capped Nanoparticles from Porous Silicon: Synthesis and Their Use in Biomedical Imaging', *ACS Appl Mater Interfaces*, vol. 4, no. 6, pp. 3285–3292, Jun. 2012, doi: 10.1021/am300642m.

[247] B. Sweryda-Krawiec, T. Cassagneau, and J. H. Fendler, 'Surface Modification of Silicon Nanocrystallites by Alcohols', *J Phys Chem B*, vol. 103, no. 44, pp. 9524–9529, Nov. 1999, doi: 10.1021/jp992298p.

[248] L. H. Lie, M. Duerdin, E. M. Tuite, A. Houlton, and B. R. Horrocks, 'Preparation and characterisation of luminescent alkylated-silicon quantum dots', *Journal of Electroanalytical Chemistry*, vol. 538–539, pp. 183–190, Dec. 2002, doi: 10.1016/S0022-0728(02)00994-4.

[249] Y. Chen, L. Sun, F. Liao, Q. Dang, and M. Shao, 'Fluorescent-stable and water-soluble two-component-modified silicon quantum dots and their application for bioimaging', *J Lumin*, vol. 215, p. 116644, Nov. 2019, doi: 10.1016/j.jlumin.2019.116644.

[250] J. P. Wilcoxon and G. A. Samara, 'Tailorable, visible light emission from silicon nanocrystals', *Appl Phys Lett*, vol. 74, no. 21, pp. 3164–3166, May 1999, doi: 10.1063/1.124096.

[251] L. Sacarescu, G. Roman, G. Sacarescu, and M. Simionescu, 'Fluorescence detection system based on silicon quantum dots–polysilane nanocomposites', *Express Polym Lett*, vol. 10, no. 12, pp. 990–1002, 2016, doi: 10.3144/expresspolymlett.2016.92.

[252] X. Cheng, R. Gondosiswanto, S. Ciampi, P. J. Reece, and J. J. Gooding, 'One-pot synthesis of colloidal silicon quantum dots and surface functionalization via thiol–ene click chemistry', *Chemical Communications*, vol. 48, no. 97, p. 11874, 2012, doi: 10.1039/c2cc35954e.

[253] J.-K. Choi, M. X. Dung, and H.-D. Jeong, 'Novel synthesis of covalently linked silicon quantum dot–polystyrene hybrid materials: Silicon quantum dot–polystyrene polymers of tunable refractive index', *Mater Chem Phys*, vol. 148, no. 1–2, pp. 463–472, Nov. 2014, doi: 10.1016/j.matchemphys.2014.08.016.

[254] Q. Li *et al.*, 'Silicon Nanoparticles with Surface Nitrogen: 90% Quantum Yield with Narrow Luminescence Bandwidth and the Ligand Structure Based Energy Law', *ACS Nano*, vol. 10, no. 9, pp. 8385–8393, Sep. 2016, doi: 10.1021/acsnano.6b03113.

[255] J. Wu, J. Dai, Y. Shao, and Y. Sun, 'One-step synthesis of fluorescent silicon quantum dots (Si-QDs) and their application for cell imaging', *RSC Adv*, vol. 5, no. 102, pp. 83581–83587, 2015, doi: 10.1039/C5RA13119G.

[256] J. Wang, D.-X. Ye, G.-H. Liang, J. Chang, J.-L. Kong, and J.-Y. Chen, 'One-step synthesis of water-dispersible silicon nanoparticles and their use in fluorescence lifetime

imaging of living cells', *J. Mater. Chem. B*, vol. 2, no. 27, pp. 4338–4345, 2014, doi: 10.1039/C4TB00366G.

[257] S. Ma, Y. Chen, J. Feng, J. Liu, X. Zuo, and X. Chen, 'One-Step Synthesis of Water-Dispersible and Biocompatible Silicon Nanoparticles for Selective Heparin Sensing and Cell Imaging', *Anal Chem*, vol. 88, no. 21, pp. 10474–10481, Nov. 2016, doi: 10.1021/acs.analchem.6b02448.

[258] Y. Liu *et al.*, 'Highly selective and sensitive fluorescence detection of hydroquinone using novel silicon quantum dots', *Sens Actuators B Chem*, vol. 275, pp. 415–421, Dec. 2018, doi: 10.1016/j.snb.2018.08.073.

[259] L. M. T. Phan *et al.*, 'Synthesis of fluorescent silicon quantum dots for ultra-rapid and selective sensing of Cr(VI) ion and biomonitoring of cancer cells', *Materials Science and Engineering: C*, vol. 93, pp. 429–436, Dec. 2018, doi: 10.1016/j.msec.2018.08.024.

[260] Y. Yi, L. Liu, W. Zeng, B. Lv, and G. Zhu, 'Bifunctional silicon quantum dots sensing platform for selective and sensitive detection of p-dihydroxybenzene with double signals', *Microchemical Journal*, vol. 147, pp. 245–252, Jun. 2019, doi: 10.1016/j.microc.2019.03.018.

[261] R. Lopez-Delgado *et al.*, 'Enhancing the power conversion efficiency of solar cells employing down-shifting silicon quantum dots', *J Phys Conf Ser*, vol. 773, p. 012087, Nov. 2016, doi: 10.1088/1742-6596/773/1/012087.

[262] M. Abdelhameed, S. Aly, P. Maity, E. Manni, O. F. Mohammed, and P. A. Charpentier, 'Impact of the chemical nature and position of spacers on controlling the optical properties of silicon quantum dots', *Physical Chemistry Chemical Physics*, vol. 21, no. 31, pp. 17096–17108, Aug. 2019, doi: 10.1039/C9CP03537K.

[263] S. Ma, T. Yue, X. Xiao, H. Cheng, and D. Zhao, 'A proof of concept study of preparing ultra bright silicon quantum dots based on synergistic effect of reductants', *J Lumin*, vol. 201, pp. 77–84, Sep. 2018, doi: 10.1016/j.jlumin.2018.04.006.

[264] Y. Wang, G. Ding, J.-Y. Mao, Y. Zhou, and S.-T. Han, 'Recent advances in synthesis and application of perovskite quantum dot based composites for photonics, electronics and sensors', *Sci Technol Adv Mater*, vol. 21, no. 1, pp. 278–302, Jan. 2020, doi: 10.1080/14686996.2020.1752115.

[265] H. Huang, L. Polavarapu, J. A. Sichert, A. S. Susha, A. S. Urban, and A. L. Rogach, 'Colloidal lead halide perovskite nanocrystals: synthesis, optical properties and applications', *NPG Asia Mater*, vol. 8, no. 11, pp. e328–e328, Nov. 2016, doi: 10.1038/am.2016.167.

[266] S. Ananthakumar, J. R. Kumar, and S. M. Babu, 'Cesium lead halide ($CsPbX_3$, X = Cl , Br, I) perovskite quantum dots-synthesis, properties, and applications: a review of their present status', *J Photonics Energy*, vol. 6, no. 4, p. 042001, Oct. 2016, doi: 10.1117/1.JPE.6.042001.

[267] J. Zou, M. Li, X. Zhang, and W. Zheng, 'Perovskite quantum dots: Synthesis, applications, prospects, and challenges', *J Appl Phys*, vol. 132, no. 22, p. 220901, Dec. 2022, doi: 10.1063/5.0126496.

[268] X. Ling *et al.*, '14.1% CsPbI3 Perovskite Quantum Dot Solar Cells via Cesium Cation Passivation', *Adv Energy Mater*, vol. 9, no. 28, p. 1900721, Jul. 2019, doi: 10.1002/AENM.201900721.

[269] Q. A. Akkerman *et al.*, 'Solution Synthesis Approach to Colloidal Cesium Lead Halide Perovskite Nanoplatelets with Monolayer-Level Thickness Control', *J Am Chem Soc*, vol. 138, no. 3, pp. 1010–1016, Jan. 2016, doi: 10.1021/jacs.5b12124.

[270] H. S. Yang *et al.*, 'Facile low-energy and high-yield synthesis of stable α-CsPbI3 perovskite quantum dots: Decomposition mechanisms and solar cell applications', *Chemical Engineering Journal*, vol. 454, p. 140331, Feb. 2023, doi: 10.1016/J.CEJ.2022.140331.

[271] M. Kim *et al.*, 'Coordinating Solvent-Assisted Synthesis of Phase-Stable Perovskite Nanocrystals with High Yield Production for Optoelectronic Applications', *Chemistry of Materials*, vol. 33, no. 2, pp. 547–553, Jan. 2021, doi: 10.1021/acs.chemmater.0c03463.

[272] X. Li *et al.*, 'CsPbX $_3$ Quantum Dots for Lighting and Displays: Room-Temperature Synthesis, Photoluminescence Superiorities, Underlying Origins and White Light-Emitting Diodes', *Adv Funct Mater*, vol. 26, no. 15, pp. 2435–2445, Apr. 2016, doi: 10.1002/adfm.201600109.

[273] Q. A. Akkerman *et al.*, 'Strongly emissive perovskite nanocrystal inks for high-voltage solar cells', *Nat Energy*, vol. 2, no. 2, p. 16194, Dec. 2016, doi: 10.1038/nenergy.2016.194.

[274] H. Huang *et al.*, 'Spontaneous Crystallization of Perovskite Nanocrystals in Nonpolar Organic Solvents: A Versatile Approach for their Shape-Controlled Synthesis', *Angewandte Chemie International Edition*, vol. 58, no. 46, pp. 16558–16562, Nov. 2019, doi: 10.1002/anie.201906862.

[275] Z. Long, H. Ren, J. Sun, J. Ouyang, and N. Na, 'High-throughput and tunable synthesis of colloidal CsPbX $_3$ perovskite nanocrystals in a heterogeneous system by microwave irradiation', *Chemical Communications*, vol. 53, no. 71, pp. 9914–9917, Aug. 2017, doi: 10.1039/C7CC04862A.

[276] Q. Pan *et al.*, 'Microwave-assisted synthesis of high-quality "all-inorganic" CsPbX $_3$ (X = Cl, Br, I) perovskite nanocrystals and their application in light emitting diodes', *J Mater Chem C Mater*, vol. 5, no. 42, pp. 10947–10954, 2017, doi: 10.1039/C7TC03774K.

[277] Y. Li, H. Huang, Y. Xiong, S. V Kershaw, and A. L. Rogach, 'Revealing the Formation Mechanism of CsPbBr3 Perovskite Nanocrystals Produced via a Slowed-Down Microwave-Assisted Synthesis.', *Angew Chem Int Ed Engl*, vol. 57, no. 20, pp. 5833–5837, May 2018, doi: 10.1002/anie.201713332.

[278] W. Zhan, L. Meng, C. Shao, X. Wu, K. Shi, and H. Zhong, 'In Situ Patterning Perovskite Quantum Dots by Direct Laser Writing Fabrication', *ACS Photonics*, vol. 8, no. 3, pp. 765–770, Mar. 2021, doi: 10.1021/acsphotonics.1c00118.

[279] E. A. Erazo, H. E. Sánchez-Godoy, A. F. Gualdrón-Reyes, S. Masi, and I. Mora-Seró, 'Photo-Induced Black Phase Stabilization of CsPbI3 QDs Films', *Nanomaterials*, vol. 10, no. 8, p. 1586, Aug. 2020, doi: 10.3390/nano10081586.

References

[280] Brewer Science, 'Overcoming spin-coating challenges for square substrates - Brewer Science'. Accessed: Nov. 05, 2023. [Online]. Available: https://www.brewerscience.com/bid-79975-overcoming-spin-coating-challenges-for-square-substrates/

[281] G. A. Luurtsema, 'SPIN COATING FOR RECTANGULAR SUBSTRATES', 1997. Accessed: Nov. 05, 2023. [Online]. Available: https://www2.eecs.berkeley.edu/Pubs/TechRpts/1997/ERL-97-49.pdf

[282] POLOS, 'Square Substrates spin coating'. Accessed: Nov. 05, 2023. [Online]. Available: https://www.spincoating.com/en/applications/square-substrates-sol-gel/209/

[283] E. and M. National Academies of Sciences, *Reproducibility and Replicability in Science*. Washington, D.C.: National Academies Press, 2019. doi: 10.17226/25303.

[284] K. N. Shinde, S. J. Dhoble, H. C. Swart, and K. Park, 'Basic Mechanisms of Photoluminescence', Springer, Berlin, Heidelberg, 2012, pp. 41–59. doi: 10.1007/978-3-642-34312-4_2.

[285] H. B. Bebb and E. W. Williams, 'Chapter 4 Photoluminescence I: Theory', in *Semiconductors and Semimetals*, vol. 8, no. C, Elsevier, 1972, pp. 181–320. doi: 10.1016/S0080-8784(08)62345-5.

[286] S. A. Empedocles, R. Neuhauser, K. Shimizu, and M. G. Bawendi, 'Photoluminescence from Single Semiconductor Nanostructures', *Advanced Materials*, vol. 11, no. 15, pp. 1243–1256, Oct. 1999, doi: 10.1002/(SICI)1521-4095(199910)11:15<1243::AID-ADMA1243>3.0.CO;2-2.

[287] Pilkington, 'Pilkington Optiwhite™ for Solar Applications'. Accessed: Mar. 22, 2021. [Online]. Available: https://www.pilkington.com/en/global/products/product-categories/solar-energy/pilkington-optiwhite-for-solar-applications#productrange

[288] B. J. Inkson, 'Scanning electron microscopy (SEM) and transmission electron microscopy (TEM) for materials characterization', in *Materials Characterization Using Nondestructive Evaluation (NDE) Methods*, Elsevier, 2016, pp. 17–43. doi: 10.1016/B978-0-08-100040-3.00002-X.

[289] A. A. Ismail, F. R. van de Voort, and J. Sedman, 'Chapter 4 Fourier transform infrared spectroscopy: Principles and applications', in *Techniques and Instrumentation in Analytical Chemistry*, vol. 18, no. C, Elsevier, 1997, pp. 93–139. doi: 10.1016/S0167-9244(97)80013-3.

[290] V. B. Apte, *Flammability testing of materials used in construction, transport and mining*. Woodhead Publishing Limited, 2006. doi: 10.1533/9781845691042.

[291] L. La Notte *et al.*, 'Influence of encapsulation materials on the optical properties and conversion efficiency of heat-sealed flexible polymer solar cells', 2014, doi: 10.1016/j.surfcoat.2013.12.058.

[292] W. Tao and Y. Du, 'The optical properties of solar cells before and after encapsulation', *Solar Energy*, vol. 122, pp. 718–726, Dec. 2015, doi: 10.1016/j.solener.2015.10.007.

References

[293] S.-Y. Lien, P.-J. Lai, W.-R. Chen, C.-H. Liu, P.-W. Sze, and C.-J. Huang, 'The Annealing Effect at Different Temperatures for Organic-Inorganic Perovskite Quantum Dots', *Crystals (Basel)*, vol. 12, no. 2, p. 204, Jan. 2022, doi: 10.3390/cryst12020204.

[294] D. Ma *et al.*, 'Stability study of all-inorganic perovskite CsPbBr3 QDs@SiO2/EVA film composites prepared by one-step', *J Cryst Growth*, vol. 560–561, p. 126045, Apr. 2021, doi: 10.1016/j.jcrysgro.2021.126045.

[295] J. Shi, W. Ge, W. Gao, M. Xu, J. Zhu, and Y. Li, 'Enhanced Thermal Stability of Halide Perovskite CsPbX $_3$ Nanocrystals by a Facile TPU Encapsulation', *Adv Opt Mater*, vol. 8, no. 4, Feb. 2020, doi: 10.1002/adom.201901516.

[296] S. Wang *et al.*, 'Thermal tolerance of perovskite quantum dots dependent on A-site cation and surface ligand', *Nat Commun*, vol. 14, no. 1, p. 2216, Apr. 2023, doi: 10.1038/s41467-023-37943-6.

[297] Y. Iso, M. Eri, R. Hiroyoshi, K. Kano, and T. Isobe, 'Improving the thermal resistance of fluorescent CsPb(Br,I) $_3$ perovskite quantum dots by surface modification with perfluorodecanoic acid', *R Soc Open Sci*, vol. 9, no. 8, Aug. 2022, doi: 10.1098/rsos.220475.

[298] K. Fujimoto, T. Hayakawa, Y. Xu, N. Jingu, and K. Saitow, 'Stability of Silicon Quantum Dots Against Solar Light/Hot Water: RGB Foldable Films and Ligand Engineering', *ACS Sustain Chem Eng*, vol. 10, no. 44, pp. 14451–14463, Nov. 2022, doi: 10.1021/acssuschemeng.2c03791.

[299] J. Bisquert and E. J. Juarez-Perez, 'The Causes of Degradation of Perovskite Solar Cells', *J Phys Chem Lett*, vol. 10, no. 19, pp. 5889–5891, Oct. 2019, doi: 10.1021/acs.jpclett.9b00613.

[300] Tektronix, '2450 Source Measure Unit (SMU) Instrument Datasheet | Tektronix'. Accessed: Jul. 15, 2023. [Online]. Available: https://www.tek.com/en/datasheet/smu-2400-graphical-sourcemeter/model-2450-touchscreen-source-measure-unit-smu-instrument

[301] 'SCHOTT Advanced Optics BG42 Bandpass NIR-cut filter'. Accessed: Jul. 07, 2022. [Online]. Available: https://www.schott.com/shop/advanced-optics/en/Matt-Filter-Plates/BG42/c/glass-BG42

[302] A. M. Borys, 'An Illustrated Guide to Schlenk Line Techniques', *Organometallics*, vol. 42, no. 3, pp. 182–196, Feb. 2023, doi: 10.1021/acs.organomet.2c00535.

[303] L. Wang *et al.*, 'Ultrafast optical spectroscopy of surface-modified silicon quantum dots: unraveling the underlying mechanism of the ultrabright and color-tunable photoluminescence', *Light: Science & Applications 2015 4:1*, vol. 4, no. 1, pp. e245–e245, Jan. 2015, doi: 10.1038/lsa.2015.18.

[304] C. Xu, L. Wang, D. Li, S. Zhang, L. Chen, and D. Yang, 'Improving the Solar Cell Module Performance by a Uniform Porous Antireflection Layer on Low Iron Solar Glass', *Applied Physics Express*, vol. 6, no. 3, p. 032301, Mar. 2013, doi: 10.7567/APEX.6.032301.

References

[305] M. Boccard *et al.*, 'High-Stable-Efficiency Tandem Thin-Film Silicon Solar Cell With Low-Refractive-Index Silicon-Oxide Interlayer', *IEEE J Photovolt*, vol. 4, no. 6, pp. 1368–1373, Nov. 2014, doi: 10.1109/JPHOTOV.2014.2357495.

[306] H. Nakaya *et al.*, 'Polycrystalline silicon solar cells with V-grooved surface', *Solar Energy Materials and Solar Cells*, vol. 34, no. 1–4, pp. 219–225, Sep. 1994, doi: 10.1016/0927-0248(94)90043-4.

[307] A. I. Privalova, Ju. P. Morozova, E. R. Kashapova, and V. Ja. Artyukhov, 'Spectral and luminescent properties of 1-substituted naphthalenes', *J Appl Spectrosc*, vol. 78, no. 3, pp. 309–317, Jul. 2011, doi: 10.1007/s10812-011-9464-3.

[308] National Center for Biotechnology Information (2024), 'PubChem Compound Summary for CID 931, Naphthalene.' Accessed: Jan. 24, 2024. [Online]. Available: https://pubchem.ncbi.nlm.nih.gov/compound/naphthalene

[309] 'X-Cite 120Q Series', Excelitas Technologies. Accessed: May 25, 2021. [Online]. Available: https://www.excelitas.com/product/x-cite-120q

[310] B. V.G. Mohan, J. Mayandi, J. M. Pearce, K. Muniasamy, and V. Veerapandy, 'Demonstration of a simple encapsulation technique for prototype silicon solar cells', *Mater Lett*, vol. 274, p. 128028, Sep. 2020, doi: 10.1016/j.matlet.2020.128028.

[311] R. P. Mirin, A. C. Gossard, and J. E. Bowers, 'Characterization of InGaAs quantum dot lasers with a single quantum dot layer as an active region', *Physica E Low Dimens Syst Nanostruct*, vol. 2, no. 1–4, pp. 738–742, 1998, doi: 10.1016/S1386-9477(98)00151-9.

[312] M. Z. Farah Khaleda, B. Vengadaesvaran, and N. A. Rahim, 'Spectral response and quantum efficiency evaluation of solar cells: a review', *Energy Materials: Fundamentals to Applications*, pp. 525–566, Jan. 2021, doi: 10.1016/B978-0-12-823710-6.00014-5.

[313] T. J. Milstein, D. M. Kroupa, and D. R. Gamelin, 'Picosecond Quantum Cutting Generates Photoluminescence Quantum Yields Over 100% in Ytterbium-Doped $CsPbCl_3$ Nanocrystals', *Nano Lett*, vol. 18, no. 6, pp. 3792–3799, Jun. 2018, doi: 10.1021/acs.nanolett.8b01066.

[314] L. Meng *et al.*, 'Improving the efficiency of silicon solar cells using in situ fabricated perovskite quantum dots as luminescence downshifting materials', *Nanophotonics*, vol. 9, no. 1, pp. 93–100, Jan. 2020, doi: 10.1515/NANOPH-2019-0320/DOWNLOADASSET/SUPPL/NANOPH-2019-0320_SUPPL.DOC.

[315] Y. Li *et al.*, 'One-Step Preparation of Long-Term Stable and Flexible $CsPbBr_3$ Perovskite Quantum Dots/Ethylene Vinyl Acetate Copolymer Composite Films for White Light-Emitting Diodes', *ACS Appl Mater Interfaces*, vol. 10, no. 18, pp. 15888–15894, May 2018, doi: 10.1021/acsami.8b02857.

[316] X. Yuan *et al.*, 'Photoluminescence Temperature Dependence, Dynamics, and Quantum Efficiencies in Mn^{2+}-Doped $CsPbCl_3$ Perovskite Nanocrystals with Varied Dopant Concentration', *Chemistry of Materials*, vol. 29, no. 18, pp. 8003–8011, Sep. 2017, doi: 10.1021/acs.chemmater.7b03311.

[317] QUANTUM SOLUTIONS, 'Certificate of Analysis for QDot^{TM} ABX3-685', 2022. [Online]. Available: www.quantum-solutions.com

References

[318] K. Aitola *et al.*, 'Encapsulation of commercial and emerging solar cells with focus on perovskite solar cells', *Solar Energy*, vol. 237, pp. 264–283, May 2022, doi: 10.1016/j.solener.2022.03.060.

[319] H. Kim *et al.*, 'Enhanced Stability of MAPbI3 Perovskite Solar Cells using Poly(p-chloro-xylylene) Encapsulation', *Sci Rep*, vol. 9, no. 1, p. 15461, Oct. 2019, doi: 10.1038/s41598-019-51945-9.

[320] J. Idígoras *et al.*, 'Enhancing Moisture and Water Resistance in Perovskite Solar Cells by Encapsulation with Ultrathin Plasma Polymers', *ACS Appl Mater Interfaces*, vol. 10, no. 14, pp. 11587–11594, Apr. 2018, doi: 10.1021/acsami.7b17824.

[321] F. Bella *et al.*, 'Improving efficiency and stability of perovskite solar cells with photocurable fluoropolymers', *Science (1979)*, vol. 354, no. 6309, pp. 203–206, Oct. 2016, doi: 10.1126/science.aah4046.

[322] M. I. Saleem, A. Katware, A. Amin, S.-H. Jung, and J.-H. Lee, 'YCl3-Substituted CsPbI3 Perovskite Nanorods for Efficient Red-Light-Emitting Diodes', *Nanomaterials*, vol. 13, no. 8, p. 1366, Apr. 2023, doi: 10.3390/nano13081366.

[323] M. Koolyk, D. Amgar, S. Aharon, and L. Etgar, 'Kinetics of cesium lead halide perovskite nanoparticle growth; focusing and de-focusing of size distribution', *Nanoscale*, vol. 8, no. 12, pp. 6403–6409, 2016, doi: 10.1039/C5NR09127F.

[324] Z. Pan *et al.*, 'Highly Stable CsPbI3 Perovskite Quantum Dots Enabled by Single SiO2 Coating toward Down-Conversion Light-Emitting Diodes', *Applied Sciences*, vol. 13, no. 13, p. 7529, Jun. 2023, doi: 10.3390/app13137529.

[325] A. Pfreundt *et al.*, 'Post-Processing Thickness Variation of PV Module Materials and Its Impact on Temperature, Mechanical Stress and Power', *36th European Photovoltaic Solar Energy Conference and Exhibition, EU PVSEC*, 2019, doi: 10.4229/EUPVSEC20192019-4CO.4.3.

[326] K. Coldrick, J. Walshe, J. Doran, and G. Amarandei, 'Evaluation of the photon contributions to the solar energy conversion for organic luminescent down-shifting liquid beam splitters in hybrid photovoltaic-thermal (PVT) applications using raytracing Monte Carlo simulations', *Solar Energy Materials and Solar Cells*, vol. 254, p. 112201, Jun. 2023, doi: 10.1016/j.solmat.2023.112201.

[327] M. Rafiee, H. Ahmed, S. Chandra, A. Sethi, and S. J. McCormack, 'Monte Carlo Ray Tracing Modelling of Multi-Crystalline Silicon Photovoltaic Device Enhanced by Luminescent Material', in *2018 IEEE 7th World Conference on Photovoltaic Energy Conversion (WCPEC) (A Joint Conference of 45th IEEE PVSC, 28th PVSEC & 34th EU PVSEC)*, IEEE, Jun. 2018, pp. 3139–3141. doi: 10.1109/PVSC.2018.8547436.

[328] M. Abderrezek, M. Fathi, F. Djahli, and M. Ayad, 'Numerical Simulation of Luminescent Downshifting in Top Cell of Monolithic Tandem Solar Cells', *International Journal of Photoenergy*, vol. 2013, pp. 1–6, 2013, doi: 10.1155/2013/480634.

[329] A. A. Abouelsaood, M. Y. Ghannam, and A. S. Al Omar, 'Limitations of ray tracing techniques in optical modeling of silicon solar cells and photodiodes', *J Appl Phys*, vol. 84, no. 10, pp. 5795–5801, Nov. 1998, doi: 10.1063/1.368844.

References

[330] M. Burgelman, P. Nollet, and S. Degrave, 'Modelling polycrystalline semiconductor solar cells', *Thin Solid Films*, vol. 361–362, pp. 527–532, Feb. 2000, doi: 10.1016/S0040-6090(99)00825-1.

[331] W. G. J. H. M. van Sark, 'Simulating performance of solar cells with spectral downshifting layers', *Thin Solid Films*, vol. 516, no. 20, pp. 6808–6812, Aug. 2008, doi: 10.1016/J.TSF.2007.12.080.

[332] S. S. Dipta, A. Uddin, and G. Conibeer, 'Enhanced light management and optimization of perovskite solar cells incorporating wavelength dependent reflectance modeling', *Heliyon*, vol. 8, no. 11, p. e11380, Nov. 2022, doi: 10.1016/j.heliyon.2022.e11380.

[333] P. Rafieipour, A. Mohandes, M. Moaddeli, and M. Kanani, 'Integrating transfer matrix method into SCAPS-1D for addressing optical losses and per-layer optical properties in perovskite/Silicon tandem solar cells', 2023, doi: https://doi.org/10.48550/arXiv.2308.01132.

[334] A. E. Benzetta, M. Abderrezek, and M. E. Djeghlal, 'Numerical study of CZTS/CZTSSe tandem thin film solar cell using SCAPS-1D', *Optik (Stuttg)*, vol. 242, p. 167320, Sep. 2021, doi: 10.1016/j.ijleo.2021.167320.

[335] M. S. Chowdhury *et al.*, 'Effect of deep-level defect density of the absorber layer and n/i interface in perovskite solar cells by SCAPS-1D', *Results Phys*, vol. 16, p. 102839, Mar. 2020, doi: 10.1016/j.rinp.2019.102839.

[336] G. Reber, R. Steiner, P. Oelhafen, and A. Romanyuk, 'ANGULAR DEPENDENT SOLAR GAIN FOR INSULATING GLASSES FROM EXPERIMENTAL OPTICAL AND THERMAL DATA', in *CISBAT*, EPFL , 2005, pp. 173–178. Accessed: Nov. 15, 2023. [Online]. Available: https://www.semanticscholar.org/paper/ANGULAR-DEPENDENT-SOLAR-GAIN-FOR-INSULATING-GLASSES-Reber-Steiner/29f01f579158190c8f2ee19cbe8e44d0af922a22

[337] R. Couderc, M. Amara, J. Degoulange, F. Madon, and R. Einhaus, 'Encapsulant for glass-glass PV modules for minimum optical losses: gas or EVA?', *Energy Procedia*, vol. 124, pp. 470–477, Sep. 2017, doi: 10.1016/j.egypro.2017.09.283.

[338] A. T. Ngoupo, S. Ouédraogo, F. Zougmoré, and J. M. B. Ndjaka, 'Numerical analysis of ultrathin Sb2Se3-based solar cells by SCAPS-1D numerical simulator device', *Chinese Journal of Physics*, vol. 70, pp. 1–13, Apr. 2021, doi: 10.1016/j.cjph.2020.12.010.

[339] D. Raval, M. Jani, B. Tripathi, D. Verma, and M. Kumar, 'Role of defect density on the electronic transport and current-voltage characteristics of the hole transporter free perovskite solar cell', *Mater Today Proc*, vol. 28, pp. 223–229, 2020, doi: 10.1016/j.matpr.2020.01.587.

[340] F. Hidayanti, 'The Effect of Monocrystalline and Polycrystalline Material Structure on Solar Cell Performance', *International Journal of Emerging Trends in Engineering Research*, vol. 8, no. 7, Jul. 2020, doi: https://doi.org/10.30534/ijeter/2020/87872020.

[341] S. Kaplanis, E. Kaplani, and P. N. Borza, 'PV Defects Identification through a Synergistic Set of Non-Destructive Testing (NDT) Techniques', *Sensors*, vol. 23, no. 6, p. 3016, Mar. 2023, doi: 10.3390/s23063016.

[342] H. Yousuf *et al.*, 'Cell-to-Module Simulation Analysis for Optimizing the Efficiency and Power of the Photovoltaic Module', *Energies 2022, Vol. 15, Page 1176*, vol. 15, no. 3, p. 1176, Feb. 2022, doi: 10.3390/EN15031176.

[343] F. Chen, S. Pathreeker, J. Kaur, and I. D. Hosein, 'Increasing light capture in silicon solar cells with encapsulants incorporating air prisms to reduce metallic contact losses', *Opt Express*, vol. 24, no. 22, p. A1419, Oct. 2016, doi: 10.1364/OE.24.0A1419.

Appendix: Permissions for third party copyright works

Figure in thesis	Work type	Source	Copyright holder and year	Permission request date	Permission licence status and number
Figure 2.1	Figure	[24]	John Wiley and Sons, 2017	10/01/2024	Granted, 5705580374827
Figure 2.2	Figure	[72]	Elsevier, 2018	10/01/2024	Granted, 5705581453815
Figure 2.3	Figure	[72]	Elsevier, 2018	10/01/2024	Granted, 5705581453815
Figure 2.4	Figure	[93]	ACS Publications, 2015	10/01/2024	Granted, N/A
Figure 2.5	Figure	[191]	Elsevier, 2014	10/01/2024	Granted, 5705591328276
	Figure	[36]	Elsevier, 2009	10/01/2024	Granted, 5705600290688